Parson, L., Hawkins, J., Allan, J., et al., 1992
Proceedings of the Ocean Drilling Program, Initial Reports, Vol. 135

10. SITE 840[1]

Shipboard Scientific Party[2]

HOLE 840A

Date occupied: 24 January 1991

Date departed: 24 January 1991

Time on hole: 9 hr, 28 min

Position: 22°13.249′S, 175°44.916′W

Bottom felt (rig floor; m, drill-pipe measurement): 754.5

Distance between rig floor and sea level (m): 11.20

Water depth (drill-pipe measurement from sea level, m): 743.3

Total depth (rig floor; m): 759.00

Penetration (m): 4.50

Number of cores (including cores with no recovery): 1

Total length of cored section (m): 4.50

Total core recovered (m): 4.11

Core recovery (%): 91.3

Oldest sediment cored:
Depth (mbsf): 4.50
Nature: nannofossil ooze with clay
Earliest age: middle Pleistocene
Measured velocity (km/s): 2.012

HOLE 840B

Date occupied: 24 January 1991

Date departed: 29 January 1991

Time on hole: 4 days, 9 hr, 17 min

Position: 22°13.259′S, 175°44.918′W

Bottom felt (rig floor; m, drill-pipe measurement): 754.5

Distance between rig floor and sea level (m): 11.20

Water depth (drill-pipe measurement from sea level, m): 743.3

Total depth (rig floor; m): 1351.80

Penetration (m): 597.30

Number of cores (including cores with no recovery): 63

Total length of cored section (m): 597.30

Total core recovered (m): 176.20

Core recovery (%): 29.5

Oldest sediment cored:
Depth (mbsf): 597.30
Nature: vitric siltstone
Earliest age: late Miocene
Measured velocity (km/s): 2.496

HOLE 840C

Date occupied: 29 January 1991

Date departed: 30 January 1991

Time on hole: 1 day

Position: 22°13.234′S, 175°44.925′W

Bottom felt (rig floor; m, drill-pipe measurement): 754.5

Distance between rig floor and sea level (m): 11.20

Water depth (drill-pipe measurement from sea level, m): 743.3

Total depth (rig floor; m): 1014.00

Penetration (m): 259.50

Number of cores (including cores with no recovery): 13

Total length of cored section (m): 123.50

Total core recovered (m): 74.83

Core recovery (%): 60.6

Oldest sediment cored:
Depth (mbsf): 259.50
Nature: volcanic sandstone
Earliest age: late Miocene
Latest age: late Pliocene
Measured velocity (km/s): 1.795

Principal results: Site 840 is located on the south-central Tonga Platform, which forms the crest of the Tonga Ridge south of 21°S. The site is in 754.4 m of water, approximately 45 km east-northeast of Ata Island, and about 130 km south-southwest from the islands of Tongatapu and 'Eua. The site is located on the west flank of the platform, which at this latitude is about 60 km wide at the 1000-m isobath. The Tonga Ridge has been in existence in some form at least since the Eocene, when it was a component of an ancestral Melanesian proto-arc, comprising the elements of the present Fiji, Lau, Tonga, and New Hebrides arcs. This proto-arc was building during the time of the early history of the South Fiji Basin (magnetic anomalies 12–7, 33–26 Ma) as the ancestral Tonga Trench represented the site of a west-dipping subduction zone. The cessation of backarc spreading in the South Fiji Basin, the rifting off of the New Hebrides Arc at around 10 Ma, the initiation of the Lau Basin rifting (around 5–6 Ma), and the subsequent onset of backarc spreading have all been major tectonic events to have affected the site. The rifting, backarc spreading, and arc volcanism have involved profound thermal upwelling (and crustal disturbance) in the arc and backarc region. These would have affected the uplift, subsidence, sedimentological, and volcanic history of the arc and its environs. It was intended that Site 840 would address the sedimentological and tectonic history of the arc throughout the middle and late Cenozoic, in particular, to understand the nature and age of regional seismostratigraphic hiatuses that are thought to be directly related to these regional events. Specific objectives for the site were (1) the identification of the age of the angular unconformity referred to as Horizon A, thought to be late Miocene/early Pliocene, and presumed to be an event coinciding with the initiation of rifting and opening of the Lau Basin; (2) the identification and timing of the onset of the volcaniclastic deposits associated with the early Tofua Arc, the assessment of their composition and temporal variations in composition, and their possible genetic relations to other source areas, such as the Lau Ridge; and (3) the identification of the rocks presumed to be

[1] Parson, L., Hawkins, J., Allan, J., et al., 1992. *Proc. ODP, Init. Repts.*, 135: Ocean Drilling Program (College Station, TX).
[2] Shipboard Scientific Party is as given in the list of participants preceding the contents.

volcaniclastics below Horizon A, and their regional relationships with potential source areas in the Lau Basin area, such as the Lau Ridge.

The sedimentary sequence recovered at Site 840 is 597.3 m thick (Fig. 1), and ranges in age from Holocene to late Miocene. The sequence is subdivided into three units. Unit I comprises the sediments from the seafloor down to 109.98 m below seafloor (mbsf) and consists of nannofossil oozes, vitric silts, vitric sands, and pumiceous gravels. Unit II extends from 109.98 to 260.5 mbsf, and is dominated by nannofossil chalks and pumiceous gravels, but vitric siltstones and vitric sandstones are also common. Three depositional cycles can be distinguished, fining upward from predominantly pumiceous gravel into predominantly nannofossil chalk. Unit III extends from 260.5 to 597.3 mbsf, and consists of a sequence of volcaniclastic turbidites of vitric sandstone and vitric siltstone, interbedded with nannofossil chalks. Near the base of the sequence, there are also beds of volcaniclastic breccia and conglomerate. Upward through the unit there is a fining and thinning of individual turbidites, indicating a change from proximal to more distal deposition. Volcanic glasses are basaltic to rhyodacitic, as estimated from their refractive indices, and are dominated by intermediate compositions. Alteration of vitric shards is low, but has locally resulted in complete replacement of volcanic glass by smectite, celadonite, and zeolites. Structures in the core appear to be related to soft sediment deformation. Dewatering structures are common in the silty upper portions of volcaniclastic turbidite flows, above planar laminated bases, and occasionally microfaults are visible in clay-rich horizons. In most cases the sense of motion indicated on these microfaults seems to be the same as the paleocurrent direction of coarser material deposited directly on top of them. Middle Pleistocene (Subzone CN14b) to late Miocene (Zone CN9) planktonic foraminifers and calcareous nannofossils were recovered at Site 840 from strata consisting mainly of vitric volcaniclastics with interbedded calcareous oozes and chalk horizons. A probable hiatus of approximately 1 m.y. lies between 95 and 101 mbsf, between Samples 135-840B-10X-CC (late Pliocene nannofossil Subzone CN12a) and -11X-CC (early Pliocene nannofossil Subzone CN10b). The seismic reflector Horizon A thought to be a regional unconformity was not identified biostratigraphically.

The sediment accumulation curve for Site 840 can be divided into five sections, illustrating changes in the rates of accumulation. The lowermost part, between 570 and 320 mbsf, shows rapid sedimentation rates of about 357 mm/k.y. Between 320 and 265 mbsf, the sedimentation rate decreases to about 110 mm/k.y., followed by a return to a very high sedimentation rate of 820 mm/k.y. over the interval from 265 to 101 mbsf. These high rates of sedimentation coincide with a period of deposition of numerous pumiceous gravel and sand beds. Between 101 and 95 mbsf, immediately before the mid-Pliocene hiatus, sedimentation accumulation rates drop to 10 mm/k.y.; above the hiatus, from 95 to 24 mbsf, these rates increase to 50 mm/k.y., and between 24 mbsf to the seafloor, rates drop to 14 mm/k.y.

Paleomagnetic measurements on samples from Holes 840B and 840C showed numerous intervals of reversed and normal polarity. Samples between 40 and 71 mbsf were all normally polarized and probably represent the Gauss Chron (2.47–3.40 Ma); however, no polarity boundaries were found in this part of the hole because of the unsuitability of much of the sediments to preserve good magnetic signatures, so the exact part of the Gauss Chron is uncertain. Beneath the middle Pliocene hiatus at about 95 mbsf, the observed polarities are in reasonably good agreement with the geomagnetic polarity reversal time scale from the Thvera Subchron (4.57–4.77 Ma, 121.8–190.8 mbsf) of the Gilbert Chron down to the top of Chron 4 (6.7 Ma, 521.7 mbsf). The magnetic stratigraphy indicates rapid sedimentation in the late Miocene, ranging from 148–213 m/m.y. Paleomagnetic measurements were obtained from eight oriented advanced hydraulic piston corer (APC) cores of early to mid-Pliocene sediments from the upper part of Hole 840C. Despite scatter caused by drilling disturbance in unconsolidated sediments, a preliminary analysis of the data indicates a $21° \pm 11°$ clockwise rotation of the Tonga Arc with respect to oriented sections in the western Lau Basin.

Although we had some safety concerns before drilling this site because of known hydrocarbon occurrences within 100 km, these proved to be groundless. Methane concentrations remained at background laboratory levels and other volatile hydrocarbon gases were not detected. The organic carbon content of these sediments is very low. Rock-Eval analysis indicated that the organic matter has no hydrocarbon potential and is presumably inertinite. The organic carbon and the carbonate contents both decrease with depth below Unit I, because of dilution by the increasing volcaniclastic contribution to the sediments in Units II and III. At Site 840, it would appear that alteration of volcanic material in the sediments is the major factor causing variations in the calcium, magnesium, and potassium gradients in the pore waters. Concentrations of sulfate and ammonia do not vary much, indicating that the bacterial activity in these sediments is minimal. This is further substantiated by the low level of dissolved manganese. In the most enriched carbonate layer, the observed decrease in alkalinity is probably caused by the precipitation of calcium carbonate in response to an increase in calcium from the alteration of the volcanogenic material.

Physical properties and downhole logging measurements correlate well with lithology. The contact between lithologic Units I and II is marked by decreases in density and velocity, whereas that between Units II and III is marked by increases in these parameters. Within Unit III, a marked increase in the average velocity at about 383 mbsf correlates with a drop in total carbonate percent from around 30%–40% to almost zero. Velocities in Unit II average about 2100 m/s, and in Unit III they average about 2300 m/s, close to values measured with refraction sonobuoys before Leg 135. However, the velocity and all index property measurements show large variations within short depth intervals, reflecting the widely varying lithologies of the turbidite sequences that make up much of the sampled section. Measurements on individual units commonly show decreasing velocity and density values from top to base of individual turbidite units; the variation can be as much as 0.4 g/cm^3 and 300 m/s within a 2-m-thick turbidite. Only one valid temperature measurement was obtained from Site 840; the temperature gradient derived from that reading and the seafloor temperature is 29.3°C/km, a value very similar to that recorded in wells on Tongatapu.

Downhole logs were acquired from 141 to 553 mbsf. The logs show wide variations in measured values, again reflecting the dominant turbidite lithology. High-quality formation microscanner (FMS) images were acquired between 250 and 505 mbsf, and these accurately image the turbidite units to show a continuous cyclicity of light to dark bands that demonstrate the changing lithology within each turbidite unit. Automatic processing of the dip data from the FMS data shows that the bedding orientations progressively increase in dip from an average of 2° at 250 mbsf to 4° at 500 mbsf. Dip direction is consistent toward the north below 250 mbsf; between 100 and 200 mbsf, the magnitude of dip is approximately 2°, but its direction is random.

BACKGROUND AND OBJECTIVES

Background

Location and Bathymetry

Site 840 is located in the central portion of the Tonga Ridge, which extends for more than 1400 km from 15°S, 173°W in the north, to 26.5°S, 177°W in the south (Fig. 2). The Tonga Ridge is readily defined by the 1000-m isobath that encloses a broad flat-lying, platform topography interrupted by the island group of the Kingdom of Tonga. Tonga includes the principal islands of Tongatapu, Vavau, and 'Eua, as well as several other subaerial volcanic outcrops and islands of mixed lithology. The active volcanic-island-arc chain, known as the Tofua Arc, lies juxtaposed to the west of the ridge and comprises several volcanic islands and numerous submarine edifices and shoals.

Site 840 lies on the south-central Tonga Platform on the crest of the Tonga Ridge in 754.4 m of water; it is approximately 45 km east-northeast of Ata island, and about 130 km south-southwest from the islands of Tongatapu and 'Eua. The site is located at 22°13′S, 175°44.9′W, where the platform is about 60 km wide at the 1000-m isobath. The platform crest deepens from the subaerial exposures of the main Tongan islands in the north to a more typical regional depth of 500 m or less that extends as far south as 25°30′S. On its eastern flank, depth increases rapidly across the Tonga forearc into the Tonga trench, where the water depth is more than 10,000 m. To the west, the more gentle gradient into the Lau Basin is interrupted by the linear chain of seamounts and volcanoes of the Tofua Arc, which parallels the Tonga Ridge northward from 24°S (Fig. 2).

On a regional scale, the platform is clearly segmented by a series of approximately orthogonal east- to southeast-striking gullies that incise the seafloor to water depths of as much as 1000 m (Herzer and Exon, 1985; Austin et al., 1989; Tappin et al., 1991). They appear to serve as sediment transport pathways across- and off-platform, and their location is generally thought to be fault-controlled. The origin of this segmentation pattern has been related to a number of factors, among them (1) differential uplift associated with subduction of Pacific Plate seamounts; (2) the location of older faults; (3) boundaries of arc sections that have different tectonic histories; and (4) the location of faults along which individual blocks have rotated in response to oblique subduction (Herzer and Exon, 1985). A comparable structure and lithologic sequence on the other blocks suggests that a similar regional tectonic history was shared by most of the Tonga Ridge. Some doubt exists, however, as to whether the suggested seismostratigraphic correlations (Herzer and Exon, 1985; Austin et al., 1989) between these blocks are valid. Published multichannel seismic data discussed in the seismic stratigraphy section below indicates that although several major unconformities can be traced across the block boundaries, unconformities observed on single-channel data may be more likely related to local events.

The detailed seismic stratigraphy of the region is described in the seismic stratigraphy section below and is only summarized here. The uppermost section of the seismic stratigraphy observed on the Tonga Platform comprises a unit that thickens and dips to the west at the same time that it onlaps the underlying section with an angular, eastward-younging unconformity (Scholl et al., 1985). This unconformity, referred to as Horizon A, was tentatively dated as early Pliocene/latest Miocene using dredged samples (Herzer and Exon, 1985). Dredge data indicates that the uppermost lithologic sequence comprised interbedded calcareous sandstones, volcanic sandstones, and vitric tuffs (Ballance et al., 1985; Exon et al., 1985). Rocks dredged from deeper levels are dominantly coarse volcaniclastic deposits and tuffs, and marls rich in volcaniclastic debris. It was proposed that these two lithologies represented rocks separated by seismic Horizon A. It is possible, but unlikely, that the youngest unit represents an easterly thinning wedge of debris shed from the eastern edifices of extinct or dormant Tofua arc volcanoes such as Ata. The date of the earliest volcanism associated with the Tofua Arc is not known with certainty, but it is widely considered to be no older than 2 Ma, and may be less than 1 Ma. The sequence overlying Horizon A locally onlaps to the east and is time-transgressive, suggesting a gradual encroachment on a paleoplatform gently tilted to the west. The present low-angle, westerly dip of the platform and its surficial sedimentary wedge indicates post-Horizon-A subsidence toward the Lau Basin. A series of major faults are exposed at the western flank of the Tonga Ridge, and these have presumably controlled these movements (Herzer and Exon, 1985).

Westward, toward the belt of Tofua arc volcanoes, the surficial wedge and older underlying beds of the platform sequences are increasingly disrupted by normal faults that offset the seafloor and step down toward the Lau Basin. Superimposed on this regional structural fabric is a dense network of small-scale, shallow fault systems that cut the upper surface of the platform. According to interpretations of GLORIA data (L. Parson, unpubl. data, 1990), these faults are seen to be oriented in approximately conjugate west-northwest trends, but are locally interrupted by more complex patterns of normal faulting. Seismic reflection profiler records confirm the neotectonic pattern as one comprising buried or outcropping systems of normal, reversed, growth faults. These are probably related to a predominantly extensional tectonic regime, but may indicate local compressional phases.

Hydrocarbon Potential at Site 840

Seeps of mature hydrocarbons have been identified on Tongatapu (Maung et al., 1981). These seeps were first recorded in 1968, and their confirmation led to the issuing of exploration licences, acquisition of seismic data, and eventually the drilling of five exploration wells on Tongatapu between 1972 and 1976. The detailed geophysical survey grid acquired by the *JOIDES Resolution* during Leg 135, the results of which are described below, was collected to ensure that Site 840 was not located over any possible hydrocarbon trap or prospect.

The first two commercial wells drilled on Tongatapu were located close to the oil seeps and sited in a basin defined solely on the basis of gravity and magnetic data, without offshore seismic control. Both were plugged as dry holes, after reaching a maximum sub-bottom depth of 1676 m, without reaching an igneous basement (Kumifonua 1 and 2, Tonga-Shell unpubl. data, 1972). After encountering over 120 m of Pliocene-Pleistocene reef limestones, the holes penetrated a thick sequence of fine to coarse volcaniclastic sediments interbedded with a few thin limestones. Both wells bottomed in early Miocene volcaniclastics, significantly younger than the Eocene limestone target predicted from outcrop evidence on the island of 'Eua, 35 km to the south east. Three more wells were drilled in 1976 without encountering hydrocarbons (Kumimonu 1, 2, and 3; Ministry of Lands, unpubl. data). The first two wells bottomed in sills, subsequently dated as Miocene intrusions cutting Oligocene or late Eocene volcaniclastics (e.g., Kumimonu 2, terminal depth = 2131 m). The third well also bottomed in a deeper section of Oligocene volcaniclastics (Kumimonu 3, terminal depth = 2631 m). In all wells, the precise dating of samples was extremely difficult because of the limited abundance of diagnostic microfossils and the apparently high number of derived fragments. Despite the unsuccessful nature of the hydrocarbon exploration in the area, these well data have provided a valuable indication of expected lithologies and regional sediment thickness.

The evidence from the oil seeps on Tongatapu and 'Eua (Sandstrom and Philp, 1984; Sandstrom, 1985) indicate that there is little doubt that a hydrocarbon source exists for the Tongatapu section (block) of the Tonga Ridge. No suitable source rocks, however, were encountered in the commercial wells. Well reports are unanimous in declaring a poor prospect for the section sampled. Total organic carbon (TOC) was low (barely above 0.4%), the spore coloration index peaked at 3.5 at only one point, and vitrinite reflectance only reached 0.28%. Marginal amounts of source rocks for gas were encountered in the wells (at Kumifonua 2), but the little or no kerogen material present showed that no source rock existed in any of the sections sampled. Proposals for a deep source for the hydrocarbons were supported by the work of Buchbinder and Halley (1985) and Sandstrom (1985), who performed gas chromatography/mass spectrometry on the seep oils and borehole samples. It has been proposed that the hydrocarbon source exists in the deeper part of the westward-thickening sedimentary sequence underlying the Tonga Ridge (Scholl and Vallier, 1985). A further possibility exists that the source downdipped to the east, and that westerly migration of oil occurred before the passage of the Louisville Seamount Chain, with the consequent uplift of the Tonga Ridge. One of the objectives of the drilling at Site 840 was to date the seismostratigraphic units to help understand the tectonic events affecting the Tonga Ridge during and postdating the Miocene.

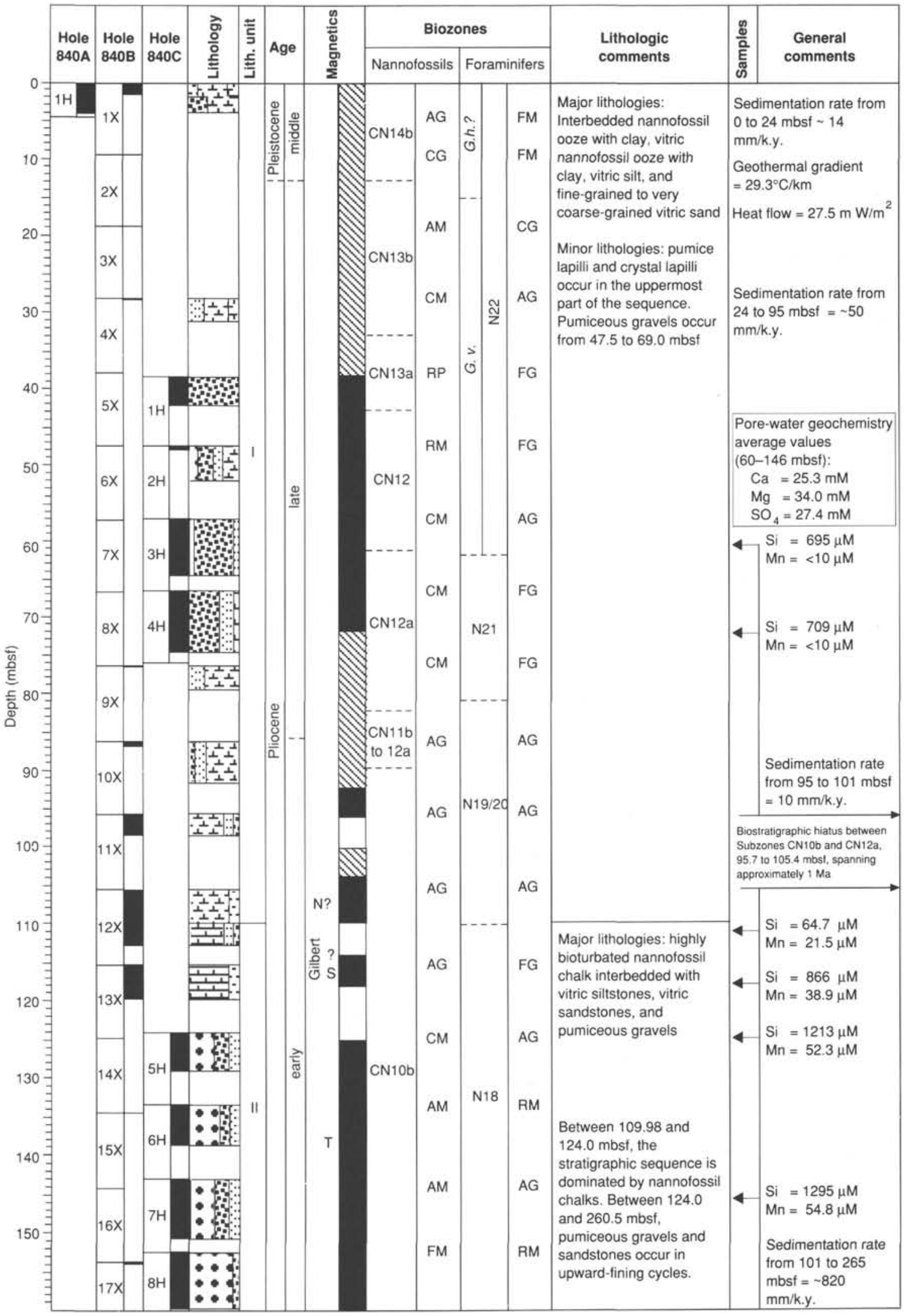

Figure 1. Site summary figure for Site 840. Abbreviations for abundance are as follows: A = abundant, C = common, F = few, R = rare, and B = barren. Those for preservation are as follows: G = good, M = moderate, and P = poor. Planktonic foraminifer zones (after Chaproniere, in press) are abbreviated as follows: *G. h.* = *Globorotalia crassaformis hessi* Subzone and *G. v.* = *Globorotalia crassaformis viola* Subzone.

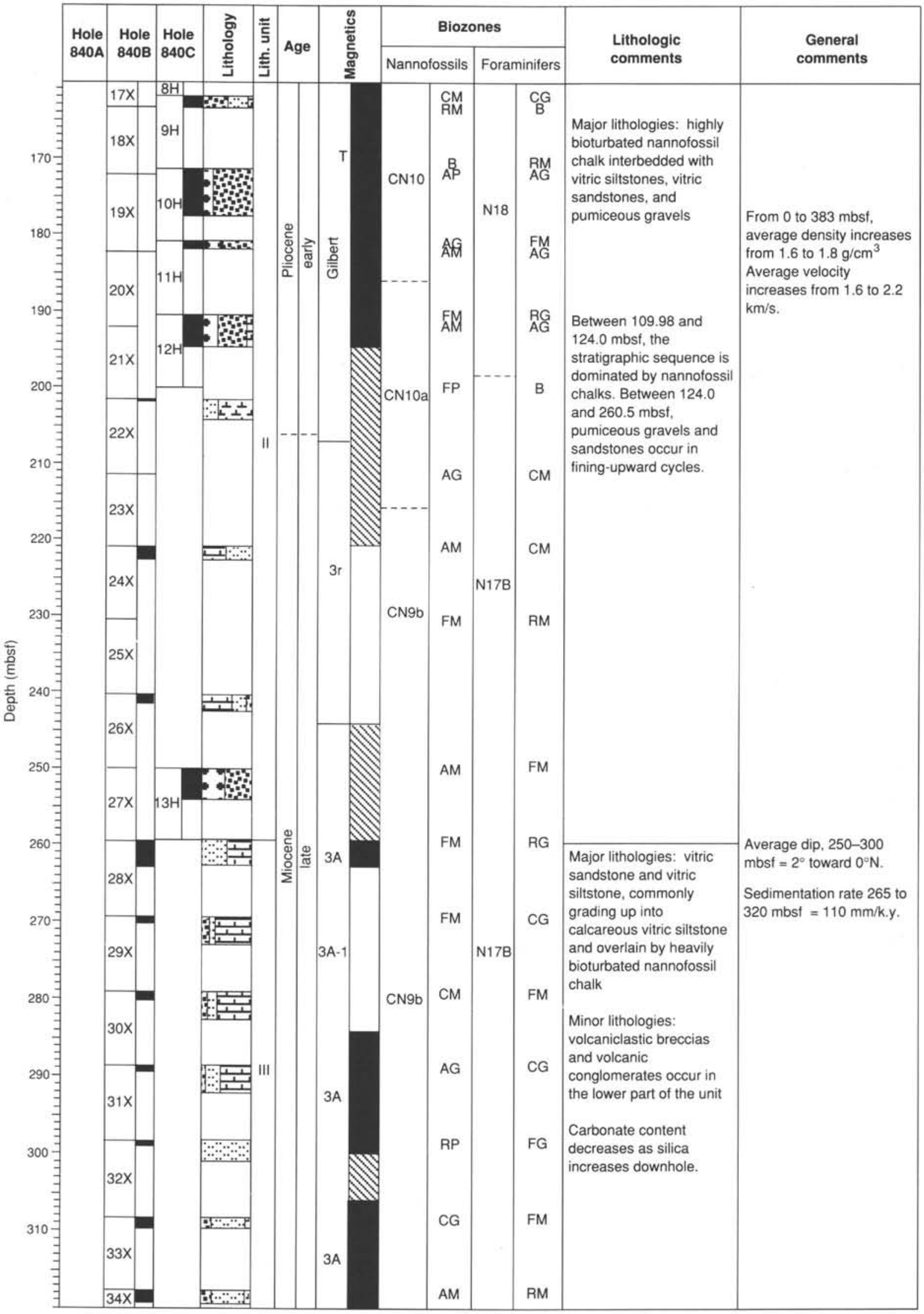

Figure 1 (continued).

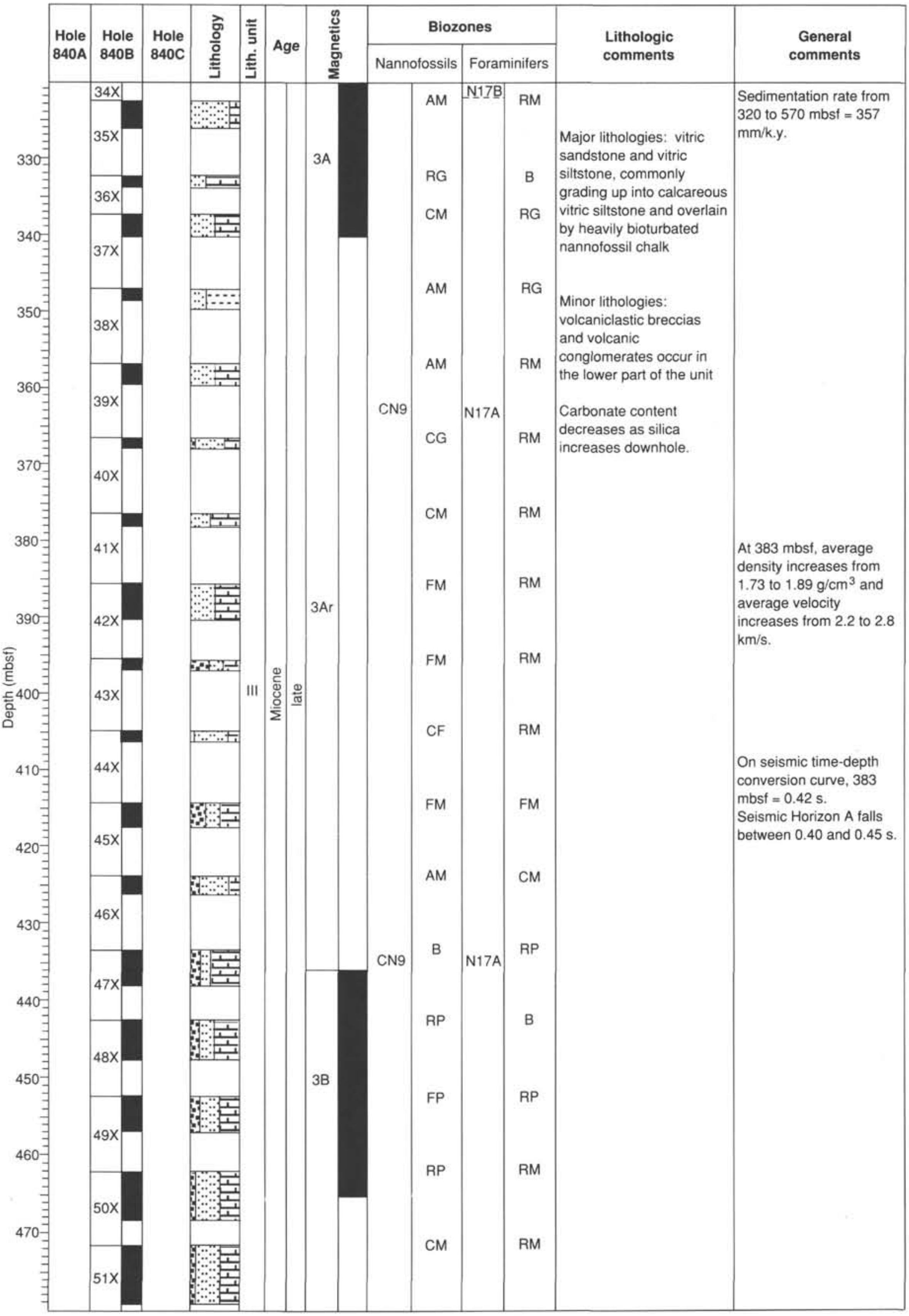

Figure 1 (continued).

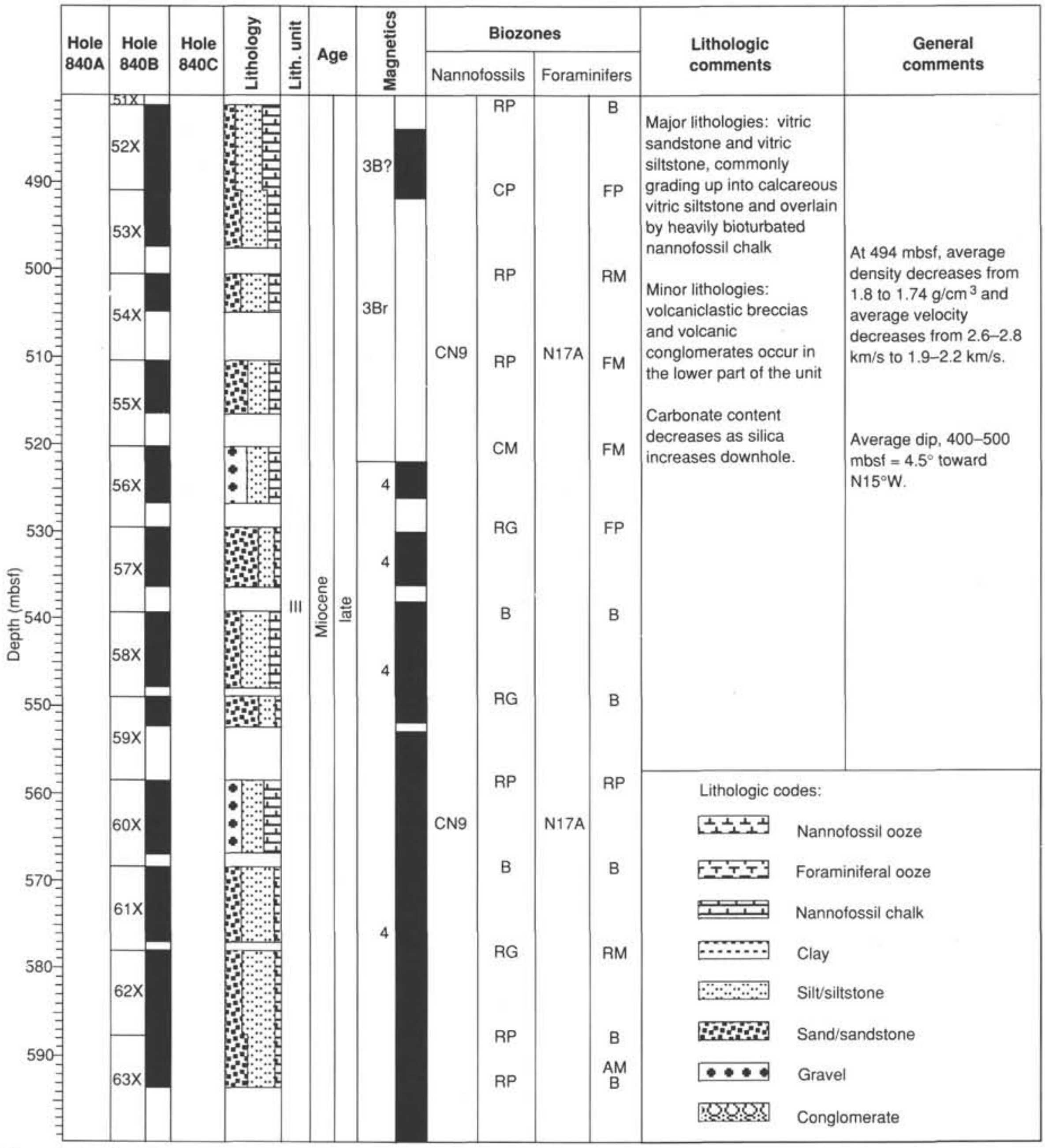

Figure 1 (continued).

Geologic Setting

The Tonga Ridge has been in existence in some form since at least the Eocene, when it was a component of an ancestral Melanesian proto-arc, comprising the Fiji, Lau, Tonga, and New Hebrides arcs, which probably came into existence after the initiation of a subduction zone at sometime during the early Eocene. The details of its evolution in terms of the plate and subplate tectonic history of the region are summarized in the "Introduction and Principal Results" chapter (this volume) and are only referred to here briefly. This Melanesian arc was building during the time of the early history of the South Fiji Basin, as the proto-Tonga Trench represented the site of a west-dipping subduction zone. Magnetic anomalies 12–7 (dated as 32.5–26 Ma, earliest to late Oligocene) have been identified in the South Fiji Basin (Weissel, 1977; Davey, 1982; Malahoff et al., 1982) and are interpreted as having been derived from a ridge-ridge-ridge triple junction that migrated southwestward during the late Oligocene (magnetic anomalies 9–7, 29–25.5 Ma). Using the interpretations of the magnetic anomalies of Malahoff et al. (in press), it appears that there was no active spreading west of the Lau Basin post-29 Ma. During the late Miocene, approximately 10–12 Ma, the New Hebrides Arc probably separated from the Lau-Tonga-Fiji segment following the initiation of subduction beneath the westerly facing New Hebrides Trench. The formation of the Lau backarc basin to the west of the Tonga Ridge from the late Miocene onward, and the initiation of the presently active Tofua Arc to the west of the Tonga Ridge, have further contributed to the uplift/subsidence history and regional tectonic development of the Tonga Ridge. The Tonga Ridge has been extant in some form

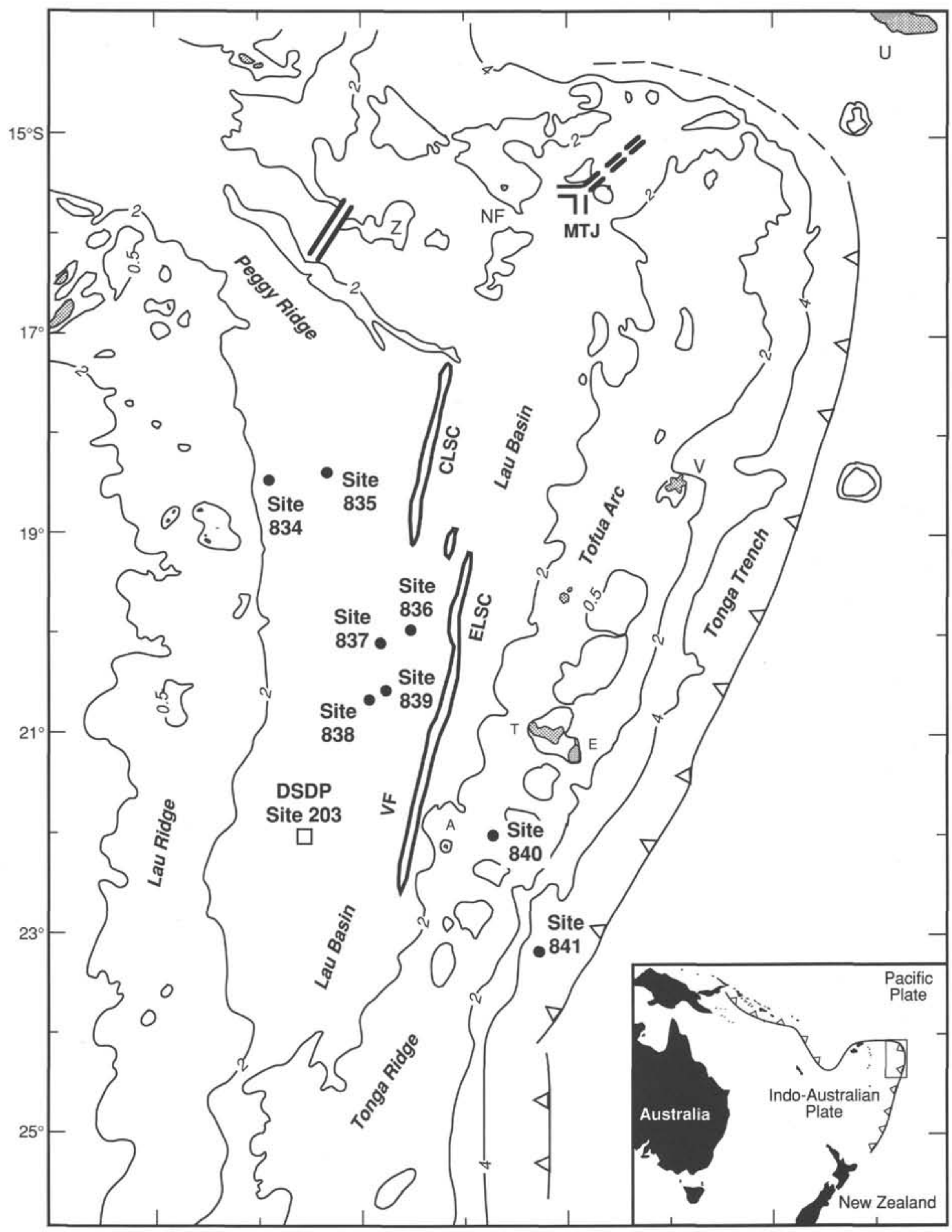

Figure 2. Regional bathymetry of the Lau Basin and the location of Site 840. The figure also illustrates the regional setting for the locations of other drill sites in the Lau Basin and the major geologic features of the Tonga Trench and Lau Basin system. Z = Zephyr Shoal; islands include T = Tongatapu, E = 'Eua, V = Vavau, NF = Niua Fo'ou, A = Ata, and U = Upolu. Locations of the Central Lau (CLSC) and Eastern Lau (ELSC) spreading centers, Valu Fa (VF) Ridge, and Mangatolu Triple Junction (MTJ) are from von Stackelberg (1990), Parson et al. (1990), Hawkins et al. (1989), and Nilsson et al. (1989). The location of DSDP Site 203 is shown as an open square. Contours in thousands of meters.

throughout this history, and the rationale for drilling Site 840 was that the history of subsidence and uplift thought to be associated with each of the regional tectonic events should be recorded in the stratigraphy.

The Tonga Ridge can be described in terms of three structural provinces: the southern, central and northern platforms. The southern platform on which Site 840 is located extends from Tongatapu to 24°S, the latitude of the northwestern part of the Louisville Seamount Chain, and shoals to 200 m. It has a surface incised with northwest-southeast distributary channels, which are probably structurally controlled, and these segments subdivide the platform into several morphological blocks. The Tofua volcanic arc in this area is submarine south of Tongatapu, except for the volcanic island Ata. The central platform extends from Tongatapu to Vavau. Water depths are shallower than on the southern platform and there are many islands and reefs. The structural segmentation of the block is more pronounced here, with deep incisions of the seafloor by the northwest-southeast transverse canyons. The northern platform extends from Vavau to the northernmost part of the Tonga Ridge, at around 15°S. Here the ridge is less well charted, but it appears that the topography is more subdued, with few subaerial expressions, except for volcanic islands of the Tofua Arc, and little clear subdivision into component blocks.

The northern and central blocks have been the most intensively surveyed portions of the Tonga Ridge because of their greater potential for the accumulation of hydrocarbons; consequently, the southern block is less well understood. Surveys completed by the United States Geological Survey during 1982 and 1984 (Scholl and Vallier, 1985; Herzer et al., in press) have provided considerable background data for drilling during Leg 135. Furthermore, the commercial wells drilled on the island of Tongatapu have provided some reconnaissance control. The data from these sites, although restricted to well logs and chippings, have nonetheless been useful to tie in seismic stratigraphy in the Tongatapu block. However, the correlation of these units across adjacent block boundaries becomes increasingly difficult as the units pass to the south.

Extensive reviews of the seismic stratigraphy of the southern platform of the Tonga Ridge have been reported by Scholl et al. (1985), Herzer and Exon (1985), and Tappin et al. (1991). Comparable syntheses of the Tonga Ridge to the north of Tongatapu have been completed by Austin et al. (1989). The conclusions are only briefly summarized here, although the details of the uppermost sequences and their significance for the drilling at Site 840 are reviewed in full.

Seismic Stratigraphy

Multichannel seismic reflection data collected during the USGS Tripartite programs in 1982 and 1984 (Scholl and Vallier, 1985; Herzer et al., 1991) and proprietary commercial seismic data have been used to establish a seismic stratigraphy for the central and southern Tonga Ridge. This stratigraphy has been presented and revised by a number of authors, including Herzer and Exon (1985), Austin et al. (1989), and Tappin (1991). The lack of published data on the northern platform precludes extrapolation of the seismostratigraphic control further north than 18°30′N. The seismic stratigraphy for the rest of the platform has been subdivided into five principal units. In order of decreasing age, the boundary horizons delineating these units have been given the nomenclature V, C, B, and A (Herzer and Exon, 1985). The units have been described in terms of their lithologies and seismic character by these earlier workers, and provisionally dated primarily using dredge samples from the fault-controlled western flanks of the Tonga Ridge. Limited support for the correlations discussed below is provided by subaerial exposures (and commercial well data) on Tongatapu and 'Eua, respectively. Despite these data, unequivocal stratigraphic control on the unconformities that mark the unit boundaries has not been possible until Leg 135 drilling.

Five industry exploration wells drilled on Tongatapu (Maung et al., 1981; Scholl et al., 1985; Katz, 1986) have been used to constrain partially the interpretation of the geophysical data. Supporting data have been derived from analyses of rock chips from holes as deep as 2631 m, outcrop information from 'Eua, and dredge samples from the western scarps of the Tonga platform. On the basis of these data, tentative dates were ascribed to the seismic events recognized as angular unconformities in the Tonga Platform multichannel data over the platform (Herzer and Exon, 1985).

The above regional seismostratigraphic events can be correlated throughout much of the Tonga Ridge, although they are not ubiquitous. More localized smaller scale tectonism of the platform is evidenced in the faulting affecting the uppermost seismic units, seen on both single-channel and multichannel seismic reflection profiles. A wide range of structures are identified, including normal, reversed, synthetic, antithetic, and growth faults. GLORIA sidescan records also image a number of outcropping faults (L. Parson, unpubl. data, 1990), the geometry of which suggests a neotectonic rectilinear conjugate system.

Horizon V marks the upper surface of acoustic basement, generally considered to be of middle to late Eocene age. These basal lithologies are suggested to comprise mainly volcanic arc components, equivalents of which crop out on 'Eua. Horizon C, a conformable horizon traced throughout the central and southern platform, overlies a predominantly volcaniclastic/pelagic mixed(?) arc sequence suggested to contain a limited amount of shallow shelf carbonate facies. The unconformity is thought to span at least the late Oligocene, but this date is largely derived from regional correlations supported by dredged material. If the provisional dating of Horizon C is correct, then it correlates directly with the timing of the decrease of tectonism in the southern Tonga Ridge as backarc extension in the South Fiji Basin began to wane around 26 Ma (Davey, 1982; Malahoff et al., 1982). While this decline in deformation of the south and central Tonga Ridge took place, the effects of the extensional system continued in the northern platform (Tappin, 1991). A major biostratigraphic hiatus involving nondeposition also occurred at the end of the Oligocene, where several complete foraminifer zones are missing throughout the Pacific (Kennett et al., 1972; Kennett, Houtz, et al., 1975; Kennett and von der Borch, 1985; G. Chaproniere, pers. comm., 1991). It is tentatively postulated that this corresponds to a proposed major drop in sea level during the late Oligocene. Additional regional events may have influence on the tectonic history of the Tonga Ridge. At about the same time (10 Ma), there was a reversal of subduction direction along the New Hebrides arc-trench system, reconfiguring the plate geometry to approximate that of the present day. A shallow-water paleoenvironment for the Lau-Tonga Ridge is supported by the absence of middle to late Miocene faunal zones (e.g., Zone N15 foraminifers; G. Chaproniere, pers. comm., 1991), presumably at a low sea-level stand.

Horizon B has been dated as early Miocene and overlies volcaniclastics characterized by discontinuous, lenticular seismic units that may be reefal bodies. The age of Horizon A has been suggested to be latest Miocene/earliest Pliocene as discussed above (Scholl and Vallier, 1985). Although the findings from Leg 135 generally support these data, early tectonic models proposed for its origin have to be revised with our new dating. Scholl and Herzer (in press) review the seismostratigraphic position of Horizon A, suggesting its origin from a period of subaerial erosion, either during rifting of the Lau-Tonga Ridge or subduction of the

Louisville Seamounts or both. After rupture and basin subsidence, the Tonga Platform is thought to have subsided in the west to form the surface onto which the early Pliocene sediments could progressively onlap. Horizon A has been recognized widely throughout the Tonga Ridge.

Detailed Seismic Stratigraphy

A total of 177 km of single-channel seismic reflection profiler records was recorded during the site survey of Site 840 by the *JOIDES Resolution* during Leg 135 (Fig. 3A). These unprocessed records have been preliminarily compiled with existing single-channel and multichannel data (recorded on *S. P. Lee,* Scholl and Vallier, 1985; and *Charles Darwin,* Parson et al., 1989; Fig. 3B). All seismic data recorded by the *JOIDES Resolution* have been recorded digitally and will be processed post cruise. The multichannel seismic reflection profile used to select the final location of Site 840 is illustrated in Figure 4A, which displays several normal synthetic faults flanking a rift block. Complex systems of synthetic and antithetic faults, some of them outcropping, are concentrated around the principal offsets.

Regional isopach maps of the seafloor to the Horizon A interval have been constructed by Herzer and Exon (1985) using multichannel seismic data collected by the *S. P. Lee* in 1982 (Scholl and Vallier, 1985). We have converted our new seismic profiles to true depth using the sonobuoy refraction velocities of Childs (1985). A revised isopach map of the area around Site 840 is presented in Figure 4D. Herzer and Exon (1985) mapped a number of faults in the upper section that roughly defined rhomb-like blocks about 20 km across between north-northwest- and west-southwest-striking conjugate fault sets. We have been able to refine the fault pattern and have traced west-dipping normal faults, with throws up to 100 m, striking around 340°. These offset the Horizon A surface that dips gently toward the north and west from around 400 m depth south of 22°17′S, to more than 650 m north of 22°09′S. Several of the larger offset structures outcrop at the seafloor (Figs. 4B–4C), but throughout the section numerous normal faults with smaller displacements are observed.

Heat Flow Data

No published heat flow data are available for the Tonga Ridge. Two of the commercial wells drilled on Tongatapu (Kumifonua 1 and 2) recorded temperature data downhole. Low thermal gradients of 3.2°C/100 m and 2.91°C/100 m were recorded at these sites.

Scientific Objectives

The scientific objectives for drilling at Site 840 focus on the timing of the regional tectonic events that have affected the Tonga Ridge before and during the evolution of the Lau Basin. The understanding of the volcanic history associated with the basin-forming events, and the subsequent deformation of the sedimentary section and underlying volcanic basement will provide important constraints on the modeling of arc evolution. Specific objectives for the site included:

1. The identification and timing of the onset of the volcaniclastic deposits associated with the early Tofua Arc, the assessment of their composition and temporal variations in composition, and their interrelationship with other source areas, such as the Lau Ridge.
2. The identification of the age of the angular unconformity at Horizon A, thought to be late Miocene/early Pliocene, and reasoned to be the event coinciding with the rifting and opening of the Lau Basin.

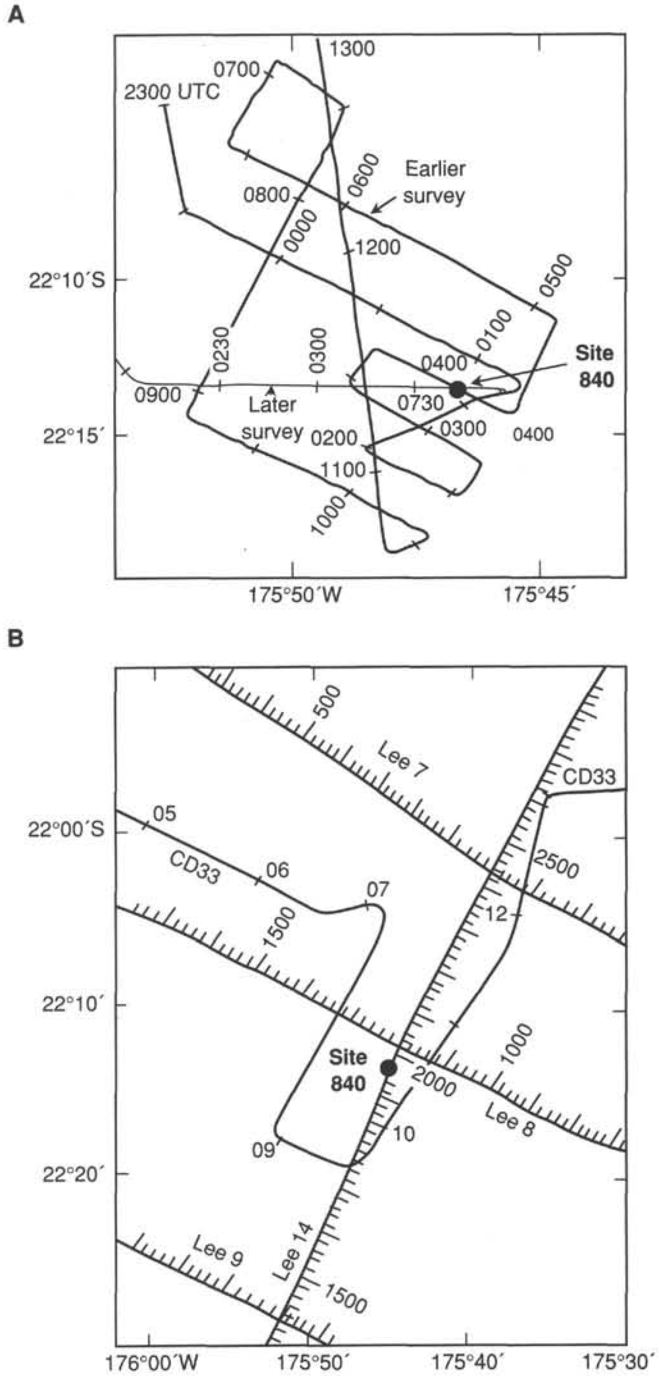

Figure 3. Track charts illustrating the locations of the seismic lines used to select Site 840. **A.** *JOIDES Resolution* during Leg 135. **B.** *Charles Darwin* (CD33; Parson et al., 1990) and *S. P. Lee* (Scholl and Vallier, 1985).

3. The identification of the composition of Subhorizon A volcaniclastics, and their regional relationships with source areas in the Lau Basin area, such as the Lau Ridge.
4. The examination of the relationship, if any, between the recent tectonic evolution of the platform with regional deformation events, such as the approach of the Louisville Seamount Chain collision zone.

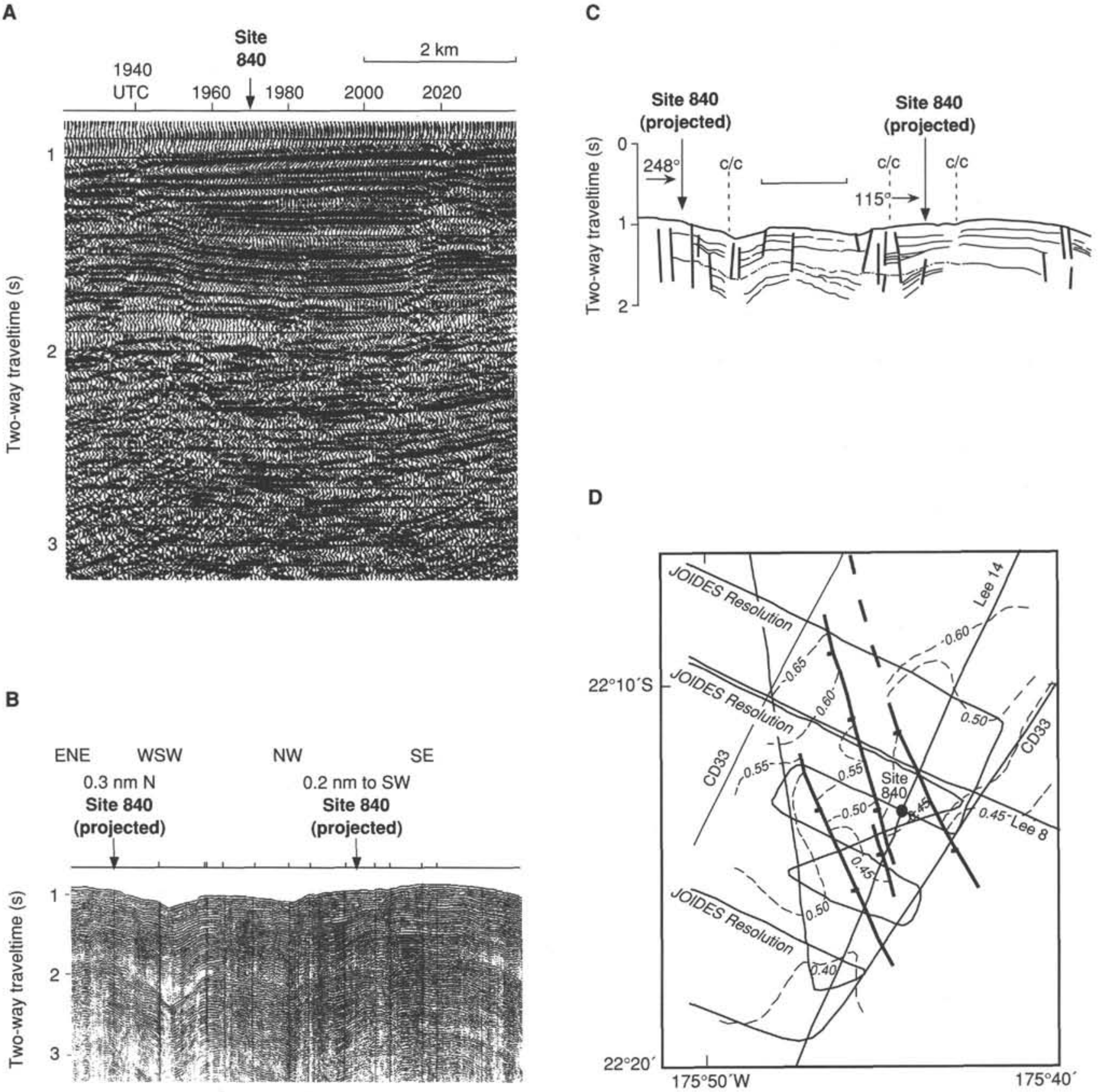

Figure 4. Seismic data for Site 840. **A.** Multichannel seismic reflection profile *S. P. Lee* 14 showing shotpoint 1970, the location of Site 840. **B.** Single-channel seismic record acquired by *JOIDES Resolution* during the site survey. Site 840 is projected into the section. **C.** Interpreted seismic profile across Site 840. Horizon A is highlighted in dot-dash ornament. **D.** Isopach map of Horizon A in kilometers as derived from single-channel seismic data acquired by *JOIDES Resolution*. Bold lines locate faults, ticks on downthrown-side. Fine dashed lines are isopach contours, solid lines are ship's tracks.

OPERATIONS

Introduction

The final location of Site 840 was approved during the cruise by the Pollution Prevention and Safety Panel (PPSP) of the Joint Oceanographic Institutions (JOI) following a review of seismic data recorded between 1100 UTC 5 January and 0100 UTC 6 January by the *JOIDES Resolution* during Leg 135. The 102-nmi transit from Site 839 to Site 840 began at 1300 UTC on 23 January 1990 and took 12.5 hr at an average speed of 8.2 kt. Site 840 lies on the shallow Tonga Platform and was designed to reach and sample a seismic reflector, interpreted as an angular unconformity using multichannel seismic reflection profiling data. The age of this postulated unconformity had been proposed to be late Miocene/early Pliocene. The site also was to serve as a complement to Site 841, helping to determine the temporal and compositional variation of arc volcanism and the history of associated tectonism.

Site Approach and Site Survey

Site 840 is situated at 22°13.25′S, 175°44.92′W in 755 m of water on the northwestern shoulder of the southern Tonga Ridge platform. It lies some 45 km east-northeast from the island of Ata of the Tofua Arc volcanic island chain and 103 km west of the axis of the Tonga Trench.

After slowing to deploy two 80-in.[3] water guns, a single-channel 60-element Teledyne hydrophone streamer, and a Geometrics 801 proton precession magnetometer, the ship completed a 3.8-hr, 19-nmi site geophysical survey (Figs. 3–4). After crossing the site (Fig. 3A), the ship made a Williamson turn to return to the site, and underway geophysical gear was recovered. The water was shallow enough that it allowed the beacon marking the site to be lowered on a taut wire from a boom on the side of the ship. The beacon was recovered after the end of drilling.

Drilling and Logging Summary

The original plan was to drill two adjacent holes at Site 840, with the principal objective of reaching the seismic reflector identified on single-channel and multichannel seismic reflection profiles, the character and age of which was unknown. Hole 840A was planned to be an APC/XCB (extended core barrel) hole that was to core through much of the approximately 450-m-thick sediments estimated to overlie the unconformity. Hole 840B was planned to be an rotary core barrel (RCB) hole that continued coring the sediments above and below the unconformity as time left in the leg would allow. Hole 840B would then be logged.

Hole 840A

Hole 840A was spudded in at 1102 UTC, 24 January 1990, at a position of 22°13.249′S, 175°44.916′W. A mud-line core established the seafloor depth as 754.5 m below the driller's datum. This mud-line core, recovered with the advanced piston corer (APC), represented the sole recovery of Hole 840A (recovery of 4.11 m from 4.0 m core; Table 1). The APC met refusal and stuck in firm pumiceous, gravelly sediments, with the core barrel being bent into an "S" shape. The lower portion of the core barrel broke off and was left in the hole.

Hole 840B

The ship was moved 20 m to the south, and Hole 840B was spudded at 1853 UTC, 24 January 1990 at a position of 22°13.259′S, 175°44.918′W. The same 11-7/16-in. bottom-hole assembly (BHA) was used as in Hole 840A, but coring initially began with the XCB. The seafloor was determined to be at 754.5 m below rig floor (mbrf), and Cores 135-840B-1X to -63X were taken from 0 to 597.3 mbsf, with 597.3 m cored and 176.16 m recovered (recovery of 29.5%). The hole proved quite stable throughout the coring, and drilling ended because of time constraints.

After conditioning the hole for logging with a short trip of the drill string, the bit was dropped with the mechanical bit release (MBR). The open end of the pipe was pulled to 94.8 mbsf, and logs were run as follows:

Run No. 1: "Quad/Combo" (induction/density/sonic/caliper/gamma ray). The log found bottom 25.7 m above the driller's total depth and required 4.08 hr to run.

Run No. 2: Geochemical. The log found bottom 45.7 m above the driller's total depth, but failed on the first run due because of a high-voltage instability in the neutron density tool. The second run of this tool string found bottom 55.5 m above the driller's total depth and required 4.0 hr to run.

Run No. 3: Formation microscanner (FMS)/gamma ray. The log found bottom 67.7 m above the driller's total depth and required 2.72 hr to run.

Hole 840C

One objective of Site 840 was the recovery of oriented cores for use in investigating the structural geology and tectonic evolution of the Tonga Ridge. The use of the XCB in Hole 840B prevented the recovery of oriented cores for these studies and also provided very poor recovery in a volcaniclastic sequence from 124 to 211 mbsf. The decision was thus made to core a third hole with the APC, washing through the initial hard, upper gravel- and pumice-bearing sediments and recoring this section of poor recovery. The nonmagnetic drill collar was again used to minimize the drill-string magnetic overprint on the cores, and the multishot tool provided orientation for all recovered cores.

Hole 840C was located 40 m north of Hole 840B, at 22°13.234′S, 175°44.925′W. After washing through the initial 124 mbsf, Cores 135-840C-5H to -12H were taken (124.0–200.0 mbsf), with 76.0 m cored and 44.46 m recovered (58.5% recovery). Only one temperature measurement could be made using the WSTP tool (at 171.5 mbsf). After recovery of Core 135-840C-12H, a center bit was latched into place in the BHA, and the hole was washed to 250 mbsf. Core 135-840C-13H was then taken, recovering 7.36 m of core from a stroke of 9.5 m (recovery of 77.5%). Coring then ended because we had run out of time at the site. The 60.6% overall recovery rate of unconsolidated volcaniclastic sediments in Hole 840C is remarkable when compared with the 0.29% recovery rate in the same interval by the XCB in Hole 840B.

LITHOSTRATIGRAPHY

Introduction

Three holes were drilled at Site 840 (see "Operations" section, this chapter). In Hole 840A, sediments were spot-cored with the APC down to 4.5 mbsf. Hole 840B was cored with the XCB to 597.3 mbsf. Hole 840C was cored with the APC to 259.5 mbsf. Core recovery was low, ranging from 33% to 47%, with an average recovery of 41%. The recovery of curated core lengths is summarized in Table 2. Because of the poor core recovery, biostratigraphic and lithologic resolution is limited within some intervals.

The stratigraphic section at Site 840 is divided into three lithologic units, based on texture, composition, sedimentary structures, and the degree of lithification. Unit I consists of clayey nannofossil ooze interbedded with vitric silt, vitric sand, and pumiceous gravel. Unit II consists of highly bioturbated nannofossil chalk interbedded with vitric sand/sandstone, vitric silt/siltstone, and volcanic gravel. Unit III is composed of highly bioturbated nannofossil chalks interbedded with vitric siltstones, vitric sandstones, and volcaniclastic breccias and conglomerates. The lithologic units and their sub-bottom depths, lithologies, and biostratigraphic ages are summarized in Figure 5.

Unit I

Intervals: Sections 135-840A-1H-1, 0 cm, through -1H-1-CC, Sections 135-840B-1X-1, 0 cm, through -12X-5, 0 cm, and Sections 135-840C-1H-1, 0 cm, through -4H-CC

Depth: 0–4.5 mbsf (Hole 840A); 0–109.98 mbsf (Hole 840B); and 0–76.0 mbsf (Hole 840C)

Age: Holocene to late Miocene

Unit I extends from the sediment/water interface to 109.98 mbsf. Total recovery (with no overlap of recovery) from the three holes through this interval was 36.37 m, representing approximately 33% of the cored stratigraphic section. The sediments recovered are primarily clayey nannofossil oozes and vitric nannofossil oozes with clay and vitric silts, but vitric sands, pumiceous gravels, and pyroclastic deposits occur in smaller amounts. The nannofossil oozes are interbedded with and often grade down into vitric silts, vitric sands, and volcanic gravels. The biostratigraphic ages of the sediments recovered range from the middle Pleistocene to the late Miocene (see "Biostratigraphy" section, this chapter). Because of poor sediment recovery just below the sediment/water interface, sediment age is inferred to range from the Holocene to the late Miocene. Unit I is characterized by relatively low sedimentation rates, ranging from 5 to 50 mm/k.y. It includes a possible 1-m.y. biostratigraphic hiatus at 95.0 mbsf (see "Sediment Accumulation Rates" section, this chapter).

Clayey Nannofossil Ooze, Vitric Nannofossil Ooze with Clay, and Vitric Silt

White to light brownish gray clayey nannofossil ooze is the dominant lithology in the upper part of Unit I. The sediment is generally soft and homogeneous, but contains isolated pumice clasts (up to 5 cm in diameter) and bioclasts that include shell fragments and echinoderm spines. In the uppermost 4.5 m of Unit I, in Core 135-840A-1H, the nannofossil ooze lacks bioturbation and contains several normally graded beds with planar laminae. Near the base of Unit I, in Core 135-840B-11X, the sediment is strongly bioturbated and planar lamination is absent. The carbonate content of the nannofossil oozes in Unit I ranges from 56% in the upper part of the unit up to a maximum of 86% at the base (see "Organic Geochemistry" section, this chapter). Beds of clayey nannofossil ooze commonly overlie and grade down into light gray to gray vitric nannofossil ooze with clay. The darker colors correspond to increasing percentages of glass in the sediment (up to 29%). Color mottling of the sediment is common as a result of the mixing of carbonate- and glass-rich sediments through bioturbation. The vitric nannofossil ooze with clay commonly overlies gray to dark grayish brown or greenish gray vitric silt, which is generally structureless, though faint planar lamination occasionally occurs.

Vitric Sand

Very fine- to very coarse-grained vitric sand is common in Unit I, and becomes an increasingly dominant constituent downhole. The fine-grained sands are dominated by clear volcanic glass shards (see below). The coarse- and very coarse-grained sands are moderately to well sorted and contain subrounded to angular pumice grains, black (mafic) volcanic grains, and clear glass shards and pumice pebbles. In Section 135-840C-3H-2, 14–54 cm, there is a planar-stratified vitric gravel that contains clasts up to 1 cm in diameter and grades upward into vitric sandstone. Accessory minerals in the sands include orthopyroxene, clinopyroxene, and translucent, angular olivine grains.

The vitric sand beds usually have sharp, scoured basal contacts and are normally graded in their lower parts. Below Section 135-840C-3H-1, 0 cm (57.0 mbsf), the sands commonly fine upward and are strongly planar, wedge planar, and cross laminated. Above this interval, normally graded bedding and faint planar laminae are common in the vitric sands, and bioturbation is rare or absent. This upward increase in the number of sand beds with preserved primary sedimentary structures corresponds to the timing of a decrease in the sedimentation rate from 50 to 14 mm/k.y. (see "Sediment Accumulation Rates" section, this chapter).

Pyroclastic Sediments

Seven well-preserved pyroclastic sediment layers were recovered from Section 135-840A-1H-3, 15–75 cm, at 3.15–3.75 mbsf. Each of the layers grades upward from crystal-rich lapilli (maximum grain size = 3 mm) into crystal-rich ash and then into nannofossil mixed sediment with feldspar clay and accessory minerals. The thickness of the layers varies from 5 to 13 cm. The lapilli and ash constitute approximately half of this thickness. These pyroclastic deposits are discussed in more detail below.

Unit II

Intervals: Sections 135-840B-12X-5, 0 cm, through -28X-1, 80 cm, and Sections 135-840C-5H-1, 0 cm, through -9H-CC
Depth: 109.98–260.50 mbsf (Hole 840B); 124.0–171.5 mbsf (Hole 840C)
Age: early Pliocene to late Miocene

Unit II extends from 109.98 to 260.50 mbsf. The total core recovery from both holes was 49.26 m, representing 32.7% of the cored interval. The lithologies recovered were mainly nannofossil chalks with clay and vitric nannofossil chalks with clay, interbedded with and often grading down into vitric siltstones and vitric sandstones. Thick pumiceous gravel beds also occur within Unit II. The biostratigraphic age of sediments recovered is early Pliocene to late Miocene (see "Biostratigraphy" section, this chapter). The estimated sedimentation rate of Unit II is 820 mm/k.y. (see "Sediment Accumulation Rates" section, this chapter).

The lithologic boundary between Units I and II in Section 135-840B-12X-4, 80 cm (at 109.98 mbsf), is interpreted as a paraconformity. It is marked by a transition from structureless nannofossil ooze above the boundary to highly bioturbated nannofossil chalk below. Volcaniclastic interbeds interpreted as turbidites increase in thickness and abundance downward from the paraconformity. The change from ooze to chalk and the increase in volcaniclastic input down through Unit II also correlates with a decrease downhole in the concentration of calcium and an increase in the concentration of silica on geochemical logs (see "Downhole Measurements" section, this chapter). Immediately above and below the unit boundary, there is a marked increase in the $CaCO_3$ content of the sediments, reaching a maximum of 86% (see "Organic Geochemistry" section, this chapter).

Nannofossil Chalk

Light gray to gray nannofossil chalk with clay dominates the lithology in the upper portion of Unit II. The carbonate content of the chalk varies from a maximum of 53% in the upper part of the unit to 41% in the lower part. The color ranges from light gray to gray, and color mottling is common because of bioturbation. Figures 6 and 7 show typical ichnofacies assemblages of the nannofossil chalk. This tiered assemblage of *Chondrites-Zoophycos-Thalassinoides-Planolites-Skolithos* is typical of shallow-sea chalk. *Zoophycos* and *Chondrites* only occur in firm but uncemented substrates and are associated with relatively high oxygen levels (Ekdale et al., 1984). Firm grounds or hardgrounds are generally indicative of shallow-water conditions (Flügel, 1984). The depositional depth of the shallow-sea chalks exhibiting this assemblage is considered to be a few tens of meters to several hundred meters (Flügel, 1984). The absence of abundant, well-preserved benthic foraminifers, however, suggests a somewhat deeper environment of deposition (see "Biostratigraphy" section, this chapter).

Vitric Silt and Vitric Siltstone

Gray to very dark gray or dark greenish gray vitric silts and vitric siltstones are very common in Unit II. Vitric silts and siltstones either occur as discrete, fining-upward interbeds, or with gradational boundaries above vitric sands and sandstones. Vitric silt is also a component of other lithologies. In Unit II, the vitric silt is generally lithified, but the degree of induration varies

Table 1. Coring summary, Site 840.

Core no.	Date (Jan. 1991)	Time (UTC)	Depth (mbsf)	Cored (m)	Recovered (m)	Recovery (%)	Age
135-840A-							
1H	24	1105	0.0–4.5	4.5	4.11	91.3	middle Pleistocene
Coring totals				4.5	4.11	91.3	
135-840B-							
1X	24	2045	0.0–9.5	9.5	1.79	18.8	middle Pleistocene
2X	24	2355	9.5–18.9	9.4	0.00	0.0	upper Pliocene
3X	25	0110	18.9–28.4	9.5	0.01	0.1	upper Pliocene
4X	25	0225	28.4–37.9	9.5	0.25	2.6	upper Pliocene
5X	25	0325	37.9–47.4	9.5	0.00	0.0	
6X	25	0410	47.4–57.1	9.7	0.00	0.0	
7X	25	0450	57.1–66.7	9.6	0.00	0.0	
8X	25	0535	66.7–76.4	9.7	0.00	0.0	
9X	25	0625	76.4–86.1	9.7	0.18	1.9	lower Pliocene
10X	25	0705	86.1–95.7	9.6	0.80	8.3	lower Pliocene
11X	25	0800	95.7–105.4	9.7	2.97	30.6	lower Pliocene
12X	25	0840	105.4–115.1	9.7	7.42	76.5	lower Pliocene–upper Miocene
13X	25	1000	115.1–124.8	9.7	4.87	50.2	lower Pliocene–upper Miocene
14X	25	1030	124.8–134.4	9.6	0.00	0.0	
15X	25	1110	134.4–144.1	9.7	0.11	1.1	lower Pliocene–upper Miocene
16X	25	1140	144.1–153.8	9.7	0.00	0.0	
17X	25	1230	153.8–163.4	9.6	0.26	2.7	Indeterminate
18X	25	1320	163.4–172.7	9.3	0.01	0.1	lower Pliocene–upper Miocene
19X	25	1410	172.7–182.4	9.7	0.01	0.1	lower Pliocene
20X	25	1455	182.4–192.0	9.6	0.01	0.1	lower Pliocene
21X	25	1600	192.0–201.7	9.7	0.00	0.0	
22X	25	1650	201.7–211.4	9.7	0.15	1.5	lower Pliocene–upper Miocene
23X	25	1740	211.4–221.0	9.6	0.01	0.1	lower Pliocene–upper Miocene
24X	25	1835	221.0–230.7	9.7	1.90	19.6	lower Pliocene–upper Miocene
25X	25	1935	230.7–240.4	9.7	0.00	0.0	
26X	25	2055	240.4–250.0	9.6	1.12	11.6	lower Pliocene–upper Miocene
27X	25	2150	250.0–259.7	9.7	0.00	0.0	
28X	25	2320	259.7–269.4	9.7	3.15	32.5	lower Pliocene–upper Miocene
29X	26	0105	269.4–279.1	9.7	0.95	9.8	lower Pliocene–upper Miocene
30X	26	0230	279.1–288.8	9.7	1.15	11.8	lower Pliocene–upper Miocene
31X	26	0415	288.8–298.5	9.7	0.81	8.4	lower Pliocene–upper Miocene
32X	26	0550	298.5–308.2	9.7	0.69	7.1	lower Pliocene–upper Miocene
33X	26	0700	308.2–317.8	9.6	1.41	14.7	lower Pliocene–upper Miocene
34X	26	0820	317.8–327.5	9.7	1.64	16.9	lower Pliocene–upper Miocene
35X	26	0920	327.5–332.4	4.9	3.64	74.3	Barren
36X	26	1010	332.4–337.4	5.0	1.35	27.0	upper Miocene
37X	26	1110	337.4–347.1	9.7	2.80	28.8	upper Miocene
38X	26	1205	347.1–356.8	9.7	1.65	17.0	upper Miocene
39X	26	1310	356.8–366.5	9.7	2.89	29.8	upper Miocene
40X	26	1400	366.5–376.2	9.7	1.40	14.4	upper Miocene
41X	26	1525	376.2–385.8	9.6	1.93	20.1	upper Miocene
42X	26	1630	385.8–395.5	9.7	4.90	50.5	upper Miocene
43X	26	1750	395.5–404.9	9.4	3.82	40.6	upper Miocene
44X	26	2000	404.9–414.2	9.3	1.57	16.9	upper Miocene
45X	26	2220	414.2–423.9	9.7	3.30	34.0	upper Miocene
46X	27	0135	423.9–433.5	9.6	2.57	26.8	Barren
47X	27	0230	433.5–442.8	9.3	4.67	50.2	Barren
48X	27	0330	442.8–452.4	9.6	5.23	54.5	Indeterminate
49X	27	0530	452.4–462.1	9.7	4.82	49.7	Indeterminate
50X	27	0620	462.1–471.7	9.6	6.02	62.7	upper Miocene
51X	27	0730	471.7–481.4	9.7	7.48	77.1	Barren
52X	27	0840	481.4–491.0	9.6	9.67	101.0	lower Pliocene–upper Miocene
53X	27	0945	491.0–500.7	9.7	6.43	66.3	Indeterminate
54X	27	1030	500.7–510.4	9.7	4.31	44.4	lower Pliocene–upper Miocene
55X	27	1120	510.4–520.2	9.8	5.92	60.4	upper Miocene
56X	27	1225	520.2–529.6	9.4	6.45	68.6	upper Miocene
57X	27	1345	529.6–539.3	9.7	6.96	71.7	Barren
58X	27	1450	539.3–549.0	9.7	8.45	87.1	Barren
59X	27	1615	549.0–558.7	9.7	3.55	36.6	lower Pliocene–upper Miocene
60X	27	1745	558.7–568.3	9.6	8.34	86.9	Barren
61X	27	1925	568.3–578.0	9.7	8.74	90.1	lower Pliocene–upper Miocene
62X	27	2150	578.0–587.7	9.7	9.85	101.0	?upper Miocene
63X	27	2305	587.7–597.3	9.6	5.82	60.6	upper Miocene
Coring totals				597.3	176.20	29.5	
135-840C-							
1H	29	0445	38.0–47.5	9.5	4.93	51.9	upper Pliocene
2H	29	0630	47.5–57.0	9.5	0.83	8.7	upper Pliocene
3H	29	0705	57.0–66.5	9.5	7.82	82.3	upper Pliocene

Table 1 (continued).

Core no.	Date (Jan. 1991)	Time (UTC)	Depth (mbsf)	Cored (m)	Recovered (m)	Recovery (%)	Age
135-840C- (cont.)							
4H	29	0825	66.5–76.0	9.5	8.10	85.2	upper Pliocene
5H	29	1110	124.0–133.5	9.5	4.95	52.1	lower Pliocene
6H	29	1150	133.5–143.0	9.5	5.45	57.3	Barren
7H	29	1300	143.0–152.5	9.5	9.82	103.0	lower Pliocene–upper Miocene
8H	29	1345	152.5–162.0	9.5	9.37	98.6	lower Pliocene
9H	29	1425	162.0–171.5	9.5	1.43	15.0	Indeterminate
10H	29	1600	171.5–181.0	9.5	9.69	102.0	lower Pliocene–upper Miocene
11H	29	1630	181.0–190.5	9.5	1.11	11.7	lower Pliocene–upper Miocene
12H	29	1715	190.5–200.0	9.5	3.97	41.8	lower Pliocene–upper Miocene
13H	29	2130	250.0–259.5	9.5	7.36	77.5	lower Pliocene–upper Miocene
Coring totals				123.5	74.83	60.6	

Table 2. Summary of the recovery percentages based on the curated length of core recovered from each of the three holes drilled at Site 840.

	Hole 840A			Hole 840B			Hole 840C			All		
Lithologic unit	Curated recovery (m)	Cored interval (m)	Recovery (%)	Curated recovery (m)	Cored interval (m)	Recovery (%)	Curated recovery (m)	Cored interval (m)	Recovery (%)	Total recovery (m)	Cored interval (m)	Recovery (%)
Unit 1 (0–109.98 mbsf)	4.11	4.5	91.3	10.6	109.98	9.6	21.68	38	57.1	36.39	109.98	33.1
Unit II (109.98–260.50 mbsf)				11.29	150.52	7.5	37.97	76	50.0	49.26	150.52	32.7
Unit III (260.50–597.3)				154.33	336.8	45.8	4.01	9.5	42.2	158.34	336.8	47.0
Totals	4.11	4.5	91.3	176.22	597.3	29.5	63.66	123.5	51.5	243.99	597.3	40.8

Note: Recovery differs from Table 1, as void spaces in the recovered core are removed from the total recovered length reported in Table 1.

downhole. It is generally indurated when interbedded with nannofossil chalk and unconsolidated when associated with coarse-grained vitric sands and pumiceous gravels.

The vitric silts and siltstones are extensively bioturbated, with the degree of bioturbation increasing upward within each bed. Thin to thick planar laminae are the most common primary sedimentary structures, but wavy laminae are also common. Lamination is usually preserved in the lower parts of vitric silt and siltstone beds, where bioturbation is less common. Isolated pumice clasts are scattered throughout the vitric silts and siltstones.

Vitric Sand and Vitric Sandstone

Vitric sand (recovered in Hole 840C) and vitric sandstone (recovered in Hole 840B) in Unit II are generally light grayish brown to dark grayish brown in color, but they may be gray to greenish gray or black. The vitric sands and sandstones usually have scoured basal contacts and are normally graded throughout. Planar stratification is common in the lower part of the beds. Coarse-grained sands often grade downward into vitric gravel. Beds with gradational lower contacts are often bioturbated. In Hole 840C, below Section 135-840C-7H-1, 0 cm, the sands are highly disturbed by drilling and any existing primary sedimentary structures are lost.

The sand is usually grain-supported and moderately well to poorly sorted. Grain shapes range from subrounded to subangular, with subrounded pumice grains dominating in the upper parts of the unit. Isolated pumice clasts up to 3.5 cm in diameter and mud clasts up to 7 cm in diameter occur in the sand matrix. Other constituents include volcanic rock fragments and sparse, angular olivine grains. In the lower parts of the unit, black, angular volcanic grains are the dominant constituent. These lower sands are finer grained but are less well-sorted and contain a higher percentage of angular grains.

Pumiceous Gravel

Light gray to black pumiceous gravel is a significant component of Unit II (Fig. 8). The gravel occurs in centimeter to meter thick beds and, in some cores, accounts for up to 90% of the recovered material (e.g., in Core 135-840C-8H; Fig. 5). The gravel beds commonly have eroded/scoured bases, are normally graded, and often fine upward into vitric sands and vitric silts; however, poorly sorted, ungraded, structureless beds also occur. Individual pumice clasts are as large as 4 cm in diameter and are generally rounded to subrounded and greenish gray to light gray in color. The light gray pumice fragments are generally those with the largest grain sizes. Reddish brown and yellowish brown pumice fragments are rare. The pumiceous gravel is relatively monomict, although nonpumice clasts, such as mafic rock fragments, are present in small amounts.

Unit III

Intervals: Sections 135-840B-28X-1, 80 cm, through -63X-CC
Depth: 260.5–597.3 mbsf
Age: late Miocene

Unit III is 336.8 m thick and is composed of a sequence of volcaniclastic turbidites and heavily bioturbated nannofossil chalks. Down through the unit, there is a general increase in bed thickness and grain size of individual turbidites. The nannofossil chalks that usually overlie the turbidites become more clay-rich down the unit. The age of Unit III is late Miocene (approximately 5.3–6.6 Ma; see "Biostratigraphy" section, this chapter). The sedimentation rate of Unit III was about 110 mm/k.y. between

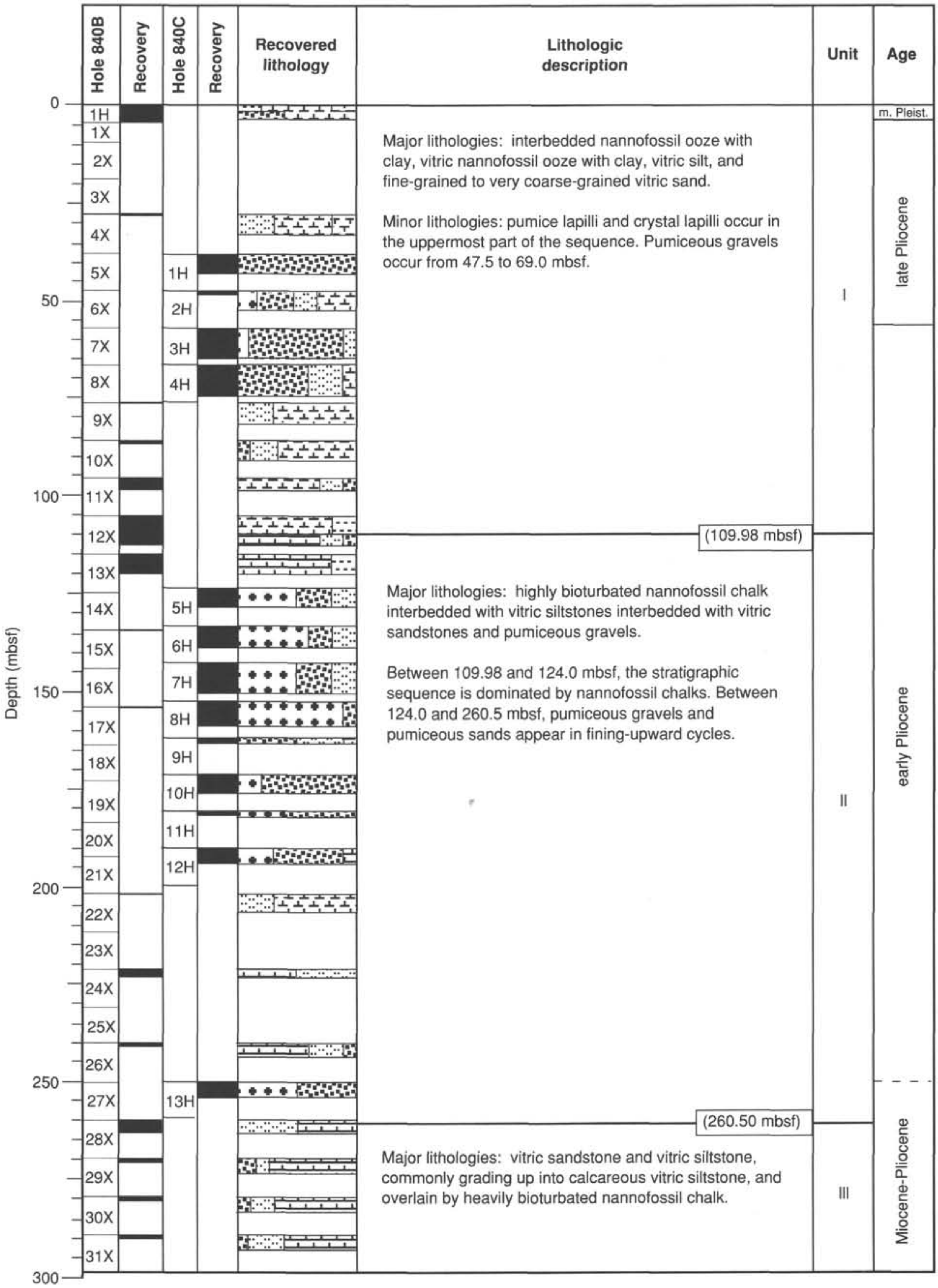

Figure 5. Lithologic summary for Site 840. The graphic representation and summary of the recovered lithologies are combined from all three holes. Recovery is based on curated length of cores.

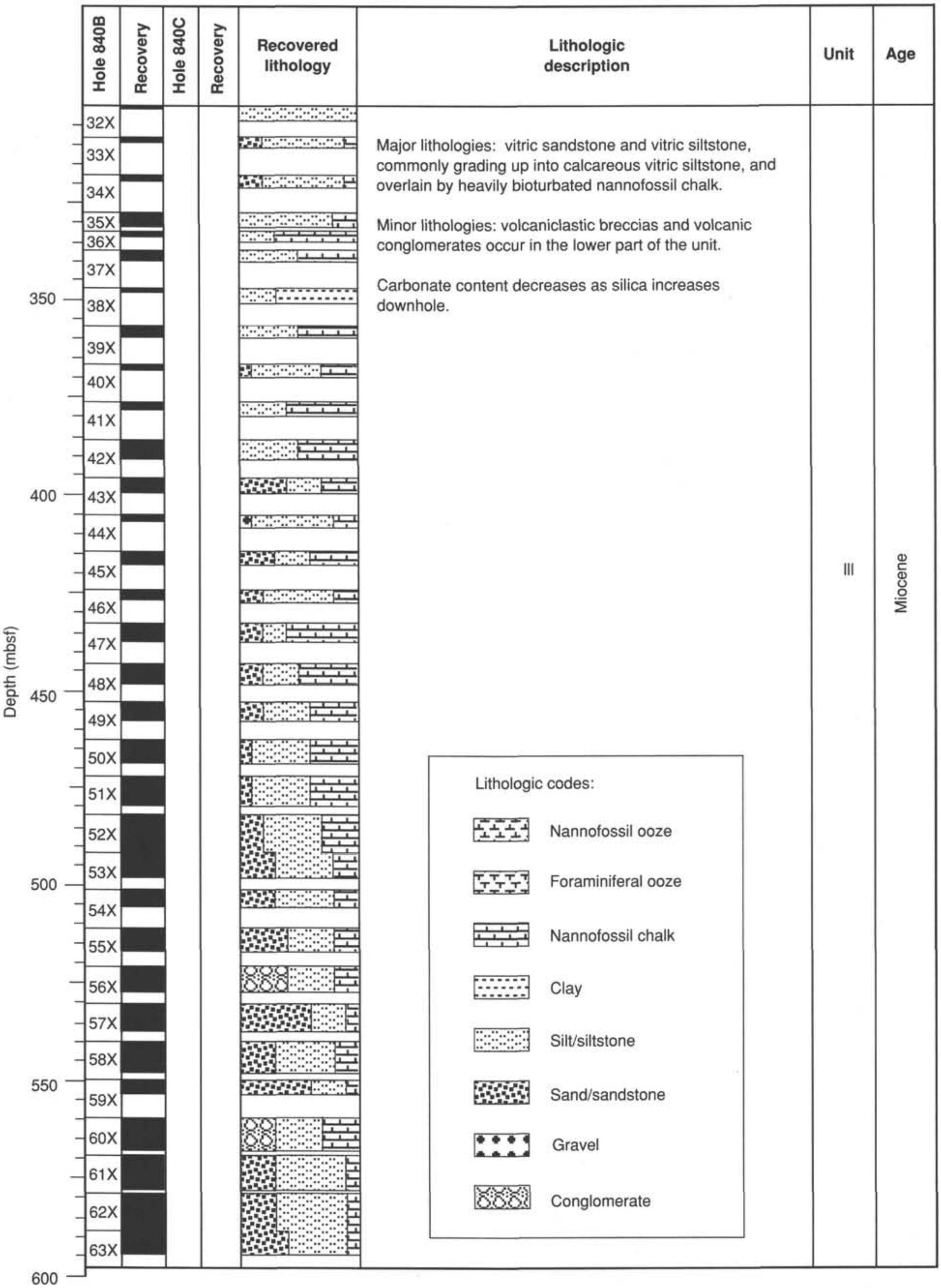

Figure 5 (continued).

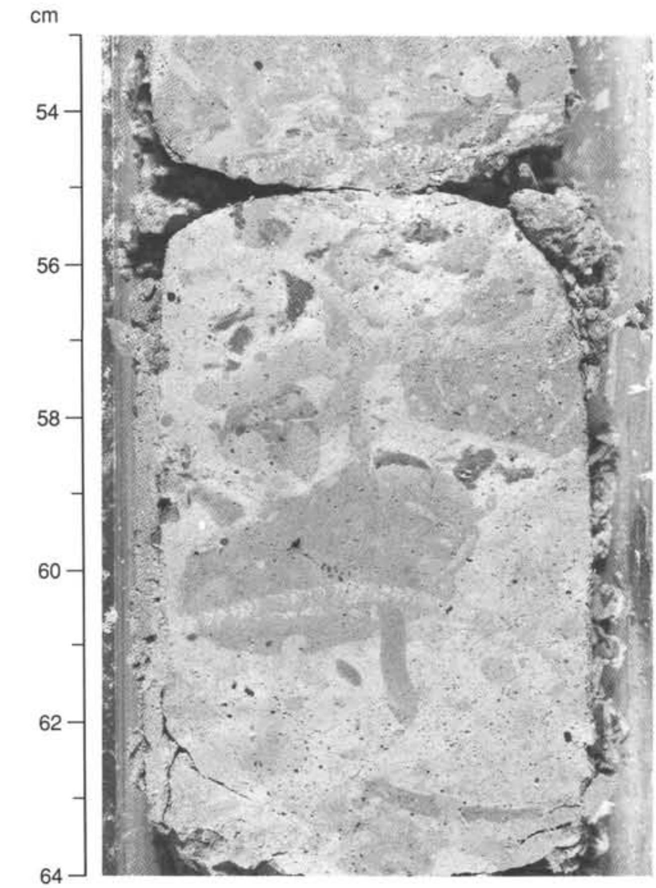

Figure 6. Typical ichnofacies of Unit II nannofossil chalk including *Thalassinoides* (59–61 cm), *Zoophycos* (53–55 and 60–61 cm), *Chondrites* (53–64 cm), and composite burrow (57–58 cm) in Section 135-840B-13X-3, 53–64 cm. Note cross-cutting relations of burrows and large, undistorted *Thalassinoides* walls indicative of a firm substrate.

250.5 and 320 mbsf and 375 mm/k.y. below this interval (see "Sediment Accumulation Rates" section, this chapter).

Above the boundary between Units II and III, at 260.5 mbsf, a sequence of gravels and very coarse-grained sands is interbedded with vitric siltstones and nannofossil chalks. Beneath this boundary, in Section 135-840B-28X-1, 80 cm (at 260.5–269.40 mbsf), the sequence is dominated by nannofossil chalks and vitric siltstones. The boundary corresponds to a sudden increase in the sonic velocity on downhole logs and to a zone of decreased density on the density logs (see "Downhole Measurements" section, this chapter). The unit boundary also corresponds to a sudden change from a highly variable bedding orientation within Unit II to a very constant orientation of the bedding within Unit III (see "Structural Geology" section, this chapter).

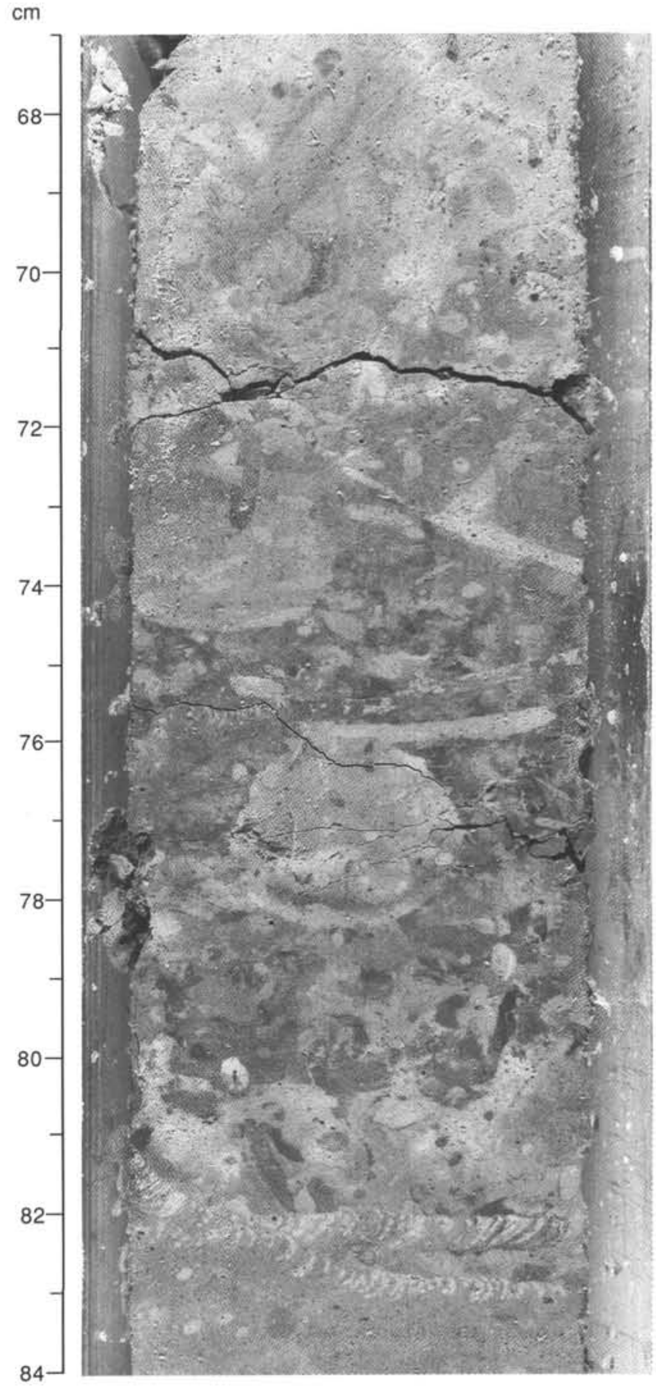

Figure 7. Typical ichnofacies of Unit II nannofossil chalk including composite *Thalassinoides* (73–74 and 76–78 cm), *Zoophycos* (81–83 cm), and abundant *Chondrites* (67–83 cm) in Section 135-840B-13X-3, 67–84 cm. Note tiering of burrows and cyclical nature of bioturbated beds.

Nannofossil Chalk

Heavily bioturbated, light gray to gray nannofossil chalks overlie most of the volcaniclastic beds in Unit III (Fig. 9). They occur as 1 cm to approximately 1 m thick beds. No systematic variation exists in the thickness of individual chalk beds with depth, however; the total volume of nannofossil chalk decreases downhole.

There is a gradual transition from nannofossil chalk into clayey nannofossil chalk with depth. Below Core 135-840B-59X, nannofossils are only rarely observed in smear slides, and the sediment could be classified as a calcareous claystone. Heavily bioturbated nannofossil chalks often contain up to 30%–40% of vitric silt, which has been worked into the nannofossil chalks by bioturbation. Thin layers of vitric silt within the nannofossil chalks are commonly completely disrupted by burrowing. Within some intervals, nannofossil chalk with foraminifers occurs, with foraminifers constituting up to 15 vol% of the sediment. The $CaCO_3$ content of these sediments ranges from 24% to 50%; therefore, by definition, not all of these beds are strictly nannofossil chalks.

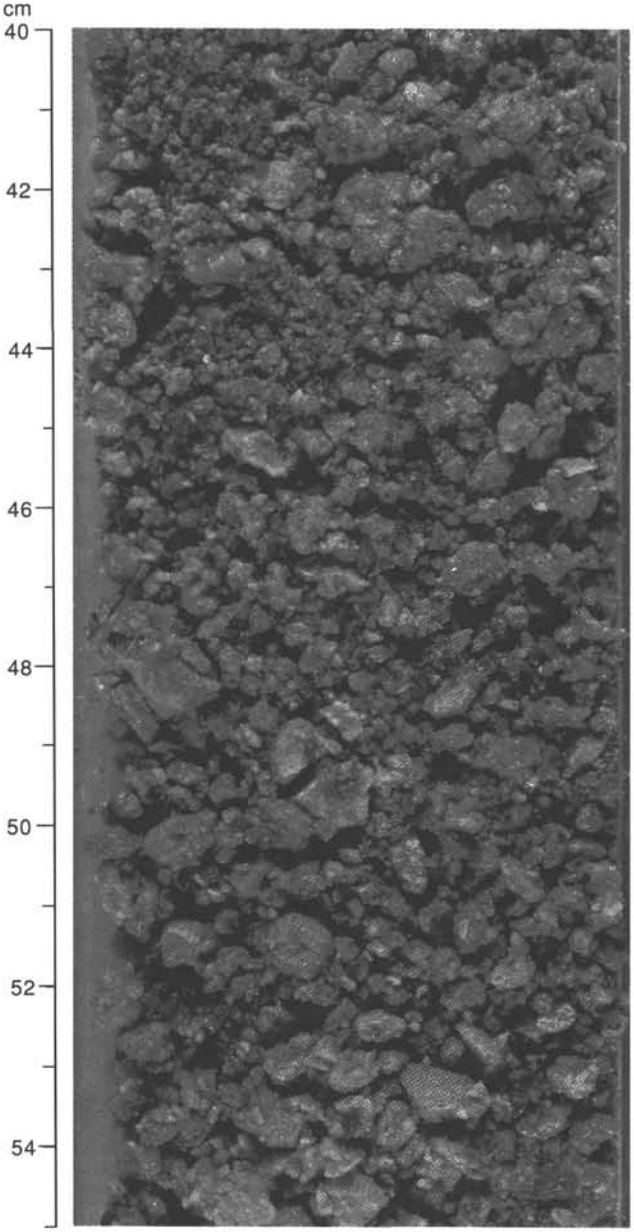

Figure 8. Thin- to medium-bedded pumiceous gravel in Section 135-840C-7H-6, 40–55 cm. Maximum clast size is approximately 2 cm.

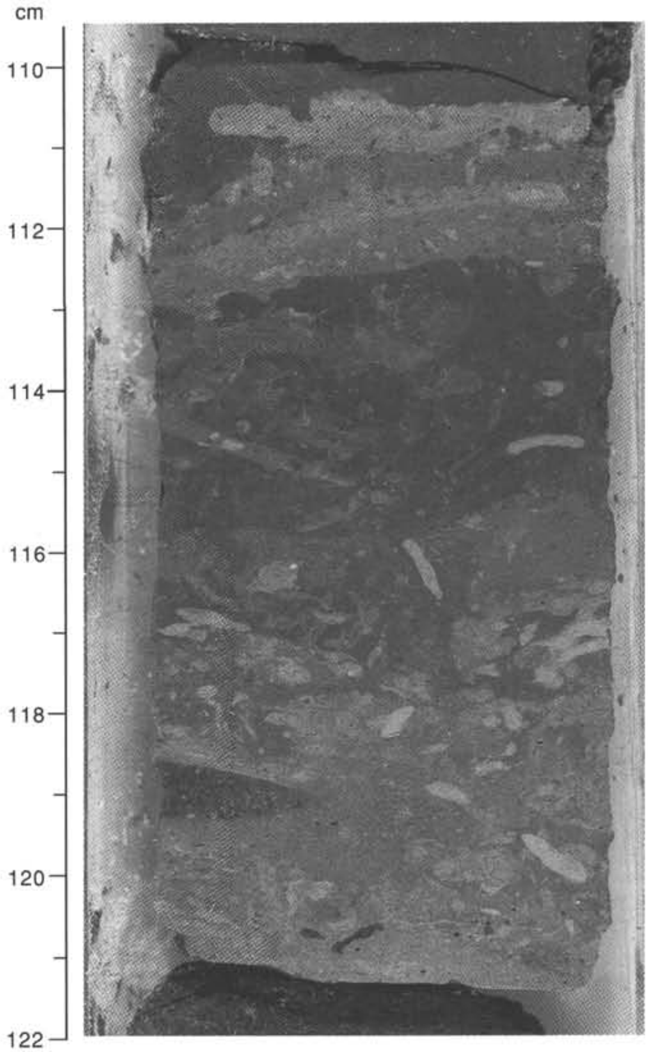

Figure 9. Nannofossil chalk overlying vitric siltstone in Section 135-840B-35X-1, 109–122 cm. Note that the boundary between the two lithologies is completely obscured by bioturbation. Trace fossils include *Thalassinoides*, *Zoophycos*, *Chondrites*, and *Planolites*. Note *Zoophycos* burrow at 109–110 cm.

However, for the purpose of simplicity, we refer here to all of these sediments as nannofossil chalks.

Faint laminae occur locally in the nannofossil chalks, but most of the primary sedimentary structures have been obscured through bioturbation. Several different types of trace fossils occur. The most common are *Zoophycos*, *Thalassinoides*, *Planolites*, and *Chondrites* (Figs. 9–11). The trace fossil assemblage in the nannofossil chalks is very similar to that seen in the nannofossil chalks in Unit II.

Vitric Siltstone

Light gray to dark gray vitric siltstone is the most common lithology in Unit III, and in some cores makes up almost 50% of the sediment volume. Vitric siltstone occurs in beds with thicknesses varying from 1 cm up to more than 1 m, and there is a general increase in the thickness of individual beds downhole.

Vitric siltstones are generally overlain by heavily bioturbated nannofossil chalks. Bioturbation commonly extends from the chalk down into the vitric siltstones, and the contacts are therefore gradational (Figs. 9–11). However, sharp boundaries between these two lithologies occur as well as gradual transitions. The vitric siltstones often grade down into vitric sandstones.

The vitric siltstones show a wide variety of sedimentary structures, including planar, wedge-planar, wavy, and trough cross-lamination. Convoluted intervals are very common, especially in the lower part of the unit. The majority of the siltstone beds fine upward.

Vitric Sandstone

Vitric sandstones within Unit III range from very fine-grained to very coarse-grained, with some sandstones grading into volcaniclastic breccias and conglomerates (Fig. 12). The color of vitric sandstones varies from black to dark gray to gray. Individual beds range in thickness from 1 cm up to more than 1 m. There is a pronounced increase in grain size and in the number and thickness

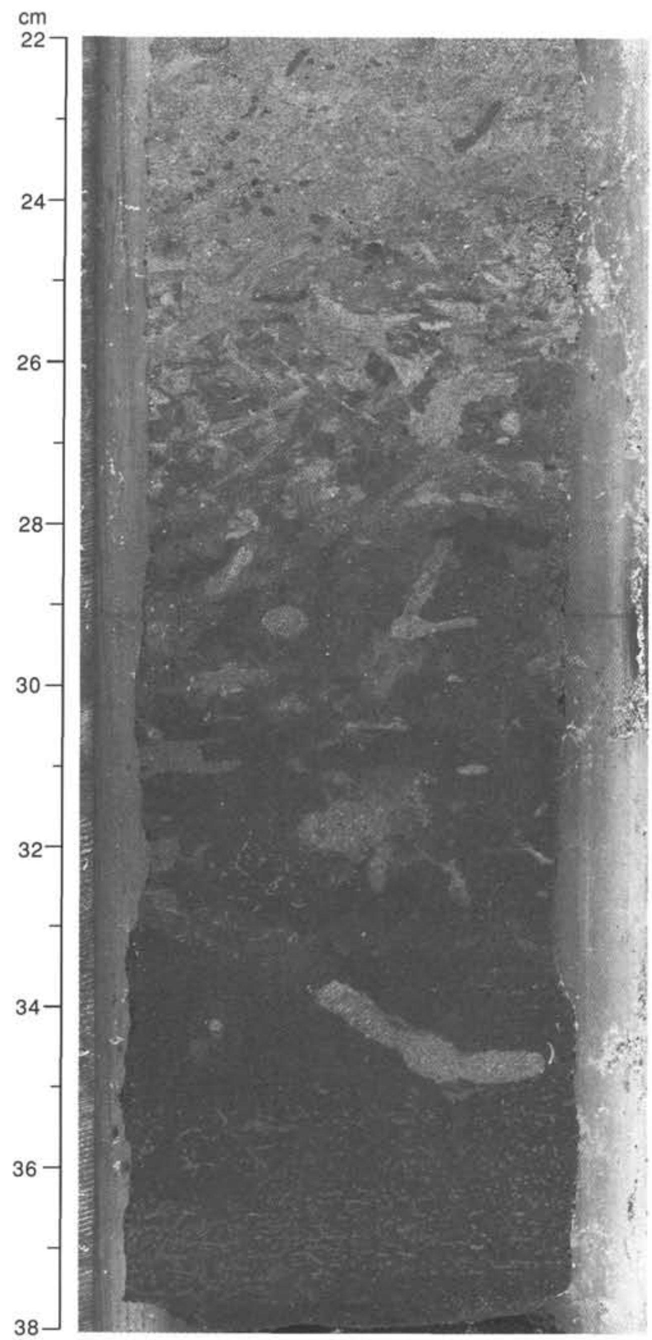

Figure 10. Trace fossils in vitric siltstone and nannofossil chalk of Unit III in Section 135-840B-35X-1, 22–38 cm. Trace fossils include *Thalassinoides, Planolites,* and *Chondrites.* Note *Chondrites* burrows at 35–38 cm.

of sandstone beds downward through the unit. In the lowermost part of Unit III, sandstones make up 40% by volume of the sedimentary sequence.

The vitric sandstones usually grade up into vitric siltstones (Fig. 13), but some are directly overlain by nannofossil chalk. In the latter case, the sandstones are commonly bioturbated. The lower boundaries of sandstone beds are sharp, either planar (Fig. 13) or with slightly eroded relief. Normal grading in the basal layers is very common, but reverse grading also occurs.

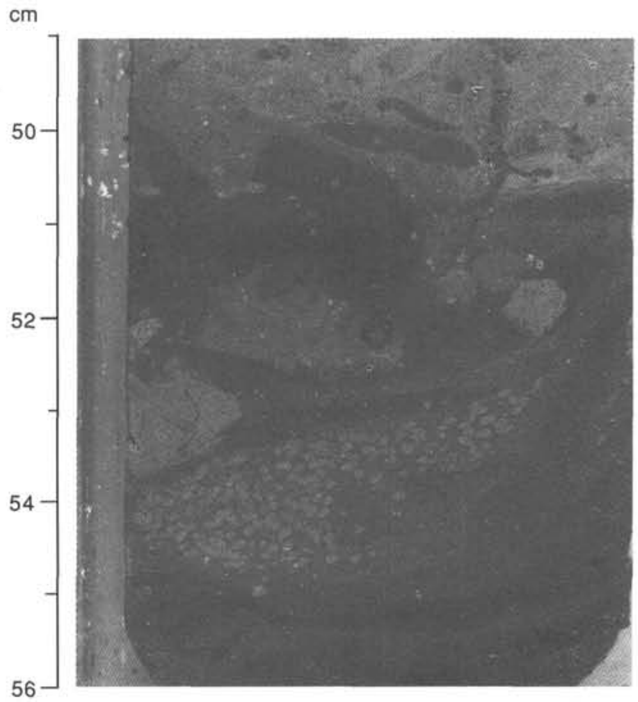

Figure 11. Trace fossils in vitric siltstone and nannofossil chalk of Unit III in Section 135-840B-48X-2, 49–56 cm. Trace fossils include *Thalassinoides* and *Planolites.* Note composite burrow at 53–55 cm.

Many different types of sedimentary structures occur in the sandstones. These include planar, wedge-planar, wavy, lenticular, and trough cross-lamination; planar stratification (very thin bedding); trough cross-stratification; water escape pillars; and convoluted laminae. Many of these structures also occur in the vitric siltstones.

Volcaniclastic Breccia and Conglomerate

The shallowest occurrence of volcaniclastic breccia and conglomerate is in Section 135-840B-47X-3, 133 cm, at 437.83 mbsf. There is an increase in the number and thickness of volcaniclastic breccia and conglomerate beds downhole, and individual beds range from 2 to 195 cm in thickness. The maximum clast size is generally <3 cm, and the mean maximum (average of ten largest clasts) within a single bed is 0.5–1 cm. Both clast- and matrix-supported breccias and conglomerates occur. They have either eroded basal contacts and lie above finer grained beds, or they may occur within planar-stratified, cross-stratified, or structureless sandstone beds (Fig. 14).

These deposits generally consist of granule- to pebble-size, gray pumice clasts in a matrix of medium- to very coarse-grained sandstone (Fig. 14). However, darker colored pumice and scoriaceous clasts also occur. The clasts are generally angular to subrounded, but subrounded to rounded pumice clasts predominate within some beds. Beds dominated by gray pumice clasts commonly show an increase in clast size upward (coarse-tail reverse grading), whereas the matrix is normally graded (fine-tail normal grading) (Fig. 15).

A greenish gray volcanic conglomerate of a unique appearance occurs in Sections 135-840B-60X-1, 0 cm, through -60X-2, 45 cm. This contains a polymict assemblage of clasts. These are mainly gray pumice, but red scoriaceous pumice, vein quartz, and strongly altered, bright green mafic fragments also occur. A yellow sulfide mineral is also present. The maximum grain size is

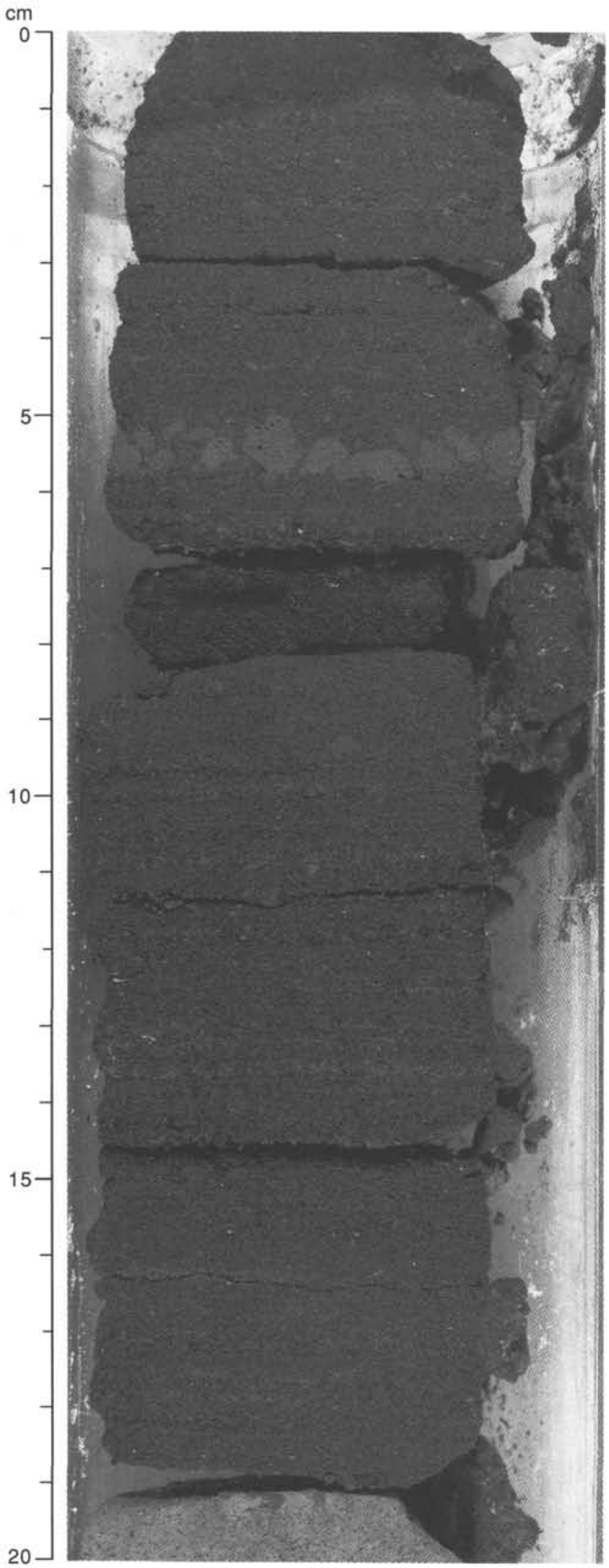

Figure 12. Planar-laminated vitric sandstone with a layer of volcaniclastic breccia/conglomerate at 5–6 cm in Section 135-840B-48X-3, 0–20 cm. The clasts are gray pumice. The vitric sandstone overlies a nannofossil chalk.

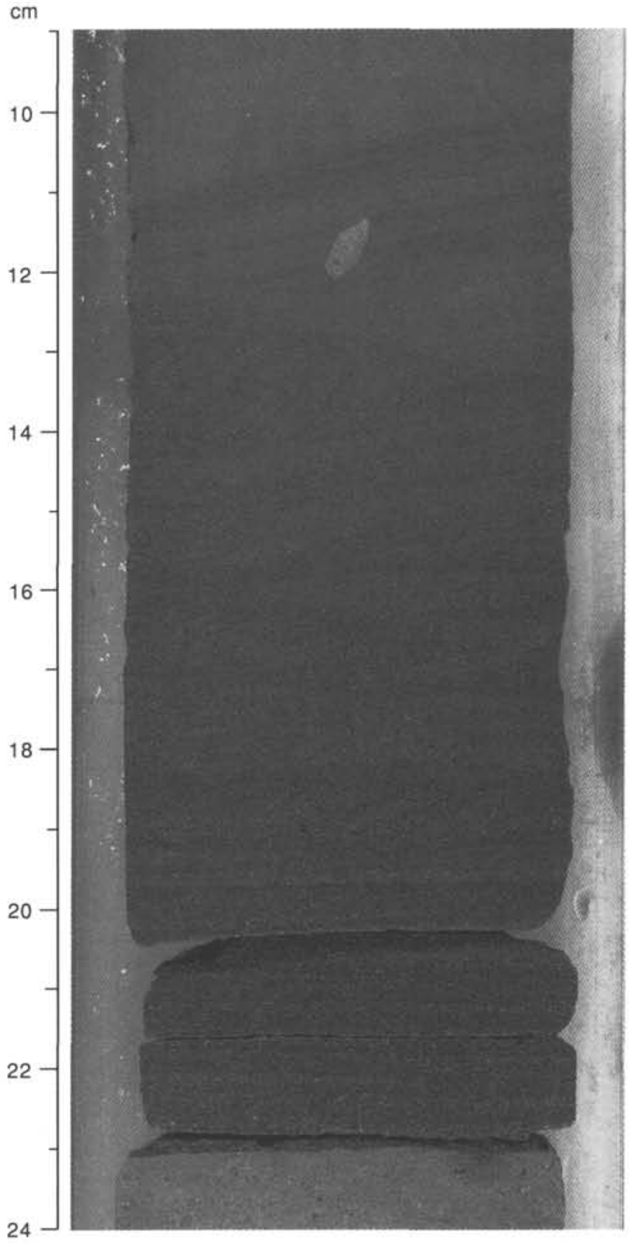

Figure 13. Vitric sandstone grading up into vitric siltstone in Section 135-840B-48X-1, 9–24 cm. Note planar-laminated lower part overlain by trough cross-laminated and trough cross-stratified sediments. Also note overturned foresets.

about 3 cm, and the mean maximum is approximately 1 cm. Clasts are generally subangular to subrounded.

Sedimentary Structures in the Vitric Siltstones and Sandstones

Lamination and Stratification

Laminated intervals are common in the vitric siltstones and vitric sandstones of Unit III. Both thin (<0.5 mm) and thick (>0.5 mm) laminae occur. Planar lamination usually occurs in the lowermost part of sandstone beds (Figs. 13 and 16). Some siltstone beds are planar laminated throughout. In coarse-grained and very coarse-grained sandstones, entire beds may be planar-stratified

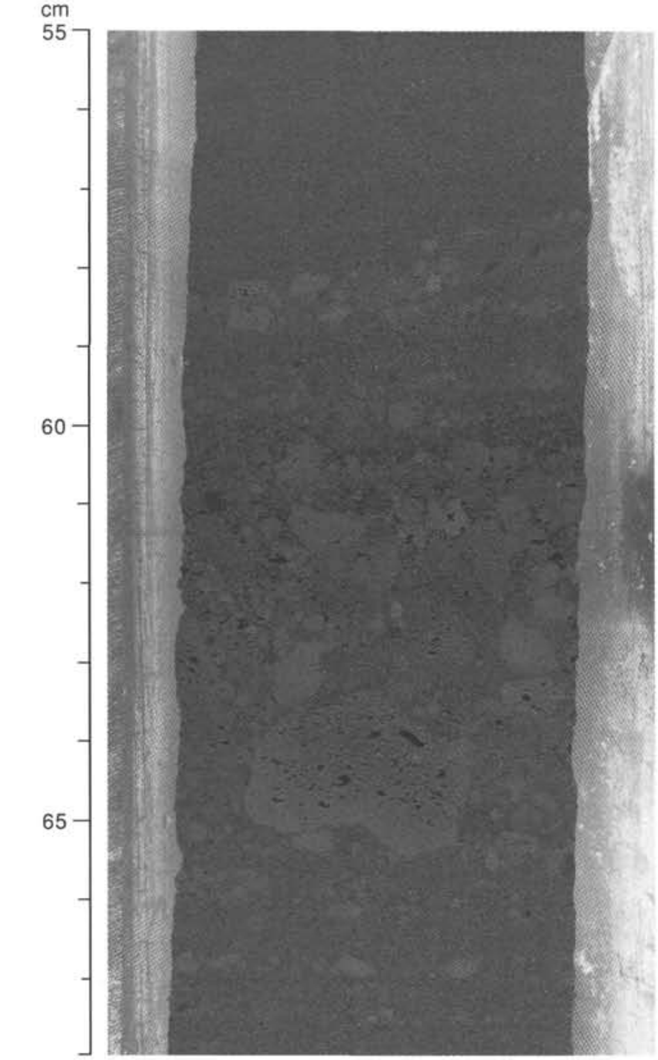

Figure 14. Volcaniclastic breccia/conglomerate interbedded with planar-stratified vitric sandstone in Section 135-840B-50X-4, 55–68 cm.

(Fig. 12). Planar-laminated intervals are commonly underlain by massive, normally graded intervals and overlain by trough cross-laminated (Fig. 13), wavy-laminated, or wedge-planar-laminated (Fig. 16) intervals. Lenticular laminae occur infrequently (e.g., Section 135-840B-50X-1, 8 and 17.5 cm; Fig. 17). Some sequences show a complex series of structures with alternating intervals of cross-lamination/cross-stratification and convoluted laminae (Fig. 17).

Soft Sediment Deformation

Sandstones and siltstones of Unit III have been strongly affected by soft sediment deformation. Convoluted intervals, varying in thickness from 3 cm (Fig. 18) up to 85 cm (in Section 135-840B-57X-1), occur throughout the unit, although there is a marked increase in the number and thickness of convoluted beds downhole. Beds are occasionally convoluted throughout, but the coarser grained trough cross-laminated and trough cross-stratified sandstone and siltstone intervals in the lower parts of beds more commonly show convoluted laminae (Figs. 19–20). Over-steepened and overturned foresets are also common (Figs. 13 and 17). Some of these may have been produced by strong current drag.

Some of the convoluted beds were obviously very fluid at the time of deformation, as they show what are interpreted as water escape structures and sand diapirs (e.g., Section 135-840B-55X-1;

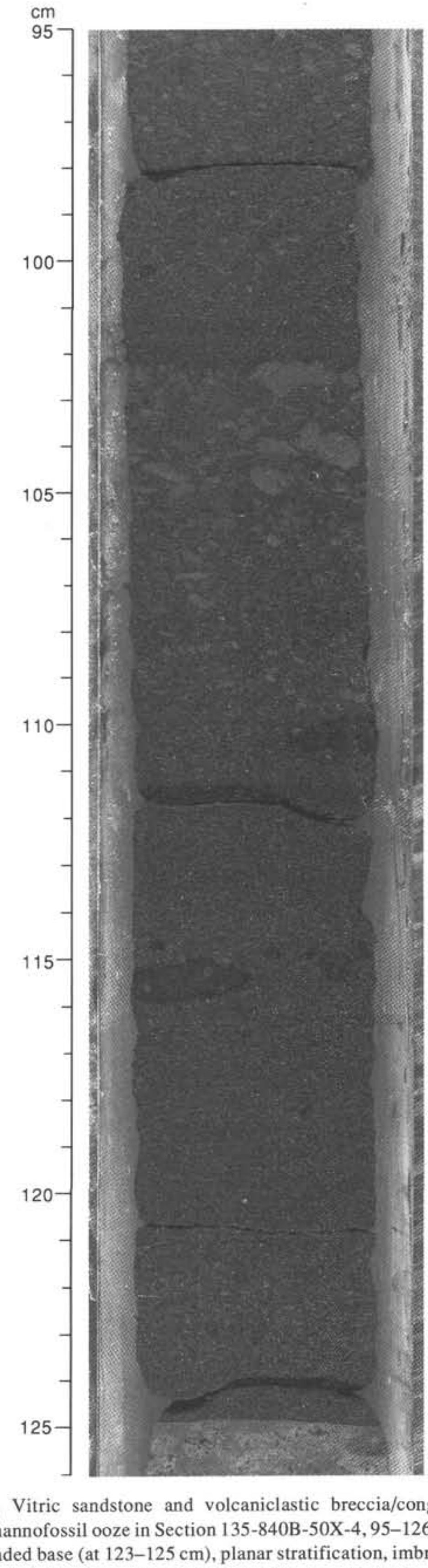

Figure 15. Vitric sandstone and volcaniclastic breccia/conglomerate overlying nannofossil ooze in Section 135-840B-50X-4, 95–126 cm. Note reverse-graded base (at 123–125 cm), planar stratification, imbrication of pumice clasts indicating paleocurrents toward the left-hand side of the photograph, and reverse grading in the volcaniclastic breccia/conglomerate (at 102–110 cm).

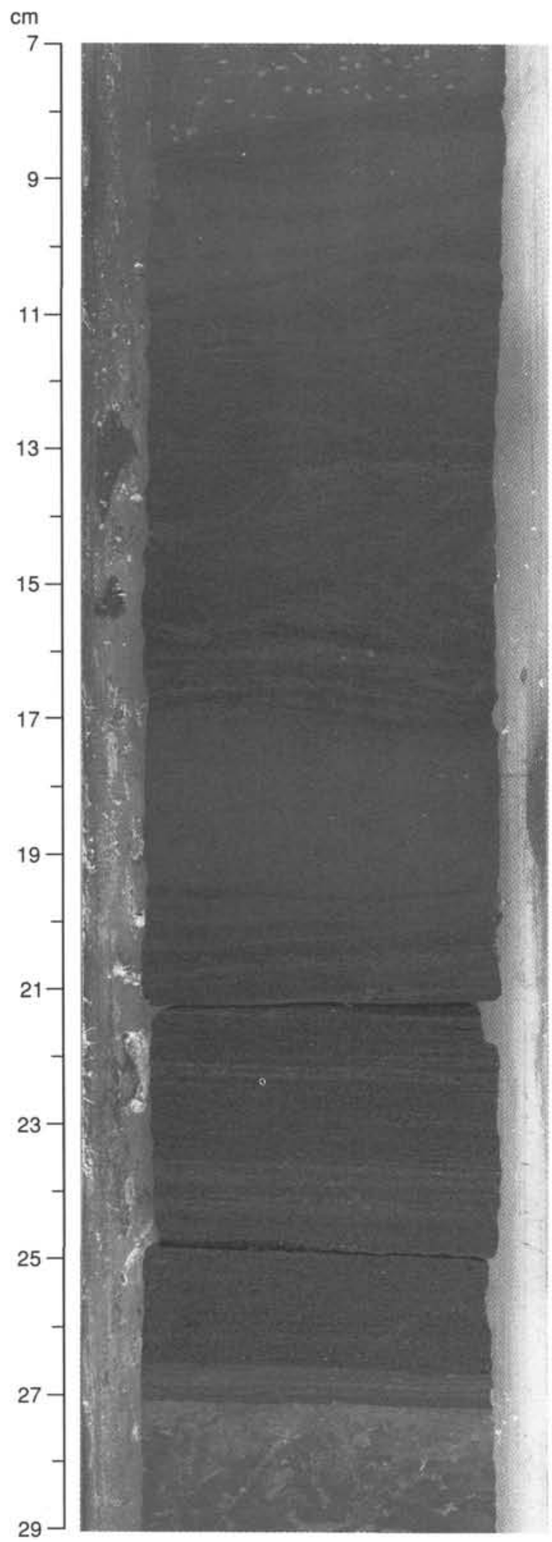

Figure 16. Vitric sandstone (20–27 cm) and vitric siltstone (9–20 cm) overlying heavily bioturbated nannofossil chalk (at 27 cm) in Section 135-840B-50X-3, 7–29 cm. Note planar lamination (21–27 cm), wedge-planar lamination (19–21 cm), trough cross-lamination (16–17 cm), and convoluted interval (11–16 cm).

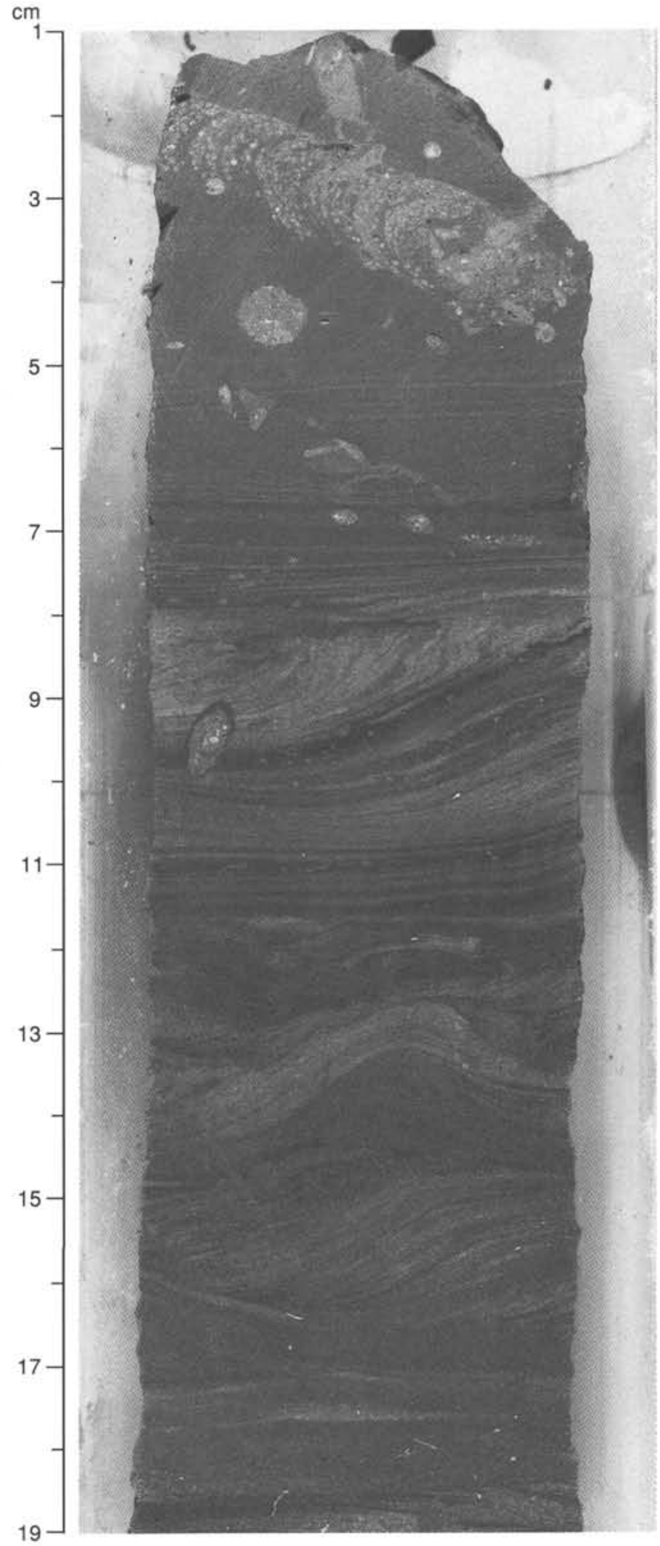

Figure 17. Vitric siltstone showing complex sequence of sedimentary structures including trough cross-lamination, wedge-planar-lamination, wavy lamination, lenticular lamination, and convolute laminae in Section 135-840B-50X-1, 1–19 cm. Note *Zoophycos* burrow in the upper part of the section and burrowed cross-stratification at 9–10 cm.

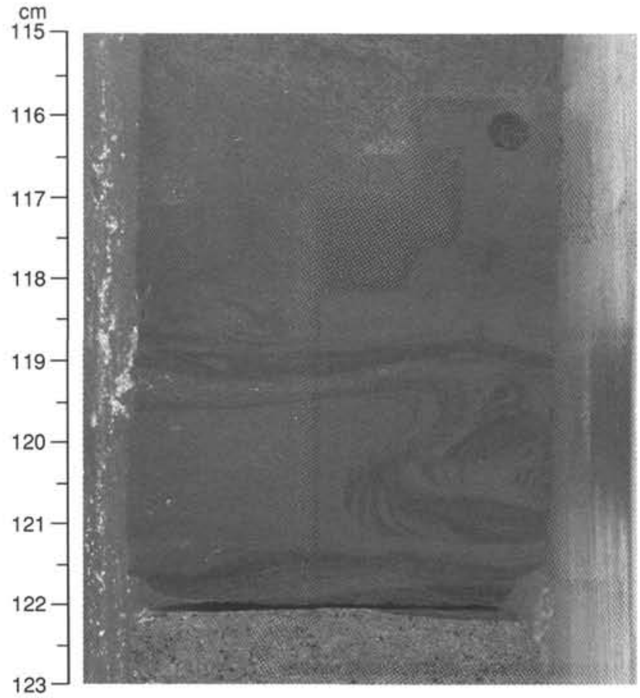

Figure 18. Vitric siltstone overlying nannofossil chalk (boundary at 122 cm) in Section 135-840B-52X-6, 115–123 cm. Note recumbent folding in trough cross-laminated siltstone produced by soft sediment deformation. Also note microfaults nearly subparallel to the axial plane of the fold.

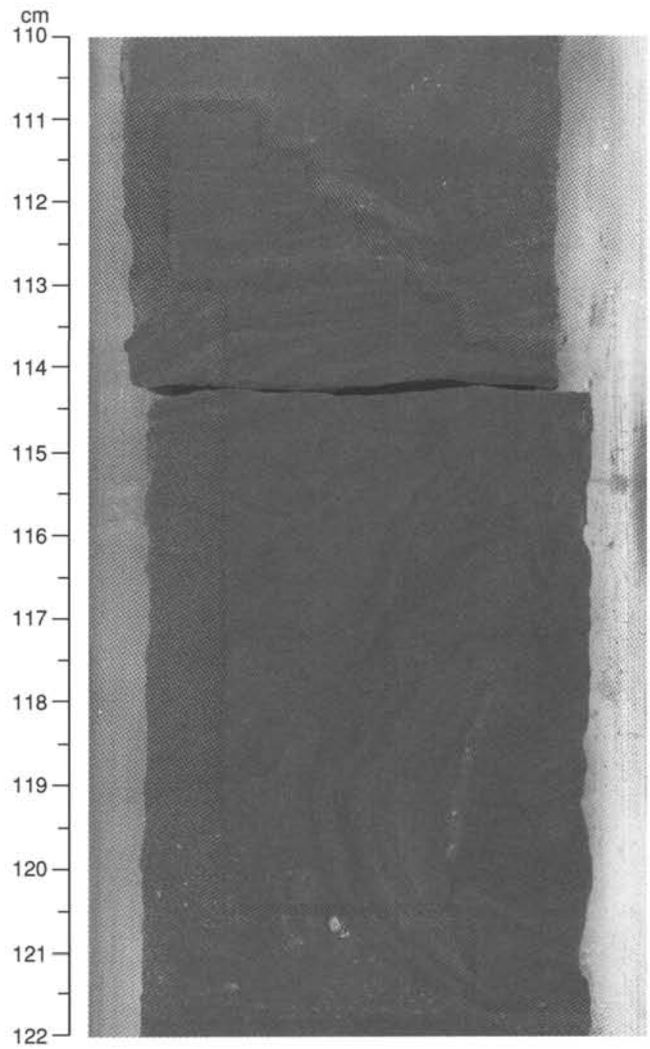

Figure 19. Convoluted interval of vitric siltstone in Unit III (Section 135-840B-51X-1, 110–122 cm).

Fig. 21). These structures do not, however, extend into overlying beds. Other convoluted beds were more consolidated at the time of deformation, as they show brittle microfaulting, possibly related to overturning and thrust folding. Some of these faults extend down into sediments that are not convoluted (e.g., Section 135-840B-55X-1, 118–121 cm; Fig. 21), and others are confined to the convoluted intervals (e.g., Sections 135-840B-37X-1, 16–20 cm, and -52X-6, 119–121 cm; Fig. 18). Microfaults sometimes trend subparallel to axial planes of folds in the vitric silts (Fig. 18). Figure 22 (Section 135-840B-58X-3, 120–132 cm) shows another example of a convoluted interval with subhorizontal microfaulting (see "Structural Geology" and "Background and Objectives" sections, this chapter).

Interpretation

Unit III consists of a sequence of volcaniclastic turbidites interbedded with heavily bioturbated nannofossil chalks. From the base of the unit upward, there is a gradual decrease in the maximum thickness and the coarseness of individual turbidites. This may be interpreted as reflecting a change from a proximal to a more distal area of deposition. The turbidites in the upper part of Unit III were possibly deposited in slightly deeper water and farther from the source area than were turbidites in the lower part of the unit. A decrease in sediment supply with time related to waning volcanism may be inferred.

Volcaniclastics

Sediments at Site 840 are characterized by a high volcaniclastic input by sediment gravity flows, mainly as silty to sandy turbidites. Primary fallout tephras are rare and were identified only in Hole 840A. The turbidites show complex internal sedimentary structures described above. We analyzed 17 samples from the vitric turbidites for refractive index measurements of glass shards to estimate their SiO_2 concentrations, using the methods described in detail in the "Lithostratigraphy" section of the Site 834 chapter (this volume). Glass compositions extend over a wide range, varying from basaltic to rhyolitic, with major peaks of abundance at basaltic andesitic, silicic andesitic, and dacitic/rhyodacitic compositions (Table 3 and Fig. 23).

Unit I

A series of seven normally graded, dark gray to light brownish gray ash layers, 5–10 cm thick, with maximum grain sizes of about 3 mm at the bases, occur in Section 135-840A-1H-3. These consist of scoriaceous lapilli and ash containing up to 15–20 vol% of coarse-grained igneous minerals, predominantly plagioclase, dark green to light green clinopyroxene, yellowish brown orthopyroxene, and rare olivine. This succession is interpreted as proximal primary fallout tephra resulting from either a shallow submarine eruption or a subaerial Strombolian-type eruption. Similar, highly porphyritic, basaltic, and basaltic andesite lavas with up to 30 vol% plagioclase, 15 vol% clinopyroxene, 8 vol% orthopyroxene, and trace amounts of olivine phenocrysts have been collected on Ata Island (Vallier et al., 1985). This island is located about 40 km to the east of Site 840 and the ashes recovered in Hole 840A may have been derived from this source.

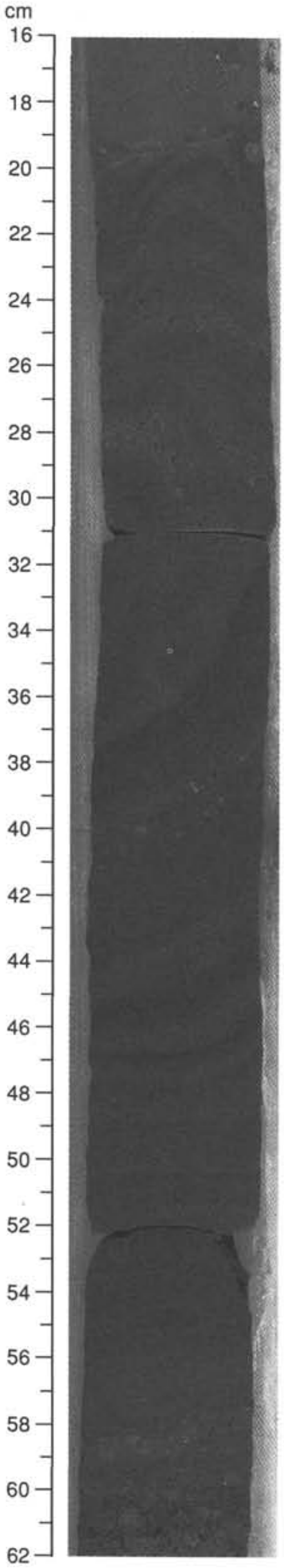

Figure 20. Convoluted bed of vitric sandstone in Section 135-840B-50X-4, 16–62 cm. Note sharp, undulating upper boundary of convoluted bed.

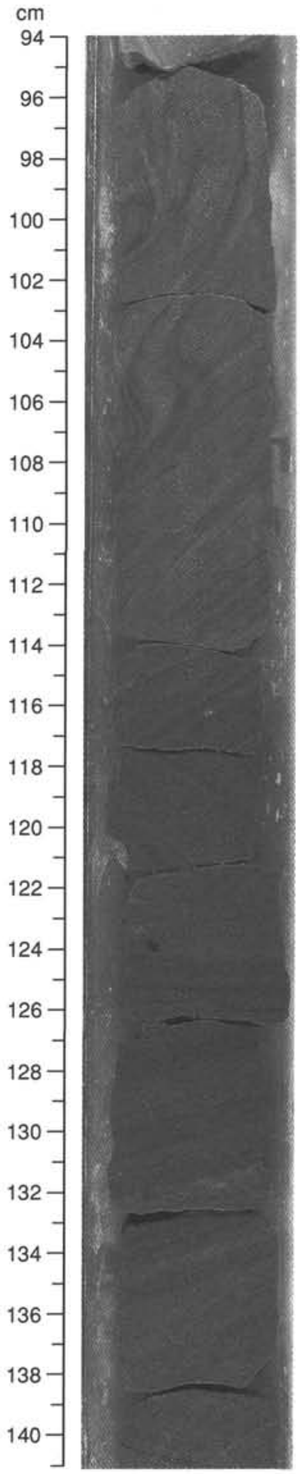

Figure 21. Convoluted trough cross-stratified vitric sandstone in Section 135-840B-55X-1, 94–141 cm. Note subvertical, flowlike structure probably produced by water escape during deformation. Note drilling biscuits and reorientation of pieces, resulting in apparent changing dip directions of the foresets. Note that the inclination of the foresets in the trough cross-bedded sequences at 110–126 and 126–141 cm decreases downward, from relatively steep foresets in the upper part of the sequences to more horizontal bottomsets at their base.

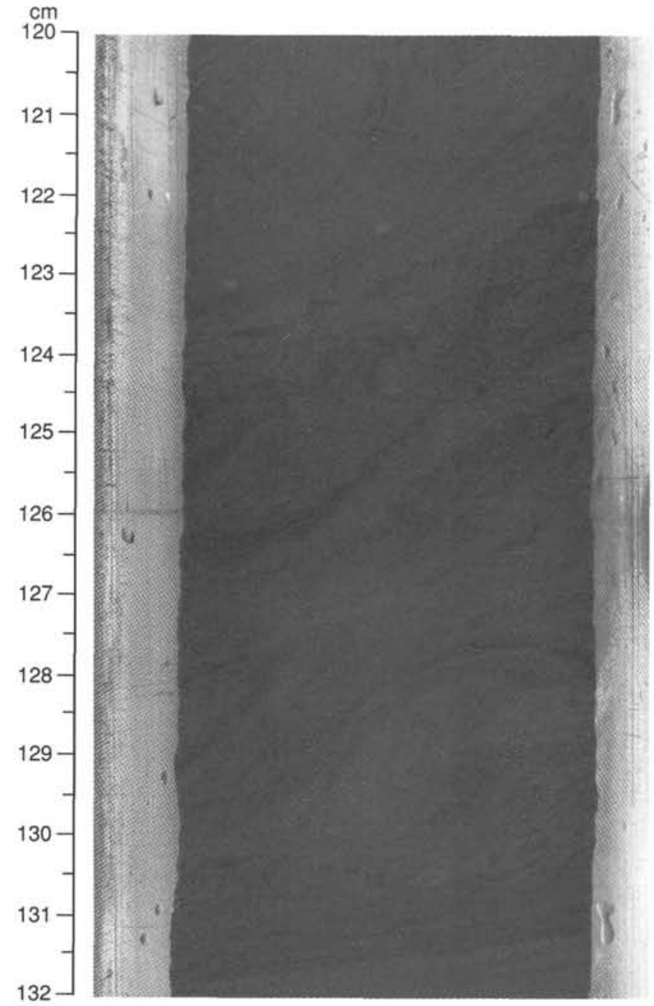

Figure 22. Soft sediment deformation and microfaulting in vitric siltstone in Section 135-840B-58X-3, 120–132 cm. Note the subhorizontal microfaults.

Sample 135-840B-3-CC, 0–1 cm, consists of only a few cubic centimeters of volcaniclastic gravel and represents the sole recovery in the uppermost interval of Hole 840B, between 5 and 37 mbsf. It consists of a polymict assemblage of subrounded to rounded volcanic lithic fragments <1 cm in diameter. Subangular, isolated, igneous-derived minerals, up to several millimeters in diameter, include clinopyroxene, orthopyroxene, plagioclase, and olivine. Fibrous pumice fragments <3 mm in diameter are rare. Fragments of volcanic rocks show a wide range in modal composition and groundmass textures, and include:

1. one clast with opaque, cryptocrystalline groundmass that has about 10 vol% vesicles, large plagioclase (20 vol%), olivine (1 vol%), and clinopyroxene (1 vol%) phenocrysts;

2. one aphyric, very pale brown to yellowish brown vitric clast with distinct flow banding, resembling groundmass textures of fragments of rhyolitic lava flows (Fig. 24);

3. one clast with opaque, cryptocrystalline groundmass with about 4 vol% of plagioclase and 4 vol% of olivine (completely altered to iddingsite) phenocrysts in a groundmass comprising some plagioclase microlite laths with fluidal texture;

Table 3. Refractive indices (*n*) and SiO_2 concentrations (estimated from Church and Johnson [1980] and Schmincke [1981]) of vitric shards (63–36 μm size fraction) from volcaniclastic turbidites in Hole 840B.

Sample (cm)	Depth (mbsf)	Comment	*n*	SiO_2 (wt%)
135-840B-				
1X-1, 23	0.23	Green	1.589	51.2
1X-1, 23	0.23	Clear, minor, partly altered	1.526	65.5
10X-CC, 2	86.25	Green	1.578	53.4
10X-CC, 2	86.25	Clear, dominant	1.518	67.7
12X-5, 49	110.47	Green, minor	1.582	52.6
12X-5, 49	110.47	Clear, majority	1.529	64.8
12X-5, 49	110.47		1.518	67.7
24X-1, 33	221.33	Clear	1.514	68.8
24X-CC, 12	234.47	Clear, majority	1.510	70.0
24X-CC, 12	234.47	Green	1.534	63.5
30X-CC, 11	279.96	Clear	1.510	70.0
30X-CC, 11	279.96	Light green, majority	1.530	64.5
30X-CC, 11	279.96	Brown	1.542	61.4
30X-CC, 11	279.96	Green	1.578	53.4
33X-1, 22	308.42	Green	1.578	53.4
34X-1, 24	318.04	Clear	1.558	57.7
34X-1, 24	318.04	Green, majority	1.566	55.9
35X-2, 89	329.89	Green	1.574	54.2
35X-2, 89	329.89	Brown	1.522	66.6
35X-2, 89	329.89	Clear	1.509	70.3
37X-1, 13	337.53	Brown	1.514	68.8
37X-1, 13	337.53	Clear, majority	1.522	66.6
37X-1, 13	337.53	Brown	1.578	53.4
39X-1, 53	357.33	Clear/brown, majority	1.514	68.8
39X-1, 53	357.33	Fibrous	1.522	66.6
39X-1, 53	357.33	Green	1.569	55.2
42X-2, 28	387.58	Clear	1.526	65.5
42X-2, 28	387.58	Green	1.550	59.5
42X-2, 28	387.58	One sample	1.548	60.0
42X-3, 92	389.72	Light green	1.542	61.4
42X-3, 92	389.72	Clear	1.530	64.5
46X-2, 9	425.49	Clear	1.490	75.9
46X-2, 9	425.49	Majority	1.598	49.6
48X-1, 91	443.71	Green, majority	1.546	60.5
52X-2, 5	482.95	Clear	1.526	65.5
52X-2, 5	482.95	Green, majority	1.566	55.9
52X-2, 5	482.95	Green, majority	1.550	59.5
53X-3, 28	484.68	Clear	1.498	73.5

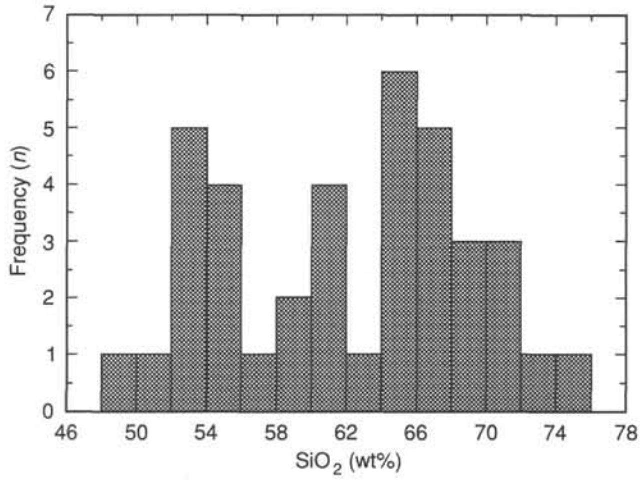

Figure 23. Frequency distribution of SiO_2 in samples studied for refractive indices. Note that the histogram is not weighted for the modal composition (i.e., frequency of populations) within individual samples.

Figure 24. Photomicrograph of vitric clast with pronounced, fluidal texture indicating extreme shearing in very viscous flow; Sample 135-840B-3X-CC, 0–1 cm; long side of photomicrograph = ~1.5 mm, plane-polarized light. Microphenocrysts are euhedral plagioclase. Aligned microlites are both plagioclase and clinopyroxene.

4. one aphyric clast with opaque, cryptocrystalline groundmass with about 2 vol% vesicles and fluidal texture of abundant groundmass plagioclase laths and less abundant clinopyroxene;
5. one clast made up of about 50 vol% predominantly euhedral clinopyroxene, 20 vol% orthopyroxene, and 30 vol% pale brown glass (websteritic cumulate?); and
6. one clast with about 20 vol% plagioclase, 2 vol% olivine (partly altered to iddingsite), and 1 vol% magnetite phenocrysts and microphenocrysts set in a granular matrix of mostly clinopyroxene and less abundant plagioclase.

The roundness and the polymict nature of the gravel indicate a relative mature sediment that has undergone several cycles of reworking and mixing of material from several different sources. The wide range in modal and inferred chemical composition suggest an origin from a seamount or an island of the Tofua Arc as the most likely source. Grains with nonvitric groundmass may indicate contributions from subaerial volcanism, whereas the abundance of fluidal textures is consistent with effusive volcanism. The scarcity of highly vesicular clasts may simply reflect the high degree of reworking of this sediment. The depositional environment of the gravel is uncertain.

Volcaniclastic input at Site 840 is 0–3 estimated depositional events per 100 k.y. in Unit I. The thickness of individual turbidites in Unit I increases downhole and reaches a maximum of about 5 m in the interval from 60 to 80 mbsf, where volcaniclastic material contributes about 50 vol% of the total sediment.

Vitric shards in Unit I range in composition from basaltic to dacitic (Fig. 25). The dominant composition, however, is basaltic (around 51 wt% SiO_2) in Sample 135-840B-1X-1, 23 cm (0.23 mbsf) and dacitic (68 wt% SiO_2) in the lower part of this unit in Sample 135-840B-10X-CC, 2 cm (86.25 mbsf).

Unit II

The boundary between Units I and II is marked by a pronounced decrease in the amount and rate of volcaniclastic input (Table 4). The volcaniclastic input in Unit II is variable and reaches peak values in the interval between 120 and 160 mbsf, where volcaniclastics constitute up to 86 vol% of the sediment. In this interval, 26 individual vitric turbidites <2 m thick (average thickness = 1–1.3 m) were estimated to have been deposited in about 50,000 yr. The lower boundary of Unit II is characterized by a distinct decrease in the rate of input and volume of volcaniclastic material.

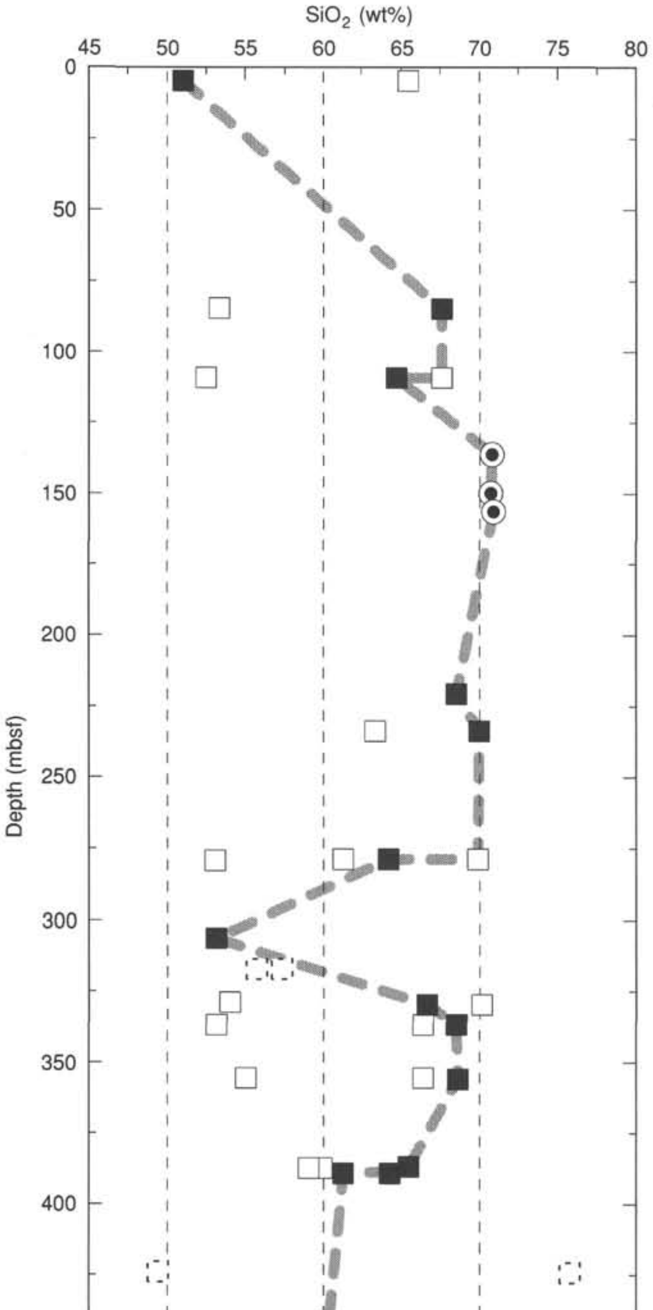

Figure 25. Downhole variation of SiO_2 concentration in Hole 840B as estimated from the refractive indices of fresh vitric glass shards. Thick, gray, dashed line connects data points from dominant populations (dark squares). The compositions of minor glass shard populations in individual samples are indicated by white squares. Squares with dashed lines represent less reliable data because of slight alteration of glass shards. White circles with black dots indicate data from X-ray fluorescence analyses of pumice clasts. Several lapilli-size clasts were collected for each analysis.

Table 4. Summary of data on mass flows in Holes 840B and 840C averaged over regular 20-m intervals.

Interval (m)	Total thickness (cm)	*N*	Abundance of volcaniclastic material (vol%)	Mean thickness (cm)
0–20	118	5	5.9	24
20–40	0	0	0	0
40–60	737	10	36.85	74
60–80	1022	8	51.1	128
80–100	34	3	1.7	11
100–120	49	4	2.45	12
120–140	1040	6	52	173
140–160	1302	20	65.1	65
160–180	154	3	7.7	51
180–200	459	4	22.95	115
200–220	0	0	0	0
220–240	71	3	3.55	24
240–260	0	0	0	0
260–280	118	9	5.9	13
280–300	43	2	2.15	22
300–320	78	5	3.9	16
320–340	321	16	16.05	20
340–360	218	10	10.9	22
360–380	163	6	8.15	27
380–400	309	17	15.45	18
400–420	261	12	13.05	22
420–440	415	16	20.75	26
440–460	532	22	26.6	24
460–480	722	29	36.1	25
480–500	1075	31	53.75	35
500–520	755	11	37.75	69
520–540	1064	24	53.2	44
540–560	837	20	41.85	42
560–580	1557	36	77.85	43
580–600	1117	19	55.85	59

Note: *N* = number of volcanic beds within the interval.

The XRF analyses were made on samples from Cores 135-840C-6H to -8H at 135.54, 150.68, and 159.28 mbsf (Table 5). Because of the small grain size of the pumice clasts, several large pumice clasts had to be sampled from intervals 10–60 cm long for each analysis. The pumice clasts are geochemically very homogeneous and of rhyolitic to rhyodacitic composition, with an average SiO_2 content of about 71 wt%. This agrees with results from refractive index determinations of two samples from the central part of Unit II (Sample 135-840B-24X-1, 33 cm, at 221.33 mbsf, and Sample 135-840B-24X-CC, 12 cm, at 234.47 mbsf). Both of these samples are dominated by clear, colorless vitric shards of rhyodacitic composition (70 wt% SiO_2).

Compared to rhyodacitic pumice from Lau Basin Sites 837 and 838, those from Site 840 (Unit II) show some slight but systematic differences. The rhyodacite analyzed from Site 839 has a distinctly different, depleted trace element pattern and is not considered further here. Pumice samples from Site 840 are slightly less silicic than those from Sites 837 and 838. They have a higher TiO_2 concentration (0.68–0.76 wt% vs. 0.48–0.58 wt% at Sites 837 and 838), and higher Al_2O_3 (14.0–14.3 wt% vs. 12.5–13.1 wt% at Sites 837 and 838). Trace element contents show less distinct dissimilarities. Slightly lower Y and Ce concentrations in pumice from Site 840 than in those from Sites 837 and 838 are probably the most pronounced dissimilarities. Higher pumice Sr concentrations at Site 840 may correlate to higher Al_2O_3, reflecting differences in the proportion of plagioclase in the fractionating assemblage.

Unit III

We interpreted 28% of the sediments in Unit III as vitric turbidites that were deposited over slightly more than 1 m.y. The

Table 5. Chemical composition (from XRF analysis) of lapilli-size rhyodacitic pumice clasts from Hole 840C (Unit III) and rhyodacitic pumice clasts drilled within the Lau Basin (Holes 837A, 838A, and 839A).

Hole	837A	838A	839A	840C	840C	840C
Core	8H	7H	10H	6H	7H	8H
Section	1	4	3	2	CC	7
Top (cm)	108	0	116	54	5	1
Bottom (cm)	116	57	135	114	15	17
Depth (mbsf)	66.08	55.7	84.66	135.54	150.68	159.28
Major elements (wt%):						
SiO_2	77.15	72.08	70.89	71.31	71.10	71.43
TiO_2	0.48	0.58	0.55	0.76	0.68	0.69
Al_2O_3	12.50	13.12	14.67	13.98	14.21	14.31
Fe_2O_3	2.46	3.45	4.80	5.10	4.31	4.39
MnO	0.11	0.14	0.13	0.18	0.14	0.14
MgO	0.58	0.94	1.15	1.09	0.95	1.00
CaO	2.16	3.02	5.07	3.83	3.47	3.50
Na_2O	4.19	4.27	3.64	4.34	4.33	4.57
K_2O	1.68	1.52	0.92	1.20	1.52	1.50
P_2O_5	0.06	0.12	0.11	0.19	0.16	0.16
Total	101.31	99.21	101.93	101.97	100.85	101.68
LOI	5.55	5.29	3.65	5.05	5.07	5.55
FeO	2.21	3.10	4.32	4.59	3.88	3.95
FeO/MgO	3.81	3.30	3.76	4.21	4.08	3.95
Trace elements (ppm):						
Nb	3	3	2	2	2	3
Zr	164	145	85	144	150	148
Y	52	49	30	44	42	42
Sr	143	176	180	188	181	148
Rb	25	22	11	12	15	15
Zn	52	56	46	80	68	70
Cu	16	10	28	13	11	11
Ni	1	1	0	2	1	2
Cr	0	0	0	0	0	0
V	19	29	71	25	26	24
Ce	36	33	19	24	27	29
Ba	286	270	234	229	259	251

Note: Because of the small grain size, several pumice grains had to be collected for each analysis. LOI = loss on ignition.

overall input of volcaniclastic material varies systematically. In the upper part of Unit III (260–320 mbsf), only 2–6 vol% of the sediments are volcaniclastic, with 1–6 turbidites estimated to have been deposited per 100 k.y. (based on biostratigraphic estimates of sedimentation rates). Turbidite numbers increase almost continuously downhole to reach peak values between 520 and 600 mbsf. In this interval, volcaniclastic sediments make up 42–78 vol% of the recovered sediment, with up to 50 individual mass flows estimated to have been deposited per 100 k.y. The average thickness of turbidites above 500 mbsf is only 18–27 cm. The thickness of individual turbidites below 500 mbsf increases to 49–69 cm. Below this depth, individual turbidites may be as thick as 2.4 m. The increasing abundance and thickness of volcaniclastic layers downhole corresponds to increasing maximum and average grain sizes. The shallowest occurrence of gravel-size clasts (maximum diameter = ~0.5 cm) is at about 455 mbsf (Section 135-840B-49X-2). Other beds of volcaniclastic gravels are found in Sections 135-840B-50X-4, -53X-5 (maximum diameter = 1 cm), -54X-3, -55X-1 (maximum diameter = 1 cm), -55X-2 (maximum diameter = 1 cm), -56X-4 (maximum diameter = 2.8 cm), -57X-5, -60X-2 (maximum diameter = 4 cm), -62X-5 (maximum diameter = 1.5 cm), -62X-6 (maximum diameter = 3 cm), and -63X-2 (maximum diameter = 2 cm).

Glass shards in the upper part of Unit III (260–360 mbsf) are colorless to pale brown, and are dominated by dacites of 64–69 wt% SiO_2 (as estimated from refractive index determinations). A second population of medium to dark brown, often slightly green shards occurs in the same 100-m depth interval and consists predominantly of basaltic andesitic glass of 53–56 wt% SiO_2. Below 360 mbsf, the majority of the shards are pale greenish brown and of intermediate, andesitic to dacitic compositions with 60–66 wt% SiO_2.

The vitric sandstones and siltstones of Unit III are made up of 30–95 vol% vitric shards, mainly of very pale brown to medium brown color. Shards are generally angular, with low internal vesicularity, but frequent bubble-wall shards and bubble-junction shards are evidence for abundant external vesicles. The volume of these external vesicles probably often exceeded the volume of the enclosing glass, indicating a high vesicularity (Fig. 26). The general scarcity of pumice shards containing tubular vesicles and elongate fibrous shards above 500 mbsf may reflect the overall intermediate compositions and small grain sizes of vitric shards. The increasing abundance of pumiceous clasts farther downhole (below Core 135-840B-54X) correlates with the increasing grain sizes of the mass-flow deposits. Pumice lapilli fragments in these deposits (e.g., in Section 135-840B-55X-2, 58–62 cm) are partially frothy, with vesicle contents of up to 90 vol% (Fig. 27).

Plagioclase is the most common igneous mineral present in the vitric turbidites of Unit III. It constitutes up to 60 vol% of a siltstone in Section 135-840B-35X-2, 90–91 cm (329.90 mbsf), but normally makes up <10 vol% of the volcaniclastic sediments. Plagioclase appears as microphenocrysts and quench microlites within the vitric groundmass of the shards (Fig. 28) but occurs more commonly as isolated grains. These individual grains throughout Unit III are characterized by abundant broken surfaces and subangular to subrounded edges (Fig. 29). Breaking of igneous minerals is commonly caused by ejection or impact during explosive volcanic eruptions (e.g., Fisher and Schmincke, 1984). Isolated pyroxene and magnetite grains occur throughout the unit, but exceed trace amounts only in a few samples.

Alteration

Vitric shards in Unit III are generally optically clear to slightly birefringent (indicating hydration and the very early stages of alteration). Interparticle pore space in the volcaniclastic siltstones and sandstones often makes up 20–25 vol% and is normally free of cementation. Induration of the volcaniclastic sediments is almost completely a result, therefore, of mechanical compaction.

Trace amounts of small rhombohedral calcite grains (with diameters usually on the order of a few microns) occur in nearly all volcaniclastic samples below 328.60 mbsf. Aggregates of iron hydroxide and coatings of iron hydroxide are also found commonly throughout Unit III.

The interval between Section 135-840B-40X-1 and -45X-1 (368–414 mbsf) was affected by a more pronounced alteration and authigenic mineralization. This resulted in the growth of brown, brownish green, and green smectite that constitutes about 25 vol% in the lowermost sample and almost completely fills the inter- and intraparticle pore spaces (Fig. 30). Zeolites, probably natrolite-thomsonite, occur in trace amounts. The birefringence of glass shards is slightly higher than in the other parts of Unit III. Despite intense cementation, volcanic glass is not replaced by secondary minerals in this section, although it is commonly surrounded by a thin rim of clay minerals with higher birefringence.

The most intense alteration at Site 840 is found in a 2-m-thick bed of green, polymict volcaniclastic breccia containing highly vesicular pumice clasts (Sections 135-840B-60X-1 and -60X-2). Fresh glass is not preserved in this deposit but is completely replaced by pale to dark brown smectite, bright green celadonite, iron hydroxides, and a platy zeolite of rather high birefringence (tentatively identified as clinoptilolite/heulandite). Vesicles, in-

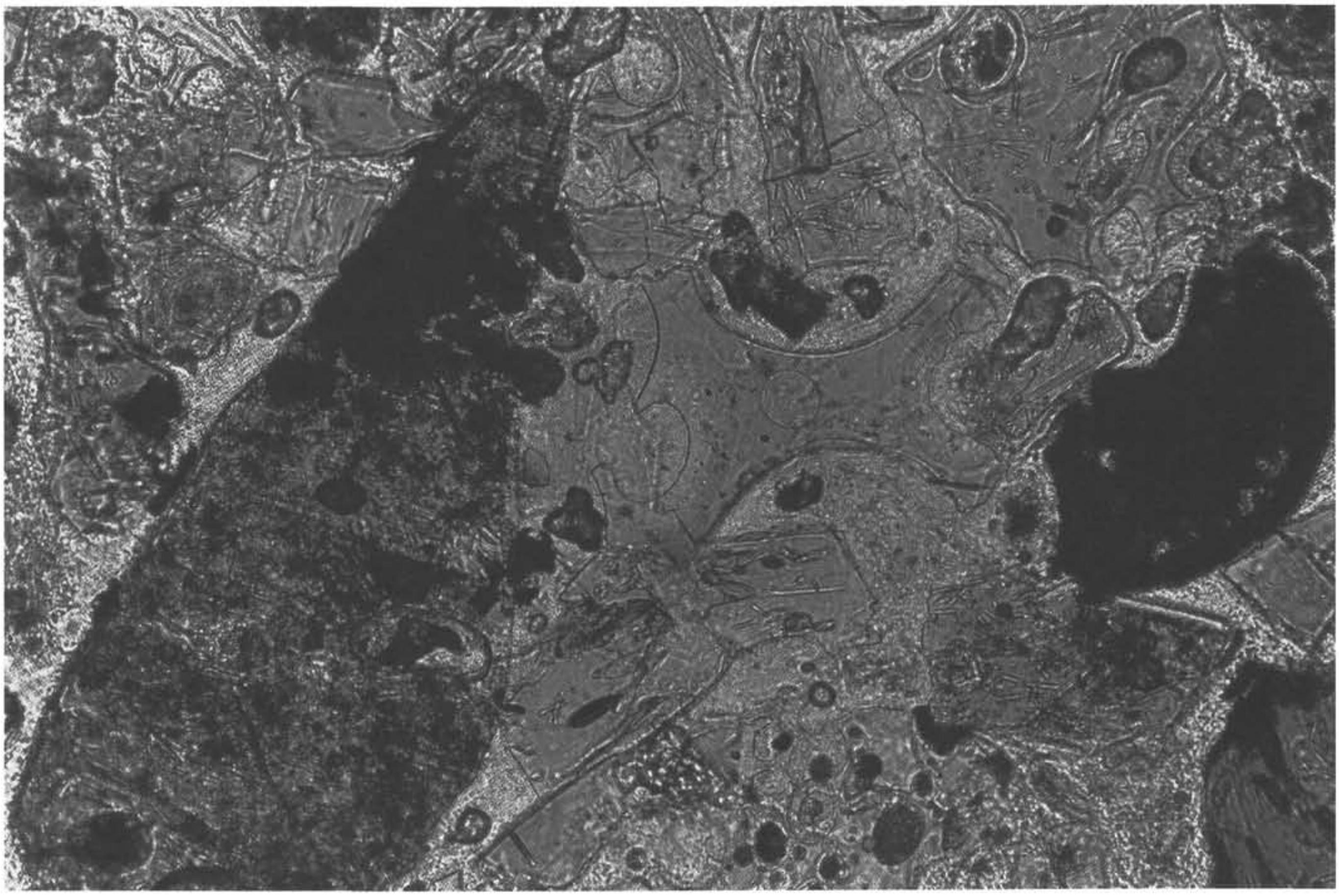

Figure 26. Photomicrograph illustrating the typical appearance of optically clear, medium brown vitric shards of low vesicularity in vitric sandstone; Sample 135-840B-48X-3, 10–11 cm; long side of photomicrograph = ~0.6 mm, plane-polarized light. The shards often have microlites of plagioclase in rosette-like clusters. Note the size and abundance of external vesicles in the delicate glass shard in the center of the photograph. These external vesicles may exceed the volume of the shard.

terparticle pore space, and veins are also filled by dark brown smectite, green celadonite (Fig. 31), and zeolites.

The volcanic content of Unit III shows an overall gradual and systematic variation in abundance, volume, grain size, and chemical composition. These variations, coupled with the high rate of volcaniclastic sediment input over the short time interval of only about 1 m.y., suggest a single relatively local, spatially restricted source of the volcanic material, probably a larger seamount or island. The occurrence of highly vesicular pumice clasts, especially in the lower part of Unit III, is strong evidence that eruptive products of shallow-water or, more likely, subaerial explosive volcanism contributed to the turbidites. The abundance of broken plagioclase fragments and the scarcity of lithic volcanic clasts and fluidal groundmass textures strongly support an explosive volcanic origin.

The observed variations in the volume, grain size, and rate of volcanic input in Unit III are likely to reflect primary variations in the chemical composition of magmas, the eruptive volume, and the frequency and style of volcanism (e.g., volume ratio of explosive over effusive volcanic products) in the source area of the turbidites. A gradually decreasing supply of volcaniclastic sediments with time may therefore reflect the waning stages in the volcanic activity of a single island on the Lau Ridge. The relatively constant average thickness of turbidites over large intervals of Unit III suggests that there have not been drastic changes in distance to the source area.

Depositional History

The oldest sediments recovered at Site 840 are of late Miocene age (approximately 6.6 Ma). The sediments at the base of Unit III are interpreted as proximal turbidites deposited near the source area. In the lower part of Unit III, deposition was rapid, with an average sedimentation rate of approximately 357 mm/k.y. In the uppermost part of the unit, between 320 and 265.5 mbsf, the sediments accumulated more slowly, with a sedimentation rate of approximately 110 mm/k.y. (see "Sediment Accumulation Rates" section, this chapter). Upward through Unit III, there is a reduction in grain size and a decrease in the maximum thickness of individual turbidites, probably reflecting deposition from a more distal source. However, the trace fossil assemblage does not

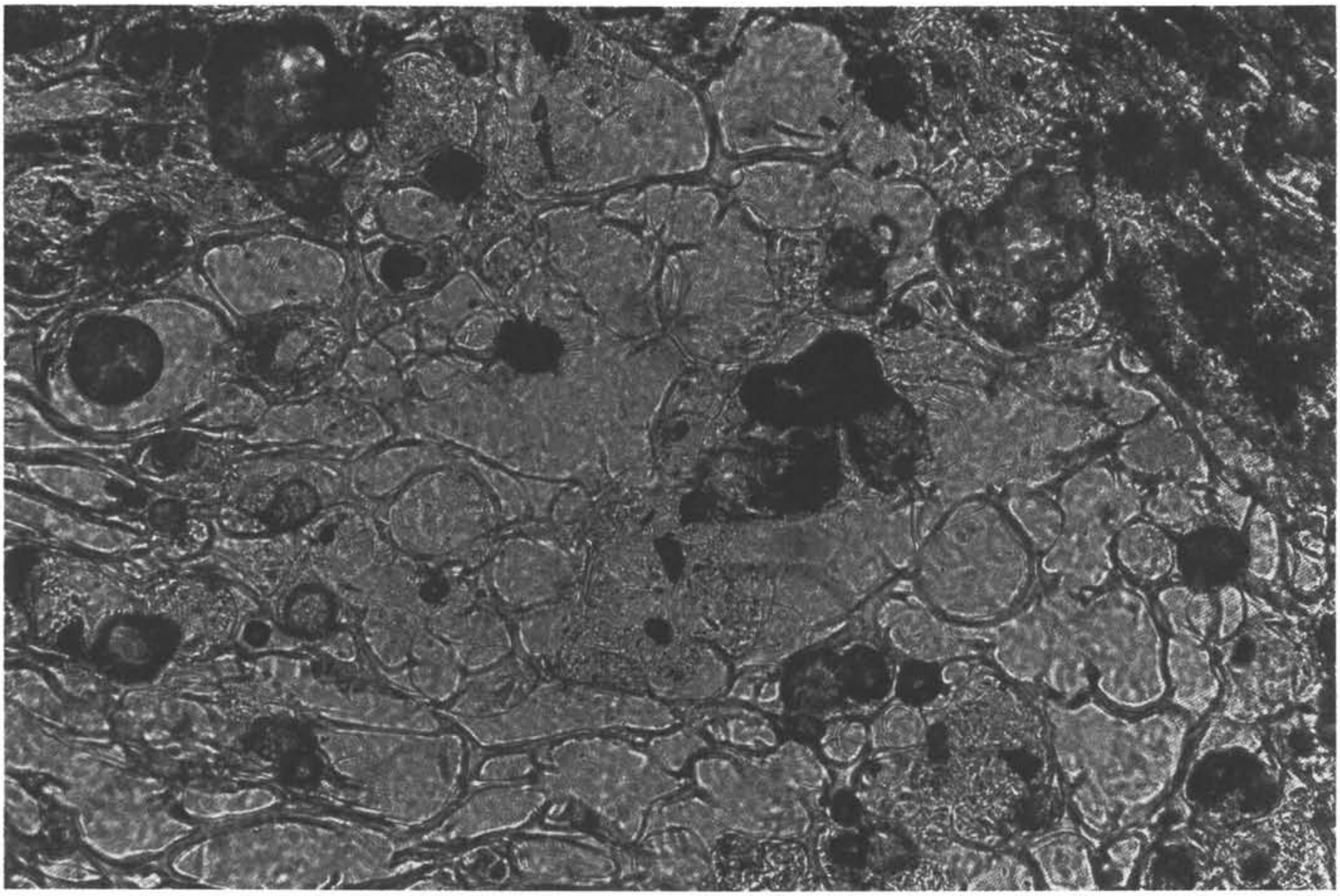

Figure 27. Photomicrograph of highly vesicular, frothy interior of pumiceous clast in pumiceous breccia; Sample 135-840B-55X-2, 58–62 cm; long side of photomicrograph = ~0.6 mm, plane-polarized light.

change appreciably downcore, and water depths deduced from micropaleontology probably did not exceed the present water depth of approximately 800 m.

The chemical composition of glasses within the volcaniclastics of Unit III varies from andesitic-dacitic (60–66 wt% SiO_2) near the base to dacitic (64–69 wt% SiO_2) in the upper part. This suggests a common source of volcanic material, probably a single seamount or island. It is inferred that, before the opening of the Lau Basin approximately 5–6 m.y. ago, the Lau Ridge was the primary source of volcaniclastic material deposited at Site 840, and that Site 840 was situated in the forearc basin at that time. The large volume of highly vesicular pumice clasts suggests that the explosive volcanic eruptions producing these glasses occurred either in very shallow water or subaerially. The thinning and fining of turbidites with time may reflect increasingly distal deposition from the Lau Ridge and/or the presence of a topographic barrier restricting or reducing the sediment supply because of the waning volcanic activity of a single island on the Lau Ridge.

The boundary between Units II and III, at approximately 5.3 Ma, reflects a change back to more proximal, coarse-grained deposition. The sediments of Unit II are dominated by pumiceous gravels and sands, interpreted as sediment gravity flow deposits. These sediments were deposited very rapidly, at a sedimentation rate of about 820 mm/k.y. (see "Sediment Accumulation Rates" section, this chapter). Close proximity to the volcanic source (probably the Lau Ridge) is suggested by the large volumes of rhyodacitic pumice (approximately 70 wt% SiO_2) deposited within only 1.5 m.y.

Interbedded with the coarse-grained, volcaniclastic sediments are numerous, heavily bioturbated, nannofossil chalk beds interpreted as hemipelagites. The trace fossil assemblage of these interbeds is typical of warm, shallow-water chalks. In the uppermost 10–15 m of Unit II, the sediment sequence is dominated by nannofossil chalks, implying a decrease in the rate of volcaniclastic sediment supply (or a period of erosion or nondeposition) at about 5.1 Ma, perhaps just before or at the time of the opening of the Lau Basin (see "Introduction and Principal Results" chapter, this volume).

The boundary between Units I and II is placed at the boundary between nannofossil ooze and chalk. Micropaleontologic data indicate a possible 1-m.y. biostratigraphic hiatus within Unit I (at about 95 mbsf). The sedimentation rate during deposition of the sediments between 95 mbsf and the lower boundary of Unit I (at 109.98 mbsf) was about 25 mm/k.y. (see "Sediment Accumulation Rates" section, this chapter). The sediments deposited during this interval were dominantly pelagic nannofossil oozes, with minimal terrigenous or volcaniclastic input. The remaining part of Unit I consists of nannofossil oozes, interpreted as hemipelagic

Figure 28. Photomicrograph of typical, angular, medium brown, optically clear vitric shards with low vesicularity in vitric siltstone; Sample 135-840B-52X-2, 12–14 cm; long side of photomicrograph = ~0.3 mm, plane-polarized light. Shards are probably of andesitic composition. Note plagioclase microlites, some with quench textures.

deposits, interbedded with fine- to coarse-grained volcaniclastic beds, interpreted as sediment gravity flow deposits. Vitric shards within the volcaniclastics range in chemical composition from basaltic (around 51 wt% SiO_2) to dacitic (68 wt% SiO_2). These sediments accumulated slowly over a period of about 3 m.y. In the uppermost part of Unit I, there are a few volcanic ash and lapilli layers, interpreted as proximal fallout tephras resulting from shallow submarine, or more likely subaerial Strombolian-type eruptions. Based on similarities in composition to lavas exposed in the Tonga Island group, these pyroclastic deposits were probably derived from Ata Island (Vallier et al., 1985).

STRUCTURAL GEOLOGY

Introduction

Site 840 was drilled on the southern part of the Tonga platform. The site is situated approximately 45 km east-northeast of the island of Ata, a volcanic island that forms part of the active Tofua volcanic arc. The platform trends north-northeast and, at the latitude of the drill site, is approximately 60 km wide. Seismic reflection profiling shows that the platform is dissected by a series of normal faults with predominant north-northwest to north-northeast trends, and is also segmented laterally into discrete blocks by east-west to northwest-southeast structures (see "Background and Objectives" section, this chapter). The profiles suggest that some of the normal faults have been active in recent times.

Attitude of Sediments

Core-derived measurements

Measurements were made of the attitude of sedimentary bedding in cores from Holes 840A, 840B, and 840C. Because of resistant ash beds in the upper sedimentary section, the multishot orientation tool could not be used extensively. Most cores, and hence bedding and structural measurements, could not be reoriented, therefore, to geographical coordinates by this technique. Although the multishot tool was used for Hole 840C, only three bedding measurements from this hole could be corrected in this way.

Paleomagnetic magnetization vectors cannot be used as a geographic reference either, because some tectonic rotation of the Tonga Platform is suspected (see "Background and Objectives" section, this chapter). Thus, it was impossible to reorient on a routine basis the sedimentary bedding and structural data measured from the core, from either Site 840 or 841.

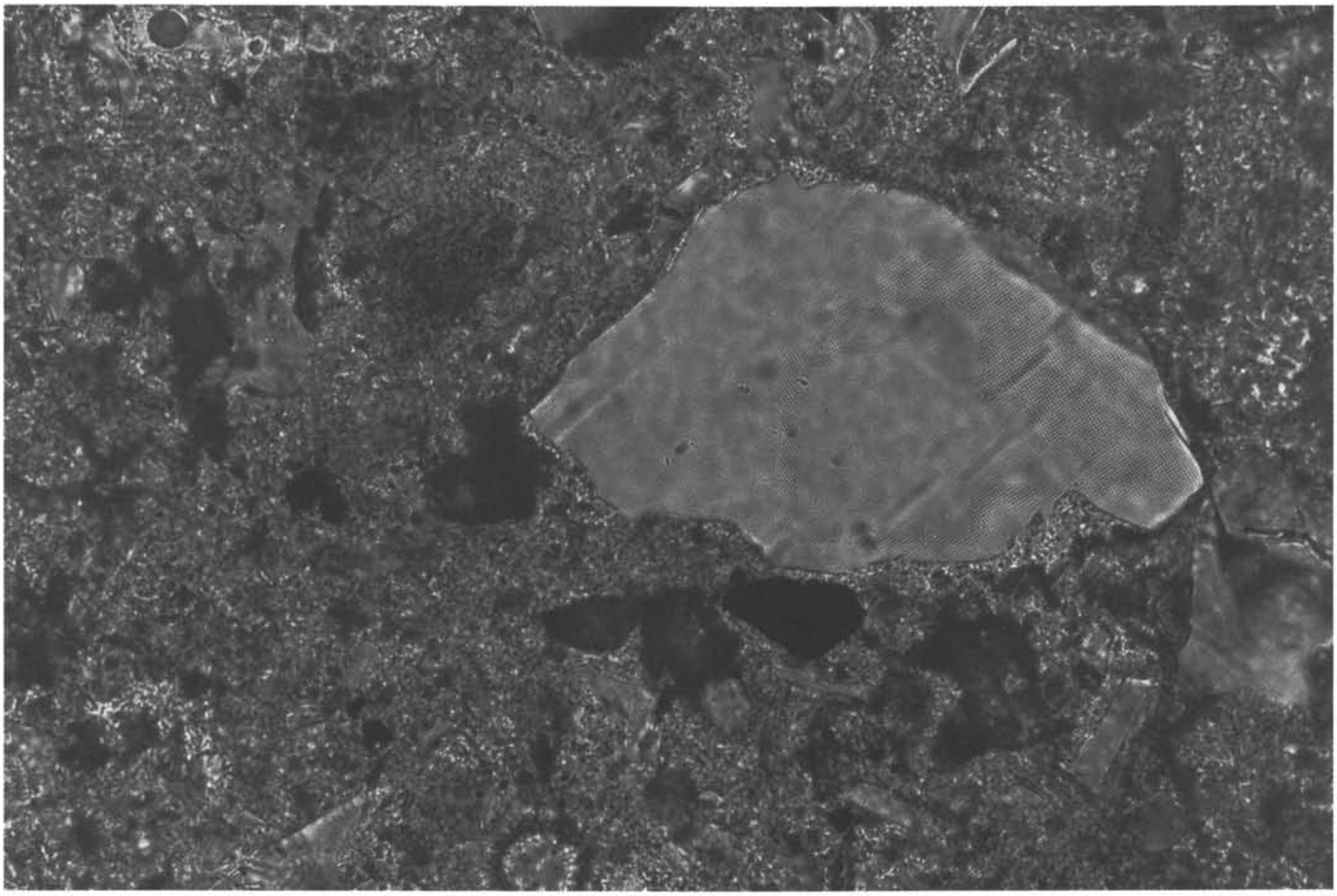

Figure 29. Photomicrograph of broken plagioclase crystal and small magnetite grain in plagioclase-rich volcaniclastic siltstone; Sample 135-840B-35X-2, 90–91 cm; long side of photomicrograph = ~0.3 mm, plane-polarized light.

The dips of 131 strata measured from core recovered from Site 840 are plotted vs. depth in Figure 32. The dips between 0 and 500 mbsf are widely scattered, falling between 0° and 14° (average = 4.3°). No systematic trends with depth are apparent from these data. Most measurements have been taken from the lower portions of turbidite flows or from bedding within calcareous rocks. The former are frequently erosional surfaces, and the latter strongly bioturbated, such that the bedding is frequently partially disrupted and may not be perfectly planar.

At approximately 500 mbsf, there is a marked increase in sediment dip from an average of 4.3° to 10.1° (in the interval from 500 to 600 mbsf). Dips of up to 25° may be consistent over a meter scale in some sections (e.g., Sections 135-840B-55X-1 and Sections 135-840B-58X-2 to -58X-6). These are measured from planar lamination in volcaniclastic sands and silts of late Miocene age. The possible significance of this increased dip is discussed below.

FMS Dipmeter Measurements

The formation microscanner (FMS) downhole logging tool was run through the interval from 87 to 516 mbsf. The FMS results are discussed in some detail in the "Downhole Measurements" section (this chapter). In addition to the generation of standard microresistivity images, mean-squares-dip (MSD) dipmeter processing was undertaken. The details of this operation and merits of the results are outlined in the "Downhole Measurements" section of the "Explanatory Notes" chapter (this volume) and are discussed further in the "Structural Geology" section of the "Site 838" chapter (this volume).

Plots of dip and dip direction vs. depth are presented in Figure 33 for 2381 measurements in the interval from 90 to 515 mbsf. These dip data show far more consistency than do those measured by hand, and they span those sections of the borehole for which recovery was poor and no core measurements were possible (e.g., 120–260 mbsf). From the dipmeter data, two distinct tectonic units are recognizable from the point of view of bedding orientations. Between the top of the logged section at 95 mbsf to approximately 250–260 mbsf, dips range from 0° to 4°, rarely reach as much as 10°, and are characterized by variable dip directions with no consistent trend. Very few measurements were picked by the dipmeter between 200 and 230 mbsf, correlating with zones dominated by massive pumiceous gravels.

In contrast, from 260 mbsf to the lowermost logged section at approximately 500 mbsf, dips and dip directions are consistent. Beds dip regularly toward the north (Fig. 33) with little variation; although there is a considerable amount of scatter, dips increase systematically from ~2° at 260 mbsf to 4°–5° at 500 mbsf. On an expanded scale (Fig. 34), the scatter of dip magnitudes appears to

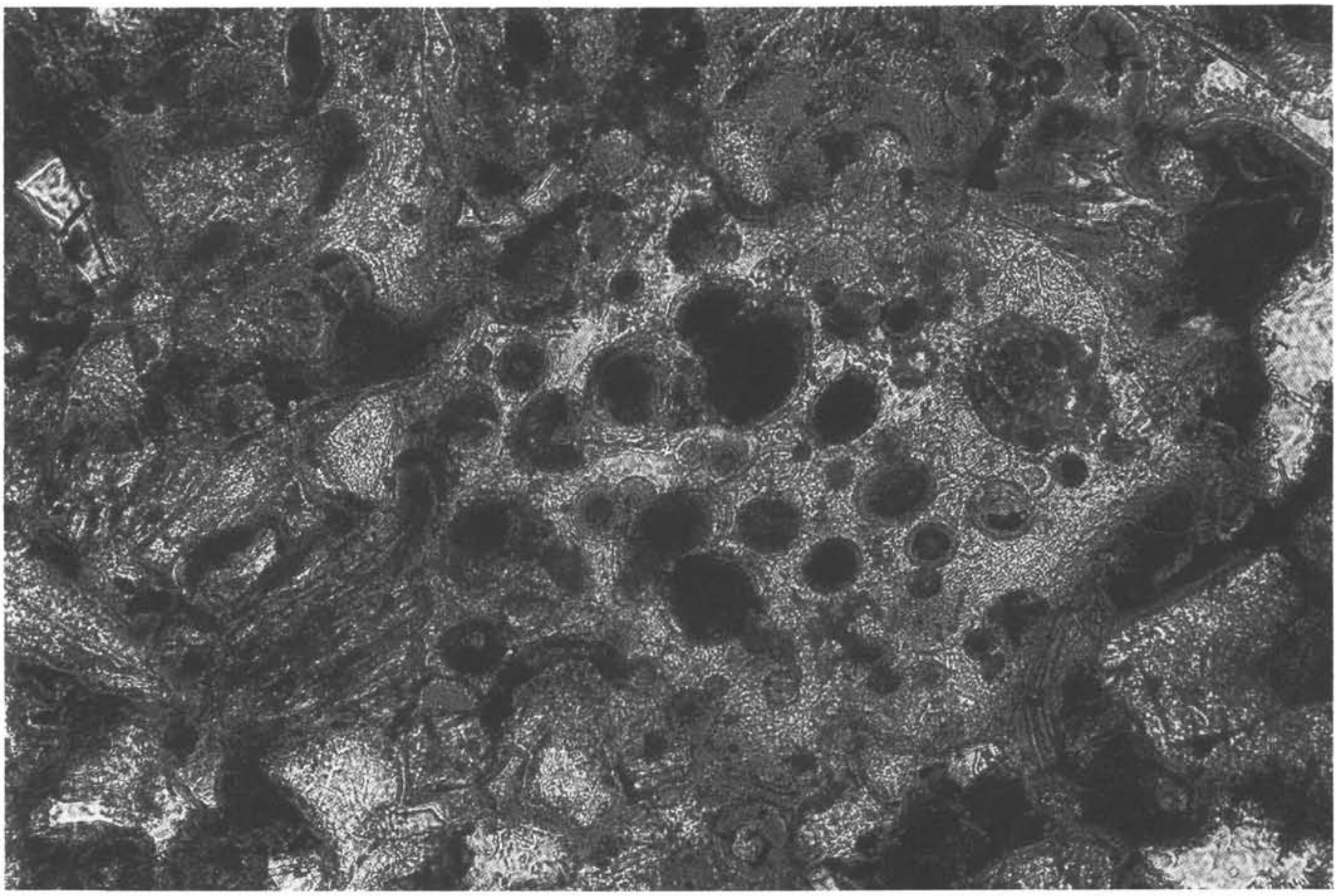

Figure 30. Photomicrograph of pale brown to medium brown vitric shards of medium vesicularity in vitric sandstone; Sample 135-840B-45X-1, 4–6 cm; long side of photomicrograph = ~0.6 mm, plane-polarized light. Vesicles and interparticle pore spaces are completely filled by greenish brown smectite.

be cyclical on a scale of tens of centimeters to a few meters. This variation is on the same order of scale as the thickness of individual turbidite units. It is possible, therefore, that part of this apparent cyclicity can be explained by invoking some component of depositional dip at the erosional bases of the turbidites, over and above a background dip recorded by the intervening layers of carbonate. This requires verification by a detailed examination and interpretation of the FMS resistivity images and lithologic logs post-cruise.

Unfortunately, no FMS data are available below 515 mbsf. It is therefore not possible to use the dipmeter to examine fully the domain of increased dip that was recognized from visual inspection of the core (see above). Nevertheless, a few steeper dips are evident in the lowermost 10–20 m of the dipmeter log (Fig. 33), and dip directions tend to lie to the west of the general northward plunge of the bedding (Fig. 33). Taken together with the core measurements of the steeper dips, it is suggested that a third structural unit can be defined at approximately 500 mbsf. This depth does not correspond to any lithologic or biostratigraphic subdivision recognized from preliminary study of the core itself. It does, however, correlate to a marked decrease in velocity and density values recognized at 494 mbsf in physical properties and downhole log data. The significance of this is discussed in the "Physical Properties" and "Downhole Measurements" sections (this chapter).

The boundary at approximately 260 mbsf, between bedding with random dip orientation above and regular and progressively increasing dip below, corresponds to the boundary between Units II and III (see "Lithostratigraphy" section, this chapter). This boundary is late Miocene in age and separates a sequence dominated by volcaniclastic sandstones and siltstones below from a sequence apparently composed predominantly of pumiceous gravels and sandstones above. The massive nature of the pumiceous gravels explains the paucity of measurements made by the dipmeter between 200 and 240 mbsf, and probably marks a significant change in depositional and tectonic environment at this stratigraphic interval. The progressive increase in dip from 2° to 4° between 260 and 500 mbsf could possibly be explained entirely in terms of primary depositional dip. Sedimentological evidence has been proposed (see "Lithostratigraphy" section, this chapter) that suggests that a change from more proximal to distal turbiditic facies with stratigraphic height can be discerned within Unit III; presumably this change could also be accompanied by a concomitant decrease in the angle of repose of the sediment. However, the regularity of this change over an interval of ~250 m, and its progressive increase, are remarkable. The increase of dip with

Figure 31. Photomicrograph of elongate vesicle in a volcanic clast, Sample 135-840B-60X-1, 92–96 cm; long side of photomicrograph = ~0.3 mm, plane-polarized light. The vesicle is completely filled by dark brown smectite along the rim and radially oriented bright green celadonite in the center. Also note the radial clusters of pale brown smectite, completely replacing groundmass glass.

depth is more easily interpreted in terms of the northward progressive tilting of the block (i.e., growth faulting) during deposition in the late Miocene. Bathymetric and seismic data (Herzer and Exon, 1985) show that Site 840 is adjacent to several small north-trending faults that terminate against an east-trending fault (see "Background and Objectives" section, this chapter). It is possible that these or other comparable structures were active in the late Miocene, in which case, to effect the rotation observed, the east-west lineament must have acted as a normal fault and the north-south structures as hinge faults, with greater displacement at their northern than southern terminations.

Structures Within Cores

Very few small-scale structures are preserved within the cores recovered from Site 840. A single microfault at 486.9 mbsf, with 1 mm of normal displacement, provides the only microscopic analog to the normal faulting inferred from the seismic records (see above). The only other microstructures that have been observed appear to be related to soft sediment deformation. These are associated with sand-silt-grade volcaniclastic turbidite flows, which often have a characteristic internal structure. Their basal portions are planar laminated, but within the turbidite unit bedding becomes contorted with increasing height and slump folding may be observed (see "Lithostratigraphy" section, this chapter). This slump folding is usually regarded as a dewatering phenomenon. Bedding appears to be obliterated by this deformation, and the uppermost silty parts of the turbidite sequence exhibit massive form. On very rare occasions, microthrusts, with maximum displacements on the order of a few millimeters, are observed within the slumped portions of the turbidite units (Fig. 22). They are restricted to the areas of disturbed bedding. In one locality, in Core 135-840B-35X-2, 80–87 cm (329.8 mbsf), a clay-rich clast contained within a fine sand matrix preserves a series of microthrusts (Fig. 35). The sense of motion of the microthrusts is parallel to the paleocurrent direction of a coarse cross-bedded sand layer that truncates the clay horizon, and it is therefore possible that the microthrusts were induced within the clay clast by the influx of the new turbidite flow, rather than reflecting regional deformation effects.

BIOSTRATIGRAPHY

Introduction

The primary objective of drilling at Site 840 was to sample and date a regional seismic unconformity referred to as Horizon A (Herzer and Exon, 1985; Austin et al., 1989), thought to be late

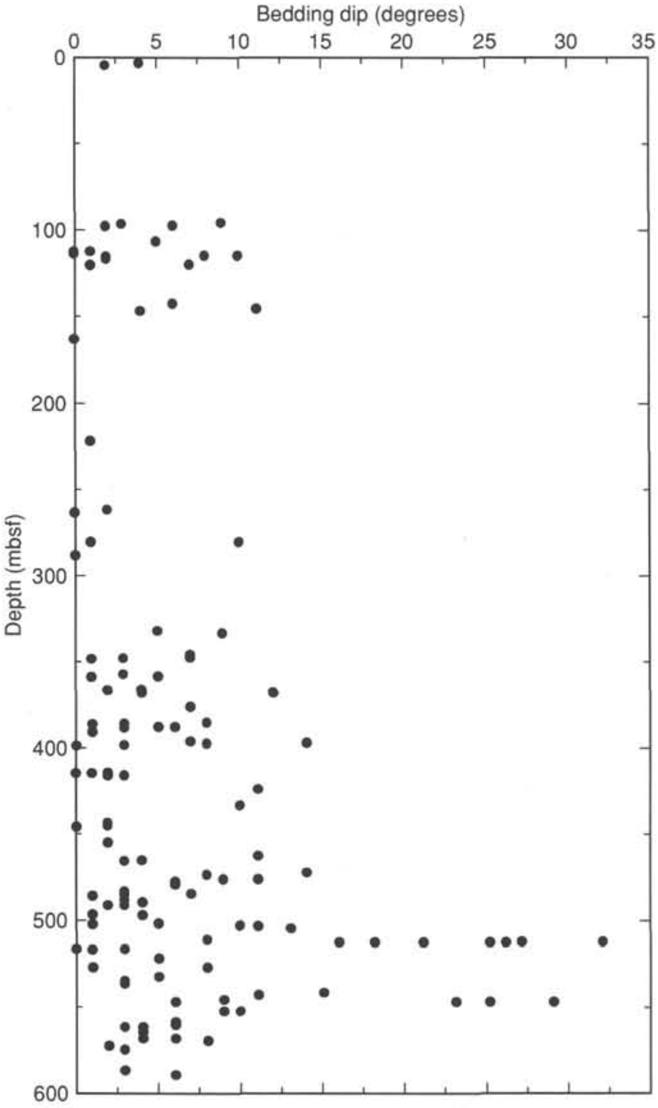

Figure 32. Sedimentary bedding dips measured from Holes 840A, 840B, and 840C plotted vs. depth. Note the increase of dip at approximately 500 mbsf. For discussion see text. $N = 131$ measurements.

Miocene or early Pliocene in age. The total depth drilled was 597 m, but Horizon A was not identified biostratigraphically.

Middle Pleistocene (Subzone CN14b) to late Miocene (Zone CN9) planktonic foraminifers and calcareous nannofossils were recovered at Site 840 from strata consisting mainly of vitric volcaniclastics with interbedded calcareous oozes and chalk horizons. A probable hiatus spanning approximately 1 m.y. is recognized between Cores 135-840B-10X (late Pliocene nannofossil Subzone CN12a) and -11X (early Pliocene nannofossil Subzone CN10b).

Planktonic foraminifer and calcareous nannofossil ages are generally in agreement; however, they differ in Samples 135-840B-22X-CC through -30X-CC. Nannofossils indicate a late Miocene age, and foraminifers indicate an early Pliocene age. Further studies are needed to resolve these differences. The biostratigraphic results are summarized for Holes 840A, 840B, and 840C in Figures 36 and 37.

Calcareous Nannofossils

Pleistocene

Samples 135-840A-1H-CC and 135-840B-1X-CC contain common to abundant, well-preserved specimens of *Gephyrocapsa oceanica*, *G. caribbeanica*, and *Pontosphaera indooceanica* but lack *Emiliania ovata* and *E. huxleyi*. They are, therefore, assigned to middle Pleistocene Subzone CN14b.

Middle Pleistocene sediments of Subzone CN14a were not recovered in Sample 135-840B-2X-CC. Sedimentation rates suggest that sediments of this age probably exist in the unrecovered section from Core 135-840B-2X (see "Sediment Accumulation Rates" section, this chapter).

Pliocene

The presence of *G. caribbeanica* and *Calcidiscus macintyrei* and the absence of *G. oceanica* in Samples 135-840B-2X-CC and -3X-CC indicate assignment to latest Pliocene Subzone CN13b. Poorly preserved specimens of reworked *Discoaster brouweri*, *D. pentaradiatus*, and *D. surculus* are common components of the floras.

Rare, poorly preserved specimens of *Emiliania ovata* and *Gephyrocapsa* sp. aff. *G. caribbeanica* and lack of *G. oceanica* suggest assignment of Sample 135-840B-4X-CC to the upper Pliocene, possibly Subzone CN13a.

Discoaster tamalis, the marker species for the top of Subzone CN12a is present in Sample 135-840B-9X-CC and Samples 135-840C-3H-CC and -4H-CC. Other species present, which also have their last occurrences higher within Zone CN12, include *D. asymmetricus*, *D. brouweri*, *D. pentaradiatus*, and *D. surculus*.

Preservation is moderate and floras are sparse in Samples 135-840C-1H-CC and -2H-CC; these samples can only be assigned a general late Pliocene age. Sample 135-840B-10X-CC contains an abundant, well-preserved flora including *Sphenolithus neoabies* and *Ceratolithus rugosus*. It is assigned to Subzones CN11b or CN12a.

Twelve samples are assigned to latest Miocene and early Pliocene Zone CN10. Of these, three samples (135-840B-11X-CC and 135-840C-8H-CC and -10H-CC) contain common to abundant, moderate- to well-preserved nannofossil floras. *Ceratolithus acutus* is present in the three samples. The first (FO) and last (LO) occurrences of this species define the bottom and top, respectively, of Subzone CN10b.

Miocene and Pliocene

Triquetrorhabdulus rugosus, the marker species for the top of Subzone CN10a, is present in Samples 135-840B-20X-CC and -22X-CC, which also contain abundant, diverse floras that include *A. delicatus* and longer ranging, late Miocene to early Pliocene species such as *Sphenolithus abies*. The presence of *T. rugosus* and the lack of *Discoaster quinqueramus* allow assignment to Subzone CN10a.

Sample 135-840C-12H-CC contains *A. delicatus*, *S. abies*, and *S. neoabies* but lacks zonal markers. It is, therefore, assigned to the upper Miocene or lower Pliocene (Subzone CN9b to Zone CN10).

Miocene

The base of Subzone CN9b is defined by the FO of *C. primus*, and the top of the subzone is defined by the LO of *D. quinqueramus* (Bukry, 1973). Five samples contain both species and are assigned therefore to Subzone CN9b. The samples are 135-840B-23X-CC, -26X-CC, -31X-CC, -32X-CC, and -45X-CC.

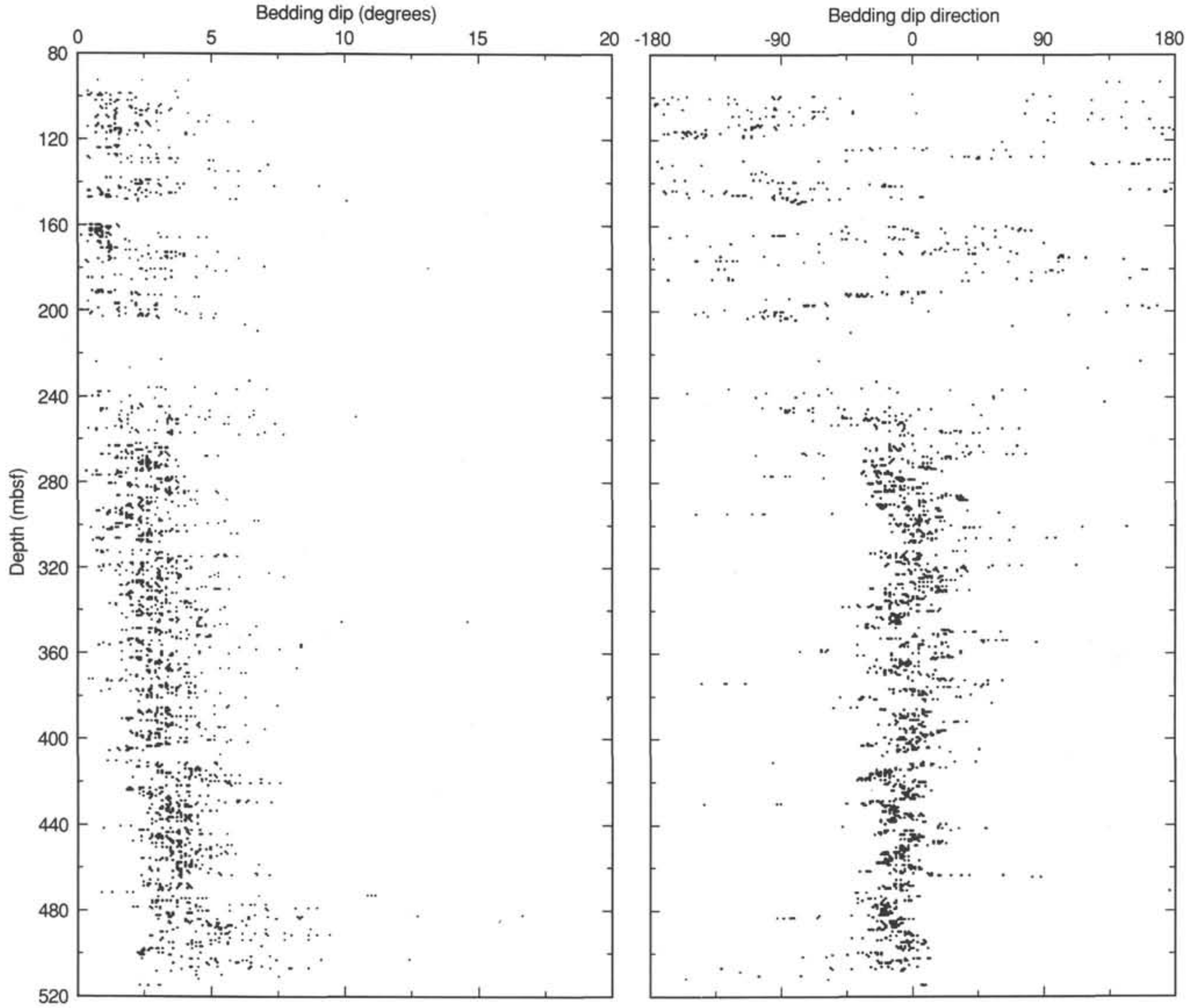

Figure 33. Sedimentary dips and dip directions of bedding, calculated by mean-squares dipmeter processing of formation microscanner downhole logging data from Hole 840B, plotted vs. depth. For discussion see text. N = 2381 measurements.

Seventeen samples contained *D. quinqueramus* but not *C. primus* and, therefore, are assigned to Zone CN9. These samples are 135-840B-24X-CC, -28X-CC, -29X-CC, -30X-CC, -33X-CC, -34X-CC, -36X-CC, -37X-CC, -39X-CC, -40X-CC, -42X-CC, -43X-CC, -50X-CC, -52X-CC, -55X-CC, -56X-CC, and -63X-CC.

Planktonic Foraminifers

A total of 77 core-catcher samples were examined for planktonic foraminifers at Site 840. Of these, ten were barren and seven contained faunas too poorly preserved to permit any age determination. In addition, no recovery was obtained for nine cores in Hole 840B, but these intervals were sampled in Hole 840C. The barren samples and those with poor faunas coincided with ash or tuffaceous beds. The remainder contained faunas ranging from middle Pleistocene to upper Miocene.

Pleistocene

Samples 135-840A-1H-CC and 135-840B-1X-CC contained *Globorotalia* (*Truncorotalia*) *truncatulinoides* without *Gr.* (*Tr.*) *tosaensis*, and without other diagnostic species for the upper Pleistocene. For this reason and because *Gr.* (*Tr.*) *tosaensis* is present in lower samples, it is assumed that these two samples are from levels above the last appearance datum (LAD) of *Gr.* (*Tr.*) *tosaensis* and so have been questionably referred to the *Gr.* (*Tr.*) *crassaformis hessi* Subzone of Zone N22.

Pliocene to Upper Miocene

Samples 135-840B-2X-CC to -4X-CC and 135-840C-1H-CC to -2H-CC contain both *Gr.* (*Tr.*) *truncatulinoides* and *Gr.* (*Tr.*) *tosaensis* without *Globigerinoides quadrilobatus fistulosus*, indicating a level within the *Gr.* (*Tr.*) *crassaformis viola* Subzone of Zone N22. The presence of either *Gr.* (*Globorotalia*) *multicamerata*, *Gr.* (*Gr.*) *cultrata limbata*, or *Globigerinoides obliquus* s.l. in these samples indicates the lower part of this subzone.

Samples 135-840C-3H-CC and -4H-CC contain *Gr.* (*Tr.*) *tosaensis* without *Gr.* (*Tr.*) *truncatulinoides* and are referred to Zone N21. The presence of *Globigerinoides quadrilobatus fistulosus* in these samples indicates that they are from the upper part of this zone.

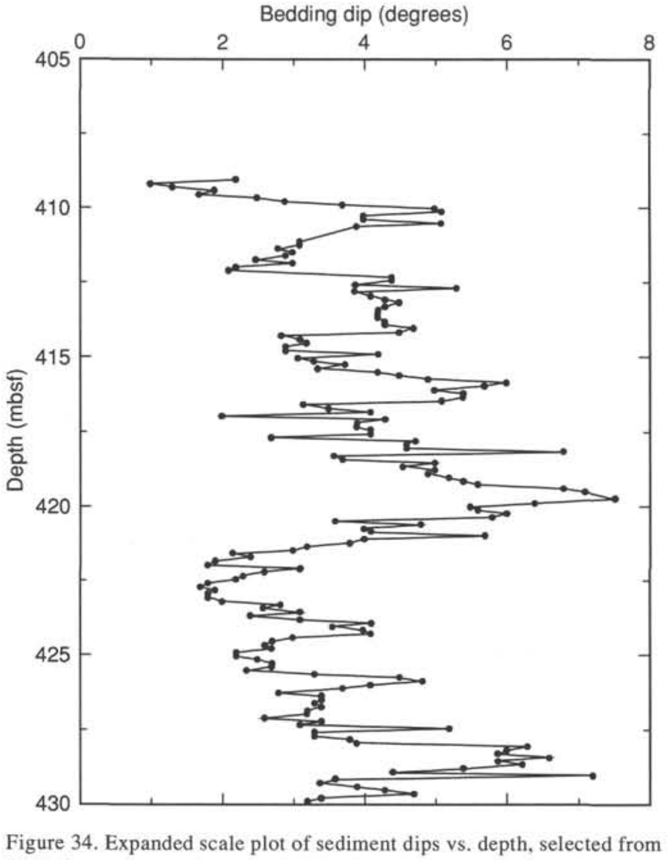

Figure 34. Expanded scale plot of sediment dips vs. depth, selected from FMS dipmeter data shown on left in Figure 33. Note the cyclicity of dip variation on a scale of a few tens of centimeters to a few meters. For discussion see text.

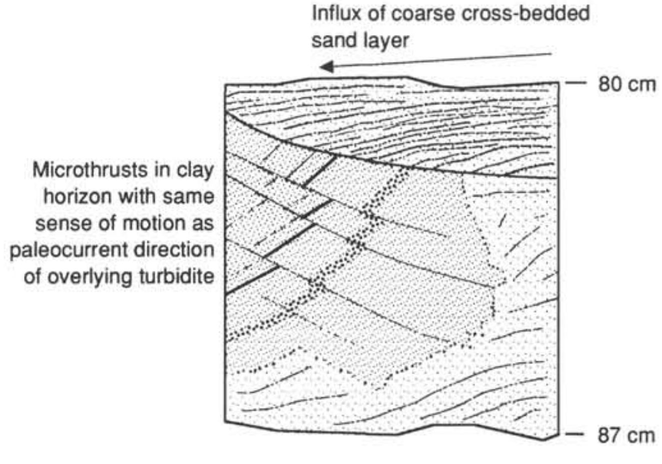

Figure 35. Sketch of microthrusts within a bedded clay-rich clast at the top of a fine-sand-grade turbidite unit (Section 135-840B-35X-2, 80–87 cm). The clast is truncated by a cross-bedded medium-sand-grade unit. The sense of motion along the microthrusts is the same as the paleocurrent direction of the overlying sand layer, suggesting that the microthrusts are syn-sedimentary, formed as a result of the influx of the new turbidite flow.

The base of Zone N19/20 is defined by the FO of *Sphaeroidinella dehiscens* and the top by the FO of *Gr.* (*Tr.*) *tosaensis*. Samples 135-840B-9X-CC to -11X-CC satisfy these criteria and are referred to this zone.

The FO of *Gr.* (*Gr.*) *tumida tumida*, an event marking the base of Zone N18, occurs in Sample 135-840B-20X-CC. For this reason, samples above this level to 135-840B-12X-CC and from 135-840C-12H-CC to -5H-CC are placed within Zone N18.

The base of Subzone N17B is defined by the FO of *Pulleniatina primalis*, an event that occurs in Sample 135-840B-26X-CC. However, both the FOs of *Globigerinoides conglobatus* and *Gr.* (*Obandyella*) *margaritae* occur within this interval (Berggren et al., 1985a, 1985b), as does the FO of *Sphaeroidinellopsis paenedehiscens* (Kennett and Srinivasan, 1983). At Site 840 these events occur below the FO of *P. primalis*, suggesting that this event may be environmentally controlled.

Of the four events, the FO of *S. paenedehiscens* occurs at the lowest position and so has been used to mark the base of Subzone 17B. Thus, Samples 135-840B-34X-CC to -21X-CC and 135-840C-13H-CC have been placed within this zone. Sample 135-840B-63X-4, 2–6 cm, contains *Gr.* (*Gr.*) *tumida plesiotumida*, indicating that the interval from the bottom of the hole to Sample 135-840B-35X-CC should be referred to Subzone N17A.

SEDIMENT ACCUMULATION RATES

Biostratigraphic and paleomagnetic data both indicate that the age of the sediments at Site 840 ranges from the middle Pleistocene to the late Miocene (Brunhes Chron to Anomaly 4). The sediment sequence consists largely of vitric volcaniclastics with interbedded calcareous ooze and chalk horizons. The amount of volcaniclastic material increases downcore. Core recovery was poor throughout most of the hole, but it improved downward from Core 135-840B-50X. Many samples below this core were barren, and others had a rare to common microfossil content. A hiatus was recognized that covered an interval from within nannofossil Subzone CN12a to within Subzone CN10c, spanning approximately 1 m.y.

Table 6 lists the depths and ages of the bioevents used to plot sediment accumulation rates. Figure 38 is a graphic presentation of depth and biostratigraphic data from Site 840. As with the previous sites, two sets of biostratigraphic data have been used: one based on the extinction level (LAD) of *Gr.* (*Tr.*) *tosaensis* at 0.6 Ma (Berggren et al., 1985a, 1985b), and the other with this event being placed at 0.9 Ma (based on the relationship between this event and the paleomagnetic data at Sites 834 and 837). In addition, paleomagnetic data, which are available below 100 m, have also been plotted with the biostratigraphic data.

The sediment accumulation curve can be divided into six sections, illustrating changes in the rates of accumulation. The lowermost part (Section A), between 570 and 320 mbsf, shows rapid sedimentation rates of about 357 mm/k.y. Between 320 and 265 mbsf (Section B), the sedimentation rate decreases to about 110 mm/k.y., followed by a return to very high sedimentation rates of 820 mm/k.y. over the interval from 265 to 101 mbsf (Section C). These high rates of sedimentation coincide with a depositional period of numerous pumiceous gravel and sand beds. Between 101 and 95 mbsf (Section D), immediately before the hiatus, sedimentation accumulation rates drop to 10 mm/k.y.; above the hiatus, from 95 to 24 mbsf (Section E), rates increase to 39 mm/k.y.; and between 24 mbsf and the seafloor (Section F), rates drop to 14 mm/k.y. That part of the sequence above 95 mbsf coincides with lithologic Unit I.

PALEOMAGNETISM

Remanent Magnetism

In contrast with previous sites, Site 840 magnetic remanence measurements were made on discrete samples because the archive core halves were unsuitable for measurement with the pass-through cryogenic magnetometer because of drilling disturbances. An extended core barrel (XCB) was used to rotary drill 82% of the cores; and, as a result, they often consisted of azi-

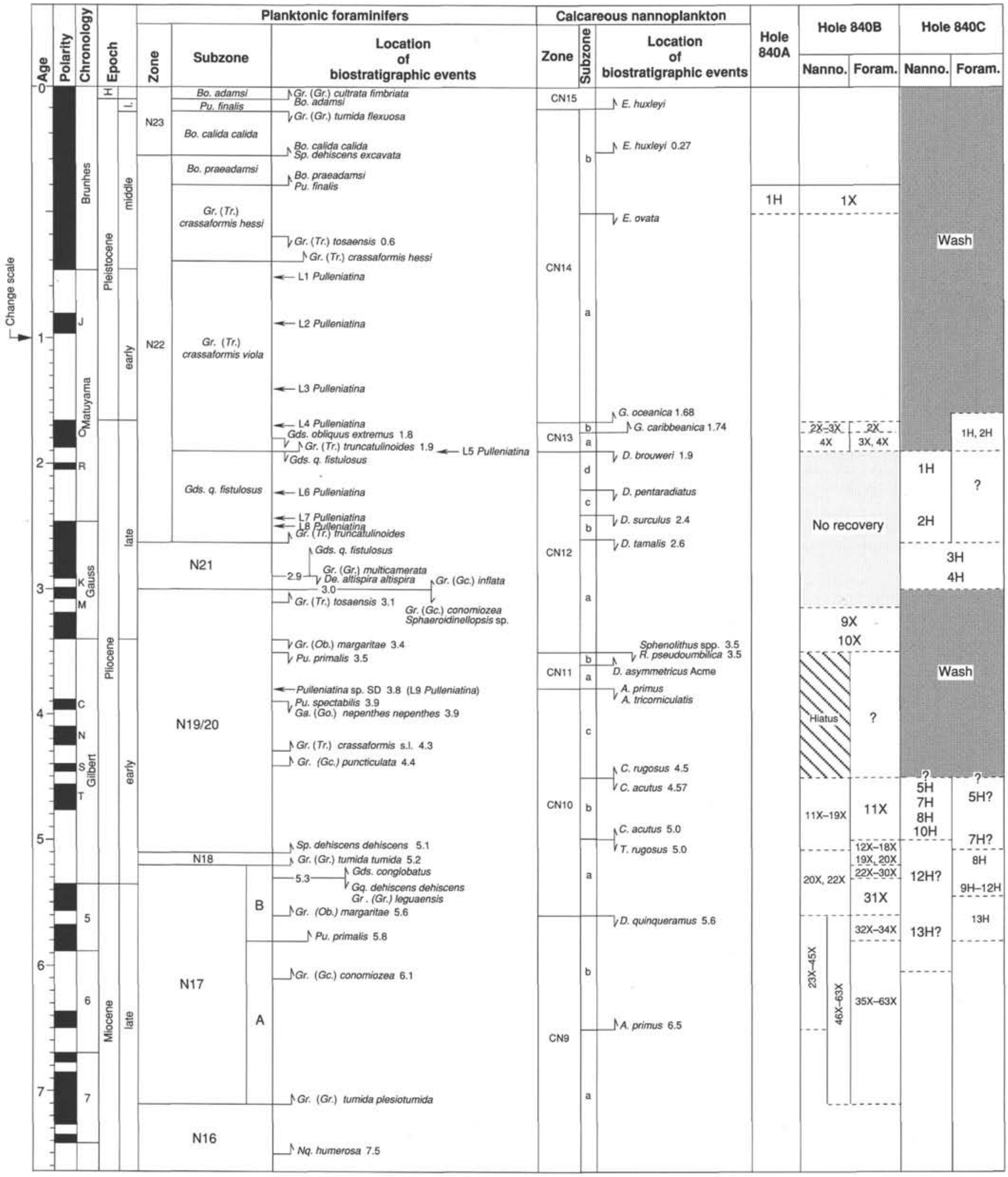

Figure 36. Biostratigraphic results, Site 840.

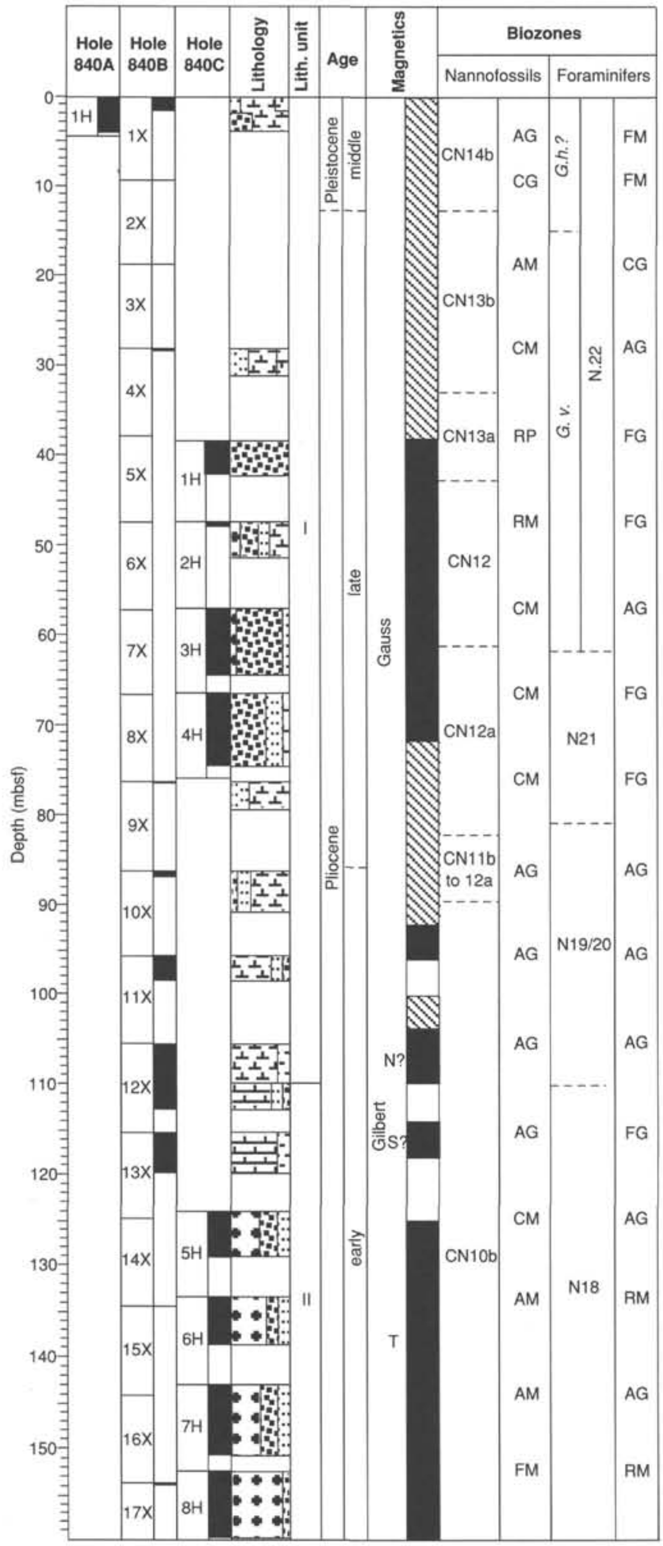

Figure 37. Paleontology summary chart, Site 840. See Figure 1 caption for an explanation of symbols and abbreviations used.

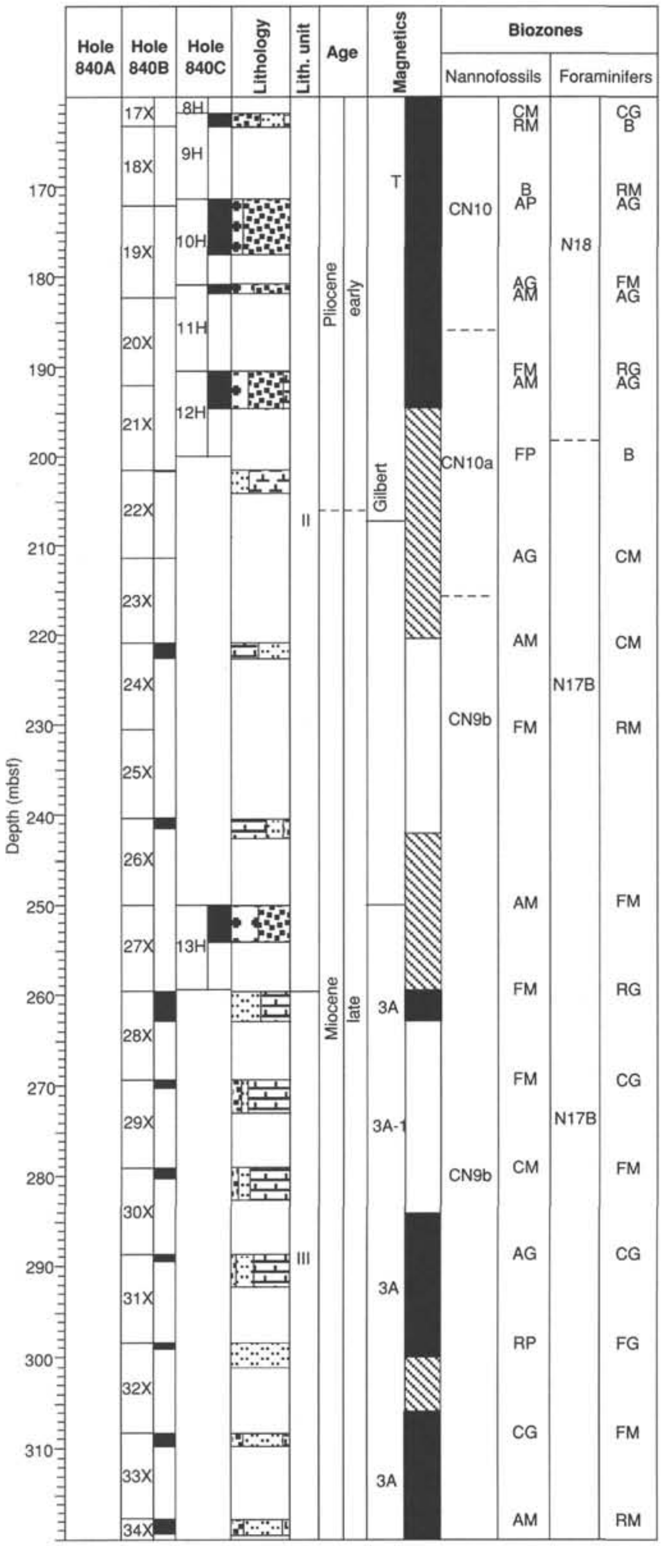

Figure 37 (continued).

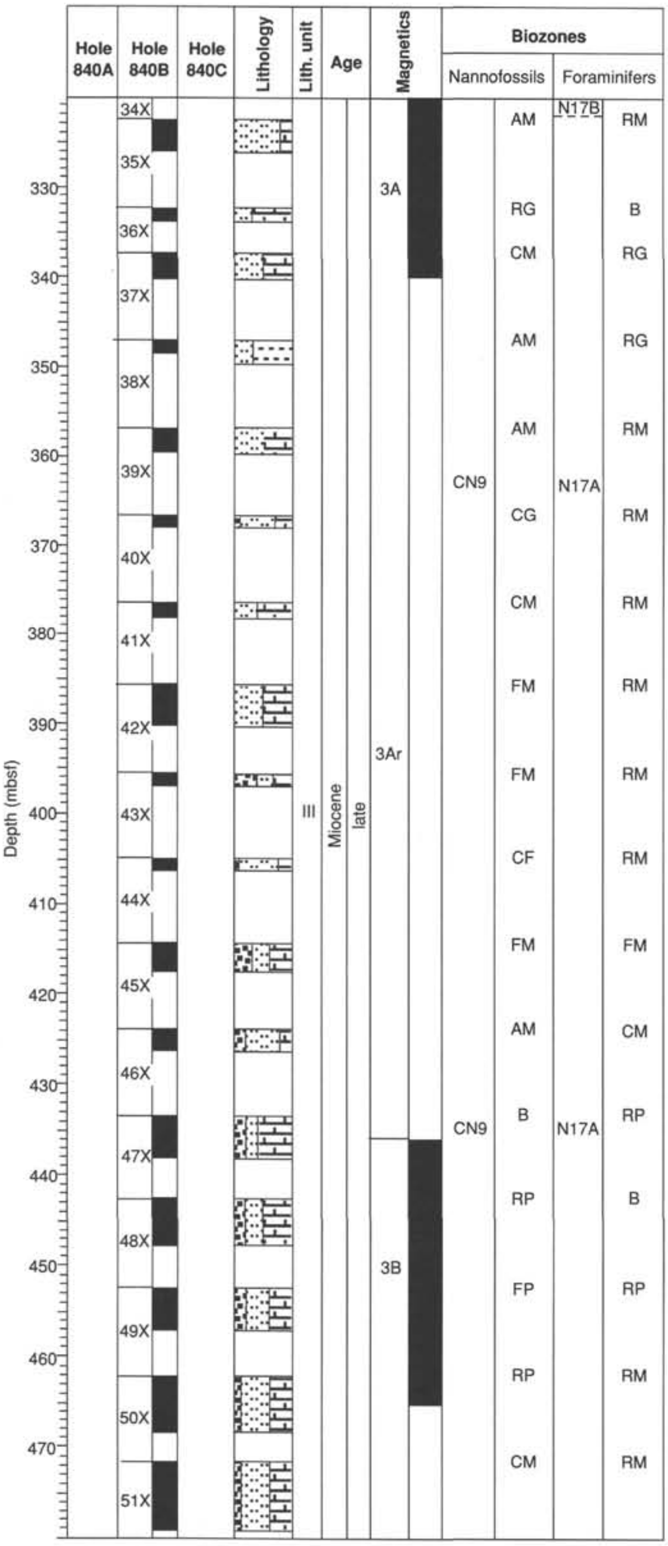

Figure 37 (continued).

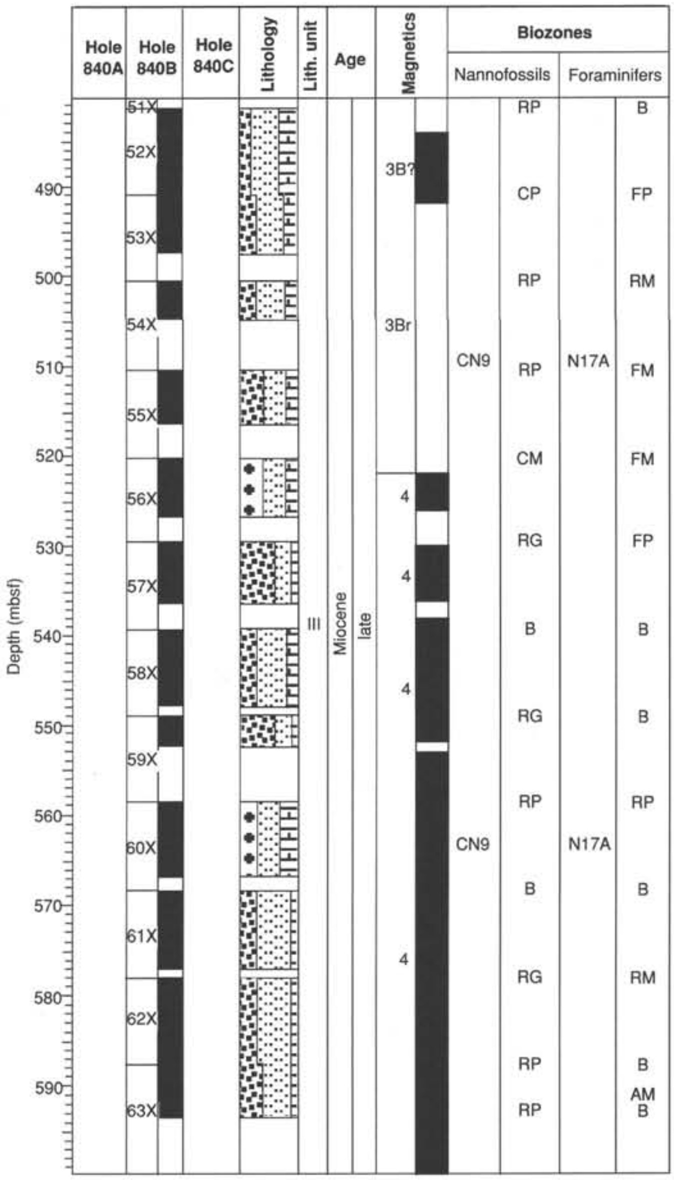

Figure 37 (continued).

Table 6. Depths and ages of bioevents used to plot accumulation rates for Site 840.

Depth (mbsf)	Age (Ma)	Events
15.0	0.60	LAD *Gr. (Tr.) tosaensis*
24.0	1.68	LAD *G. oceanica*
95.0	3.50	Base CN12a
95.1	4.50	Base CN10c
101.0	5.10	FAD *S. dehiscens dehiscens*
187.0	5.20	FAD *Gr. tumida tumida*
265.0	5.30	FAD *Gds. conglobatus*
294.0	5.60	FAD *Gr. margaritae*
320.0	5.80	FAD *Pu. primalis*
570.0	6.50	FAD *A. primus*

Note: LAD = last appearance datum and FAD = first appearance datum.

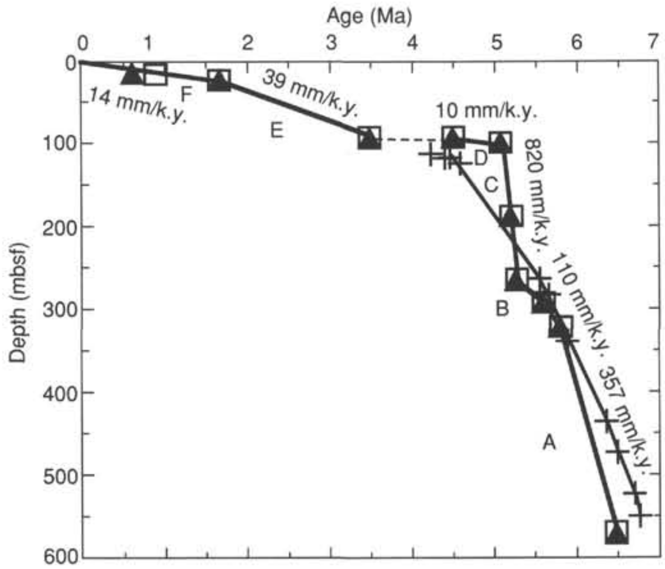

Figure 38. Graphic representation of age vs. depth data illustrating the sedimentation rates at Site 840 by means of the bioevents and depths given in Table 6. A plot of the paleomagnetic data is also included for comparison. Filled triangles = biostratigraphic data, open squares = biostratigraphic data with modified ages for *Globorotalia* (*Truncorotalia*) *tosaensis*, plus signs = paleomagnetic data, and dashed line = hiatus.

muthally rotated pieces small enough that several would fit simultaneously within the sensing region of the cryogenic magnetometer. Moreover, because they contain mostly unconsolidated sands and gravels, the advanced hydraulic piston corer (APC) cores recovered from Hole 840C were disturbed by handling and splitting.

In all, 284 samples were measured with the cryogenic magnetometer in a discrete sample mode. Alternating-field (AF) demagnetization was used to remove magnetic overprints and isolate the characteristic remanence direction. In addition to the natural remanent magnetization (NRM), most samples were measured after AF demagnetization at levels of 1, 2, 4, 7, 10, 15, 20, 25, 30, 40, 50, and 60 mT. Initially, higher AF steps were used; however, it was found that these measurements gave spurious results, perhaps because of an anhysteretic remanent magnetization (ARM) imparted by the AF demagnetizer. Each sample was analyzed by making orthogonal vector (Zijderveld) and stereonet plots of the remanence directions during AF demagnetization.

Magnetic Properties

Natural remanent magnetization (NRM) intensities of Site 840 sediments are strong and range over 2 orders of magnitude, from 9 to 2212 mA/m in Hole 840B and from 20 to 632 mA/m in Hole 840C. They show approximately log-normal distributions (Fig. 39), with logarithmic means of 129 and 205 mA/m for Holes 840B and 840C, respectively. The high NRM intensities are probably caused mainly by the high content of volcanic material in the sediments.

The behavior of the sediments during AF demagnetization was similar to that encountered at other Leg 135 sites. Most samples showed the pervasive, upward-directed overprint (Fig. 40) that has been found on virtually all samples measured on Leg 135. This overprint is thought to be an isothermal remanent magnetization (IRM) caused by the exposure of the cores to high magnetic fields in the core barrel and drill string. It resides mainly in low-coercivity magnetic grains and is easily removed in most samples by AF demagnetization.

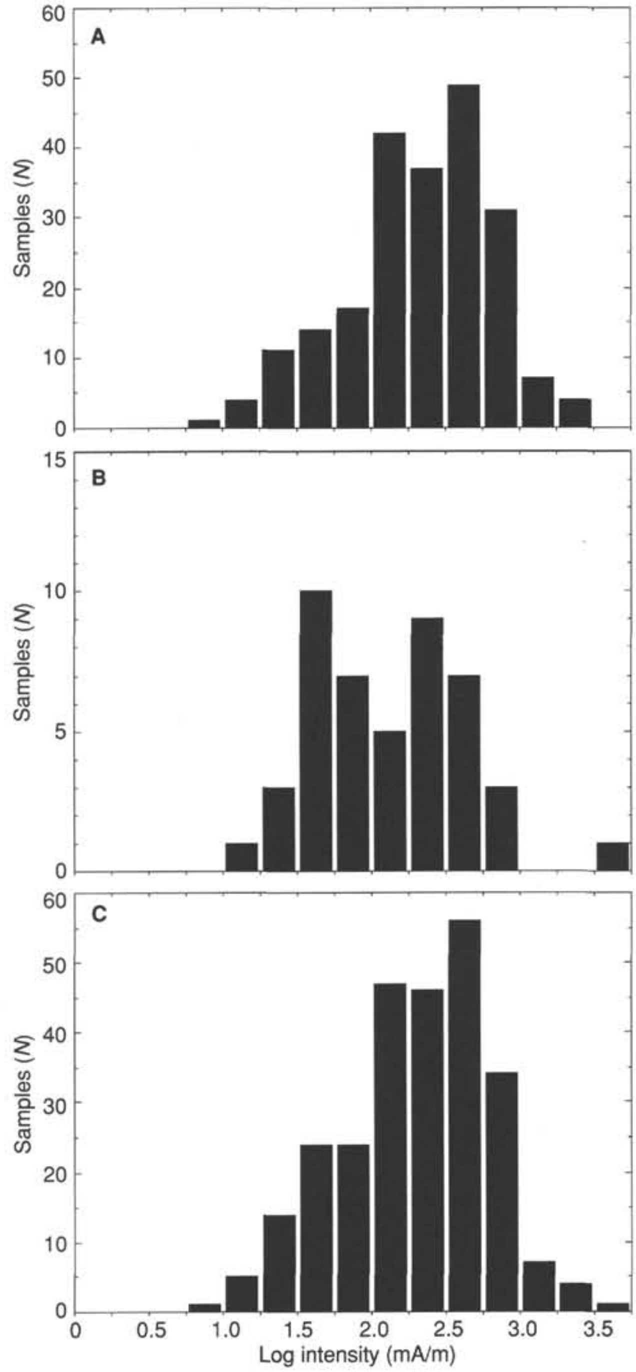

Figure 39. Logarithmic histograms of natural remanent magnetization (NRM) intensities from Site 840 paleomagnetic samples. **A.** Results from Hole 840B, $N = 218$. **B.** Results from Hole 840C, $N = 46$. **C.** Both Holes 840B and 840C combined, $N = 264$.

Site 840 yielded more material with moderate to high coercivities than did previous Leg 135 sites. Although samples with low median destructive fields (MDF) of 2–4 mT were common, as at other Leg 135 sites, many had MDFs of 10–15 mT or greater (Fig. 40). Indeed, the characteristic remanent magnetization direction was sometimes not evident until high AF demagnetization steps.

Though most samples gave reliable results, about 15% did not. Some behaved erratically, apparently susceptible to the acquisi-

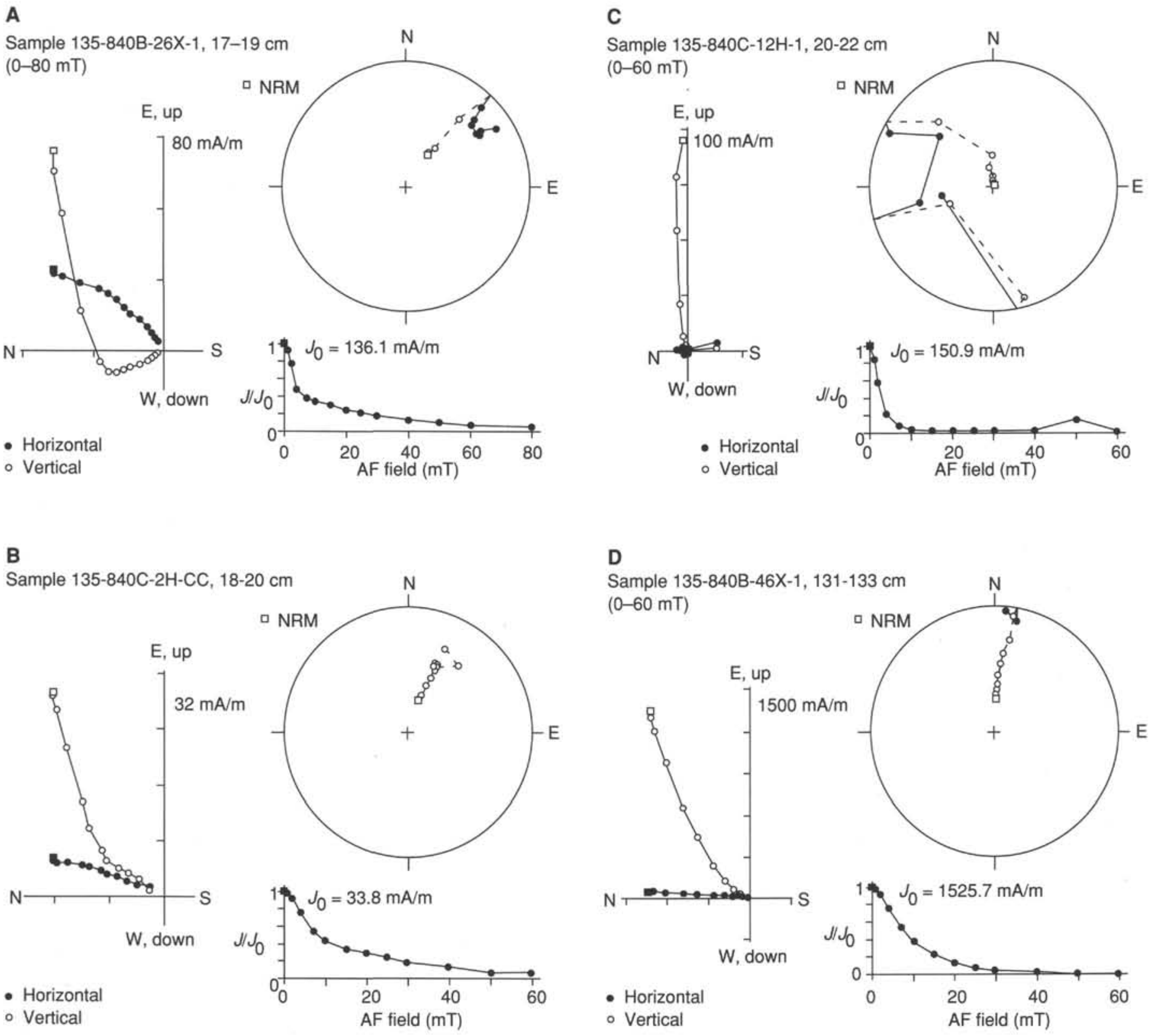

Figure 40. Typical alternating-field (AF) demagnetization behavior of Site 840 paleomagnetic samples. Diagrams A and B are samples with stable characteristic remanent magnetization directions, whereas diagrams C and D are unstable samples. In each set of plots, a stereographic plot of magnetization directions during AF demagnetization is at upper right, normalized magnetization intensity plot is at lower right, and an orthogonal vector (Zijderveld) plot of magnetization vector endpoints during AF demagnetization is at left. **A.** Reversely polarized sample. **B.** Normally polarized sample. **C.** Sample with erratic directions during demagnetization. **D.** Sample with less erratic behavior that never reached a stable, characteristic magnetization direction. Unstable samples such as these made up approximately 15% of those measured at Site 840.

tion of spurious magnetizations from their environment (Fig. 40). Others behaved less erratically, but never reached a stable magnetization direction (e.g., Fig. 40). The unstable samples usually were from coarse-grained sedimentary rocks (such as sandstones) and often had large NRMs, possibly indicative of large, unstable magnetic grains.

Magnetic Polarity Stratigraphy

Without contiguous APC cores to show magnetic declination changes, polarity interpretations had to be made solely on the basis of inclinations. Because of the variable magnetic coercivities mentioned above, the best inclination for each sample was determined by examining orthogonal vector and stereonet plots showing sample behavior during AF demagnetization. Typically, reliable inclinations were revealed by demagnetizations of 20–40 mT. Inclinations from Holes 840B and 840C were plotted vs. depth (Fig. 41); and, because the site is in the Southern Hemisphere, negative values indicate normal polarity and positive values show reversed polarity.

Numerous normal and reversed polarity intervals are indicated by the magnetic results. Biostratigraphic markers show that the upper part of the sedimentary section is Pleistocene to late Pliocene in age, whereas the lower and middle part is of late Miocene age (see "Biostratigraphy" section, this chapter). These data also

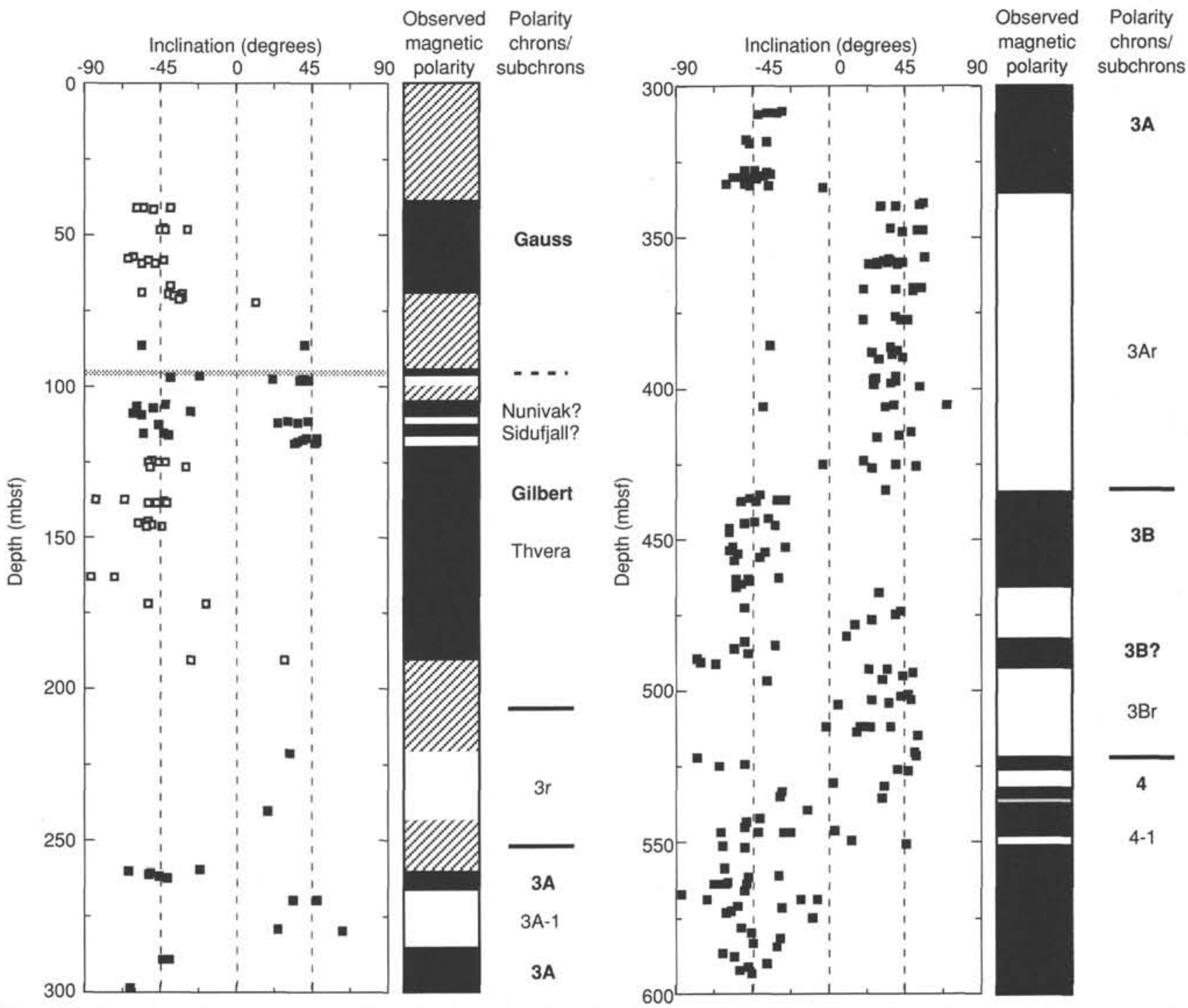

Figure 41. Magnetic polarity stratigraphy, Site 840. Paleomagnetic inclinations measured from discrete samples that were AF demagnetized at 20–40 mT are shown in wide columns. To the right of each inclination plot are shown interpreted magnetic polarities (black = normal, white = reversed, and hachure = undetermined). Polarity chron and subchron names are given at right in bold and plain type, respectively. Open squares denote measurements from Hole 840C, whereas filled squares represent Hole 840B results. Stippled line at 95 mbsf represents a significant hiatus (see "Biostratigraphy" section, this chapter).

indicate a hiatus of approximately 1-m.y. duration at a depth of about 95 mbsf. Using the biostratigraphy as a guideline, the reversals can be matched with the geomagnetic polarity reversal time scale (Berggren et al., 1985a, 1985b).

Above the 95-mbsf hiatus, discrete samples were obtained mainly from Hole 840C between 40.7 and 71.5 mbsf. Virtually all of these samples are normally polarized (Fig. 41). Because the biostratigraphic data indicate that the sediments at this depth are of late Pliocene age, this normal interval probably represents some part of the Gauss Chron (2.47–3.40 Ma). However, with no clear polarity boundaries in this section, the part of the chron within which these sediments were deposited cannot be ascertained.

Below the hiatus, a relatively good match between observed polarity intervals and the geomagnetic reversal time scale can be achieved. A long reversed interval between 336.3 and 434.2 mbsf is the key to interpreting the polarity record. It fits best with the biostratigraphic ages (see "Biostratigraphy" section, this chapter) if interpreted as the reversal that occurred before marine magnetic anomaly 3A (i.e., Subchron 3Ar; Fig. 41 and Table 7). Two normal polarity intervals directly above Subchron 3Ar match the two normal polarity periods of Chron 3A. Above Chron 3A a long normal polarity interval is present that is probably the first normal polarity period of the Gilbert Chron (i.e., the Thvera Subchron). Above the Thvera Subchron and just below the hiatus, two short normal and two short reversed sections are interpreted as the Sidufjall and Nunivak subchrons of the Gilbert Chron. In the section deeper than Subchron 3Ar, the normal polarity interval between 434.2 and 470.0 mbsf matches with Chron 3B of the geomagnetic polarity time scale. At the bottom of Hole 840B, deeper than 521.7 mbsf, samples are mostly normal in polarity and are thought to record the end of Chron 4 (Fig. 41).

Some time-scale mismatches occur in the deeper section at Site 840. A normal polarity section is found between the intervals interpreted as Chrons 3B and 4 (483.0–492.0 mbsf), but it has no counterpart in the geomagnetic reversal time scale. Furthermore, three short reversed sections are found in the upper part of Chron 4, whereas the time scale implies one at most. Nevertheless, to

Table 7. Magnetic polarity zones, Site 840.

Depth (mbsf)	Polarity	Age (Ma)	Chron/subchron
0.0			
	N		BRUNHES
1.5			
	I		
40.7			
	N		GAUSS
71.5			
	I		
96.3			
	N		GILBERT
97.0			
	R		
102.1			
	N		Nunivak?
110.3		4.24	
	R		
112.4		4.40	
	N		Sidufjall?
116.5		4.47	
	R		
121.8		4.57	
	N		Thvera
190.8			
	I		GILBERT
221.6			
	R		3r
240.6			
	I		
259.9			
	N		3A
266.0		5.53	
	R		3A-1
284.5		5.68	
	N		3A
336.3		5.89	
	R		3Ar
434.2		6.37	
	N		3B
470.0		6.50	
	R		
483.0			
	N		3B?
492.0			
	R		3Br
521.7		6.70	
	N		
525.3			4
	R		
532.3			
	N		
535.2			
	R?		
537.4			
	N		
545.4			
	R?		
546.3			
	N		
548.3			
	R		4-1
550.9			
	N		
593.3			
	I		
TD			

Notes: Ages from magnetic polarity reversal time scale of Berggren et al. (1985a, 1985b). Chron names in capital letters and subchron names in lower case.

interpret the observed polarity intervals differently would require a significant departure from the biostratigraphic ages or major changes in the sedimentation rate that are not evident in either the biostratigraphy or the sediments. Two factors might cause the shorter unidentified reversals. First, the deepest Site 840 cores consist largely of ash turbidites having coarse-grained basal sediments that may yield spurious magnetic results. Second, the sedimentation rate during the late Miocene at this site was extremely high (see "Sediment Accumulation Rates" section, this chapter), so it is possible that reversals were measured that were too short to be recognized in marine magnetic anomaly profiles and hence have not been included in the geomagnetic polarity reversal time scale.

A plot of age vs. depth constructed from the geomagnetic reversal time scale and the interpreted reversals shows the rapid sedimentation rate below 100 mbsf at Site 840 (Fig. 42). The spacing between the top of the Thvera Subchron and Chron 3A implies a sedimentation rate of 147.9 mm/k.y., whereas the Chron 3A to Chron 4 section indicates a rate of 213.2 mm/k.y. These rates are within those determined for this section from the biostratigraphic data (110–820 mm/k.y., see "Sediment Accumulation Rates" section, this chapter). A much slower sedimentation rate is implied by the spacing between reversals above the Thvera Chron. This also is consistent with the biostratigraphic data, which indicates a hiatus just above. These slow rates probably show a significant decline in sedimentation before the hiatus.

Oriented Cores and Paleomagnetic Declinations

One of the purposes of Hole 840C was to obtain oriented APC cores from the shallow sedimentary section. We obtained 12 oriented APC cores (Table 8) between 47.5 and 259.5 mbsf, but the orientation tool failed for one (Core 135-840C-12H). The APC cores contain mainly unconsolidated volcanic sands and gravels that were severely disturbed by drilling and handling. Indeed, two cores (135-840C-8H and -13H) contain nothing but this type of material. Two others (135-840C-9H and -10H) contain very little material that can be sampled for paleomagnetic study. Moreover, the short ooze sections of some APC cores, infiltrated by water from the adjacent coarse-grained sections, are thought to have moved during handling. An example is present in the two sections of Core 135-840C-5H that have paleomagnetic declinations of 7° and 92°, respectively (Table 9), and probably show a rotation of one section relative to the other.

Despite these problems, relatively consistent paleomagnetic results were obtained from most of the APC cores (Table 9). Paleomagnetic declination results range from 328° to 92°, and most cores suggest a clockwise bias. If the results from all APC cores are averaged, a declination of 21° ± 11° results, implying a 21° clockwise rotation of the Tonga Arc since the Pliocene. A more conservative approach is to exclude from the average those cores with less than three measured samples and whose mean declinations are different from the 21° average by more than 2 standard errors (i.e., Ψ_{95}; McElhinny, 1973), or 47° in this case. This leaves declinations from four cores (135-840C-2H, -3H, -4H, and -7H) whose mean declination is 34° ± 10°. Three of these cores (135-840C-2H through -4H) are late Pliocene in age (see "Biostratigraphy" section, this chapter), suggesting that the apparent 34° clockwise rotation occurred since that time.

Magnetic Susceptibility

Using the Bartington MS-2 susceptibility meter with a 100-mm sensor loop, volume susceptibility measurements were made at a spacing of 3 cm on all whole-core sections that appeared to be relatively full in cross-section. Because most cores displayed drilling disturbance and recovery was partial, the susceptibility record with depth is not as continuous as at previous sites where

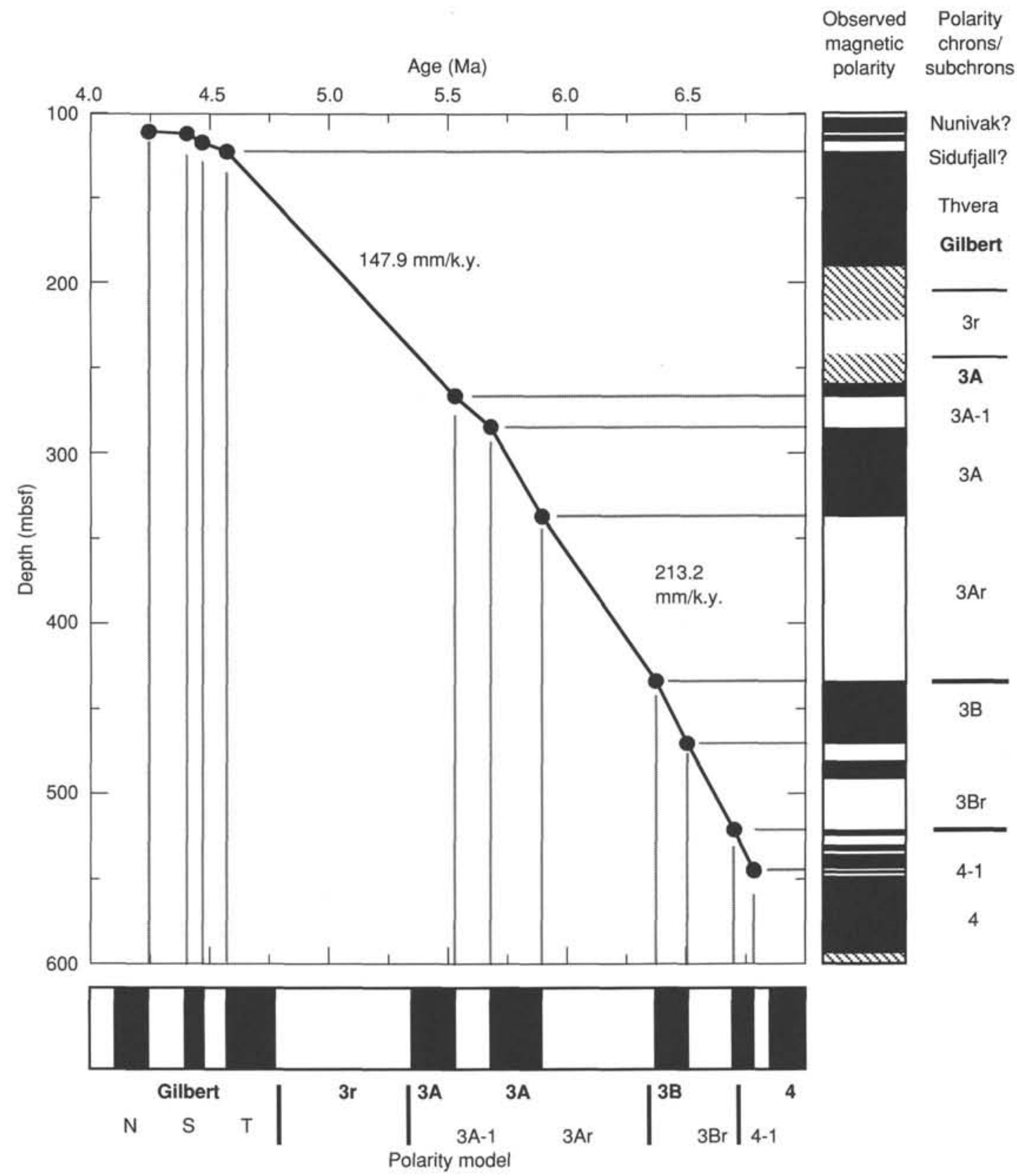

Figure 42. Age vs. depth data, Site 840, derived from magnetic polarity stratigraphy. Dots show dated polarity chron and subchron boundary ages. At right, the observed magnetic polarities are shown; the polarity model (Berggren et al., 1985a, 1985b) is represented at bottom. Interpreted magnetic polarity chrons and subchrons are labeled in bold and plain type, respectively. N = Nunivak, S = Sidufjall, and T = Thvera.

contiguous APC cores were obtained (Fig. 43). Susceptibility values range from 1×10^{-6} to 1318×10^{-6} cgs in Hole 840B and 19×10^{-6} to 1805×10^{-6} cgs in Hole 840C; average values are 188 $\times 10^{-6}$ cgs and 385×10^{-6} cgs for Holes 840B and 840C, respectively. There is no significant variation in susceptibility relative to sedimentary units (Fig. 43). Indeed, the within-core variation is usually greater than the broad-scale variation downhole. However, in Unit III, there is a decreasing susceptibility trend from 480 to 520 mbsf and again from 560 to 590 mbsf, whereas an increasing trend is found from 535 to 560 mbsf. A plot of susceptibility vs. depth for the deepest four cores (Fig. 44) shows the downward-decreasing susceptibility trend at the bottom of Hole 840B. Most of the sediment in these cores is made up of ash turbidites. Many of the small susceptibility peaks apparently correlate to ash turbidites. However, the trend implies that the concentration of magnetic minerals in these turbidites decreases with depth, suggesting a long-term compositional trend at the source of the ash layers or a time-varying winnowing process.

INORGANIC GEOCHEMISTRY

Introduction

Six interstitial water samples were collected at Site 840 (two in Hole 840B from Cores 135-840B-12X and -13X, and four in Hole 840C from Cores 135-840C-3H, -4H, -5H, and -7H). In the uppermost 300 mbsf, the low recovery and the coarse-grained

Table 8. APC core orientation data, Hole 840C.

Core no.	Camera no.	Compass	Inclination Direction	Inclination Drift	Declination
135-840C-					
2H	3250	A	N325°E	2°	234°
3H	3250	A	310°	2°	157°
4H	3250	A	310°	2°	268°
5H	3209	B	310°	1.3°	14°
6H	3209	B	300°	1.2°	5°
7H	3209	B	330°	1.3°	258°
8H	3209	B	345°	1.2°	253°
9H	3250	A	345°	1°	337°
10H	3250	A	305°	0.7°	201°
11H	3250	A	270°	1.0°	81°
12H	3250	A		No data	
13H	3209	B	325°	0.7°	324°

Notes: Magnetic declination at site is 14°E. Compass B was misaligned with the APC fiducial mark; declination values can be corrected by adding 13°. Inclination is the off-vertical angle of the core. Drift and direction are the dip angle and dip direction (clockwise from north) of a plane perpendicular to the core axis. Declination is the angle between the double line on the core liner and magnetic north (measured clockwise).

sand nature of the sand volcanic gravel lithologies prevented further sampling. Below 300 mbsf, the relatively hard and well-lithified sediments at Site 840 were so well lithified that no pore water could be squeezed from them. Standard ODP squeezing techniques were used for the removal of water samples (see "Explanatory Notes" chapter, this volume). Results are summarized in Table 10. Hole 840C was drilled 80 m to the south of Hole 840B; assuming that a comparison of data can be made between these two holes, the depth-concentration distributions are combined in Figure 45.

In Holes 840B and 840C, dissolved major constituents (chloride, sodium, calcium, magnesium, potassium, and sulfate) were determined. Subsequent charge-balance calculations yielded sodium concentrations. Ammonia, silica, strontium, and manganese analyses were also conducted using colorimetric methods and flame AA spectrophotometry.

Chemical Components

The chemical distribution presented in Figure 45 show that the data obtained in Hole 840B can be favorably compared with those obtained in Hole 840C. Pore-water chloride and sodium concentrations are fairly uniform and closely match those of the average seawater concentrations (Broecker and Peng, 1982; Fig. 45). Na^+ concentrations were obtained from charge-balance calculations. The comparison between the average seawater composition and calcium and magnesium concentrations indicates an increase in Ca concentration and a decrease in Mg concentration in the uppermost 60 mbsf (Fig. 45). These Ca and Mg changes with depth are moderately high for deep-sea sediment pore waters (Lawrence and Gieskes, 1981; Gieskes and Lawrence, 1981) and probably reflect, therefore, the alteration of volcanogenic material in the sediments. Holes 840B and 840C were drilled in the shallow platform sequence of the Tonga Ridge; the igneous basement should be expected from the seismic data to lie at more than 2000 mbsf. In Unit I (0–120 mbsf) (see "Lithostratigraphy" section, this chapter), although the bulk sediment is enriched in carbonate, it is primarily composed of clay and volcanogenic materials, from which the clay was probably derived. The noncarbonate fraction of the sediment in this interval averages 55% ± 24% for 25 samples (see "Organic Geochemistry" section, this chapter). Below 120 mbsf, the percentage of the carbonate fraction decreases and the sediments are composed mostly of volcanogenic materials. With respect to the average seawater concentrations, Ca and Mg concentrations also indicate that the Ca gains of about +14 mM are less than the Mg losses of about −19 mM. These deviations suggest a nonconservative behavior that could be related to a precipitation of calcium carbonate, derived from increased calcium following the alteration of the volcanogenic material. This is also suggested by the low alkalinity values determined in the most enriched carbonate layer (e.g., from 70 to 120 mbsf).

Concentrations of sulfate and ammonia (Table 10) do not vary much, indicating that the bacterial activity in these low organic carbon sediments (see "Organic Geochemistry" section, this chapter) is minimal. This is consistent with an alkalinity controlled by carbonate precipitation, and with the low level of dissolved manganese identified in Holes 840B and 840C. Below 120 mbsf, the slight increase in Mn suggests that the sub-bottom redox conditions were just reduced enough to mobilize manganese.

The presence of the dissolved sulfate, however, argues against the formation of dolomite and rules out the possibility that this mineral is a significant sink for magnesium (Baker and Kastner, 1981). This reinforces the interpretation that the magnesium depletion is the result of removal during alteration reaction involving volcanogenic materials. The concentration-depth profile of potassium observed at Site 840 (Fig. 45) indicates that the decrease found for this element results from uptake by solid phases at low temperatures (<100°C; Gieskes, 1983).

Dissolved silica concentrations (Fig. 45) probably increase from standard seawater values at the mud line to the first pore-

Table 9. Paleomagnetic results from oriented APC cores, Hole 840C.

	N	Inclination	Declination	Decl. corr	Corr. decl.	R	α_{95}	k
Core 135-840C-								
2H	3	−43.1°	168.5°	248°	56.5° ± 8.5°	2.955	12.0°	45.1
3H	6	−56.4°	224.5°	171°	35.5° ± 7.7°	5.817	10.9°	27.4
4H	7	−33.1°	106.9°	268°	14.9° ± 14.9°	6.042	21.1°	6.3
Section 135-840C-5H-1	4	−49.2°	51.5°	41°	92.4° ± 4.8°	3.972	6.8°	107.1
Section 135-840C-5H-2	2	−40.5°	326.3°	41°	7.3° ± 13.1°	1.965	18.6°	28.2
Core 135-840C-								
6H	5	−50.5°	296.4°	32°	328.4° ± 4.3°	4.903	9.7°	41.5
7H	6	−53.4°	287.1°	285°	32.1° ± 4.3°	5.942	6.1°	86.5
9H	2	−79.3°	4.3°	351°	355.3° ± 9.0°	1.983	12.7°	60.8
10H	2	−34.9°	134.6°	215°	349.6° ± 23.0°	1.892	32.5°	9.3
Means								
All cores	37	−54.2°	21.2°	±11°		8.129	15.5°	92.0
Restricted set[d]	22	−47.6°	34.0°	±10°		3.879	14.1°	24.8

Note: N = number of samples; Decl. corr. = declination correction, from orientation tool; Corr. decl. = corrected declination. The restricted data set includes Cores 135-840C-2H, -3H, -4H, and -7H. See text for discussion.

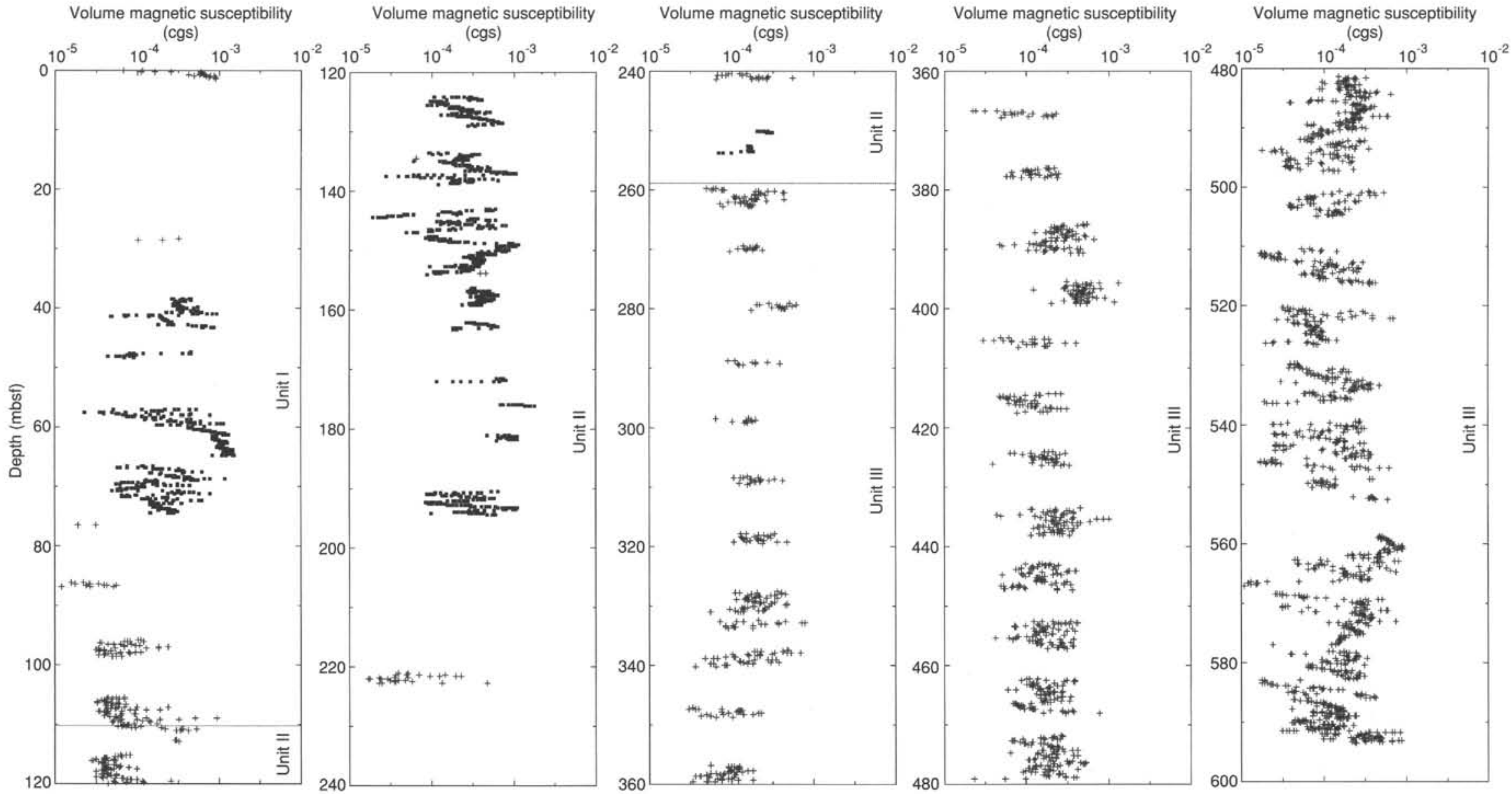

Figure 43. Volume magnetic susceptibility values plotted vs. depth, Site 840. Data from both Holes 840B and 840C are combined; the five panels show different depth ranges in the holes. Plus signs = susceptibility values from Hole 840B, whereas filled squares = Hole 840C measurements. The susceptibility scale is logarithmic.

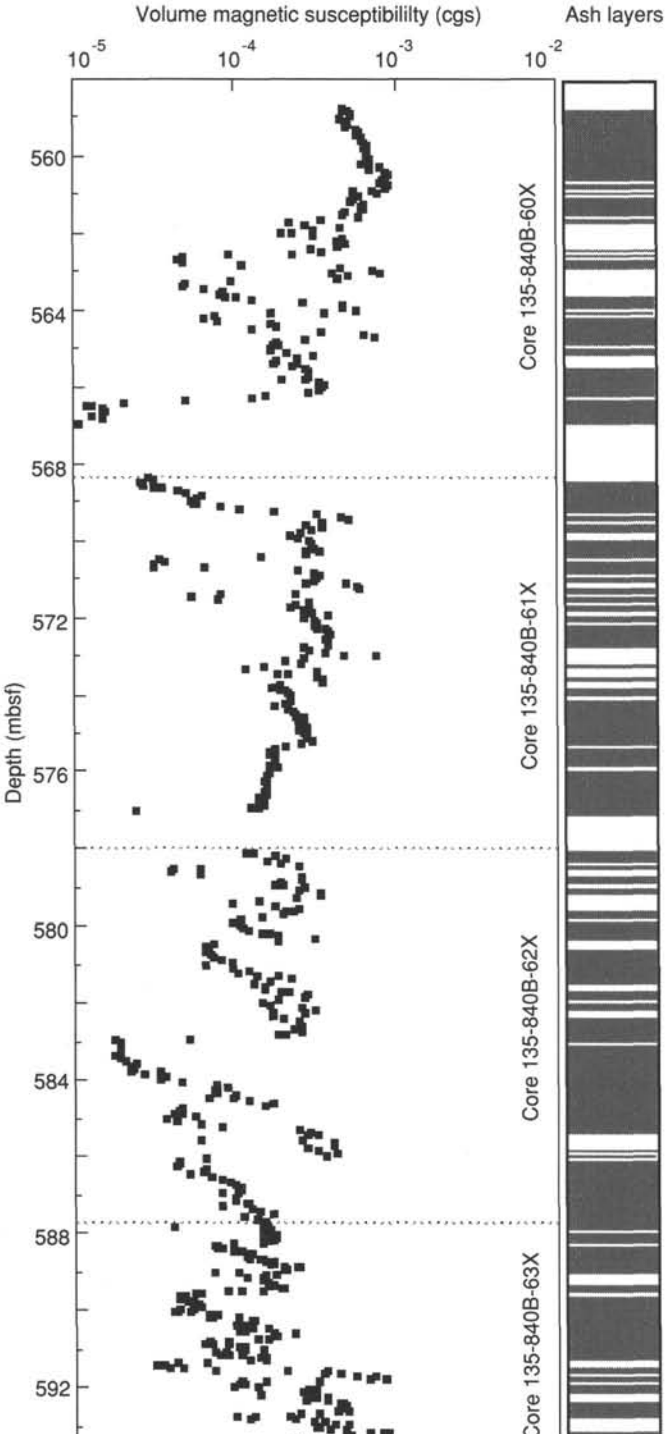

Figure 44. Volume magnetic susceptibility plotted vs. depth for the deepest four cores of Hole 840B. At right is shown a lithologic column in which ash turbidite layers are denoted by the stippled pattern. The susceptibility scale is logarithmic.

water sample taken in lithologic Unit I. Silica concentrations remain fairly constant about 684 ± 32 mM throughout Unit I. In Unit II, from 112 to 125 mbsf, a sharp increase in silica is observed, and it reaches 1213 mM at 125.5 mbsf. The value of Si concentrations obtained from the deepest sample at 146 mbsf is slightly higher (1295 mM). This feature is probably related to the volcanogenic material contents in Units I and II (see "Lithostratigraphy" section, this chapter). Note that the silica profile can be compared with the Ca and Si chemical log data (see "Downhole Measurements" section, this chapter) and with the carbonate content profile (see "Organic Geochemistry" section), which correlates with the concentration-depth profile of the alkalinity.

The concentration-depth profile of dissolved strontium (Fig. 45) suggests an increase in Sr from standard seawater concentrations at the mud line to 70 mbsf. Below Unit I, lower values are observed. This feature of the Sr profile can be best understood in terms of carbonate diagenesis. This implies that while recrystallization of carbonate has already taken place in the upper column, it is almost complete in Unit II where chalks have been recovered (see "Lithostratigraphy" section, this chapter).

Conclusions

At Site 840, it would appear that alteration of volcanic material in the sediments is the major factor causing the observed changes in the calcium, magnesium, and potassium gradients in the pore waters. Concentrations of sulfate and ammonia do not vary much, indicating that the bacterial activity in these low organic carbon sediments is minimal. This is further substantiated by the low level of dissolved manganese. In the most enriched carbonate layer, the observed decrease in alkalinity is probably caused by the precipitation of calcium carbonate in response to an increase in calcium from the alteration of the volcanogenic material. The variation in the concentration-depth profile of the dissolved silica is probably related to the relative amount of volcanogenic materials in lithologic Units I and II.

ORGANIC GEOCHEMISTRY

Shipboard organic geochemical analysis of samples from Site 840 included a total of 41 determinations of total nitrogen, carbon, and sulfur using the Carlo Erba NCS analyzer, 114 determinations of total inorganic carbon using the Coulometrics 5011 coulometer equipped with a System 140 carbonate/carbon analyzer, and 10 analyses with the Rock-Eval instrument. In addition, 26 determinations of volatile hydrocarbons in sediments from Hole 840B using the Carle gas chromatograph were made. Details of the analytical procedures used are outlined in the "Organic Geochemistry" section (this chapter) and the "Explanatory Notes" chapter (this volume), and are described in detail by Emeis and Kvenvolden (1986).

The volatile hydrocarbon gases were obtained from the bulk sediment using the head-space sampling technique and were routinely monitored for methane, ethane, and propane. The head-space samples were taken from Cores 135-840B-1X, -4X, -10X, -12X, -26X to -33X, -36X, -37X, -41X, -43X, -46X, -47X, -48X, -51X to -55X, -57X, and -59X. Some safety concerns had been raised about drilling at this site because within 100 km there are surface hydrocarbon seeps on Tongatapu (Fig. 2). These concerns proved groundless as methane concentrations in all the samples were between 2 and 4 ppm, which is very low and at the laboratory background level. Ethane and propane were not detected. The extremely low concentration of methane indicates that methanogenesis is not occurring in these sediments. Sulfate levels remain at a relatively high level throughout the sediments at this site (see "Inorganic Geochemistry" section, this site chapter); consequently, at no time were conditions favorable for methanogenesis. Furthermore, the very low levels of organic carbon and the type of organic matter (see below) in these sediments were not enough to sustain microbial activity.

Determinations of inorganic carbon (IC) contents were performed on the samples used for physical properties and on addi-

Table 10. Interstitial water chemistry data, Holes 840B and 840C.

Core, section, interval (cm)	Depth (mbsf)	pH	Alkalinity (mM)	Salinity	Ca^{2+} (mM)	Mg^{2+} (mM)	K^{+} (mM)	Cl^{-} (mM)	SO_4^{2-} (mM)	NH_4^{+} (μM)	Si^{4+} (μM)	Sr^{2+} (μM)	Mn^{2+} (μM)	Na^{+} (mM)
135-840B-														
12X-4, 140–150	111.5	7.43	1.745	35.2	25.8	33.8	8.76	549	27.7	36	647	145	21.5	475
13X-2, 140–150	118.1	7.35	1.418	35.2	25.6	34.3	8.57	550	27.5	42	866	136	38.9	477
135-840C-														
3H-2, 136–146	59.9	8.48	2.328	35.2	23.8	33.5	9.97	548	27.7	31	695	157	<10	478
4H-4, 140–150	72.5	7.42	1.279	35.2	25.4	33.3	9.08	547	26.9	73	709	150	<10	474
5H-1, 139–147	125.5	7.69	2.296	35.2	24.8	34.7	8.44	546	27.3	29	1213	133	52.3	473
7H-2, 143–150	146.0	7.47	2.391	35.5	26.4	34.5	8.18	552	27.2	70	1295	128	54.8	476

tional samples selected by the sedimentologists. Percent $CaCO_3$ is calculated according to the equation:

$$CaCO_3 = IC \cdot 8.334.$$

This equation assumes that all the carbonate is present as calcite. The data from these analyses are presented in Table 11 and plotted in Figure 46. Carbonate values range from <0.2% to 86.3%. Carbonate values decrease with depth. The highest values are in Unit I, which extends downhole to a depth of 109.98 m and consists of nannofossil ooze. The volcaniclastic content in Units II and III generally increases with depth and is matched by a corresponding reduction in the carbonate content of the sediments. This is discussed in more detail in the "Lithostratigraphy" section (this chapter).

Also shown in Table 11 are the percentages of total carbon, nitrogen, and sulfur for the 41 samples measured. Total organic carbon (TOC) is defined here as the difference between the total carbon and the inorganic carbon values. The sediments from Site 840 have total organic carbon contents between 0.0% and 0.61%. TOC content appears to show some correlation with depth and with percentage of carbonate (Fig. 46). This is because the samples with the low TOC contents tend to have a high volcaniclastic content and hence have a low carbonate content. Nitrogen was detected in extremely low abundance in four of the samples. Sulfur was detected in nine of the samples analyzed and ranged as high as 1.57% (in the sample at 563.05 mbsf). The sulfur content does not show any correlation with any other measured compositional variable such as percentage carbonate or TOC content.

Ten samples were analyzed using the Rock-Eval instrument. The results are shown in Table 12. These samples include those with the highest TOC values as well as other representative samples at depth. The S1 value represents the amount of "free hydrocarbons" in the sample, and the S2 and S3 values represent the amount of hydrocarbons and carbon dioxide, respectively, that can be released from the kerogen during pyrolysis or thermal maturation of the sediment (Espitalié et al., 1977). A more detailed explanation of these parameters is provided in the "Explanatory Notes" chapter (this volume). Total organic carbon (TOC) measurements were not provided by the Rock-Eval instrument because the TOC module was not working. The TOC values provided in Table 12 are the difference between the total carbon and inorganic carbon values and hence are the same as those given for these samples in Table 11.

It is evident from the S2 values in Table 12 that these samples have absolutely no hydrocarbon potential. The organic matter present in these sediments is presumably inertinite or "dead carbon" that has been completely oxidized. The very poor source rock quality of the samples from Site 840 is in agreement with the results of Buchbinder and Halley (1985) for Pleistocene-Eocene sediments from the Tongatapu-'Eua area, and those of Sandstrom (1985) for Miocene and younger sediments dredged from the southern Tonga Platform in the vicinity of Site 840.

Earlier ODP cruises that drilled open-ocean sediments with a high volcaniclastic contribution, such as Leg 126 in the Bonin Arc-Trench System (Taylor, Fujioka, et al., 1990) or Sites 752–758 of Leg 121 at the Broken Ridge (Peirce, Weissel, et al., 1989), also reported a very low organic carbon content throughout the sediment sequence with extremely low or no volatile hydrocarbon gases present. It is expected that open-ocean sediments with a large volcaniclastic contribution should have low TOC contents. Primary productivity in the upper waters of the open ocean is low and efficient scavenging by organisms or oxidation deeper in the water column means that open-ocean sediments normally contain a low abundance of organic carbon (Tissot and Welte, 1984). The addition of volcaniclastic sediments further dilutes this carbon, which is, in any case, mostly inertinite with no metabolic value for bacteria. The lack of enough carbon for the sulfate-reducing bacteria to metabolize is possibly the reason why sulfate levels at the Leg 135 sites show little change with depth (see the "Inorganic Geochemistry" sections of the other site chapters in this volume). Hence, two of the diagenetic stages that are generally observed in sediments—sulfate reducing and methanogenesis—do not occur in these sediments, which should have important consequences for inorganic diagenesis.

PHYSICAL PROPERTIES

Introduction

A full suite of standard ODP physical properties measurements was made at Site 840. Index properties on sediments and sedimentary and rocks from Holes 840A, 840B, and 840C were determined by using a pycnometer and balance, and include bulk density, grain density, porosity, water content, and void ratio. Bulk density was also measured using the continuous gamma-ray attenuation porosity evaluator (GRAPE), but valid data were acquired only in one core at Hole 840A. Cores from Holes 840B and 840C contained void spaces around the cored rocks, and the GRAPE method requires full core liners for accurate measurements.

Compressional wave velocities were measured on discrete samples using the Hamilton Frame apparatus. Velocities of unconsolidated sediments that could not be removed from the core liner were measured in only one direction. Velocities were measured in both horizontal and vertical directions when possible in unconsolidated sediments and on most of the consolidated sedimentary rocks. Few valid data were acquired with the *P*-wave logger, because most cores contained void spaces around recovered core material (Hole 840B), or the acoustic signal was highly attenuated by the material that filled the core (particularly Hole 840C).

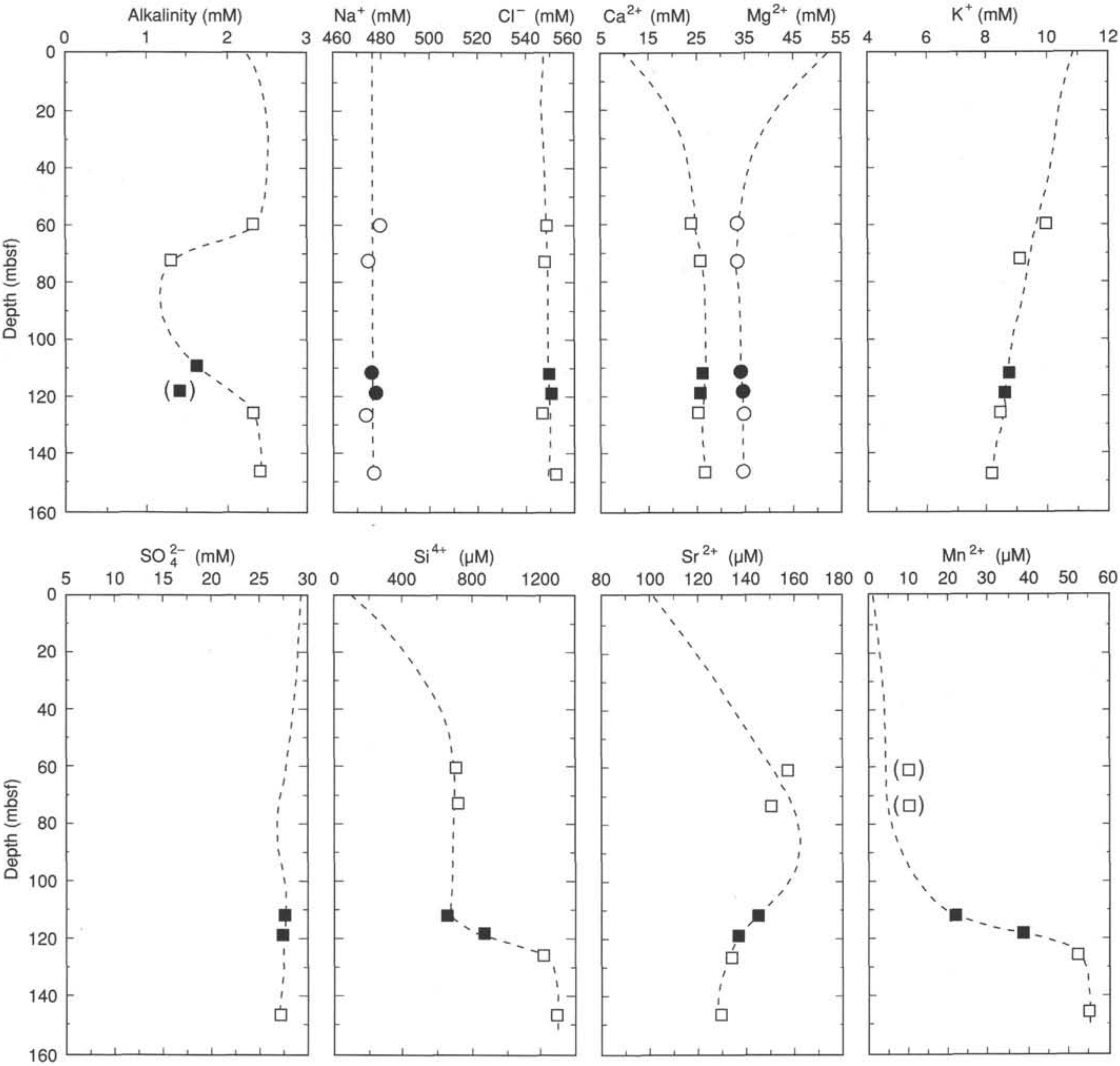

Figure 45. Concentration vs. depth profiles for alkalinity, sodium and chloride, calcium and magnesium, potassium, sulfate, silica, strontium, and manganese, Holes 840B and 840C. Filled symbols = samples from Hole 840B, and open symbols = samples from Hole 840C. Dashed lines begin at 0 mbsf at standard seawater concentrations.

At the end of drilling, the hole was logged with a full suite of logging tools; the results of velocity and bulk density measurements are included here as a comparison with the measurements taken on discrete samples on board. Log values were acquired only between 141 and 553 mbsf. Velocity and bulk density measurements for every 0.305 m were smoothed with a 9-point average (thus averaging the values for a 2.44-m section of the hole) and are shown in Figures 47 and 48. More details of logging results are given in the "Downhole Measurements" section (this chapter).

Vane shear strength was measured only on the one core from Hole 840A; all other recovered material was too consolidated for the method. Thermal conductivity was measured on full cores from Holes 840A and 840C, and on split sediment cores from Hole 840B. Temperature measurements were obtained at three locations in the hole during drilling to measure the geothermal gradient and allow an estimate of heat flow.

The lithologic units referenced here are those described in the "Lithostratigraphy" section of this chapter. Three units were identified: Unit I from 0 to 109.98 mbsf, Unit II from 109.98 to 260.5 mbsf, and Unit III from 260.5 to 395.5 mbsf. The breaks between these units are also observable in the physical properties data. However, two additional areas are present in Unit III where major changes occur in measured physical properties: at 383 and 494 mbsf (these are discussed below). Results from laboratory measurements are listed in Table 13, and downhole and laboratory measurements are plotted in Figures 47–55.

Table 11. Concentrations of inorganic and organic carbon, and total nitrogen and sulfur at Site 840.

Core, section, interval (cm)	Depth (mbsf)	Total carbon (%)	Inorganic carbon (%)	Organic carbon (%)	$CaCO_3$ (%)	N (%)	S (%)	Organic C/N	Organic C/S
135-840B- 1X-1, 13–14	0.13	3.33	3.24	0.09	27				
1X-1, 41–42	0.41		3.37		28.1				
135-840A- 1H-1, 45–46	0.45		4.21		35.1				
135-840B- 1X-1, 67–68	0.67		4.42		36.8				
135-840A- 1H-1, 137–138	1.37		6.66		55.5				
135-840B- 1X-CC, 20–21	1.55		0.88		7.3				
135-840A- 1H-2, 13–14	1.68		5.25		43.7				
1H-2, 106–107	2.61		4.42		36.8				
1H-3, 9–10	3.14		4.51		37.6				
1H-3, 55–56	3.6	0.89	0.83	0.06	6.9				
135-840B- 4X-CC, 12–13	28.52	6.42	5.92	0.5	49.3				
135-840C- 1H-1, 10–11	38.1		0.07		0.6				
1H-2, 91–92	40.41		4.21		35.1				
1H-2, 127–128	40.77	5.65	5.46	0.19	45.5				
2H-1, 17–18	47.67		0.04		0.3				
2H-CC, 6–7	48.08		0.3		2.5				
3H-1, 61–62	57.61		0.08		0.7				
3H-1, 101–102	58.01		4.05		33.7				
4H-1, 29–30	66.79		0.04		0.3				
4H-2, 103–104	69.03	8.76	8.46	0.3	70.5				
4H-3, 39–40	69.89		3.84		32				
4H-4, 53–54	71.53		7.18		59.8				
135-840B- 9X-CC, 4–5	76.44	4.89	4.63	0.26	38.6		0.22		1.2
10X-1, 12–13	86.22	9.97	9.7	0.27	80.8	0.01		27	
10X-CC, 17–18	86.69		6.1		50.8				
11X-1, 42–43	96.12		10.36		86.3				
11X-2, 70–71	97.9	8.8	8.52	0.28	71	0.01		28	
12X-1, 48–49	105.88		10.32		86				
12X-4, 104–105	109.52	10.53	10.3	0.23	85.8				
12X-CC, 7–8	112.62		0.69		5.7				
135-840C- 5H-1, 134–135	125.34		5.51		45.9				
135-840B- 15X-CC, 0–1	134.4	6.95	6.89	0.06	57.4				
135-840C- 6H-4, 52–53	138.02	6.76	6.41	0.35	53.4		0.42		0.83
135-840C- 6H-4, 116–117	138.66		0.5		4.2				
7H-2, 54–55	143.89		1.74		14.5				
9H-1, 27–28	162.27		0.11		0.9				
10H-1, 12–13	171.62		0.74		6.2				
10H-1, 52–53	172.02	4.33	3.85	0.48	32.1				
10H-7, 10–11	175.95		0.28		2.3				
10H-CC, 6–7	175.56		0.05		0.4				
11H-1, 9–10	181.09		0.32		2.7				
11H-1, 60–61	181.6		0.1		0.8				
12H-1, 45–46	190.95		0.04		0.3				
12H-2, 45–46	192.45		0.04		0.3				
12H-3, 45–46	193.95		0.03		0.2				
135-840B- 22X-CC, 7–8	201.77	5.27	4.94	0.33	41.2		0.56		0.59
135-840C- 13H-5, 38–39	253.03		0.08		0.7				
135-840B- 29X-1, 13–14	269.53	5.14	4.94	0.2	41.2		1.06		0.19
30X-1, 71–72	279.81	0.08	0.08	0	0.7				
31X-1, 44–45	289.24	2.97	2.84	0.13	23.7				
32X-1, 11–12	298.61	2.13	2.05	0.08	17.1				
33X-1, 67–68	308.87		0.13		1.1				
34X-1, 44–45	318.24		1.37		11.4				
34X-1, 123–124	319.03		1.46		12.2				
35X-1, 18–19	327.68	3.68	3.67	0.01	30.6		0.18		0.06
36X-1, 64–66	333.04	3.52	3.52	0	29.3				
37X-1, 60–61	338	3.62	3.62	0	30.2				
38X-1, 124–125	348.34	5.32	4.71	0.61	39.2	0.03		20	
39X-2, 91–92	359.18	4.15	4.06	0.09	33.8				
41X-1, 27–28	376.47	5.99	5.92	0.07	49.3				
42X-1, 47–49	386.27		5.15		42.9				
42X-3, 8–10	388.88	4.27	4.09	0.18	34.1				
42X-3, 57–59	389.37		0.28		2.3				
42X-3, 64–66	389.44		3.82		31.8				
43X-1, 14–15	395.64	1.94	1.89	0.05	15.7				
43X-2, 20–22	397.2		0.03		0.2				
44X-1, 61–62	405.51	0.32	0.32	0	2.7				
46X-1, 132–133	425.22		0.08		0.7				
46X-2, 49–50	425.84	0.75	0.66	0.09	5.5				
47X-1, 137–138	434.87		0.08		0.7				
47X-2, 16–17	435.07		0.15		1.2				
47X-3, 19–20	436.6		0.06		0.5				
47X-3, 49–50	436.9		0.33		2.7				
47X-3, 90–91	437.31		0.6		5				
47X-3, 107–108	437.48	0.02	0.02	0	0.2				
48X-1, 55–56	443.35	0.77	0.68	0.09	5.7				

Table 11 (continued).

Core, section, interval (cm)	Depth (mbsf)	Total carbon (%)	Inorganic carbon (%)	Organic carbon (%)	$CaCO_3$ (%)	N (%)	S (%)	Organic C/N	Organic C/S
135-840B-48X-2, 120–122	445.5		0.05		0.4				
48X-3, 77–78	446.57		0.07		0.6				
49X-1, 68–69	453.08	3.67	3.36	0.31	28				
50X-1, 74–75	462.84	2.57	2.55	0.02	21.2		1.02		0.02
51X-1, 83–84	472.53		0.09		0.7				
51X-3, 39–40	475.09		0.11		0.9				
51X-5, 44–45	478.14	3.38	3.25	0.13	27.1				
52X-1, 66–67	482.06		3.04		25.3				
52X-3, 55–56	484.95	0.44	0.42	0.02	3.5		0.99		0.02
52X-6, 70–71	489.6		0.03		0.2				
52X-7, 20–21	490.6		0.07		0.6				
53X-1, 25–26	491.25		0.05		0.4				
53X-4, 59–60	496.09	4.2	4.17	0.03	34.7	0.01		3	
54X-1, 39–40	501.09	0.69	0.67	0.02	5.6				
54X-3, 80–81	504.37		0.14		1.2				
55X-1, 133–134	511.73		0.06		0.5				
56X-1, 32–34	520.52		0.11		0.9				
56X-1, 84–85	521.04		3.04		25.3				
56X-2, 56–57	522.22	6.13	6.01	0.12	50.1		0.39		0.31
56X-3, 96–97	524.05		0.13		1.1				
56X-4, 5–6	524.64		0.13		1.1				
56X-5, 35–36	526.41		0.09		0.7				
57X-2, 30–31	531.4		0.18		1.5				
57X-3, 70–71	533.24		0.05		0.4				
57X-4, 97–98	534.91		0.05		0.4				
57X-5, 14–15	535.51	0.41	0.37	0.04	3.1				
58X-3, 141–142	543.59		0.92		7.7				
58X-4, 107–108	544.75	1.79	1.78	0.01	14.8				
58X-5, 94–95	546.06		0.07		0.6				
59X-2, 79–81	551.29		0.09		0.7				
60X-1, 3–4	558.73		0.18		1.5				
60X-3, 135–136	563.05	1.48	1.43	0.05	11.9		1.57		0.03
60X-6, 61–63	566.76		0.04		0.3				
61X-2, 104–106	570.84		2.93		24.4				
62X-3, 83–84	581.83	3.46	3.45	0.01	28.7				
63X-1, 31–32	588.01		0.12		1				
63X-2, 49–50	589.69		0.23		1.9				
63X-3, 16–17	590.86	0.2	0.19	0.01	1.6				

Index Properties

Discrete Samples

Wet-bulk density, grain density, porosity, water content, and void ratio for sediments and sedimentary rocks from Holes 840A, 840B, and 840C are plotted vs. depth in Figure 49.

For all the index properties, large variations are present in the measured values; this variation is especially large in the turbidite sequences of Units II and III, in which individual turbidite beds range from nannofossil ooze or chalk at the top to vitric sandstone or very coarse vitric gravel at the base. These variations are observed in the discrete samples measured on board and are also seen in the more complete measurements obtained during logging. Commonly, in measurements on discrete samples, each turbidite unit shows decreasing density and increasing porosity, water content, and void ratio from the top to the base. The decrease in density from top to base reflects the higher content of vitric sand and gravel within the coarse sediment fraction at the base of each unit. These vitric sediments have high intergranular pore space, and thus relatively low bulk density as compared with the fine-grained overlying sediments.

On a larger scale, the trends in index properties throughout Units II and III are consistent with sediments undergoing consolidation. Thus, the bulk density increases and the porosity, water content, and void ratio decrease with increasing depth. Bulk density (Fig. 49) increases from about 1.6 g/cm^3 at the top of the hole to an average value of about 1.8 g/cm^3 at 600 mbsf, although the single core with GRAPE data had a density of about 1.8 g/cm^3 from 0 to 3 mbsf. Changes in the bulk density occur between Units I and II, as the measured density decreases within Unit II from an average of about 1.65 g/cm^3 at 110 mbsf to around 1.5 g/cm^3 by 200 mbsf. In the first 123 m of Unit III (from 260 to 383 mbsf), the bulk density increases from about 1.6 to almost 1.9 g/cm^3 in the discrete samples. Below 383 mbsf, bulk density maintains an average value of about 1.85 g/cm^3 to the base of the hole, but it exhibits wide variations in values between 1.6 and 2.1 g/cm^3.

The grain density values (Fig. 49) are highly variable, reflecting the considerable variation in sediment composition. Low grain densities from 2.2 to 2.4 g/cm^3 were commonly measured from vitric sands and gravels, reflecting the pumiceous or volcanic glass component. Grain densities in the range from ~2.6 to 2.8 g/cm^3 were commonly measured on the fine-grained tops of turbidite sequences that include chalks and calcareous siltstones.

Porosity, water content, and void ratio (Fig. 49) are relatively constant in the upper 260 mbsf of the hole, then show decreasing values with depth, and approach relatively constant levels in the lower 300 m of the hole. Between 260 and 340 mbsf in the upper part of Unit III, porosity decreases from around 70% to about 60%, water content from 80% to 40%, and the void ratio from around 2 to between 1 and 1.5. The relatively small decreases, as compared with previous Leg 135 sites, all are consistent with the observation that the sampled sediments are well consolidated even at shallow levels in the hole. At the base of the hole, these three index properties all tend to decrease in value between about 550 and 560 mbsf, then increase again to the base of the hole. This

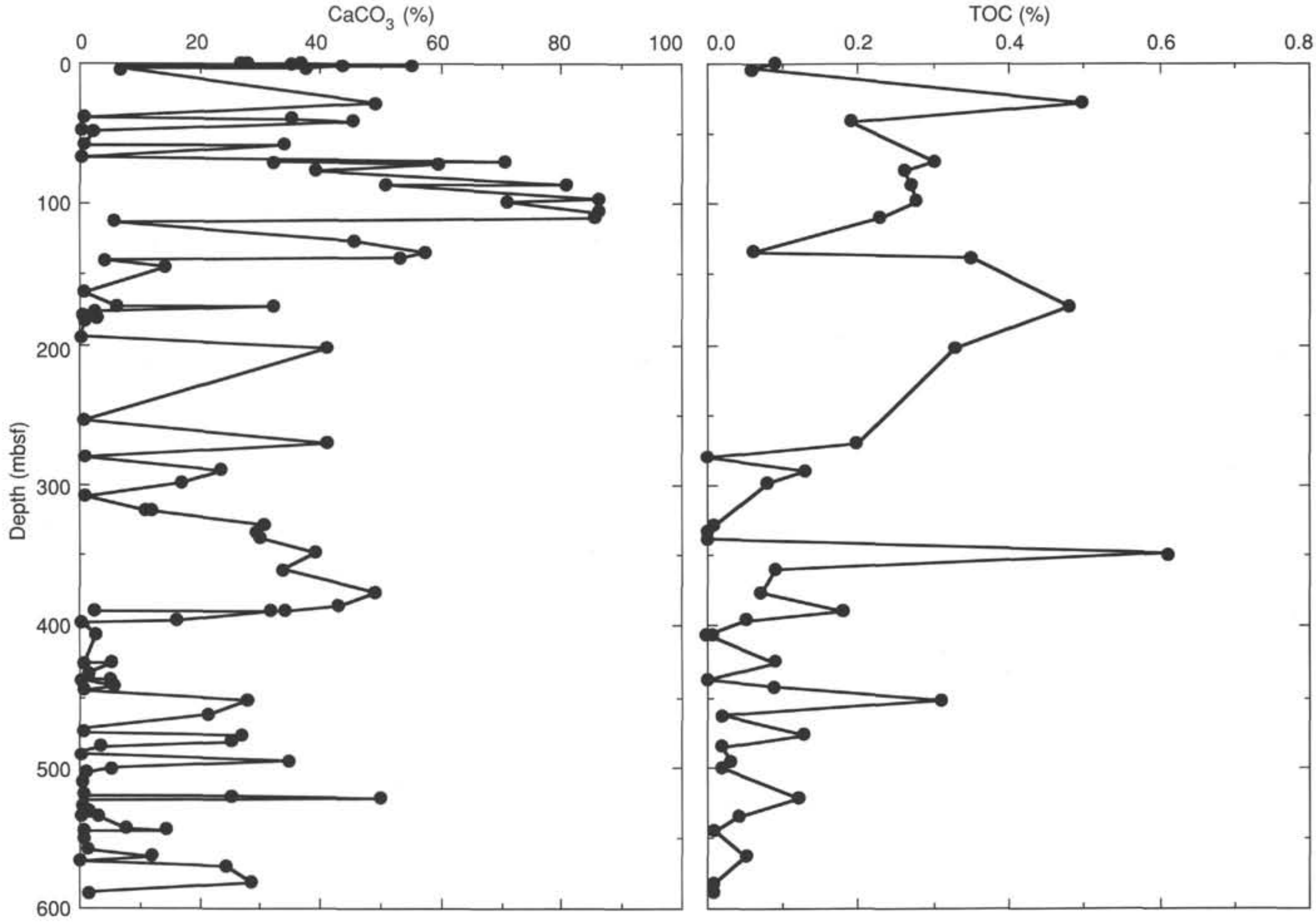

Figure 46. Percentage $CaCO_3$ and total organic carbon (TOC) vs. depth for samples from Site 840.

Table 12. Results of Rock-Eval analysis for Site 840.

Core, section, interval (cm)	Depth (mbsf)	S1 (mg/g)	S2 (mg/g)	S3 (mg/g)	T_{max} (°C)	TOC (%)
135-840A-1H-3, 55–56	3.6	0.03	0	0.99	274	0.06
135-840B-4X-CC, 12–13	28.52	0.04	0	1.2	309	0.5
135-840B-11X-2, 70–71	97.9	0.07	0	1.31	274	0.28
135-840C-10H-1, 52–53	172.02	0.05	0	0.86	254	0.48
135-840B-22X-CC, 7–8	201.77	0.14	0.07	1.67	437	0.33
135-840B-35X-1, 18–19	327.68	0.06	0	0.94	297	0.01
135-840B-38X-1, 124–125	348.34	0.04	0	1.05	373	0.62
135-840B-43X-1, 14–15	395.64	0.06	0	1.43	296	0.05
135-840B-49X-1, 68–69	453.08	0.03	0	1.81	309	0.31
135-840B-53X-4, 59–60	496.09	0.04	0	1.66	273	0.03

Note: Total organic carbon (TOC) values are not from Rock-Eval analysis but are the difference between the total carbon and inorganic carbon values.

swing in values is caused by a zone of alteration where pore spaces are filled with clay and zeolite cements (see "Lithostratigraphy" section, this chapter).

Bulk Density from Lithodensity Logging Tool

The bulk density in the drilled formation was measured with a lithodensity logging tool, which uses neutron scattering from a radioactive source on the tool body; details of the logging tool and results are discussed further in the "Explanatory Notes" chapter (this volume) and in the "Downhole Measurements" section (this chapter).

A comparison between the bulk density values acquired from discrete samples and from the bulk density logging tool is shown in Figure 47, together with the inferred lithologic boundaries and the velocity data. Some of the lowest values on the bulk density plot are associated with a widening of the borehole as measured with calipers during logging; these values may not be valid indications of the real bulk density until post-cruise corrections have been applied, and include the apparent bulk density lows at 208, 233, 255, 301, 326, and 345 mbsf.

The logging data can be interpreted at two scales, first by observing only very broad bulk density variations (over tens of meters) in the measured values, then by looking at some of the fine-scale details (on the order of a few meters) that may be caused by individual turbidite units or groups of units within the formation.

Several major changes in overall bulk density trends are present in the log values of Figure 47. The first is a density low between about 200 mbsf and the base of Unit II at 260.5 mbsf. The density between 141 and 200 mbsf averages 1.65 g/cm^3, whereas the average is 1.6 g/cm^3 between 200 and 260 mbsf. The sands and gravels within this interval are highly pumiceous, with large volumes of intergranular pore space, thus leading to wide density swings within individual turbidite units.

The other major changes are breaks in the bulk density trends from low to high density values at 383 mbsf, and from high to low density values at about 494 mbsf (Figs. 47–48). At 383 mbsf (Figs. 47–48), the increase is from an average of 1.73 g/cm^3 above 383 mbsf to 1.84 g/cm^3 below 383 mbsf. At 494 mbsf (Figs. 47–48),

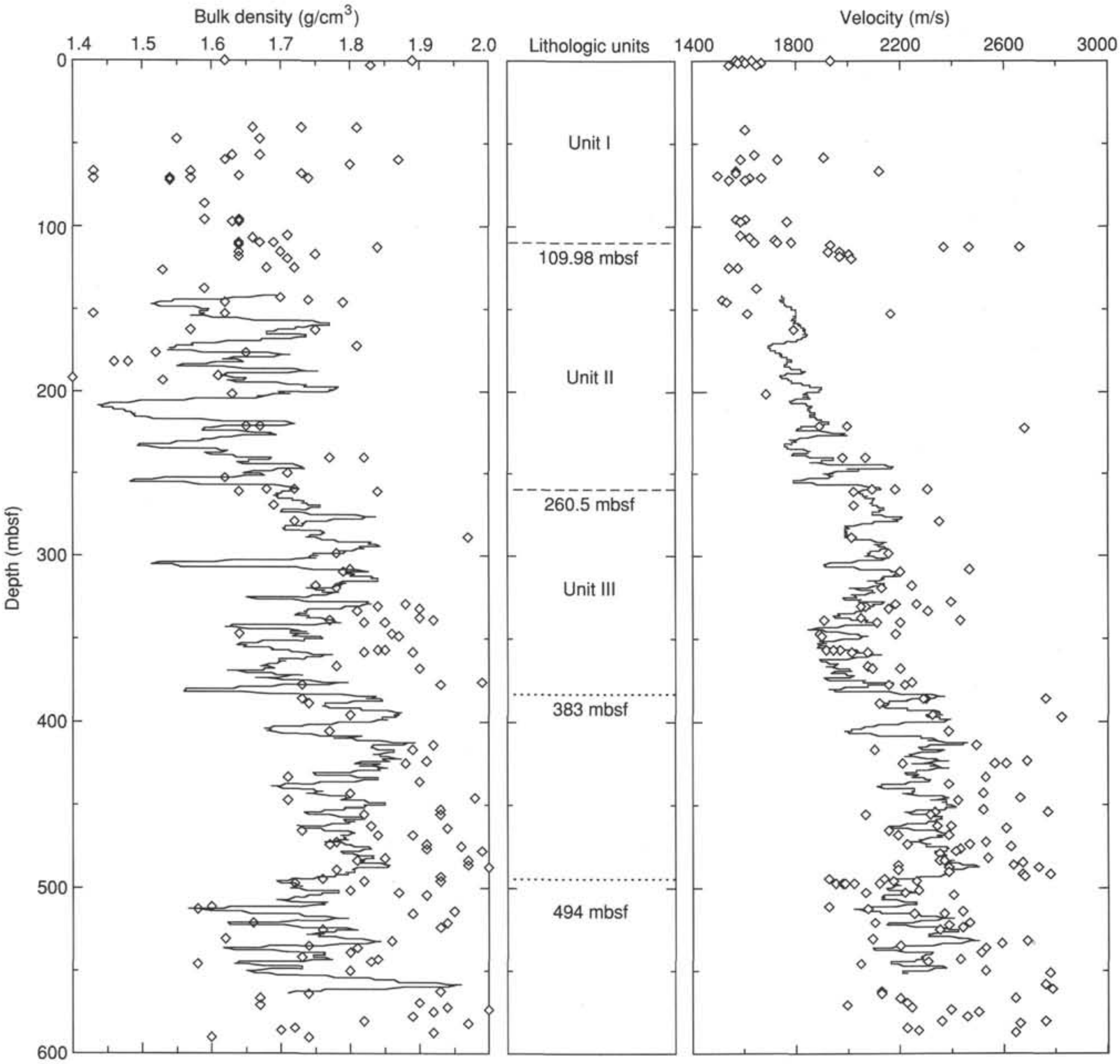

Figure 47. Discrete density measurements and lithodensity tool logging values, inferred lithologic units of Holes 840A, 840B, and 840C, and discrete velocity measurements and sonic velocity logging tool values vs. depth. Open diamonds = values for discrete samples and lines = values from logs. Density and velocity changes at 383 and 494 mbsf are annotated on lithologic units. Logging values are derived from measurements taken every 0.305 m and smoothed with a 9-point running average.

the change is from 1.80 to 1.72 g/cm^3. Both of these breaks coincide with changes in the velocity data (discussed below). Within the intervals 260–383 mbsf and 383–494 mbsf, density values gradually increase to maxima at 320 and 430 mbsf, respectively, then decrease to the base of each interval.

The wide variation in individual measurements evident in the discrete samples is even more obvious on the log values (Figs. 47–48). Superimposed on the broad trends of the density values are shorter wavelength changes of variable amplitude. The changes can be as much as 0.4 g/cm^3, as for example at 510 and 534 mbsf (Fig. 48) where the ranges are 1.5–1.88 g/cm^3 and 1.54–1.9 g/cm^3, respectively.

Compressional Velocity

Discrete Sample Velocities

Compressional velocity data measured with a Hamilton Frame device are shown in Figures 47–48 and 50 and are listed in Table 13. On most samples, multiple measurements of the velocity were made; all of the values are listed in the tables, and plotted values are averages of these measurements.

Compressional velocity, like the index properties, increases with depth and exhibits a similar high degree of variability caused by the different lithologies (Fig. 47). The velocity in the upper

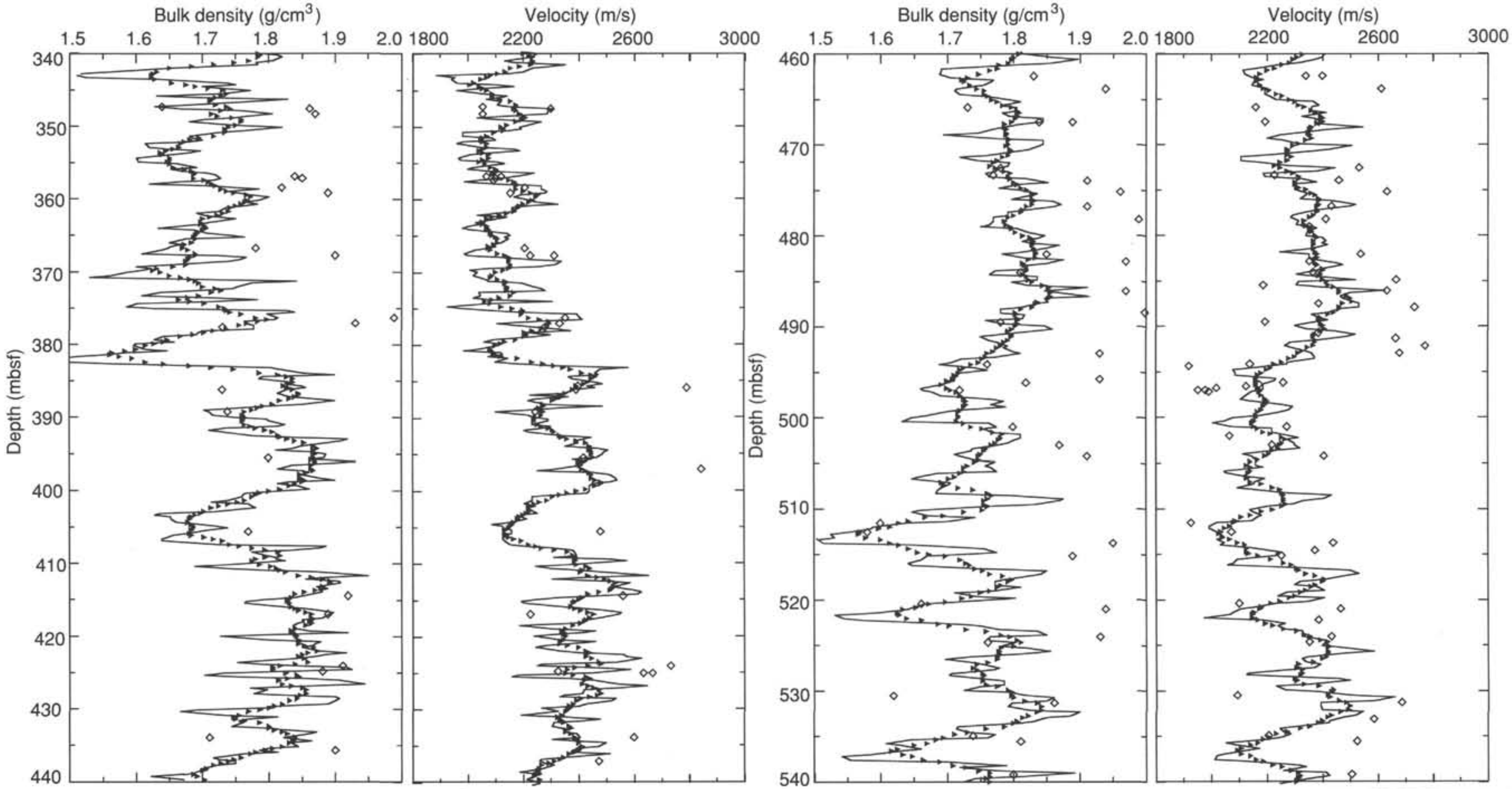

Figure 48. Lithodensity and sonic velocity logging tool values plotted vs. depth for the intervals from 340–440 mbsf and 460–540 mbsf to show details of logging values (line), averaged logging values (filled triangles), and discrete sample values (open diamonds) in the vicinity of the density-velocity changes at 383 and 494 mbsf, respectively. Note the increased velocity and density values below 383 mbsf that result from cementation of the sediments by clay minerals and zeolites. Also note the increased content of highly vesicular, pumiceous sands and gravels below 494 mbsf. These latter changes could also be caused by a small fault at about 494 mbsf.

Table 13. Physical properties data, Holes 840A, 840B, and 840C.

Core, section, interval (cm)	Depth (mbsf)	Su (kPa)	TC (W/[m · °K])	Bulk density (g/cm^3)	Grain density (g/cm^3)	Porosity (%)	Water content (%)	Void ratio	V_P (m/s)	V_P dir.[a]
135-840A-										
1H-1, 10–12	0.10								1842	C
1H-1, 10–12	0.10								2024	C
1H-1, 40–41	0.40	13.10								
1H-1, 46–47	0.46			1.62	2.73	67.3	74.1	2.1	1598	C
1H-1, 135–136	1.35	11.40								
1H-1, 136–137	1.36			1.76	2.82	62.9	57.7	1.7	1603	C
1H-2, 13–15	1.68								1580	C
1H-2, 15–16	1.70	13.10								
1H-2, 105–106	2.60			1.83	2.80	57.7	47.6	1.4	1547	C
1H-2, 135–136	2.90	19.20								
1H-3, 5–6	3.10	44.50							1651	C
1H-3, 8–9	3.13			2.03	2.91	58.9	42.4	1.4		
1H-3, 55–56	3.60			2.03	2.92	50.3	34.0	1.0		
1H-3, 64–65	3.69			2.48	3.06	42.1	21.0	0.7		
1H-CC, 10–11	3.89				2.11	2.95	48.3	30.6	0.9	
135-840B-										
1X-1, 41–43	0.41			1.89	2.76	54.4	41.9	1.20	1630	C
1X-1, 76–78	0.76								1573	C
1X-CC, 20–22	1.55			2.19	2.86	43.0	25.2	0.76	1670	C
10X-1, 18–18	86.28		1.0775							
10X-1, 36–38	86.46		1.1070	1.59	2.59	68.9	79.4	2.22		
11X-1, 31–33	96.01			1.59	2.46	65.6	72.8	1.91		
11X-1, 44–46	96.14			1.64	2.71	65.6	69.1	1.90	1601	C
11X-1, 60–60	96.30		0.9996							
11X-1, 63–65	96.33								1569	C
11X-1, 90–90	96.60		0.9653							
11X-2, 34–36	97.54			1.63	2.62	66.6	72.4	2.00	1587	C
11X-2, 74–76	97.94			1.64	2.71	69.2	76.1	2.24	1762	C
11X-2, 90–90	98.10		1.2062							
12X-1, 44–46	105.84			1.71	2.72	61.5	58.6	1.60	1588	A
12X-1, 60–60	106.00		1.0633							
12X-2, 58–60	107.48								1747	C
12X-2, 60–62	107.50			1.66	2.72	66.6	69.5	2.00	1498	A
12X-2, 110–110	108.00		1.1215							
12X-4, 21–23	108.69								1723	C
12X-4, 100–102	109.48			1.67	2.79	69.5	74.5	2.28	1734	C
12X-5, 10–12	110.08			1.69	2.69	66.5	67.4	1.99	1789	A
12X-5, 10–12	110.08								1782	C
12X-5, 46–48	110.44								1640	A
12X-5, 46–48	110.44			2.04	2.61	39.6	24.8	0.66		
12X-5, 66–68	110.64			1.64	2.75	67.9	73.6	2.11	1786	A
12X-5, 143–145	111.41			1.64	2.81	68.2	74.1	2.15	1905	C
12X-5, 143–145	111.41								1966	A
12X-5, 30–30	111.70		1.1162							
12X-6, 73–75	112.21			1.84	2.75	63.5	54.6	1.74	2431	A
12X-6, 73–75	112.21								2442	A
12X-6, 73–75	112.21								2511	B
12X-6, 73–75	112.21								2500	B
12X-CC, 7–9	112.62			2.02	2.74	50.7	34.6	1.03	2650	A
12X-CC, 7–9	112.62								2643	A
12X-CC, 7–9	112.62								2678	B
12X-CC, 7–9	112.62								2696	B
12X-CC, 21–23	112.76								2367	C
13X-1, 26–28	115.36			1.70	2.68	69.5	72.1	2.27	1935	A
13X-1, 26–28	115.36								1952	A
13X-1, 26–28	115.36								1983	B
13X-1, 26–28	115.36								2009	B
13X-1, 97–99	116.07			1.64	2.73	69.3	75.9	2.25	1927	A
13X-1, 97–99	116.07								1960	A
13X-1, 97–99	116.07								1908	B
13X-1, 97–99	116.07								1917	B
13X-1, 125–125	116.35		1.0861							
13X-2, 28–28	116.88		1.1829							
13X-2, 69–71	117.29			1.75	2.63	63.5	59.3	1.74	1983	A
13X-2, 69–71	117.29								2025	B
13X-2, 90–90	117.50		1.1154							
13X-3, 68–70	118.78			1.64	2.77	70.4	78.3	2.38	1978	A
13X-3, 68–70	118.78								1979	A
13X-3, 68–70	118.78								1963	B

Notes: Su = undrained vane shear strength, TC = thermal conductivity, V_p = compressional P-wave logger) velocity, and V_p dir. = velocity direction, where A is the vertical velocity along the core, B is the horizontal velocity parallel to the cut core face, and C is the horizontal velocity perpendicular to the core face. The complete table is given in back-pocket microfiche.

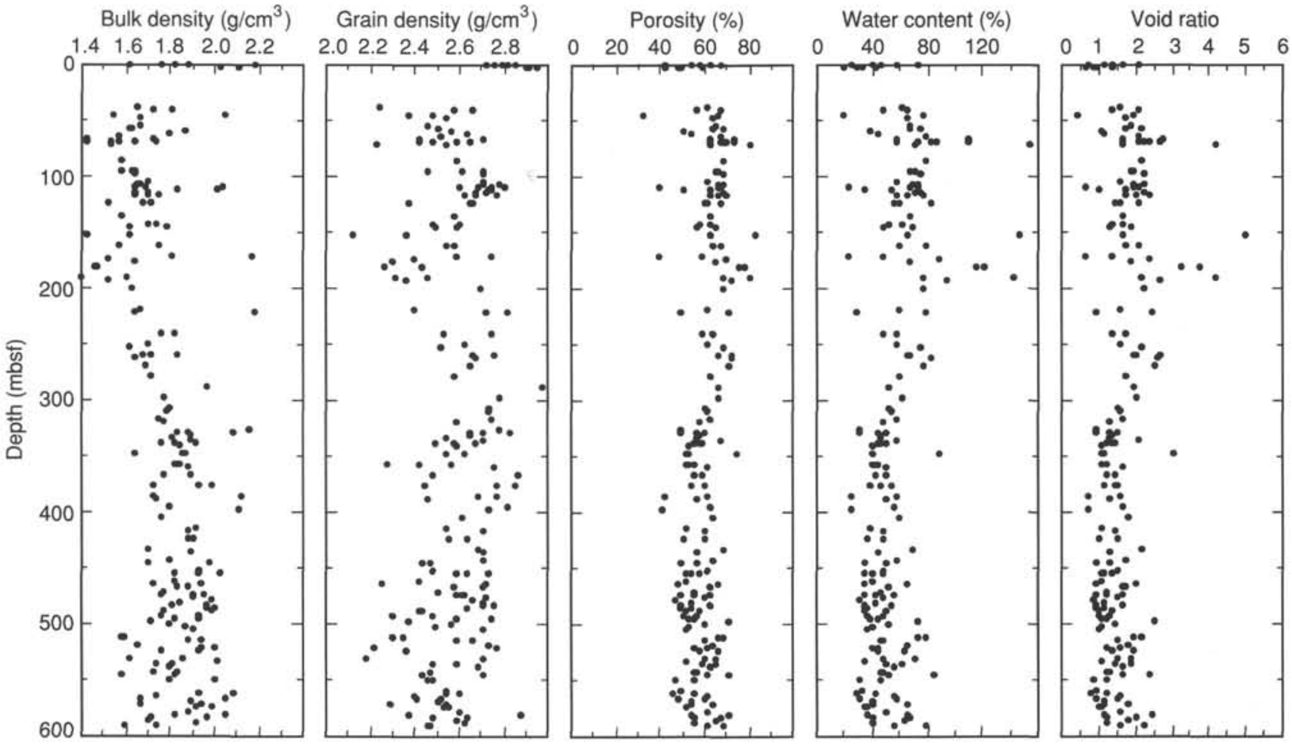

Figure 49. Index property data (bulk density, grain density, porosity, water content, and void ratio) vs. depth, Holes 840A, 840B, and 840C.

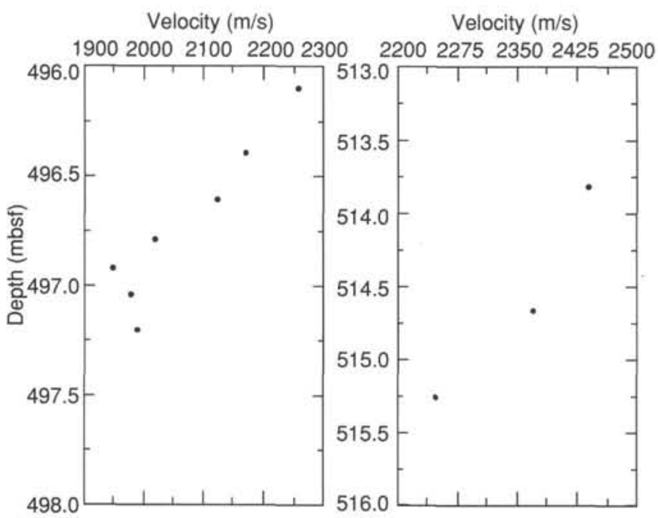

Figure 50. Discrete velocity values measured on individual turbidite units: 496–498 and 513–516 mbsf. In each case, a marked velocity decrease from the top to the base of the unit is evident; densities also decrease from the top to the base in these units.

part of the hole is around 1600 m/s, increasing to about 1800 m/s by 100 mbsf, to around 2200 m/s by 260 mbsf, and to between 2400 and 2600 m/s in the lower 200 m of the hole. Within these averages, however, the variation can be as much as 800 m/s within only a few meters.

Sonic velocity was measured in detail over a few individual turbidite units; two examples are shown in Figure 50. In a 1.1-m-thick turbidite unit between 496.11 and 497.21 mbsf, the velocity changes from 2259 m/s at the top to as low as 1952 m/s at the base (Fig. 50). In a 1.43-m-thick unit between 513.83 and 515.26 mbsf, the velocity changes from 2441 to 2266 m/s (Fig. 50). The bulk density mirrors these changes, although fewer density measurements were made. The velocity and density would normally be expected to increase with increasing grain size. The controlling factor in the observed decrease is apparently that the sand and gravel grains at the base of the turbidites are mainly composed of volcanic components with a large amount of pore space, and with consequent low velocity and density.

Velocity from the Sonic Logging Tool

Sonic velocities were acquired with a sonic logging tool over the same depth range as the lithodensity logging tool, between 141 and 553 mbsf (Fig. 47). Details of the sonic velocity logging tool and results are discussed further in the "Explanatory Notes" chapter (this volume) and in the "Downhole Measurements" section (this chapter). Sonic velocity logging values are also shown on the detailed plots of Figure 48. As was true with the logging bulk density values, some of the lowest values on the velocity plot are associated with a widening of the borehole at 208, 233, 255, 301, 326, and 345 mbsf; these values may not be valid indications of the velocity.

The velocity variations are similar to those seen on the bulk density log, with major changes in the average velocity values at 260.5, 383, and 494 mbsf, and with smaller scale, rapidly varying velocity values superposed on the average value. These areas of velocity and density change are clearly defined on the logging values plotted in Figures 47–48.

The velocity curve is rather smooth in the interval from 141 to 220 mbsf, increasing from about 1800 to about 1850 m/s (Fig. 47). At 260.5 mbsf the velocity increases from an average of 1836 m/s to an average of 2043 m/s at the boundary between Units II and III, then slowly decreases to 383 mbsf. At this depth, the velocity rapidly increases to an average of 2294 m/s and varies about that average to 494 mbsf, where the average velocity decreases to 2247 m/s.

The velocities for both discrete samples and sonic log values are shown in detail at 383 and 494 mbsf in Figure 48. At 383 mbsf, discrete values increase from a high of 2200 m/s above 383 mbsf to as high as 2800 m/s below 383 mbsf. At 494 mbsf, the contrast is even more pronounced, with the discrete values decreasing from a range of 2600–2800 m/s down to a range of 1900–2200 m/s.

Large velocity variations are present over short depth intervals in the sonic log values, and these variations mirror changes in the bulk density plot, with corresponding high and low peaks. The variation can be as much as 625 m/s over a distance of 7 m, as for example between 531 and 538 mbsf where the velocity changes from 2000 to 2625 m/s (Fig. 48).

A comparison between velocity values measured on discrete samples and those acquired with the sonic logging tool (Fig. 47) shows that the discrete samples commonly give higher values than the sonic log. General trends remain the same, but the discrete samples are shifted by 100 to 200 m/s to higher values. Values for both data sets were averaged over a 20-m interval to allow a comparison of the gross velocity variation and to prepare a time-to-depth conversion curve (Fig. 51A). The discrepancy between discrete and logging values is also apparent on this plot. Although fairly good agreement is present between the two averaged curves, the logging velocities are again lower than the discrete values over most of the interval covered by both data sets by as much as 200 m/s.

The sonic tool probably measures values closer to real formation velocities, because the tool averages the measured velocities across all units and unit boundaries, and across individual fractures or zones of fracturing within the formation. Also, because the tool averages over a 0.6-m region, the highest and lowest values tend to be filtered out. In contrast, discrete measurements are only taken on the most competent samples (those most likely to be recovered), and this sampling procedure is probably biased toward higher velocity samples. The discrete samples are also probably not representative of the rapid changes that can occur within the lithologies that make up the turbidite sequences. Bulk density values (Fig. 47) are similarly biased to higher values for discrete samples as compared to lithodensity logging values, for the same reasons.

The velocity measurements provide a way of determining depths on seismic reflection sections from the two-way traveltime. The sonic log velocity values averaged over 20-m intervals have been used to create a time-to-depth conversion curve for correlating the depths in the borehole to two-way seismic traveltime (Fig. 51B). The resulting relation shows that the two-way traveltime in seconds is roughly equal to the depth below the seafloor in kilometers.

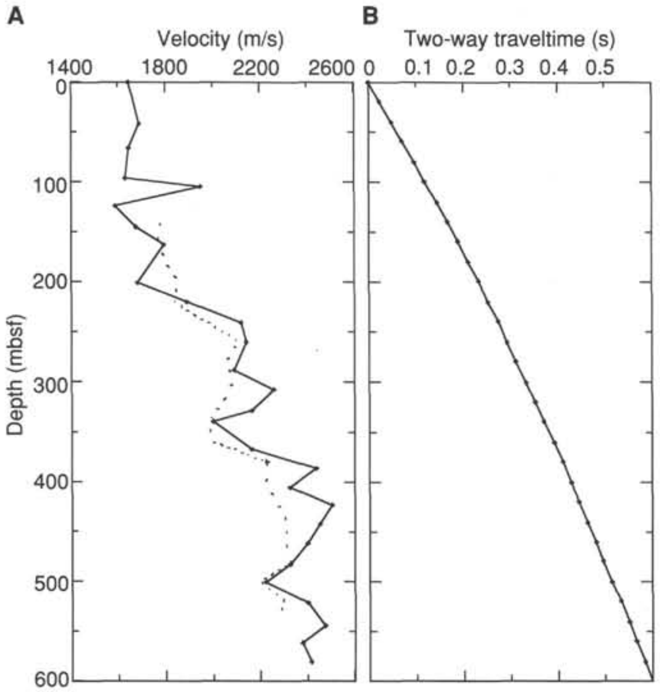

Figure 51. **A.** Discrete (solid line) and sonic log (dashed line) velocity values averaged over 20-m intervals and plotted vs. depth. **B.** Curve for converting two-way seismic reflection data traveltime to depth. The curve is derived from the 20-m averaged interval velocities of Figure 51A and is approximately fit by the equation $d = 380t^2 + 770t$, where d = depth in meters and t = two-way traveltime in seconds.

Undrained Vane Shear Strength

Only four vane shear strength measurements were made at Site 840; all were in the single core recovered from Hole 840A. In the other holes, sediments were too compacted for the method to be valid. The measured values showed a low shear strength between 10 and 40 kPa in the first 3.5 m below the seafloor. Clearly, sediment deposition at this site is slow (as confirmed by sedimentation rates), and little unconsolidated sediment has accumulated at the seafloor.

Thermal Conductivity

Thermal conductivity values were measured on lithified sediments with the half-space method. Thermal conductivity results are illustrated in Figure 52 and listed in Table 13.

Thermal conductivity values mainly range from 1.0 to 1.25 W/(m · °K) over the hole, with only a few measured values exceeding 1.25 W/(m · °K). The velocity and density breaks at 383 and 494 mbsf are weakly correlated to changes in thermal conductivity values, with a general increase below 383 mbsf and a decrease below 494 mbsf. The increased values below 383 mbsf are caused by the decreasing water content and increasing grain contact as cementation fills the pore space. Increased pore space in the pumiceous material below 494 mbsf leads to the slightly lower conductivity values. The average thermal conductivity throughout the hole is 1.12 W/(m · °K).

Temperature Measurements

The downhole water sampler temperature probe (WSTP) was used to make temperature measurements at three depths in Hole 840C: at 47.5, 66.5, and 171.5 mbsf (Fig. 53). Only the temperature at 47.5 mbsf is considered valid. During the other two measurements, the temperature probe was apparently unable to penetrate the formation at the base of the hole, and consistent results were not obtained because of the fluctuating water temperature around the exposed section of the probe.

With only one valid subsurface temperature, a temperature gradient can be obtained only by using the temperature measured at the seafloor during the probe measurements as an additional point (Fig. 54). The result of this approach is a temperature gradient of 29.3°C/km. This gradient is very similar to gradients of 32°C/km and 29.1°C/km derived from bottom-hole temperature measurements made in two commercial exploratory wells on the island of Tongatapu (Maung et al., 1981).

Thermal conductivity measurements (Fig. 52) were used to calculate thermal resistivity and were integrated over depth. When

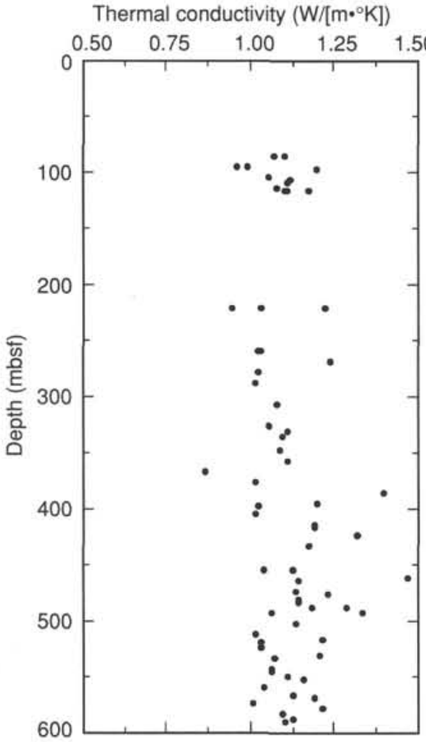

Figure 52. Thermal conductivity vs. depth, Holes 840A, 840B, and 840C.

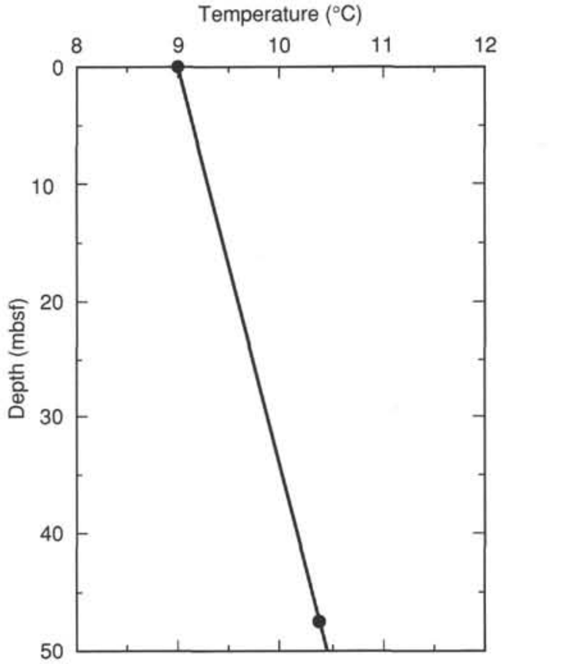

Figure 54. Temperature gradients vs. depth, Hole 840A, with line showing geothermal gradient, using a seafloor temperature measured at 9°C. The calculated geothermal gradient is 29.3°C/km.

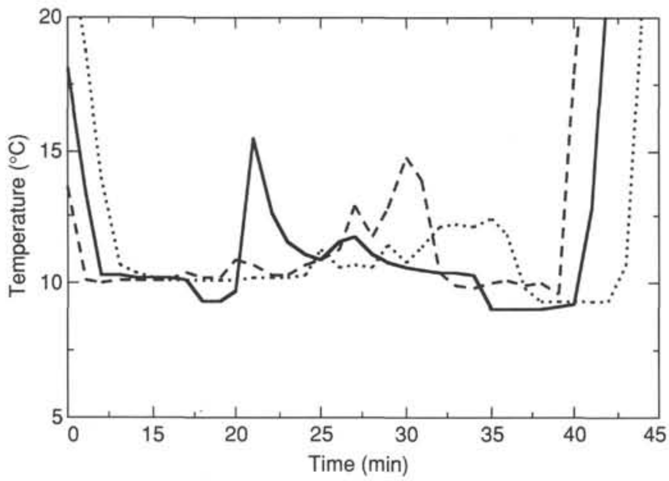

Figure 53. Heat flow measurements, Hole 840C, from various depths, based on WSTP probe temperature runs. Solid line = 47.5 mbsf, short dashes = 66.5 mbsf, and long dashes = 171.5 mbsf.

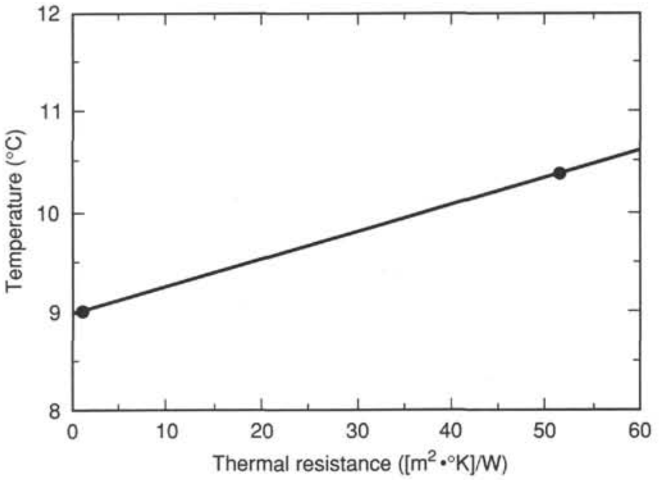

Figure 55. Thermal resistance vs. temperature, Site 840. The slope of the line indicates the magnitude of the heat flow for this site, which is about 27.5 mW/m^2.

thermal resistance is plotted with the temperature measurements from the WSTP temperature probe (Fig. 55), the slope of the regression line indicates that the heat flow in the region is 27.5 mW/m^2.

Discussion

The logging measurements show that small-scale variations in physical properties are related to sediment composition or deposition rates (which control the thickness and frequency of turbidite input). Comparison of the bulk density and velocity values acquired during logging with the core recovered and the observed depths and thicknesses of the turbidite units (see "Lithostratigraphy" section, this chapter) shows that the short wavelength variations are commonly caused by groups of turbidite units. For example, the high values for density and velocity between 395 and 400 mbsf (Fig. 48) are associated with 6 measured turbidite units, whereas the high values between 528 and 537 mbsf (Fig. 48) can be correlated with at least 13 thin turbidites. In both cases, the measured units are mainly <50 cm thick, with only two approaching 1 m thick. Variation in the velocity and density measurements is an average, therefore, over many units of variable thickness.

The major changes seen in the density and velocity values at 383 and 494 mbsf can be correlated with changes in lithology (Fig. 47). The break at 383 mbsf occurs within a zone of sediment alteration, where pore spaces are filled with clay minerals (mainly smectite) and zeolites (see "Lithostratigraphy" section, this chapter). The zone of alteration begins at about 367 mbsf, and alteration ends at about 410–430 mbsf. The density and velocity changes at 383 mbsf are within this zone of alteration and may occur because most of the pore space is filled by clay cementation at that depth. The zone of maximum alteration probably occurs where the density and velocity values reach high values at 410–420 mbsf.

The density and velocity changes at 494 mbsf may occur in part because of an increasing percentage of highly vesicular pumiceous sediments in the coarse sediment fraction. The increasing number of vesicles and the larger pore space in these sediments could cause a density and velocity decrease, and could also lead to the wide swings in values seen in the lower part of the hole. The velocity and density changes at 494 mbsf could also be caused by a fault. Dip measurements on cores showed significantly higher dips below about 490–500 mbsf than above (2°–3° above and occasionally 20° below; see "Structural Geology" section, this chapter). The FMS dipmeter data also show small changes in dip and azimuth in the lower part of the hole (below about 494 mbsf; see "Downhole Measurements" section, this chapter), with the average dip changing from 2° to 4° and the azimuth from due north to N15°W.

A second zone of alteration characterized by cementation by zeolites and clay minerals occurs between 559 and 570 mbsf (see "Lithostratigraphy" section, this chapter). This interval was not logged, and discrete density and velocity values show wide scatter. However, the other index properties of porosity, water content, and void ratio (Fig. 49) show a negative gradient from about 520 to 560 mbsf, then a positive gradient from 560 to the base of the hole. These gradients may be caused by the alteration. No other zones of major sediment alteration were observed within the drilled section; elsewhere the sediments are affected only by compaction.

One of the primary goals of drilling Site 840 was to penetrate a horizon identified on seismic reflection data as an unconformity. The horizon was mapped at about 0.4 to 0.45 s at the drill site. This horizon, termed Horizon A, was presumed to mark a period of erosion or nondeposition within the sedimentary sequence, and was interpreted as an indication of the time of separation of the Lau Ridge from the Tonga forearc. No pronounced lithologic break or paleontologic break was found in the drilled section at a depth corresponding to the observed seismic reflection time for Horizon A. However, the velocity and density changes at 383 mbsf fall at a two-way traveltime of 0.42 s, or almost exactly at the interpreted position of Horizon A. Furthermore, the velocity and density changes at 383 mbsf should give rise to a recognizable seismic reflection. Thus, seismic reflection Horizon A may correspond to the zone of sediment alteration that extends from about 383 to about 420 mbsf (see also "Downhole Measurements" section, this chapter).

DOWNHOLE MEASUREMENTS

Operations

Logging operations at Hole 840B began at 0400 hr UTC, 28 January 1991 and ended at 0000 hr UTC, 29 January 1991. The driller's mud line was at 754.5 mbrf, and the driller's total depth was 597.3 mbsf. The end of the drill pipe was at 94.8 mbsf, except in those cases when the driller raised the pipe (by 30 m) to the top of the rig to open an additional portion of the hole. Well logging operations at Hole 840B consisted of three logging runs using the Quad-tool combination, the geochemical string, and the formation microscanner (FMS) logging string.

The first logging run, the Quad-tool combination, consisted of the long-spaced sonic, the phasor dual induction tool, the high-temperature lithodensity tool, the compensated neutron porosity tool, and a natural gamma-ray tool. On this run, a main uplog from 589.8 to 138.0 mbsf was recorded openhole. A repeat section was also recorded openhole from 189.2 to 136.4 mbsf. The logging speed for both passes was 396 to 457 m/hr (1300–1500 ft/hr).

The second logging run used the geochemical tool string, which includes the aluminum clay tool, the gamma-ray spectrometry tool, a compensated neutron porosity tool, and a natural gamma-ray tool. The logging run with the geochemical string recorded a main uplog from 537.9 to 67.2 mbsf openhole and 67.2 mbsf to the mud line in pipe, and another uplog from 136.4 to 79.1 mbsf. This tool string is run at about 183 m/hr (600 ft/hr).

The third logging run was with the formation microscanner (FMS) string, and it recorded a main pass and a repeat section openhole. The main pass extended from 516.7 to 87.1 mbsf, and the repeat pass extended from 530.4 to 432.8 mbsf. The logging speed for both passes was 488 m/hr (1600 ft/hr).

On-board Processing and Data Quality

Standard processing was applied to the acquired logs (see "Downhole Measurements" section in the "Explanatory Notes" chapter, this volume). Depths should be considered as uncorrected preliminary depths, which could change as much as 5 m during post-cruise processing. The FMS processing was performed on board. For a portion of the hole, from 200 to 250 mbsf, the diameter of the hole was greater than 39.4 cm (15.5 in), and the FMS pads did not make sufficient contact with the borehole walls to produce images of satisfactory quality in that zone. Elsewhere, data quality is excellent. The FMS data were also processed to produce dip information using the mean square dip technique (see "Downhole Measurements" section in the "Explanatory Notes" chapter, this volume). The results of the logging measurements in Hole 840B are shown in Figures 56–63.

Lithologic Summary

The lithologic units identified at Site 840 are shown in Figure 56 and can be summarized as follows (see "Lithostratigraphy" section, this chapter). Unit I, from 0 to 109.98 mbsf, consists of nannofossil ooze interbedded with hemipelagic vitric nannofossil ooze and vitric silt, vitric sand, and pumiceous gravel. Unit II, from 109.98 to 260.5 mbsf, consists of turbidite sequences composed of nannofossil chalk, vitric siltstones, vitric sandstones, and pumiceous gravels. From 109.98 to 124 mbsf, the sequence is dominated by highly bioturbated chalks and marls. From 124 to 260.5 mbsf, the lithology is dominated by pumiceous gravels, sandstones, and siltstones in upward-fining turbidite sequences. Unit III, from 260.5 to 597 mbsf, is dominated by volcaniclastic turbidites composed of pumiceous gravels, vitric sandstones, and vitric siltstones in upward-fining sequences. These are overlain by heavily bioturbated nannofossil chalk. The thickness of the turbidite beds and the grain size of the coarse fraction decreases with time (upward in the hole). The clasts in pumiceous and vitric gravels and sands are highly vesicular, especially at the base of the sequence, but lithic fragments are rare. The downhole logs recorded data only in part of Unit II and in Unit III.

Within the sedimentary sequence of Site 840, the sediments are mainly affected by compaction. Two alteration zones are present where pore space is partially to completely filled by clay minerals and zeolites. The first zone of alteration is between ~367 and 430 mbsf, and this zone is clearly seen by changes in the logging values. The second zone of alteration is between 559 and 570 mbsf, but this zone is below the logged section of the hole.

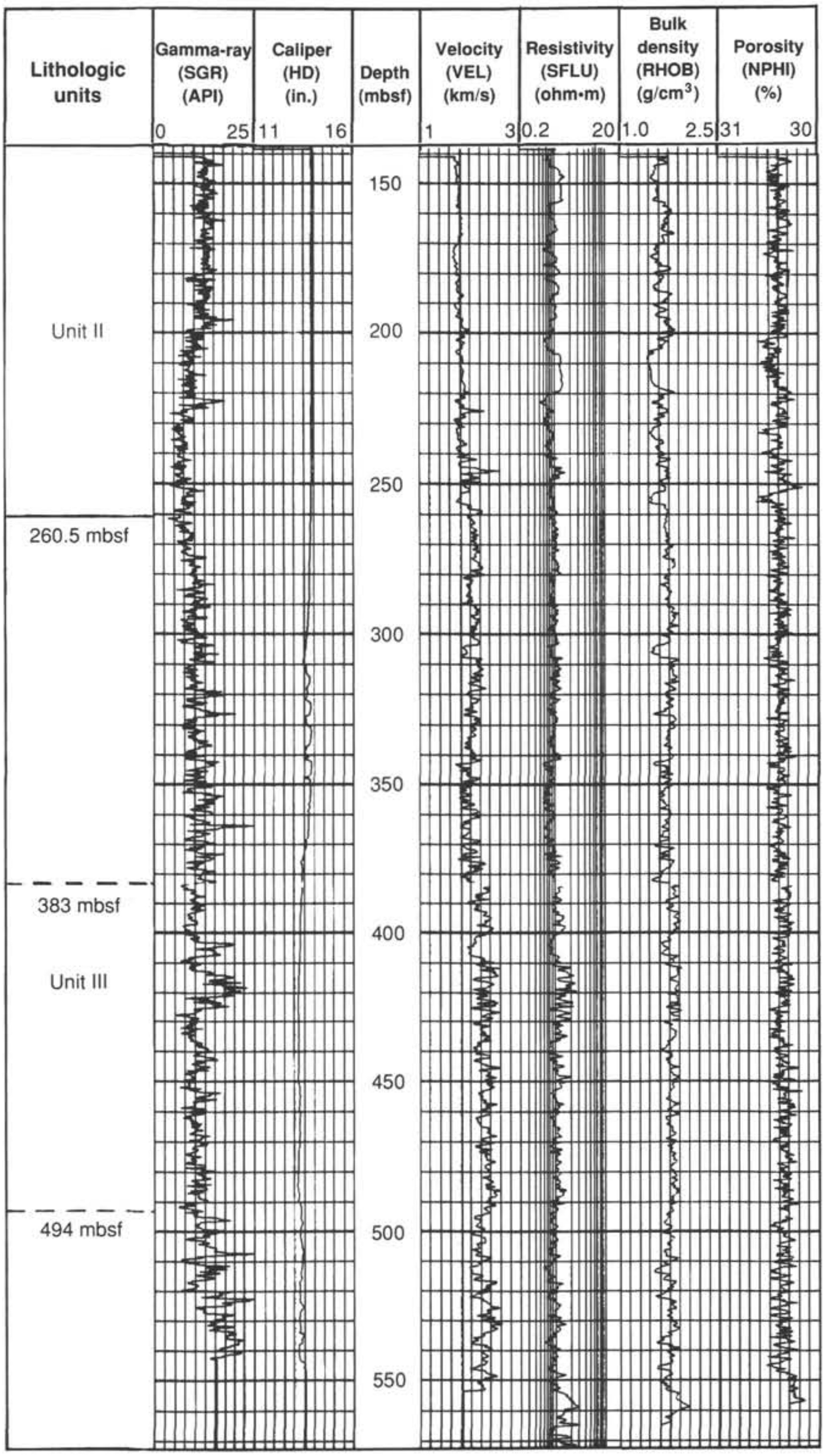

Figure 56. Seismic stratigraphic tool-string logs vs. depth, Hole 840B. The logs illustrated are as follows: total gamma ray (SGR, American Petroleum Institute [API] units); caliper hole diameter (in inches); sonic velocity, spherically focused (SFLU) resistivity (on a logarithmic scale), bulk density (RHOB), and neutron porosity (NPHI). Lithologic units are shown at left; breaks at 383 and 494 mbsf are discussed in text.

Results and Interpretation

Caliper Logs

The caliper logs record the diameter of the hole and are useful in determining whether logging data over a given interval are valid. The caliper on the Quad-tool combination (HD; Fig. 56) shows that the entire hole has a diameter of <36 cm. The four pads of the FMS tool provide a better indication of diameter and ellipticity than the Quad caliper (Fig. 57). The FMS caliper shows the hole as >39 cm wide between 90 and 120 mbsf, and from 200 to 250 mbsf; hole rugosity is rather extreme between 120 and 200 mbsf. Therefore, between 90 and 250 mbsf, FMS data are largely invalid. Elsewhere, data from all logs should be little affected by hole diameter. The FMS caliper also shows that the hole is elliptical between 120 and 170 mbsf and between 260 and 310 mbsf, in both cases with a difference of up to 6 cm between the long and short axis of the ellipse. Turning of the FMS tool, resulting in invalid data, could occur as the tool readjusts to the ellipticity.

Sonic Velocity, Resistivity, Lithodensity, and Neutron Porosity Logs

The sonic velocity, resistivity, and density logs (Fig. 56) are positively correlated with each other and are negatively correlated with the porosity log. Therefore, the four logs are discussed together here. The values measured by the resistivity and velocity logs are a function of density, porosity, and fracturing within the formation. The positive correlation of these two logs indicates that the velocity is dominantly controlled by the porosity. The logs have samples every 0.1525 m, and will yield a vertical resolution of about 0.6 m that will aid in defining individual turbidite units that were not sampled during coring.

The bulk density log data (RHOB on Figs. 56 and 58) are generally valid throughout Hole 840B (see caliper log on Fig. 56 and FMS caliper on Fig. 57). The extreme density lows (including those at 208, 233, 255, 306, 327, and 345 mbsf), however, correlate with borehole rugosity as shown on the FMS calipers; these values must be treated with caution until after post-cruise processing. The neutron porosity measurement (NPHI, Fig. 56) is inversely correlated with the density, lending confidence to the porosity trends measured.

Three intervals are present on the logs where the average log values make large changes; these are shown on the velocity and bulk density logs at an expanded scale in Figure 58, together with the lithology. The first region of change is at 260.5 mbsf, which corresponds to the boundary between lithologic Units II and III. At the unit boundary, the amount of pumiceous sediments increases in Unit II, and these less dense and highly vesicular sediments probably cause the decreasing values seen on the logs.

The second area of change is at 383 mbsf (Fig. 58). At this depth, the velocity, resistivity, and density all increase in value. The velocity increase is from an average value of 2.04 km/s in the zone above the break to 2.29 km/s below the break. The density increases from 1.7 to 1.85 g/cm^3. This break occurs in the zone of sediment alteration discussed earlier, and the increased density and velocity probably are caused by clay cement filling the pore space within the volcanic sands and gravels.

The third area of density and velocity changes is at 494 mbsf (Figs. 58–59), where the average values decrease. The velocity average for the sediments on either side of 494 mbsf decreases by about 50 m/s, and the density by about 0.08 g/cm^3.

When viewed in detail, the logs contain small-scale variations superposed on the average trends. Some of this variation can be observed in an expanded-scale plot of logging values for sonic velocity and bulk density for the interval between 450 and 550

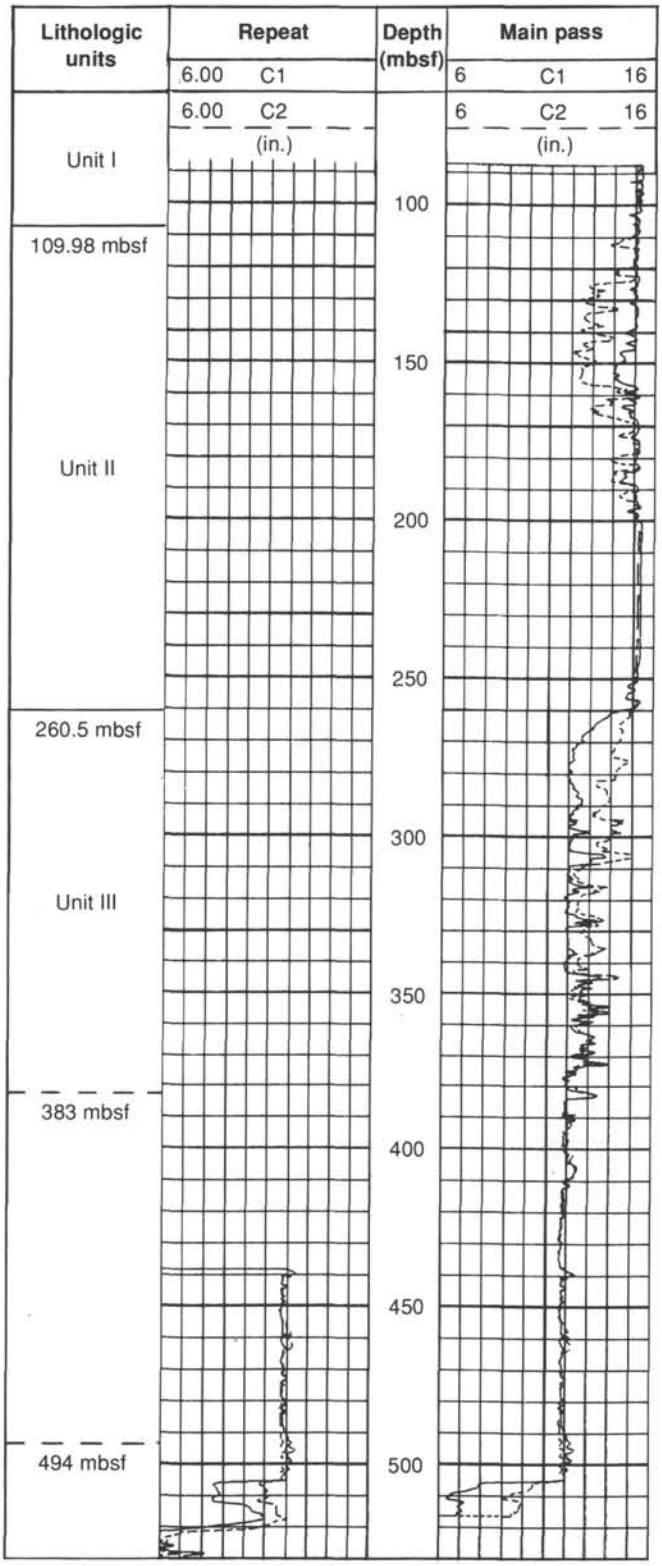

Figure 57. FMS calipers vs. depth obtained from the main pass and a repeat pass with the formation microscanner tool, Hole 840B. C1 (caliper 1–3, solid line) and C2 (caliper 2–4, dashed line) are plotted on a scale of 6–16 in. Breaks at 383 and 494 mbsf are discussed in text.

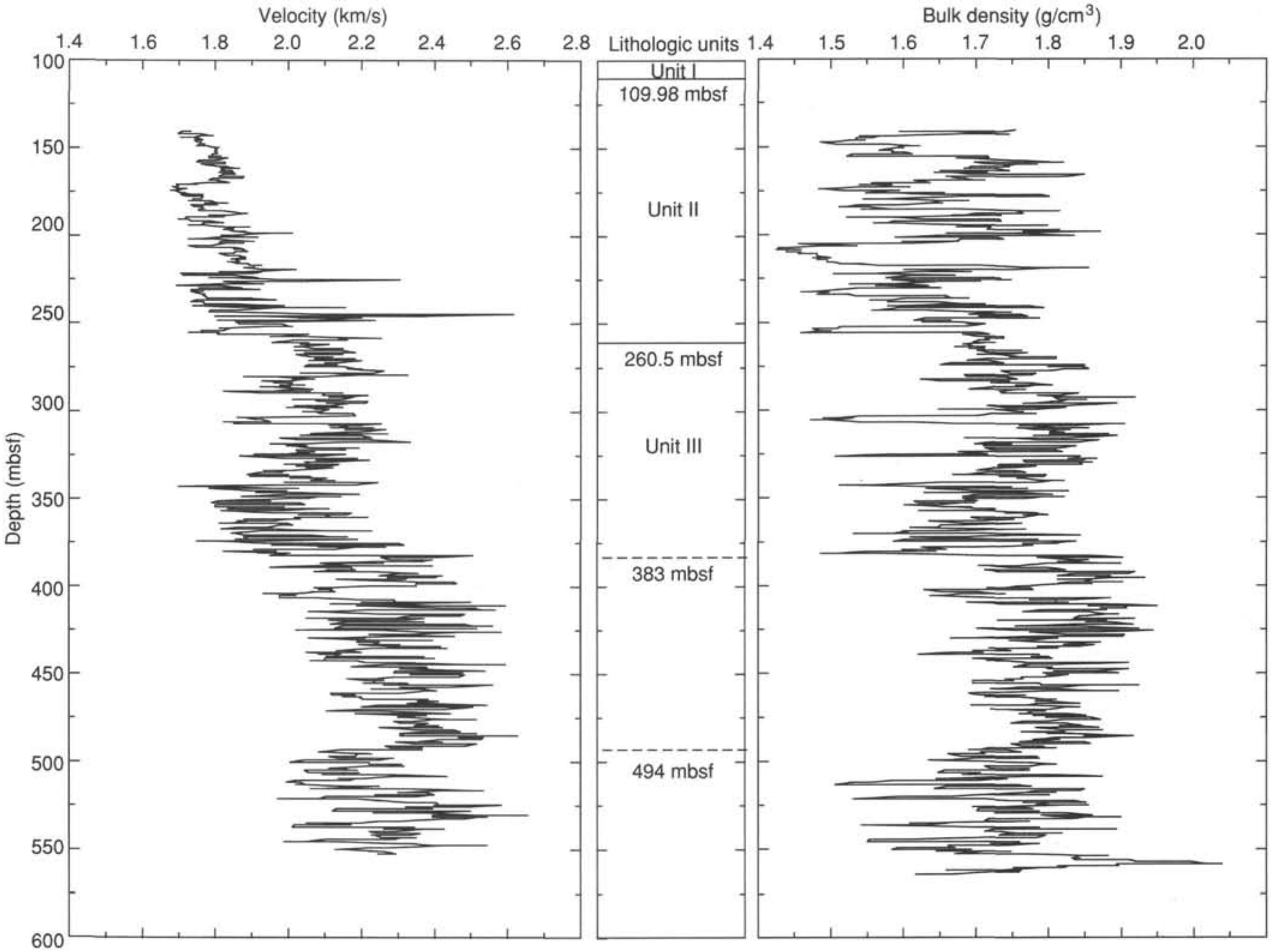

Figure 58. Sonic velocity (km/s) and bulk density (g/cm^3) replotted vs. depth at an expanded scale and correlated with the lithology, Hole 840B. Breaks at 383 and 494 mbsf are based on changes in density and velocity at those depths.

mbsf (Fig. 59). An example of the variability is demonstrated by changes in density and velocity of 0.3 g/cm^3 and 650 m/s, respectively, between 531 and 537 mbsf, with five individual peaks superimposed on the overall increase within the interval. The interval contains 11 turbidite units as measured on cores (see "Lithostratigraphy" section, this chapter). The logging values also show a characteristic pattern that may be caused by the turbidites. The logs have a sawtooth pattern, with a gradually upward-increasing velocity and resistivity, followed by abrupt sharp decreases. Finally, high density values are present on the density log at 559 mbsf (Fig. 58). At this depth, a 1.95-m-thick volcanic breccia unit was sampled between 558.7 and 560.65 mbsf. In shipboard samples, this unit had both high density and velocity values (see "Physical Properties" section, this chapter), and clearly causes the response observed on the logs.

Gamma-ray Log

The gamma-ray log data acquired with the geochemical tool string (Fig. 60) are of higher quality than the data acquired with the Quad-tool string (SGR, Fig. 56) because the geochemical tool is run at a slower speed. Descriptions of the gamma-ray results, therefore, are primarily based on the geochemical string data. The gamma-ray tool records results through the drill pipe; the tool exited the pipe at 67.5 mbsf.

The gamma-ray intensities seem to be negatively correlated with the velocity, resistivity, and density logs. The gamma-ray logging tool may be sensing the volcanic component within the turbidite units, thus returning high intensities in the regions where the velocity, resistivity, and density are all low because of the volcanic content.

Average gamma-ray intensities and values of Th, U, and K are relatively constant from 0 to 120 mbsf; they then began to increase near or slightly below the Unit I/II boundary. A slow, gradual increase in values below 120 mbsf culminates in a broad high centered between 150 and 170 mbsf, after which values gradually decrease to about 250 mbsf near the base of Unit II. The upper part of Unit II is dominated by nannofossil chalk, with gradually increasing volcaniclastic content in the lower part of the unit. The general increase in the gamma-ray intensities and the Th, U, and K curves from the base to the top of the unit may be reflecting the upward increase in nannofossil ooze and clay content.

Within Unit III, gamma values slowly increase to just above 400 mbsf. Sharp increases between 400 and 430 mbsf occur before values return to an average trend similar to that between 260 and 400 mbsf. Increased values are also present below the 494 mbsf velocity and density break.

The gamma-ray tool is sensitive to clays. Thus, the increased gamma-ray intensities and Th, U, and K values between 400 and

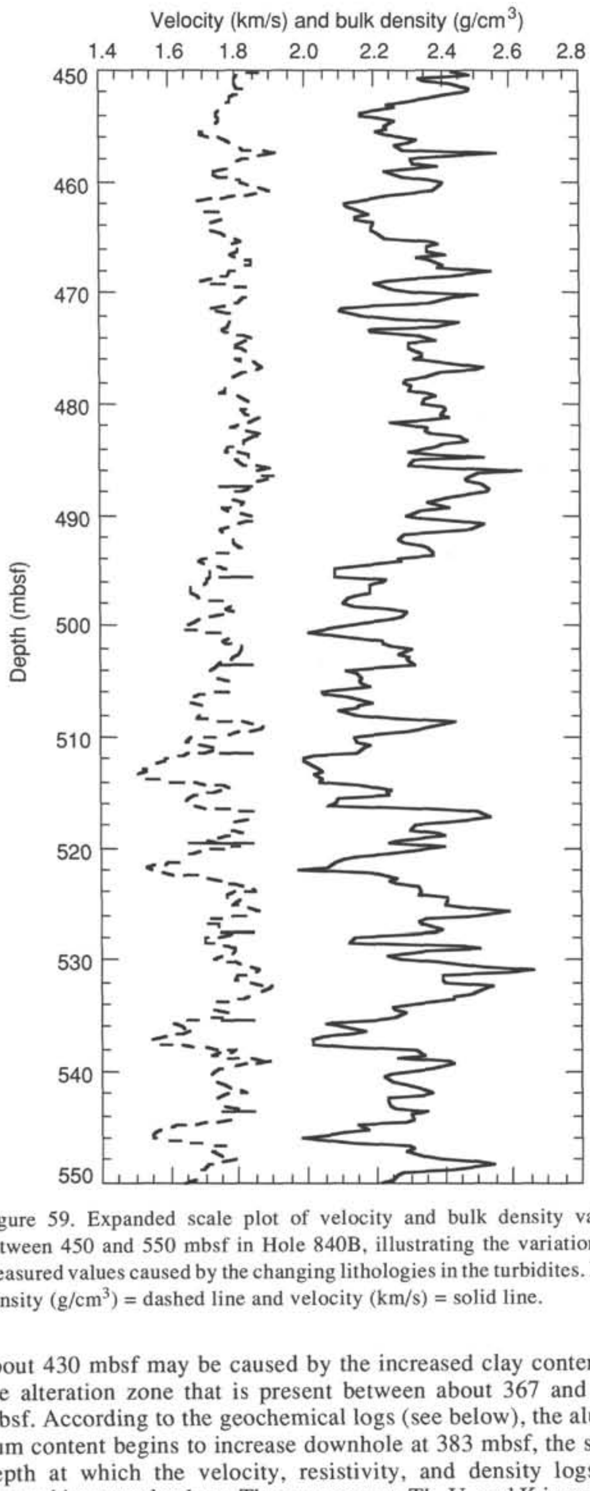

Figure 59. Expanded scale plot of velocity and bulk density values between 450 and 550 mbsf in Hole 840B, illustrating the variations in measured values caused by the changing lithologies in the turbidites. Bulk density (g/cm^3) = dashed line and velocity (km/s) = solid line.

about 430 mbsf may be caused by the increased clay content in the alteration zone that is present between about 367 and 430 mbsf. According to the geochemical logs (see below), the aluminum content begins to increase downhole at 383 mbsf, the same depth at which the velocity, resistivity, and density logs all showed increased values. The gamma-ray, Th, U, and K increases are greatest between 400 and 430 mbsf, and probably indicate the zone of maximum alteration. The base of the altered zone may lie at about 424 mbsf, coincident with a sharp decrease in the thorium curves. The gamma-ray intensity and U and K values decrease in value more slowly over the interval from 420 to 430 mbsf.

Geochemical Yields

The gamma-ray spectrometry tool (GST; Fig. 61) will be reprocessed post-cruise to calculate oxide percentages of six elements (Ca, Si, Fe, S, H, and Cl). The tool exited the drill pipe at 65 mbsf, accounting for the large jump in values at that depth. All of the curves show small differences in general trends except in a few areas.

Ca and Si show changes between 70 and 120 mbsf, with Ca increasing to a local maximum between 100 and 120 mbsf, and Si showing a relative low between 65 and 120 mbsf. Between 110 and 124 mbsf, the section is dominated by nannofossil chalks. Si may decrease because of the decreasing volcaniclastic content in the sediments. Small-scale variations show an inverse correlation between Si and Ca; Si increases and concomitant Ca decreases probably reflect individual volcaniclastic turbidite horizons. The Ca increase is coincident with the region of highest carbonate values in sediments recovered from the hole. Ca decreases sharply and Si increases at 120 mbsf, as the nannofossil-chalk-dominated section is replaced by sediments with a higher volcaniclastic content. Average Si values increase downhole, whereas H and Cl generally decrease downhole.

Areas of major change seen on other curves change only slightly on the geochemical yield plots. The change from Unit II to Unit III at 260.5 mbsf is coincident with only a slight rise in Si and Fe, although Fe in Unit III is consistently slightly higher than in the overlying units.

Formation Microscanner

Data were acquired with the formation microscanner (FMS) from 87 to 516 mbsf, but only the data from below 250 mbsf are of high quality. Above 250 mbsf, either the borehole was too wide (wider than 39 cm) or the hole rugosity and ellipticity were too great to ensure that the FMS pads made sufficient contact with the walls. Below 250 mbsf, spectacular banded images were obtained from the turbidites. The FMS are presented on microfiche in the back pocket of this volume.

An example of FMS images from the section between 310 and 330 mbsf is shown in Figure 62. On these images, the dark bands are areas of low resistivity, and the light bands are areas of high resistivity. The FMS images show frequent changes from dark to light banding, commonly with the dark bands thicker than the light bands. The dark bands generally correlate with zones of low density and low velocity on the velocity and density logs, and probably correspond to the vitric sands and gravels in the lower part of the turbidite units. The light bands, associated with high velocities and densities, are probably caused by the chalk interbeds.

An FMS image of three turbidites is shown in Figure 62. In particular, a 1.19-m-thick turbidite between 496.1 and 497.45 mbsf in the recovered cores was measured in detail for velocity and density on board (see "Physical Properties" section, this chapter). This turbidite showed a change in velocity from 2259 m/s at the top to 1952 m/s at the base, and the density changed by about 0.4 g/cm^3. The FMS image for the region from 496 to 500 mbsf (Fig. 62, all within Core 135-840B-53X) shows three probable turbidite units: from 496.3 to 497.3 mbsf (1 m thick); from 497.3 to 499.35 mbsf (2.05 m thick); and from 499.35 to 499.95 mbsf (0.6 m thick). During coring, when recovery is <100%, a unit can lose but not gain apparent thickness, so the measured turbidite must correspond to the FMS unit between 497.3 and 499.35 mbsf, a slight shift from the assigned depth but still within the core (post-cruise depth corrections could further affect this correlation). The measured unit did not have a thick fine-grained top, and thus appears to correlate well with the FMS unit, where the high-resistivity region at the top of the unit is thin and not as resistive as tops on the other two turbidites shown. This unit also shows the correlation of highly resistive bands with the high-velocity, high-density, fine-grained part of an individual turbidite, and the correlation of low resistivity bands with low velocity and

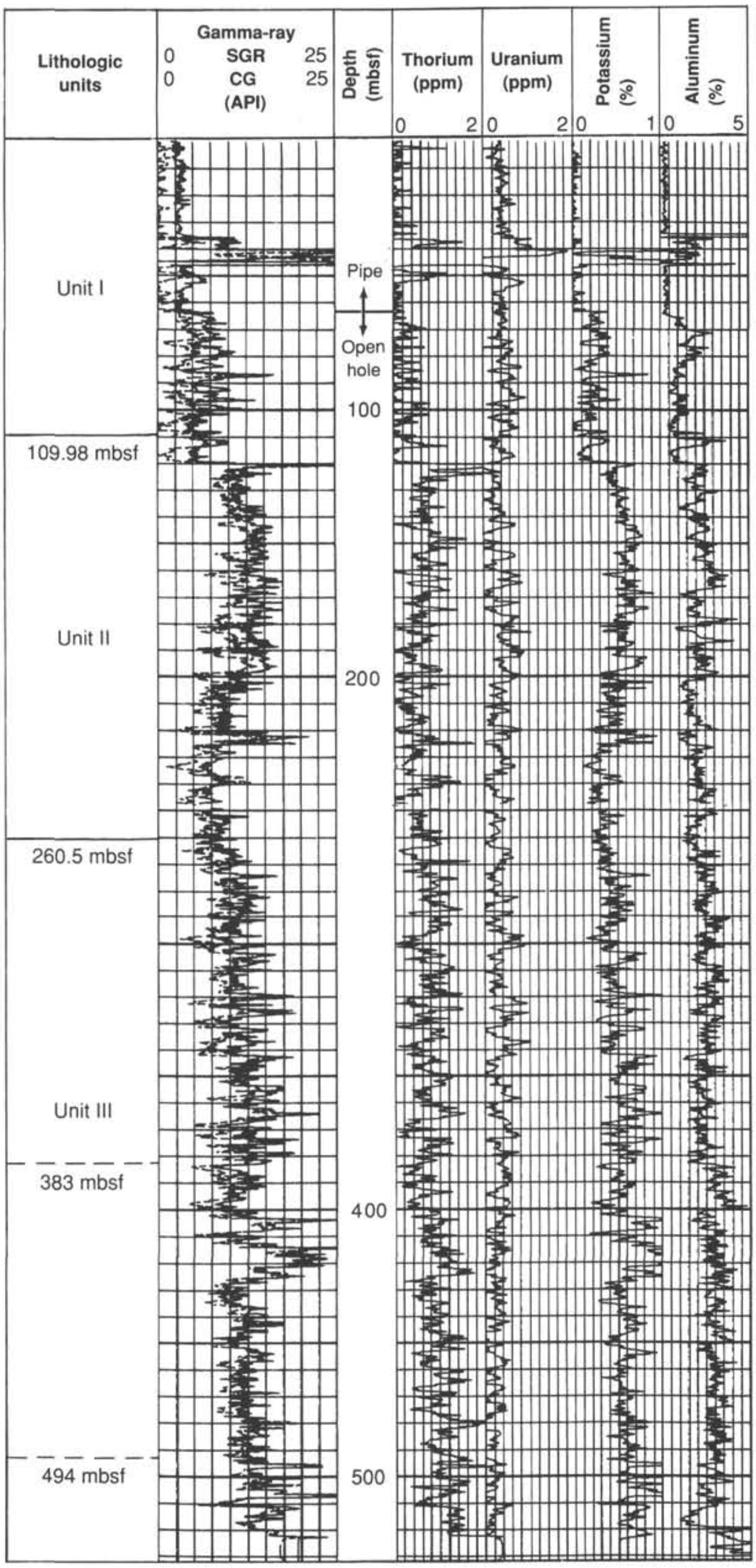

Figure 60. Natural gamma-ray curves from the geochemical tool string vs. depth, Hole 840B. The logs illustrated are as follows: total gamma ray (SGR, in American Petroleum Institute [API] units), computed gamma ray (in API units); thorium, uranium, potassium, and aluminum. The lithologic units are given on the left.

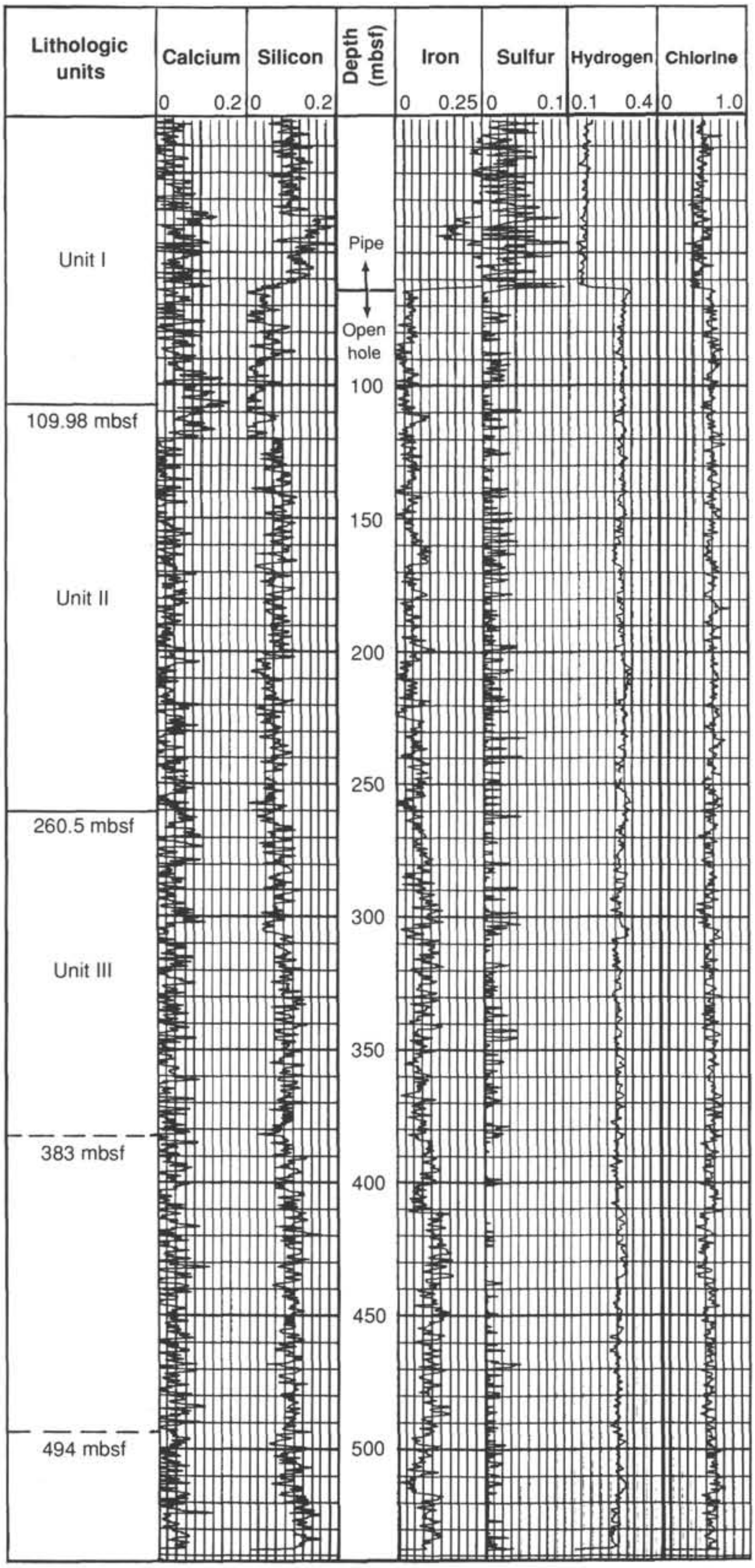

Figure 61. Geochemical yield logs vs. depth, Hole 840B. The logs illustrated are as follows: calcium, silicon, iron, sulfur, hydrogen, and chlorine. The lithologic units are given on the left.

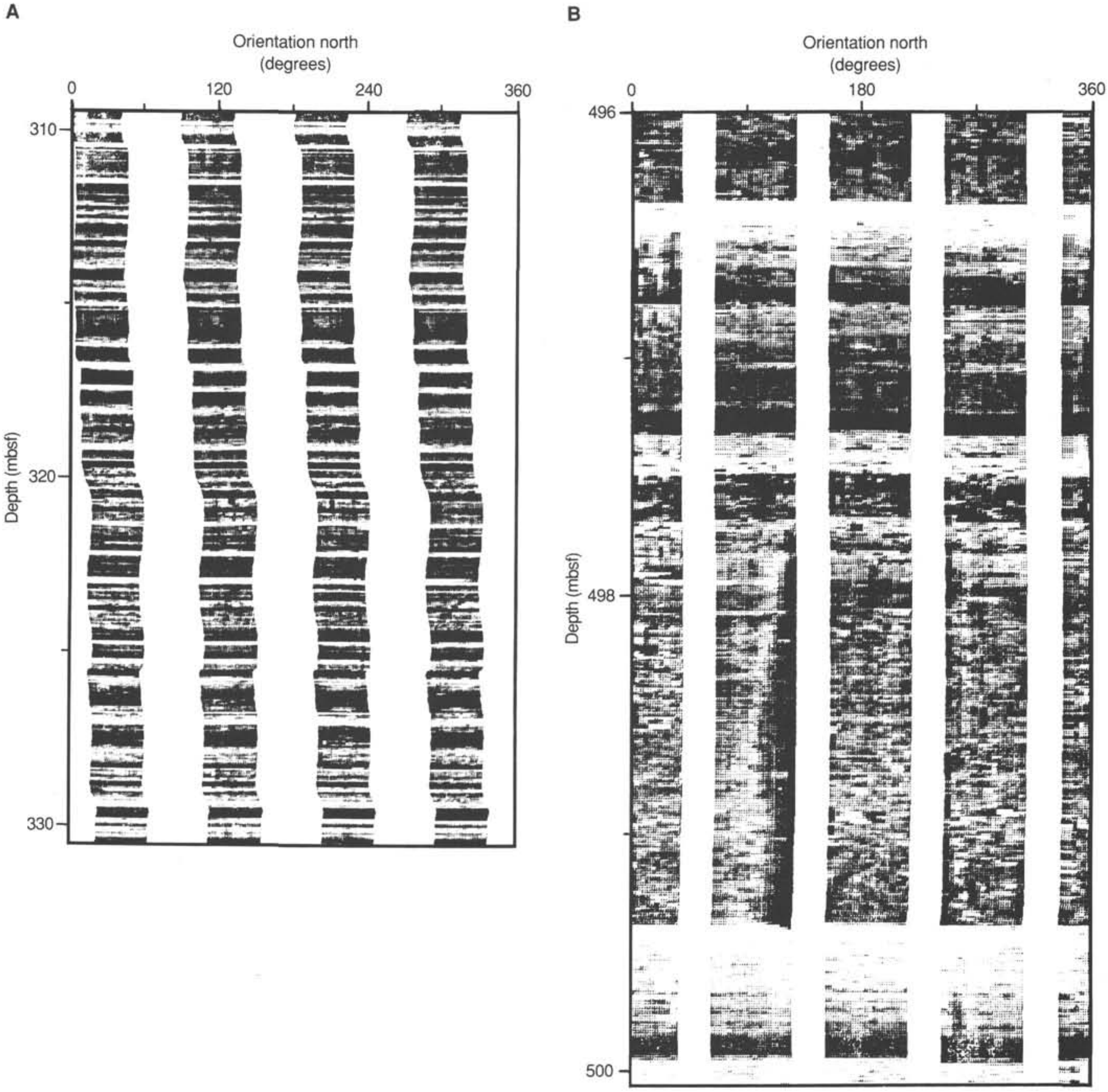

Figure 62. **A.** Formation microscanner images from 310 to 330 mbsf illustrating horizontal banding correlated with turbidites. Dark represents low resistivity; light represents high resistivity. Dark bands are correlated with the vitric or pumiceous gravels and sands at the base of the turbidites; light bands correspond to the fine grained chalk at the top of the turbidites. Vertical to horizontal scale is 1:1. **B.** Formation microscanner images from 496 to 500 mbsf illustrating three individual turbidites. The 2.1-m-thick turbidite between 497.3 and 499.4 mbsf is correlated with a turbidite measured on board in recovered core as 1.19 m thick and from 496.1 to 497.45 mbsf. Vertical to horizontal scale is 5:1.

low density in the turbidite. The FMS images could eventually allow correlation of many, if not most, of the recovered turbidites back into the subsurface formation and should improve the assignments of thickness and depth.

FMS Dipmeter Information

In addition to providing gray-scale images, FMS data can be processed to yield a dipmeter plot. A discussion of the methods of dipmeter processing, and of the hazards and pitfalls of correlating between the dipmeter results and core measurements, is presented in the "Downhole Measurements" section of the "Explanatory Notes" chapter (this volume). Results of the dipmeter processing for Hole 840B are presented in Figure 63; only the highest quality dipmeter picks are plotted.

Between 87 and 250 mbsf, the dip magnitude and direction are highly scattered, a consequence of the poor data quality in this section of the hole caused by hole width, ellipticity, and rugosity exceeding the tool capabilities. From 250 to 516 mbsf, however, the data give extremely consistent results. The dip averages about 2° at 250–300 mbsf and increases steadily downhole to about 4.5°

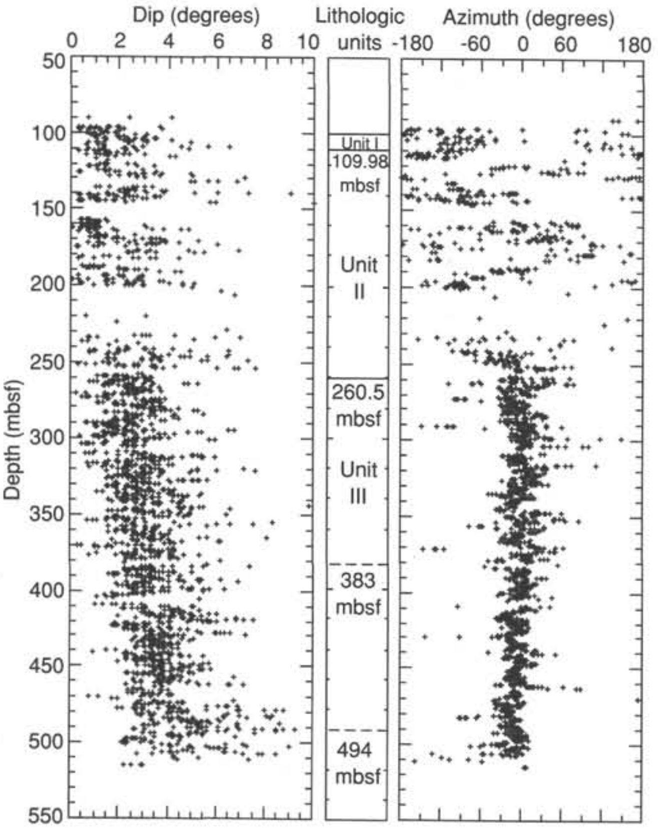

Figure 63. Dip in degrees and azimuth of dip calculated from formation microscanner data. Data above 250 mbsf are scattered because of the poor hole conditions; data below yield a well-constrained dip of 2° (250 mbsf) to 4° (500 mbsf) to the north.

at 500 mbsf. The range in values is as much as 10°, but most of the values are within 2° of the average. The azimuth averages 0° from 250 to about 400 mbsf, with a range of about 30° west and east. The azimuth gradually changes to slightly westerly beginning at about 350 mbsf and averages about N15°W at the base of the hole. Thus, from the base of the hole to 250 mbsf, the azimuth changes from slightly northwesterly to northerly.

DISCUSSION

The objectives at Site 840 were addressed in three holes that collectively penetrated a total of 597.2 mbsf. One of the principal objectives for this site was to be able to identify a seismic reflector (Horizon A) seen in the regional seismostratigraphy. This was successfully achieved, not as we expected on biostratigraphic, lithostratigraphic, or structural criteria, but on variations in physical properties and downhole logging data. A marked increase in the average velocity at about 383 mbsf correlates with a drop in total carbonate percent from about 30%–40% to almost zero, and a discrete zone of significant smectitic alteration of the vitric sandstones and siltstones. We think that this corresponds to the 400–420 mbsf level of Horizon A on seismic reflection profiles, as predicted using sonobuoy velocities.

We had expected that the main sediment types to be cored at Site 840 would be a platform carbonate section with lesser amounts of volcaniclastic material. We cored mainly Miocene age turbidites with a very large contribution of volcaniclastic sediments. The sediment textures, and the numerous relatively thin turbidites, imply that the site was located on the distal end of sediment deposits derived from some former volcanic edifice on the Lau Ridge before rifting of the Lau Basin. The lowermost sediments comprise volcaniclastic breccia and conglomerate, which fine upward to turbiditic vitric sandstones, interpreted as indicating the transition from a proximal to a more distal source. This downward coarsening of the sediment suggests either that volcanic activity at the source had diminished with time and the supply of sediments was decreased or that the locus of volcanism had retreated westward, thereby diminishing the gradient to the depocenters. The Miocene sediment accumulation rate varied from an average of 357 mm/k.y. in the depth range from 320 to 570 mbsf to an average rate of 820 mm/k.y. in the depth range from 101 to 265 mbsf. These high rates reflect the large volumes of volcaniclastic sediments being supplied and must reflect the high rate of volcanic eruptive activity.

A probable biostratigraphic hiatus of approximately 1 m.y. lies between 95 and 101 mbsf; it corresponds to a steep decrease in sedimentation rates. The Pliocene and younger sedimentation rate is markedly less relative to the Miocene; between 95 and 101 mbsf it is 10 mm/k.y. The rate increases to 50 mm/k.y. between 24 and 95 mbsf and then decreases again, above 24 mbsf to 14 mm/k.y. The sharp decrease in sedimentation rate in the early Pliocene is not surprising as the present evidence is that the first stages of breakup of the crust to form the Lau Basin must have been at about 5.6 Ma or before. Although it is speculative to suggest that the hiatus has any bearing on this timing of beginning of rifting, it could reflect thermally driven regional uparching at the onset of backarc crustal rifting.

Paleomagnetic data below this hiatus show a well-behaved agreement with the late Miocene geomagnetic reversal history down to the top of Chron 4 (6.7 Ma, 521.7 mbsf), and the magnetic stratigraphy confirms the rapid volcaniclastic sedimentation in the late Miocene, ranging between 148 and 213 mm/k.y. Paleomagnetic data recovered from oriented APC cores in the upper part of the Site 840 section indicate a 21° ± 11° clockwise rotation of the Tonga Arc with respect to oriented sections in the western Lau Basin.

REFERENCES

Austin, J., Taylor, F. W., and Cagle, C. D., 1989. Seismic stratigraphy of the Central Tonga Ridge. *Mar. Pet. Geol.,* 6:71–92.

Baker, P. A., and Kastner, M., 1981. Constraints on the formation of sedimentary dolomite. *Science,* 213:215–216.

Berggren, W. A., Kent, D. V., Flynn, J. J., and Van Couvering, J. A., 1985a. Cenozoic geochronology. *Geol. Soc. Am. Bull.,* 96:1407–1418.

Berggren, W. A., Kent, D. V., and Van Couvering, J. A., 1985b. The Neogene: Part 2. Neogene geochronology and chronostratigraphy. *In* Snelling, N. J. (Ed.), *The Chronology of the Geological Record.* Geol. Soc. London Mem., 10:211–260.

Broecker, W. S., and Peng, T.-H., 1982. *Tracers in the Sea:* Palisades, NY (Eldigio Press).

Buchbinder, B., and Halley, R. B., 1985. Source rock evaluation of outcrop and borehole samples from Tongatapu and 'Eua Islands, Tonga, and from Viti Levu and Vanua Levu Islands, Fiji. *In* Scholl, D. W., and Vallier, T. L. (Eds.), *Geology and Offshore Resources of Pacific Island Arcs—Tonga Region.* Circum-Pac. Counc. Energy Miner. Resour., Earth Sci. Ser., 2:335–349.

Bukry, D., 1973. Low-latitude coccolith biostratigraphic zonation. *In* Edgar, N. T., Saunders, J. B., et al., *Init. Repts. DSDP,* 15: Washington (U.S. Govt. Printing Office), 685–703.

Childs, J. R., 1985. Acoustic properties of sediment on the southern Tonga platform as determined from seismic sonobuoy studies. *In* Scholl, D. W., and Vallier, T. L. (Eds.), *Geology and Offshore Resources of Pacific Island Arcs—Tonga Region.* Circum-Pac. Counc. Energy Miner. Resour., Earth Sci. Ser., 2:39–48.

Church, B. N., and Johnson, W. M., 1980. Calculation of the refractive index of silicate glasses from the chemical composition. *Geol. Soc. Am. Bull.,* 91:619–625.

Davey, F. J., 1982. The structure of the South Fiji Basin. *Tectonophysics,* 87:185–241.

Eguchi, T., 1984. Seismotectonics of the Fiji Plateau and Lau Basin. *Tectonophysics*, 102:17–32.
Ekdale, A. A., Bromley, R. G., and Pemberton, S. G. (Eds.), 1984. *Ichnology: Trace Fossils in Sedimentology and Stratigraphy*. SEPM Short Course, No. 15.
Emeis, K.-C., and Kvenvolden, K. A., 1986. Shipboard organic geochemistry on *JOIDES Resolution*. *ODP Tech. Note*, No. 7.
Espitalié, J., Laporte, J. L., Leplat, P., Madec, M., Marquis, F., Paulet, J., and Boutefeu, A., 1977. Méthode rapide de caractérisation des roches mères, de leur potentiel pétrolier et de leur degrée d'évolution. *Rev. Inst. Fr. Pet.*, 32:23–42.
Exon, N. F., Herzer, R. H., and Cole, J., 1985. Mixed volcaniclastic and sedimentary rocks from the Cenozoic southern Tonga platform and their petroleum potential. *In* Scholl, D. W., and Vallier, T. L. (Eds.), *Geology and Offshore Resources of Pacific Island Arcs—Tonga Region*. Circum-Pac. Counc. Energy Miner. Resour., Earth Sci. Ser., 2:75–108.
Fisher, R. V., and Schmincke, H.-U., 1984. *Pyroclastic Rocks:* New York (Springer-Verlag).
Flügel, E., 1984. *Microfacies Analysis of Limestones:* Berlin (Springer-Verlag).
Gieskes, J. M., 1983. The chemistry of interstitial waters of deep-sea sediments: interpretation of Deep-Sea Drilling data. *In* Riley, J. P., and Chester, R. (Eds.), *Chemical Oeanography* (Vol. 8): London (Academic Press), 222–269.
Gieskes, J. M., and Lawrence, J. R., 1981. Alteration of volcanic matter in deep-sea sediments: evidence from the chemical composition of interstitial waters from deep-sea drilling cores. *Geochim. Cosmochim. Acta*, 45:1687–1703.
Hamburger, M. W., and Isacks, B. L., 1988. Diffuse back-arc deformation in the southwestern Pacific. *Nature*, 332:599–604.
Hawkins, J. W., 1989. Cruise Report—ROUNDABOUT Expedition, Legs 14, 15, R/V *Thomas Washington*. SIO Ref. Ser., No. 89-13.
Herzer, R. H., Ballance, and Stevenson, A. J., in press. Contributions to the marine and onland geology and resource assessment of the Tonga-Lau-Fiji region.
Herzer, R. H., and Exon, N., 1985. Structure and basin analysis of the southern Tonga forearc. *In* Scholl, D. W., and Vallier, T. L. (Eds.), *Geology and Offshore Resources of Pacific Island Arcs—Tonga Region*. Circum-Pac. Counc. Energy Miner. Resour., Earth Sci. Ser., 2:55–74.
Katz, H. R., 1986. Stratigraphy of the SW Pacific. *In* Cronan, D. S. (Ed.), *Sedimentation and Mineral Deposits in the Southwestern Pacific Ocean:* London (Academic Press), 5–82.
Kennett, J. P., Burns, R. E., Andrews, J. E., Churkin, M., Jr., Davies, T. A., Dumitrica, P., Edwards, A. R., Galehouse, J. S., Packham, G. H., and van der Lingen, G. J., 1972. Australian- Antarctic continental drift, paleo-circulation change and Oligocene deep-sea erosion. *Nature*, 239:51–55.
Kennett, J. P., Houtz, R. E., Andrews, P. B., Edwards, A. E., Gostin, V. A., Hajos, M., Hampton, M., Jenkins, D. G., Margolis, S. V., Ovenshine, A. T., and Perch-Nielsen, K., 1975. Cenozoic paleoceanography in the southwest Pacific Ocean, Antarctic glaciation, and the development of the Circum-Antarctic Current. *In* Kennett, J. P., Houtz, R. E., et al., *Init. Repts. DSDP*, 29: Washington (U.S. Govt. Printing Office), 1155–1169.
Kennett, J. P., and Srinivasan, M. S., 1983. *Neogene Planktonic Foraminifera: A Phylogenetic Atlas:* Stroudsburg, PA (Hutchinson Ross).
Kennett, J. P., and von der Borch, C. C., 1986. Southwest Pacific Cenozoic paleoceanography. *In* Kennett, J. P., von der Borch, C. C., et al., *Init. Repts. DSDP*, 90: Washington (U.S. Govt. Printing Office), 1493–1517.
Lawrence, J. R., and Gieskes, J. M., 1981. Constraints on water transport and alteration in the oceanic crust from the isotopic composition of pore water. *J. Geophys. Res.*, 86:7924–7934.
Malahoff, A., Feden, R. H., and Fleming, H. S., 1982. Magnetic anomalies and tectonic fabric of marginal basins north of New Zealand. *J. Geophys. Res.*, 87:4109–4125.
Malahoff, A., Kroenke, L. W., Cherkis, N., and Brozena, J., in press. Magnetic and tectonic fabric of the North Fiji Basin and Lau Basin. *In* Kroenke, L., and Eade, J. V. (Eds.), *Basin Formation, Ridge Crest Processes, and Metallogenesis in the North Fiji Basin*. Circum-Pac. Counc. Energy and Miner. Resour., Earth Sci. Ser.
Maung, T. U., Anscombe, K. J., and Tongilava, S. L., 1981. Assessment of petroleum potential of the southern and northern parts of the Tonga platform. Tech. Rep.—U. N. Econ. Soc. Comm. Asia Pac., CCOP/SOPAC, No. 18.
McElhinny, M. W., 1973. *Palaeomagnetism and Plate Tectonics:* Cambridge (Cambridge Univ. Press).
Nilsson, K., Florendo, F. F., and Hawkins, J. W., et al., 1989. Petrology of a nascent triple junction, northeastern Lau Basin. *Eos*, 70:1389.
Parson, L. M., et al., 1989. *RRS Charles Darwin* Cruise 33/88, 5 May–1 June 1988. Geophysical and geological investigations of the Lau back-arc basin, SW Pacific. Inst. Oceanogr. Sci. Deacon Lab. Cruise Report, No. 206.
Parson, L. M., Pearce, J. A., Murton, B. J., Hodkinson, R. A., Bloomer, S., Ernewein, M., Huggett, Q. J., Miller, S., Johnson, L., Rodda, P., and Helu, S., 1990. Role of ridge jumps and ridge propagation in the tectonic evolution of the Lau back-arc basin, southwest Pacific. *Geology*, 18:470–473.
Peirce, J., Weissel, J., et al., 1989. *Proc. ODP, Init. Repts.*, 121: College Station, TX (Ocean Drilling Program).
Sandstrom, M. W., 1985. Organic chemistry of dredge samples and oil seeps from the southern Tonga platform. *In* Scholl, D. W., and Vallier, T. L. (Eds.), *Geology and Offshore Resources of Pacific Island Arcs—Tonga Region*. Circum-Pac. Counc. Energy and Miner. Resour., Earth Sci. Ser., 2:129–129.
Sandstrom, M. W., and Philp, R. P., 1984. Biological marker analysis and stable carbon isotopic composition of oil seeps from Tonga. *Chem. Geol.*, 43:167–180.
Schmincke, H.-U., 1981. Ash from vitric muds in deep sea cores from the Mariana Trough and fore-arc regions (south Philippine Sea) (Sites 453, 454, 455, 458, 459). *In* Hussong, D. M., Uyeda, S., et al., *Init. Repts. DSDP*, 60: Washington (U.S. Govt. Printing Office), 473–481.
Scholl, D. W., and Vallier, T. L. (Eds.), 1985. *Geology and Offshore Resources of Pacific Island Arcs—Tonga Region*. Circum-Pac. Counc. Energy Miner. Resour., Earth Sci. Ser., No. 2.
Scholl, D. W., Vallier, T. L., and Packham, G. H., 1985. Framework geology and resource potential of the southern Tonga platform and adjacent terranes—a synthesis. *In* Scholl, D. W., and Vallier, T. L. (Eds.), *Geology and Offshore Resources of Pacific Island Arcs—Tonga Region*. Circum-Pac. Counc. Energy Miner. Resour., Earth Sci. Ser., No. 2:457–488.
Tappin, D. R., Herzer, R. H., and Stevenson, A. J., in press. Structure and history of an oceanic forearc—the Tonga Ridge 22° to 26° South. *In* Stevenson, A., and Ballance, P. (Eds.), *Tonga Arc:* Berlin (Springer-Verlag).
Tappin, D. R., in press. The Tonga forearc basin. *In Sedimentary Basins of the World—The South Pacific*.
Taylor, B., Fujioka, K., et al., 1990. *Proc. ODP, Init. Repts.*, 126: College Station, TX (Ocean Drilling Program).
Tissot, B. P., and Welte, D. H., 1984. *Petroleum Formation and Occurrence* (2nd ed.): Heidelberg (Springer-Verlag).
Vallier, T. L., Stevenson, A. J., and Scholl, D. W., 1985. Petrology of igneous rocks from Ata Island, Kingdom of Tonga. *In* Scholl, D. W., and Vallier, T. L. (Eds.), *Geology and Offshore Resources of Pacific Island Arcs—Tonga Region*. Circum.-Pac. Counc. Energy Miner. Resour., Earth Sci. Ser., 2:301–316.
von Stackelberg, U., 1990. R. V. Sonne cruise S048: summary of results testing a model of mineralization. *Mar. Min.*, 9:135–144.
Weissel, J. K., 1977. Evolution of the Lau Basin by the growth of small plates. *In* Talwani, M., and Pitman, W. C. (Eds.), *Island Arcs, Deep Sea Trenches and Back Arc Basins*. Am. Geophys. Union, Maurice Ewing Ser., 1:429–436.

Ms 135A-110

NOTE: All core description forms ("barrel sheets") and core photographs have been printed on coated paper and bound separately as Part 2 of this volume, beginning on page 681.

Formation microscanner images for this site are presented on microfiche in the back of Part 2.

Hole 840B: Resistivity-Sonic-Natural Gamma Ray Log Summary

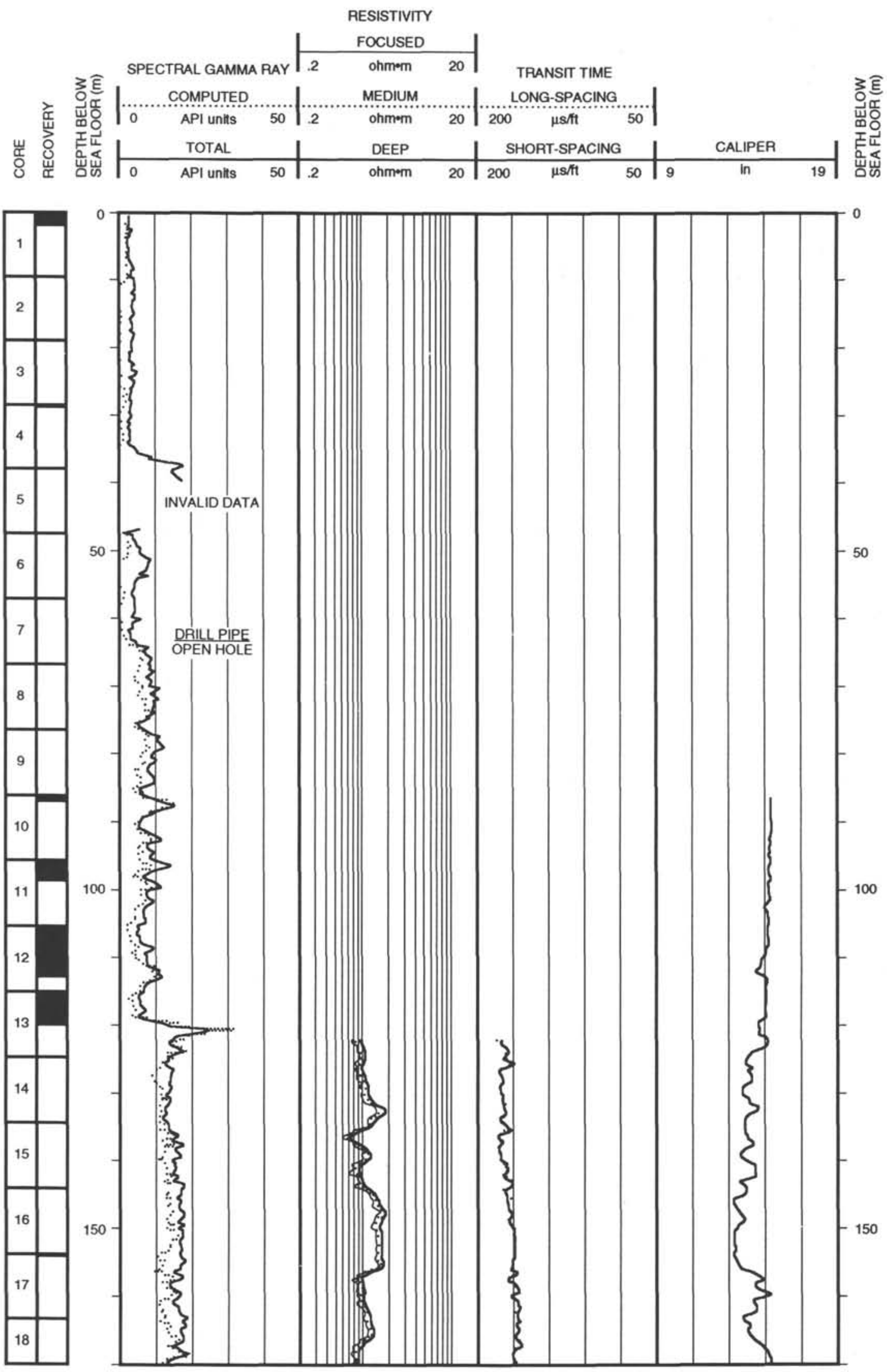

Hole 840B: Resistivity-Sonic-Natural Gamma Ray Log Summary (continued)

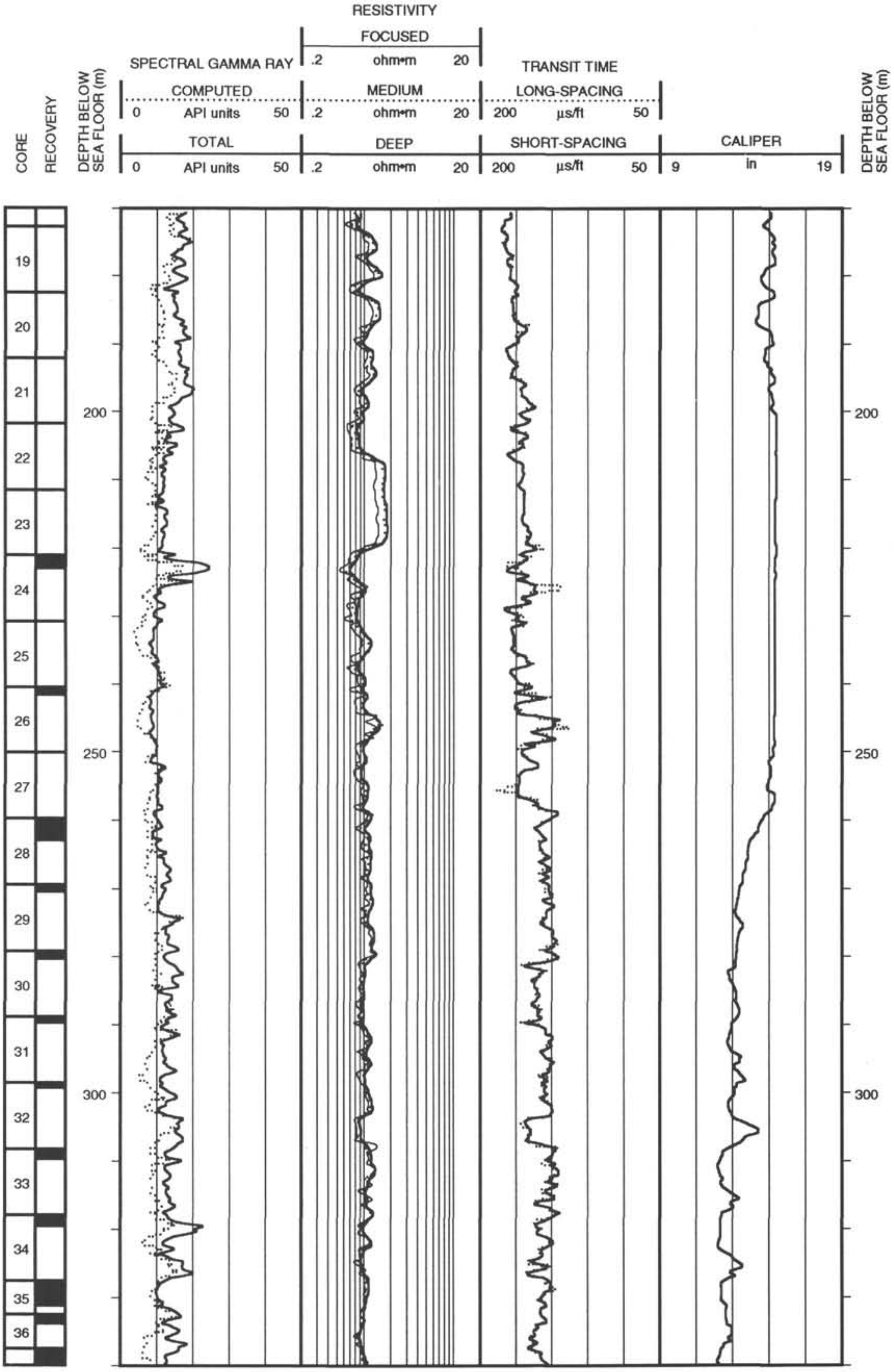

Hole 840B: Resistivity-Sonic-Natural Gamma Ray Log Summary (continued)

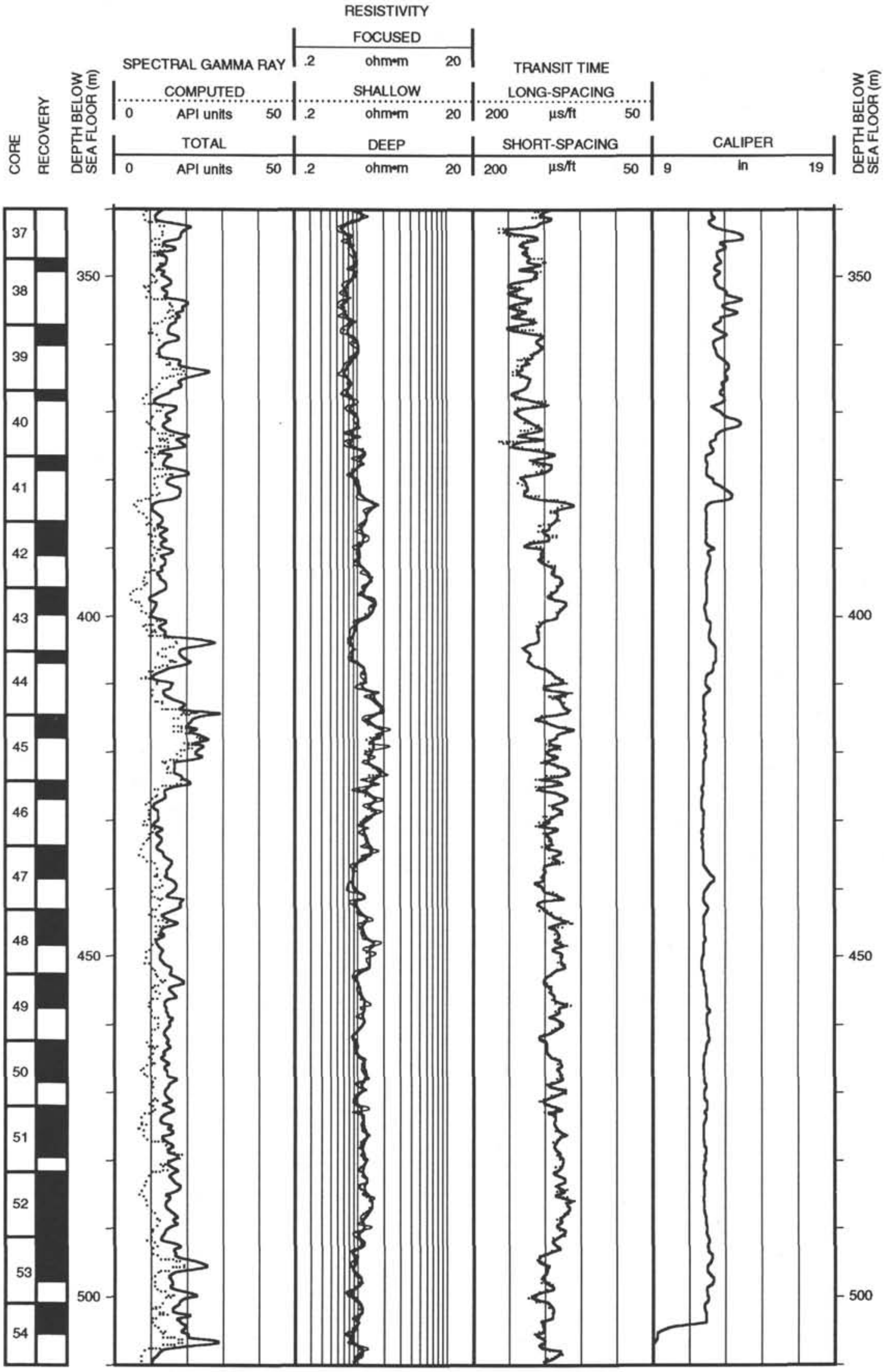

Hole 840B: Resistivity-Sonic-Natural Gamma Ray Log Summary (continued)

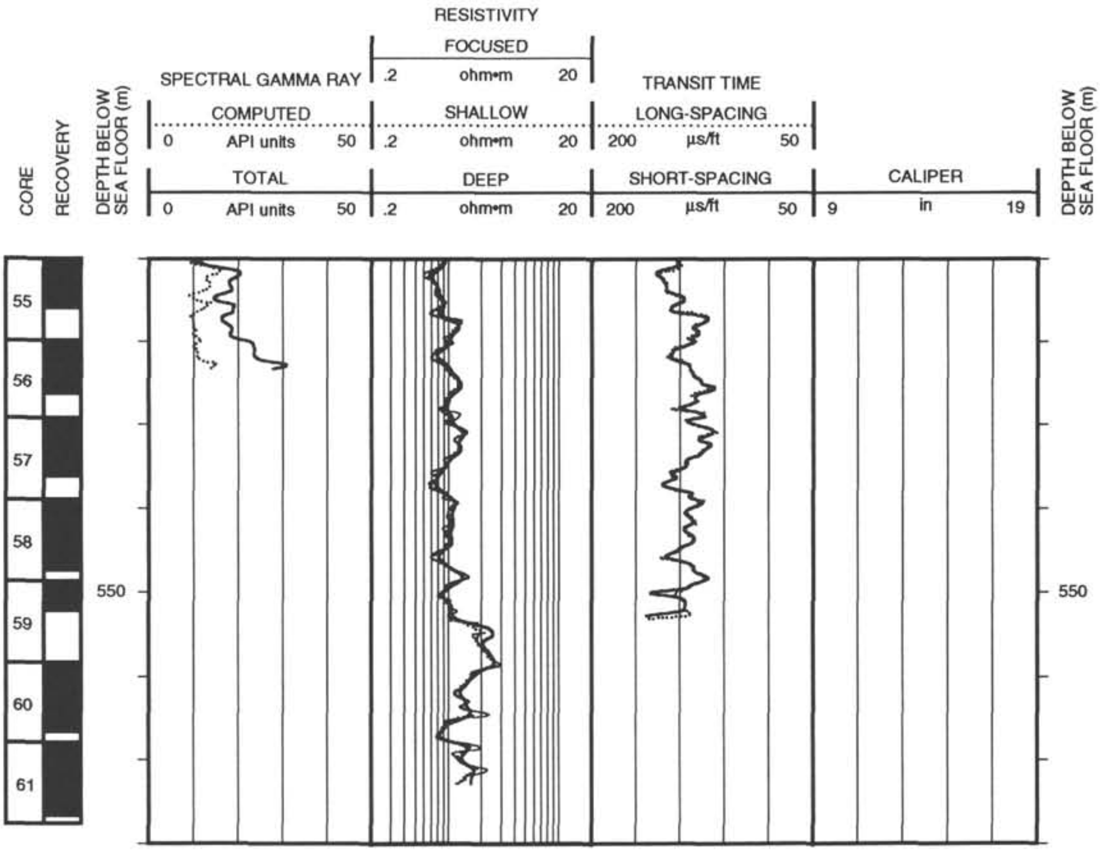

Hole 840-B: Density-Natural Gamma Ray Log Summary

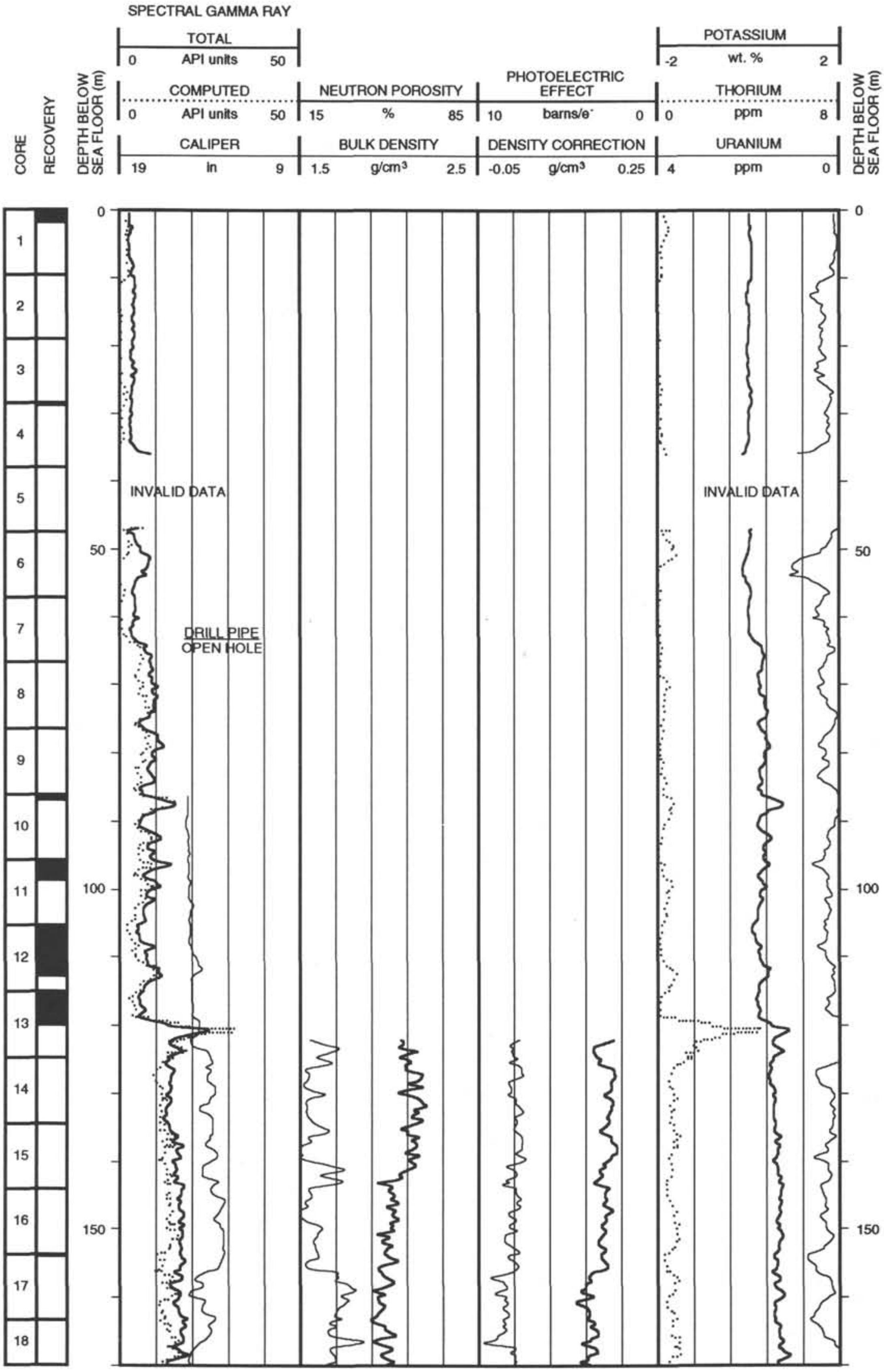

Hole 840-B: Density-Natural Gamma Ray Log Summary (continued)

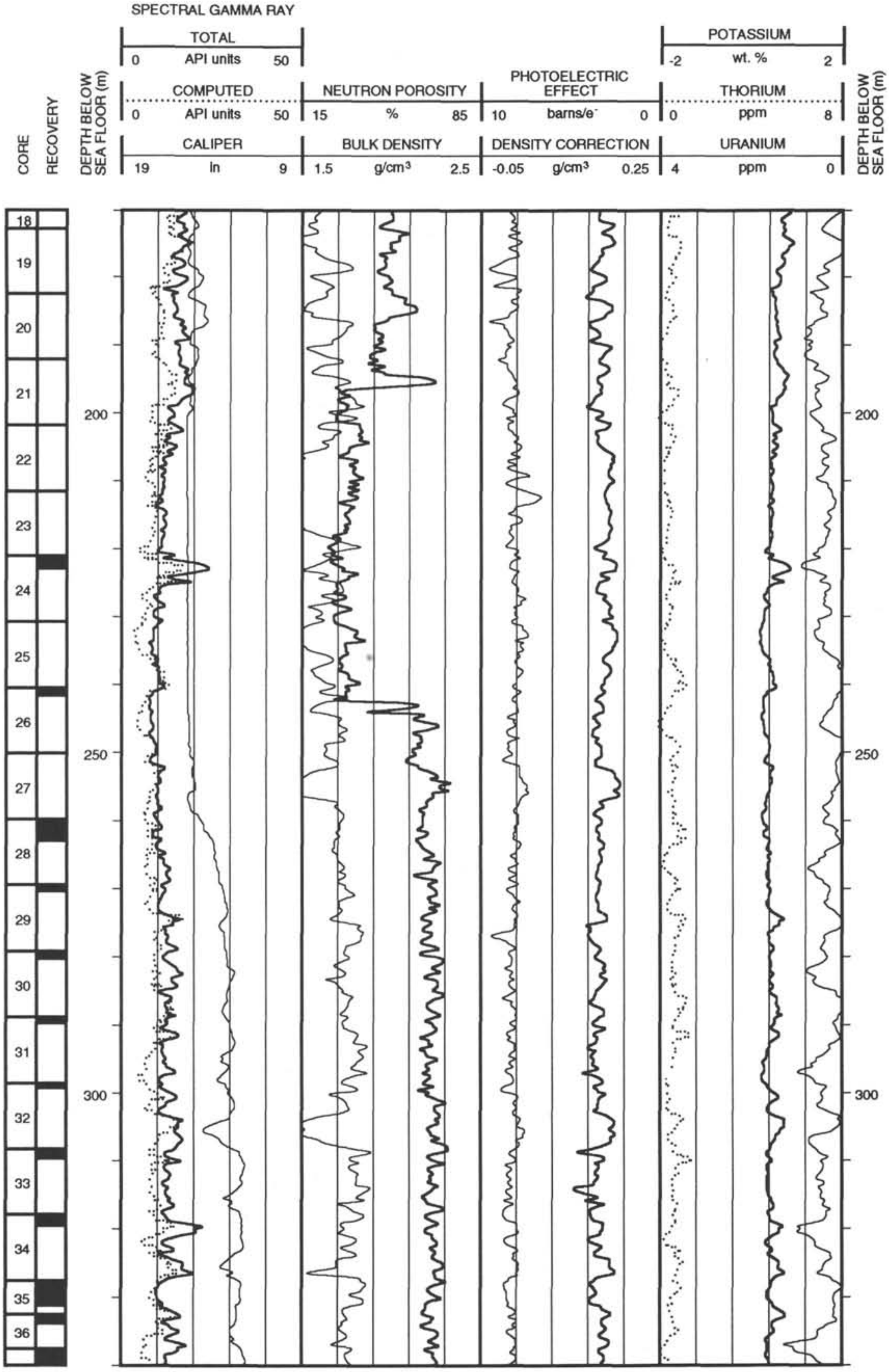

Hole 840-B: Density-Natural Gamma Ray Log Summary (continued)

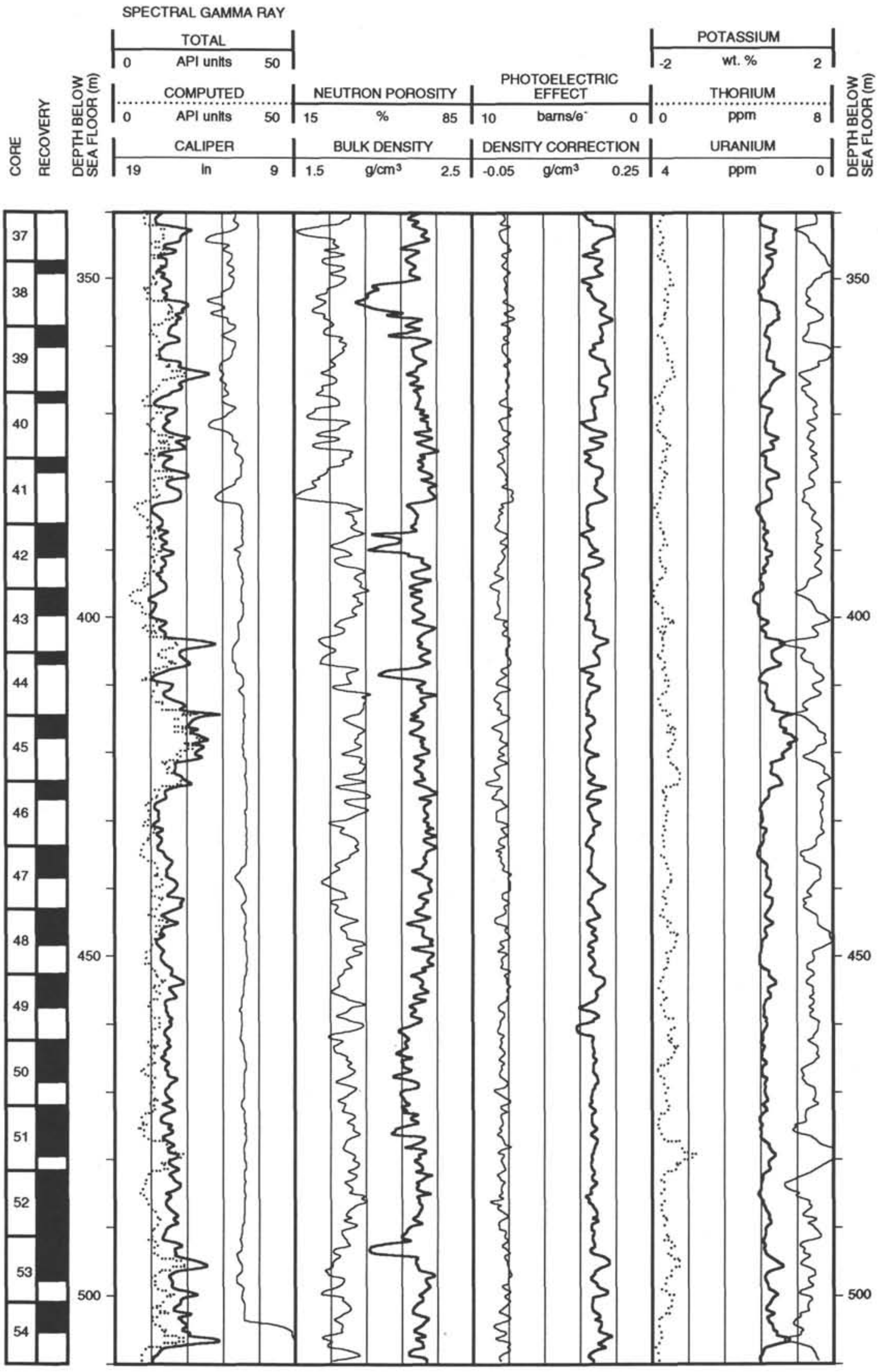

Hole 840-B: Density-Natural Gamma Ray Log Summary (continued)

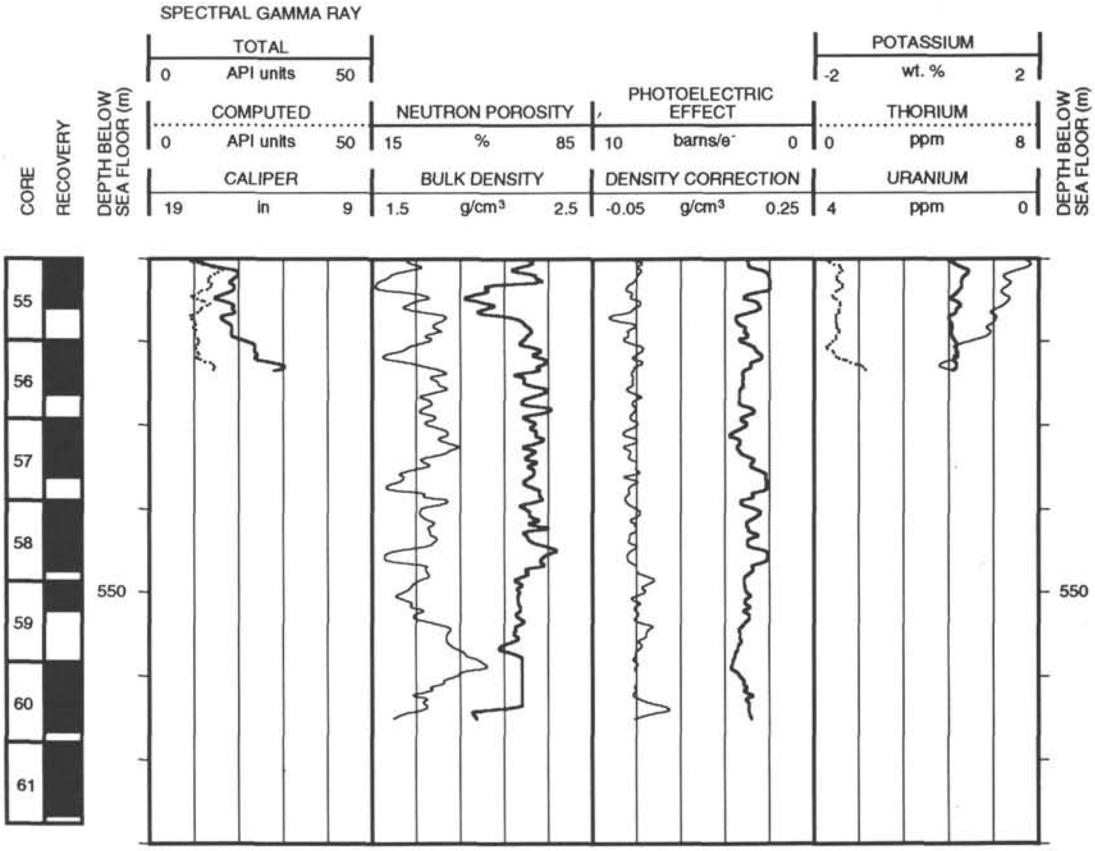

Hole 840B: Geochemical Log Summary

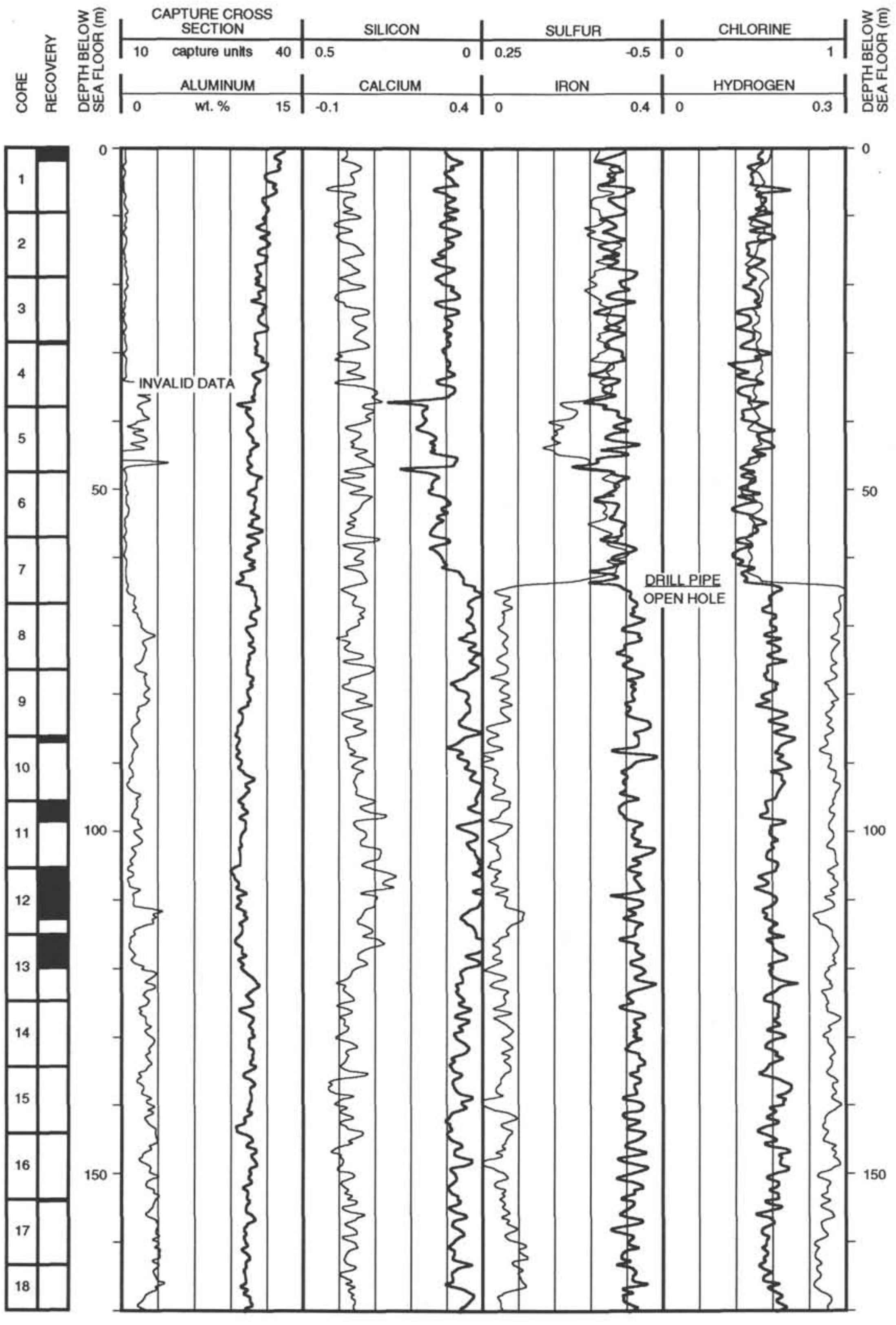

Hole 840B: Geochemical Log Summary (continued)

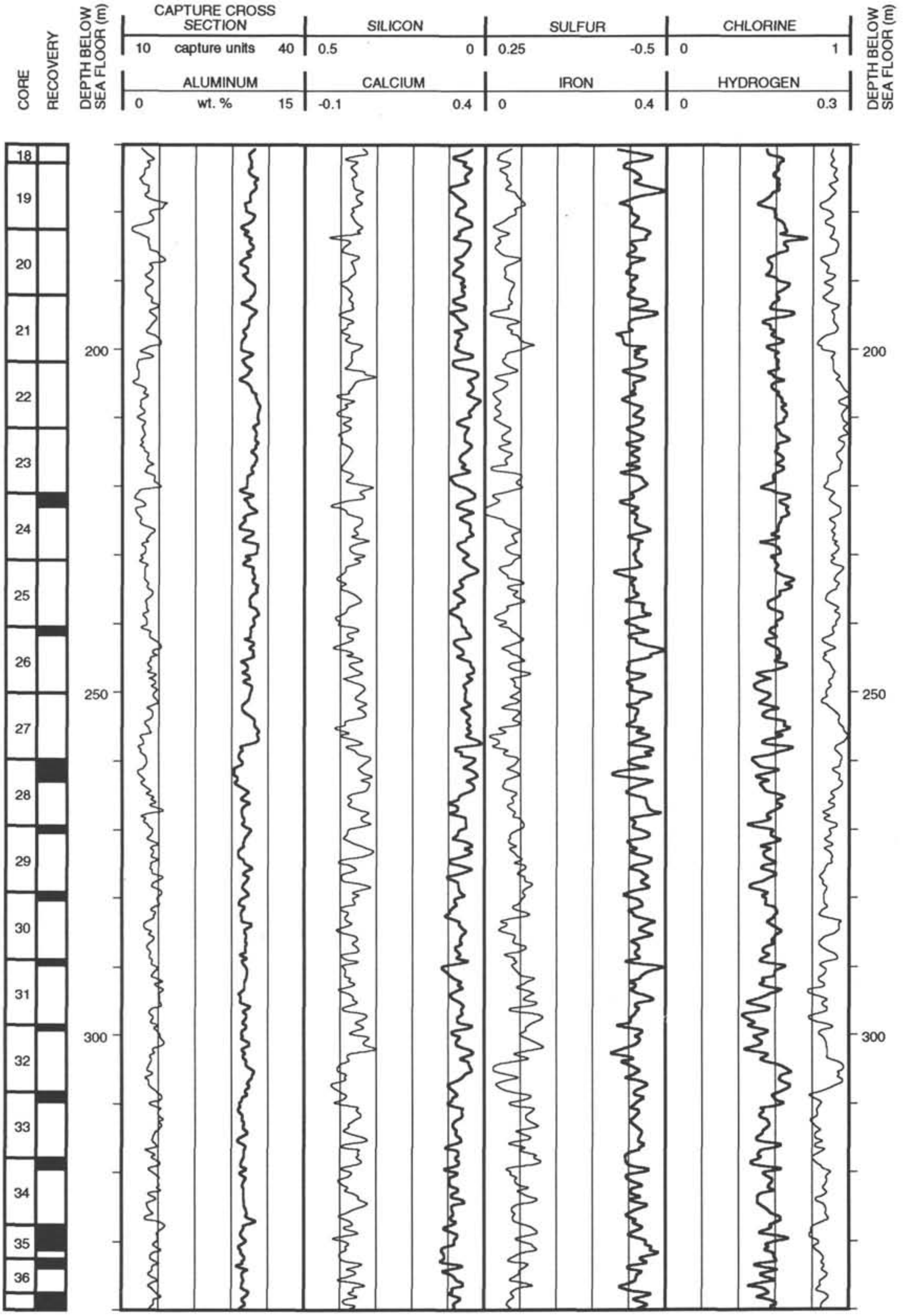

Hole 840B: Geochemical Log Summary (continued)

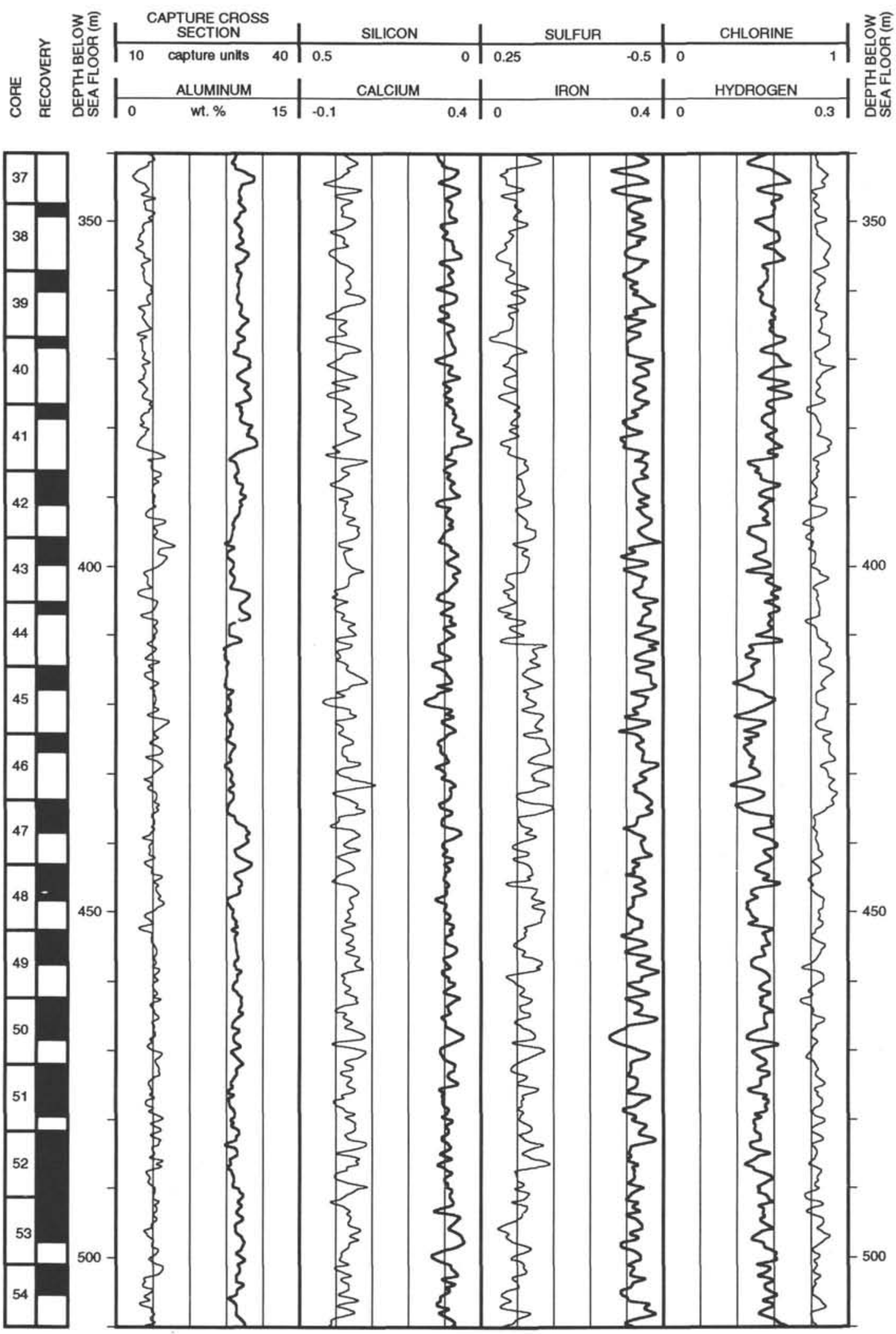

Hole 840B: Geochemical Log Summary (continued)